Magnetostriction and Magnetic Anisotropy in Non-oriented Electrical Steels and Stator Core Laminations

by

Sakda Somkun

A thesis submitted to the Cardiff University in candidature for the degree of Doctor of Philosophy

Wolfson Centre for Magnetics

Cardiff School of Engineering

Cardiff University

Wales, United Kingdom

September 2010

ProQuest LLC
789 East Eisenhower Parkway
P.O. Box 1346
Ann Arbor, MI 48106-1346

DECLARATION

This work has not previously been accepted in substance for any degree and is not concurrently submitted in candidature for any degree.

Signed ..... (candidate) Date 17/12/2010

STATEMENT 1

This thesis is being submitted in partial fulfillment of the requirements for the degree of PhD.

Signed ..... (candidate) Date 17/12/2010

STATEMENT 2

This thesis is the result of my own independent work/investigation, except where otherwise stated. Other sources are acknowledged by explicit references.

Signed ..... (candidate) Date 17/12/2010

STATEMENT 3

I hereby give consent for my thesis, if accepted, to be available for photocopying and for inter-library loan, and for the title and summary to be made available to outside organisations.

Signed ..... (candidate) Date 17/12/2010

Acknowledgements

This work was carried out at the Wolfson Centre for Magnetics, Cardiff School of Engineering, Cardiff University to which I am grateful for providing the resources needed to complete this project. I would also like to thank those below.

Special thanks to my primary supervisor Professor Anthony Moses for his guidance and stimulation. He always challenged me in alternative views and his insight knowledge improved this work significantly.

I am very grateful to my second supervisor Dr Philip Anderson. This work might have not been completed without his expertise in magnetic measurement. Collaboration with my colleague Mr Piotr Klimczyk also fulfilled this project. Dr Stanislaw Zurek, his wonderful 2D magnetisation system was a solid foundation of my work. Invaluable comments of Professor Philip Beckley and Professor Ernie Freeman contributed significantly on this project. Staff and students at the Wolfson Centre, their help and suggestions are deeply appreciated.

I might have not finished this work on time without the helps of supporting staff of the Cardiff School of Engineering, particularly Miss Nicola Davies of the Wolfson Centre, Mr Brian Hargreaves of the IT Services, Mr Des Sanford of the A.C.E. Laboratories, Mr Steve Mead of the mechanical workshop, and Mr Alan Davies of the electrical and electronic workshop.

The Ministry of Science and Technology, the Royal Thai Government gave me this opportunity not only to study this doctoral degree but also to see the world. The Office of the Civil Service Commission, and Office of Educational Affairs, the Royal Thai Embassy, London have facilitated me throughout this project. ThyssenKrupp Electrical Steel GmbH, their non-oriented electrical steel was a good lesson for this study.

I am very grateful to my beloved girlfriend Wan who has been always with me throughout this project. Last but not least, my greatest thanks go to my father Prakob, my mother Samrarn, my brother Somsak, and my sister Sudapa for their love and support since I was born.

Summary

Magnetostriction is a source of vibration and acoustic noise of electrical machines and it can be highly anisotropic even in non-oriented electrical steel. Understanding of magnetostriction under magnetisation and stress conditions present in stator core laminations can help predict the core vibration and radiated noise.

Anisotropy of magnetostriction of a 0.50 mm thick non-oriented steel investigated in Epstein strips cut at angles to the rolling direction was much higher than the anisotropy of its magnetic and elastic properties because magnetostriction arises directly from magnetic domain processes. Magnetostriction of a disc sample of the 0.50 mm thick steel was measured under 1D and 2D magnetisation and compared with that of a 0.35 mm thick steel with different anisotropy level. A 2D magnetostriction model and an analytical simple domain model were used to explain the experimental results. 2D magnetostriction is dependent on the magnetostrictive anisotropy and the ratios of the transverse to longitudinal magnetostriction. AC magnetostriction measured in the disc samples was larger than in the Epstein strips due to the form effect.

An induction motor model core was constructed from the 0.50 mm thick steel for measurements of localised flux density and deformation. Core deformation due to Maxwell forces was calculated. Magnetostriction and specific power loss of the core material under magnetisation conditions present in the core was measured. The localised loss in the stator teeth, tooth roots and back iron differed from their average value by 52%, 19% and 36% due to the magnetic anisotropy. Magnetostriction was estimated to be about 55% and 80% of the radial deformation at the tooth root and back iron regions respectively. Stator teeth deformed asymmetrically and the magnitude of the space harmonics increased due to the magnetostrictive anisotropy.

The measurement results inferred that 2D magnetostriction can be predicted from the magnetostrictive anisotropy and vice versa. Also, core deformation and vibration of large machines, where segmented stator core laminations are used, can be estimated analytically with the knowledge of 2D magnetostriction of the core material.

List of Abbreviations and Symbols

Abbreviations

1D	One-dimensional or unidirectional
2D	Two-dimensional
AC	Alternating current
ACW	Anticlockwise direction
CGO	Conventional grain-oriented
CW	Clockwise direction
DAQ	Data acquisition
FEM	Finite element method/modelling
FF	Form factor
FFT	Fast Fourier transformation
GO	Grain-oriented
HGO	Highly grain-oriented
NO	Non-oriented
NPT	Needle probe technique
ODF	Orientation distribution function
PWM	Pulse-width modulated
RCP	Rogowski-Chattock potential
RD	Rolling direction
RMS	Root mean square
SST	Single strip/sheet tester
TD	Transverse direction
THD	Total harmonic distortion

Subscripts

x	Variables in the RD
y	Variables in the TD
xy	Variables between the RD and TD
n	Variables in the normal direction
r	Variables in the radial direction
t	Variables in the tangential direction
rt	Variables between the radial and tangential directions
PP	Peak to peak value

Symbols

α	Misalignment angle of rosette strain gauges
α_1, α_2, α_3	Cosines of the magnetisation direction relative to the [100], [010] and [001] axes of a cubic crystal respectively
β_1, β_2, β_3	Cosines of the observed magnetostriction direction relative to the [100], [010] and [001] axes of a cubic crystal respectively
χ	Susceptibility

δ	Angle for stress and strain transformations
δ_{ij}	Kronecker delta
ε	Strain
$\boldsymbol{\varepsilon}$	Strain tensor
$\varepsilon_1, \varepsilon_2$	Maximum and minimum strains in the principal axis
ε_x	Strain component along the x or rolling directions
ε_y	Strain component along the y or transverse directions
ε_r	Strain component along the radial direction
ε_t	Strain component along the tangential direction
$\boldsymbol{\varepsilon}^{\mathbf{M}}$	Strain tensor due to Maxwell forces
ε_r^M	Component of strain due to Maxwell forces along the radial direction
ε_t^M	Component of strain due to Maxwell forces along the tangential direction
ϕ_e	Electrical angle in the stator core
ϕ_m	Mechanical angle in the stator core
γ_{rt}	Shear strain component between the radial and tangential directions
γ_{xy}	Shear strain component between the RD and TD or x and y directions
γ_{rt}^{λ}	Shear magnetostriction between the radial and tangential directions
γ_{xy}^{λ}	Shear magnetostriction between the RD and TD
γ_{rt}^{M}	Shear strain between the radial and tangential directions due to Maxwell forces
λ	Magnetostriction
$\boldsymbol{\lambda}$	Magnetostriction tensor
λ_1, λ_2	Maximum and minimum magnetostriction components in the principal axis
λ_r	Magnetostriction component along the radial direction
λ_t	Magnetostriction component along the tangential direction
λ_x	Magnetostriction component along the RD
λ_y	Magnetostriction component along the TD
$\lambda_{\parallel}$	Longitudinal magnetostriction
$\lambda_{\perp}$	Transverse magnetostriction
μ	Permeability
μ_0	Permeability of the free space
μ_r	Relative permeability
$\mu_{r_{AC}}$	Relative permeability under alternating magnetisation
ν	Poisson's ratio
ν_{eff}	Effective number of the degrees of freedom of the standard uncertainty
ν_i	Number of the degrees of freedom of the standard uncertainty u(x_i)
θ	Angle between the major magnetisation direction and the RD
ρ	Resistivity of electrical steel laminations

ρ_m	Mass density of electrical steel laminations
σ	Stress
$\boldsymbol{\sigma}$	Stress tensor
σ_1, σ_2	Maximum and minimum stresses in the principal axis
σ_r	Stress component along the radial direction
σ_t	Stress component along the tangential direction
σ_x	Stress component along the x or rolling directions
σ_y	Stress component along the y or transverse directions
$\boldsymbol{\sigma}^M$	Maxwell stress tensor
σ_n^M	Maxwell stress component along the normal direction
σ_r^M	Maxwell stress component along the radial direction
σ_t^M	Maxwell stress component along the tangential direction
τ	Shear stress
τ_m	Time constant of the 2D magnetostriction model
τ_{xy}	Shear stress component between the RD and TD or x and y directions
τ_{rt}	Shear stress component between the radial and tangential directions
ω	Frequency in radian per second
ξ	Magnetic Poisson's ratio
ξ_x, ξ_y	Magnetic Poisson's ratios along the RD and TD
ξ_{d1}, ξ_{d2}	Rayleigh damping factors
$\overline{\psi}_{ag}$	Average flux under each pole of the induction motor model core

a	Axis ratio of the flux density loci
A	Area
A_x	Anisotropy factor of variable x
B, $\mathbf{B}$	Flux density
b	Instantaneous flux density
b_n	Instantaneous flux density component along the normal direction
b_r	Instantaneous flux density component along the radial direction
b_t	Instantaneous flux density component along the tangential direction
b_x	Instantaneous flux density component along the RD
b_y	Instantaneous flux density component along the TD
$\hat{B}$	Peak value of flux density
$\hat{B}_x$	Peak value of flux density component along the RD
$\hat{B}_y$	Peak value of flux density component along the TD
$\hat{B}_r$	Peak value of flux density component along the radial direction
$\hat{B}_t$	Peak value of flux density component along the tangential direction
$\hat{B}_1$, $\hat{B}_2$	Peak flux density in the major and minor axes
B_r	Remanent flux density
$\mathbf{B}_{ed}$	Strain-displacement matrix

$\mathbf{C}$	Damping matrix
c_{11}	Elastic modulus of a single crystal
c_{12}	Elastic modulus of a single crystal
c_i	Sensitivity coefficients of measurement uncertainties
d	Thickness of electrical steel laminations
D	Diameter of the stator core
$\mathbf{d}_e$	Element displacement matrix
$\mathbf{d}_n$	Nodal displacements matrix
$\mathbf{D}_s$	System displacement
D_{xy}	Shear magnetic modulus between the RD and TD
d°	Electrical angle between two adjacent stator slots
e	Induced voltage due to Faraday's law
e_x	Induced voltage along the RD
e_y	Induced voltage along the TD
E	Young's modulus
$\mathbf{E}$	Stress-strain operator
E_a	Crystal anisotropy energy
E_N	Magnetostatic energy
E_{ph}	Back emf voltage in each phase of the stator winding
F	Force
$\mathbf{F}$	Body force matrix
f_m	Magnetising frequency
G	Shear modulus
h	Instantaneous magnetic field
h_x	Instantaneous magnetic field component along the RD
h_y	Instantaneous magnetic field component along the TD
H	Magnetic field
$\hat{H}$	Peak value of magnetic field
H_c	Coercive force
i_x, i_y	Magnetisation currents in the x and y axes of the 2D magnetisation system
i_A, i_B, i_C	Instantaneous currents of the motor model core
I_A, I_B, I_C	RMS currents of the motor model core
J	Magnetic polarisation
k	Axis ratio of an ellipsoid
K_1	Material anisotropy constant
K_2	Material anisotropy constant
K_d	Distribution factor of the stator winding
K_g	Gauge factor of a resistance strain gauge
K_{h_x}, K_{h_y}	Area-turn constants of the orthogonal h coils
K_p	Pitch factor of the stator winding
k_s	Stiffness coefficient

$\mathbf{K}_s$	System stiffness matrix
$\mathbf{k}_s$	Element stiffness matrix
l	Sample length
L	Axial length of the stator core
l_b	Width of b coils
l_m	Mean path length of the SST
m	Mass of specimens
M	Magnetisation
M_s	Saturation magnetisation
$\mathbf{M}_a$	Mass matrix
M_r	Remanent magnetisation
$\mathbf{N}$	Shape function matrix
N_0	Initial demagnetised factor before deformation of an ellipsoid
N_1, N_2	Turn numbers of the primary and secondary windings of the SST
N_c	Turn number per coil of the stator winding
N_{ph}	Total turn numbers in series per phase of the stator winding
p	Number of pole pairs of the stator winding
P	Magnetic modulus
P_{clas}	Classical eddy current loss in electrical steel laminations
P_{cu}	Copper loss of the induction motor model core
P_{fe}	Iron loss of the induction motor model core
P_s	Specific power loss in electrical steel laminations
P_{tot}	Total loss of the induction motor model core
P_x, P_y	Magnetic moduli along the RD and TD
p°	Pitch factor of the stator winding
R_{sh}	Shunt resistor
t	Time
T	Time period
T_C	Curie temperature
u	Displacement along the x direction
U_0	Strain energy density
$u_A(x)$	Type A uncertainty of the variable x
$u_B(x)$	Type B uncertainty of the variable x
$u(x)$	Standard uncertainty of the variable x
$U(x)$	Expanded uncertainty of the variable x
v	Displacement along the y direction
W	Mechanical work
W_ε	Strain energy

List of Contents

Chapter 1

Aims of the Investigation

Non-oriented (NO) electrical steel commonly used in electrical machines, is often treated as being magnetically and mechanically isotropic in its plane. However, there can be a significant anisotropy in the $B-H$ characteristics in some grades of NO steel. It has been reported that the magnetic anisotropy in NO steel increases air gap flux harmonics [*1.1*], cogging torque [*1.2*], and overall core losses [*1.3*] of electrical machine cores. Magnetomechanically coupled properties such as magnetostriction in NO steel have been reported to be possibly far more anisotropic than its specific power losses [*1.4*].

In AC machine stator cores, two-dimensional (2D) flux mainly occurs in the tooth roots and back iron. At the tooth roots, the flux loci are nearly circular then become elliptical when moving towards the back iron [*1.5*]. Magnetostriction under such 2D magnetisation is much higher than that under unidirectional (1D) magnetisation [*1.6-8*]. It is highly sensitive to the magnitude and wave shape of the flux density. The angles (θ) of the major axes of elliptical flux loci to the rolling direction (RD) also play an important role in high value of 2D magnetostriction similar to that under alternating magnetisation [*1.9*].

Vibration and emitted acoustic noise of AC machines are of increasingly concern. The radial component of the Maxwell forces across the air gap acting on the tips of stator teeth of a rotating electrical machine is generally considered to be a main magnetic source of stator core vibration [*1.10*]. Magnetostrictive force in the core material has been reported to be another harmful vibration source [*1.11*], and it can be

responsible for up to 50 % of the total electromagnetic force [*1.12*]. Core deformation and vibration due to magnetostriction have been calculated separately from the Maxwell forces based on an assumption of weak coupling between the magnetic and mechanical systems [*1.13*].

The relationship between 2D magnetostriction and magnetostrictive anisotropy in NO steel is investigated and the effect of magnetostriction and its anisotropy on the deformation of induction machine stator cores, where NO steel laminations are subjected to 2D magnetisation under the dynamic Maxwell stresses, is quantified. This information could be very important to transformer or motor manufacturers who then could predict core deformation, vibration and radiated acoustic noise at the design stage.

In summary, the main aims of this work are as follows:

- To investigate magnetic and magnetostrictive anisotropy of Epstein strips of NO electrical steels.
- To measure 1D and 2D magnetostriction of NO steel laminations, and to compare and correlate with the magnetostrictive anisotropy of Epstein samples.
- To construct an induction motor model core for measurement of localised flux density and deformation.
- To investigate 2D magnetostriction under magnetisation conditions present in the induction motor model core, and to quantify the effects of magnetostriction and its anisotropy on core deformation.

1.1 References for Chapter 1

[*1.1*] I. Zagradišnik and B. Hribernik, "Influence of anisotropy of magnetic material on the saturation harmonics in the 3-phase induction motor," *IEEE Transactions on Magnetics*, Vol. 24, pp. 491-494, 1988.

[*1.2*] S. Yamaguchi, A. Daikoku, and N. Takahashi, "Cogging torque calculation considering magnetic anisotropy for permanent magnet synchronous motors," *International Journal for Computation and Mathematics in Electrical and Electronic Engineering (COMPEL)*, Vol. 23, pp. 639-646, 2004.

[*1.3*] F. N. Isaac, A. A. Arkadan, and A. El-Antably, "Magnetic field and core loss evaluation of ALA-rotor synchronous reluctance machines taking into account

material anisotropy," *IEEE Transactions on Magnetics*, Vol. 34, pp. 3507-3510, 1998.

[*1.4*] O. Hubert, L. Daniel, and R. Billardon, "Experimental analysis of the magnetoelastic anisotropy of a non-oriented silicon iron alloy," *Journal of Magnetism and Magnetic Materials*, Vol. 254, pp. 352-354, 2003.

[*1.5*] G. Díaz, C. González-Morán, P. Arboleya, and J. Gómez-Aleixandre, "Analytical interpretation and quantification of rotational losses in stator cores of induction motors," *IEEE Transactions on Magnetics*, Vol. 43, pp. 3861-3867, 2007.

[*1.6*] M. Enokizono, S. Kanao, and G. Shirakawa, "Measurement of arbitrary dynamic magnetostriction under alternating and rotating field," *IEEE Transactions on Magnetics*, Vol. 31, pp. 3409-3411, 1995.

[*1.7*] A. Hasenzagl, B. Weiser, and H. Pfützner, "Magnetostriction of 3%SiFe for 2-D magnetization patterns," *Journal of Magnetism and Magnetic Materials*, Vol. 160, pp. 55-56, 1996.

[*1.8*] C. Krell, K. Kitz, L. Zhao, and H. Pfützner, "Multidirectional magnetostriction of different types of silicon iron materials," *Proceedings of The 16th Soft Magnetic Materials Conference (SMM16)*, Vol. 1, pp. 191-196, Düsseldorf, Germany, September 9-12, 2003.

[*1.9*] D. Wakabayashi, Y. Maeda, H. Shimoji, T. Todaka, and M. Enokizono, "Measurement of vector magnetostriction in alternating and rotating magnetic field," *Przegląd Elektrotechniczny (Electrical Reviews)*, Vol. R. 85, pp. 34-38, 2009.

[*1.10*] J. Le Besnerais, V. Lanfranchi, M. Hecquet, and P. Brochet, "Optimal slot numbers for magnetic noise reduction in variable-speed induction motors," *IEEE Transactions on Magnetics*, Vol. 45, pp. 3131-3136, 2009.

[*1.11*] L. Låftman, "Magnetostriction and its contribution to noise in a PWM inverter fed induction machine," *Journal de Physique IV*, Vol. 8, pp. 567-570, 1998.

[*1.12*] O. A. Mohammed, T. Calvert, and R. McConnell, "Coupled magnetoelastic finite element formulation including anisotropic reluctivity tensor and magnetostriction effects for machinery applications," *IEEE Transactions on Magnetics*, Vol. 37, pp. 3388-3392, 2001.

[*1.13*] T. G. D. Hilgert, L. Vandevelde, and J. A. A. Melkebeek, "Numerical analysis of the contribution of magnetic forces and magnetostriction to the vibrations in induction machines," *IET Science Measurement & Technology*, Vol. 1, pp. 21-24, 2007.

Chapter 2

Theoretical Bases

This chapter provides basic theories of magnetism, ferromagnetic material and magnetisation processes. Magnetisation characteristics and microstructures of electrical steel sheets are discussed. Electrical steel subjected to 2D magnetisation and Maxwell forces, commonly found in electrical machines are also described.

2.1 Basic Terms in Magnetism

A magnetic field (H) is produced whenever an electric charge is moving such as in a current-carrying wire or the orbital motions and spins of electrons in a permanent magnet [*2.1*]. It can be detected by a force acting on a magnetic material or dipole. The response to H in any medium is called flux density or magnetic induction (B). Permeability (μ) is used to define the relationship between B and H as

$$B = \mu H . \tag{2.1}$$

In free space, the relationship between B and H is written as

$$B = \mu_0 H \tag{2.2}$$

where μ_0 is the permeability of free space ($\mu_0 = 4\pi \times 10^{-7}$ H/m). In other mediums, B is expressed relative to free space as

$$B = \mu_r \mu_0 H \tag{2.3}$$

where μ_r is the dimensionless relative permeability of the material. Some SI units used in magnetism are listed in Table 2-1.

The relative permeabilities of paramagnetic materials such as air and aluminium are slightly higher than unity. Diamagnetic material such as copper has μ_r marginally less than unity. Paramagnetic and diamagnetic materials respond linearly to a magnetic field. Relative permeability of ferromagnetic material varies with H and is much greater than unity thanks to the alignment of atomic magnetic moments or dipoles inside the material. This is discussed in the next section. There are other kinds of magnetism such as antiferromagnetism, metamagnetism, ferrimagnetism and parasitic ferromagnetism, but since they are of minor importance to this investigation they are not be discussed here.

Table 2-1 SI units of magnetism

Variables	SI units
Magnetic field H	A/m
Magnetisation M	A/m
Flux density B	T
Polarisation J	T
Permeability μ	H/m
Susceptibility χ	-

2.2 Ferromagnetic Material and Magnetisation Process

Regions in a ferromagnetic material are formed by atomic dipoles lined up, even with no external magnetic field. Each atomic dipole can be considered as a north-south bar magnet with constant magnetisation as illustrated in Fig. 2-1. These dipoles can be influenced by external magnetic fields. A region with all the dipoles pointing along the same direction is called *a magnetic domain.* Domains are separated by domain walls containing layers of atoms. The thickness of a domain wall of iron is approximately 160 atomic layers [*2.1*]. Magnetisation (M) is used to represent the intensity of dipoles per unit volume of a solid aligned in a given direction. At 0 K, all the dipoles line up in the same direction without any external magnetic field and the magnetisation reaches saturation magnetisation, M_s. The saturation magnetisation varies from material to material. However, if the material is heated to its Curie temperature (T_C), the dipoles point in random (disordered) and

the material becomes paramagnetic. For iron, M_s=1.71×10^6 A/m relating to flux density of 2.15 T, and T_C=770°C [*2.1*].

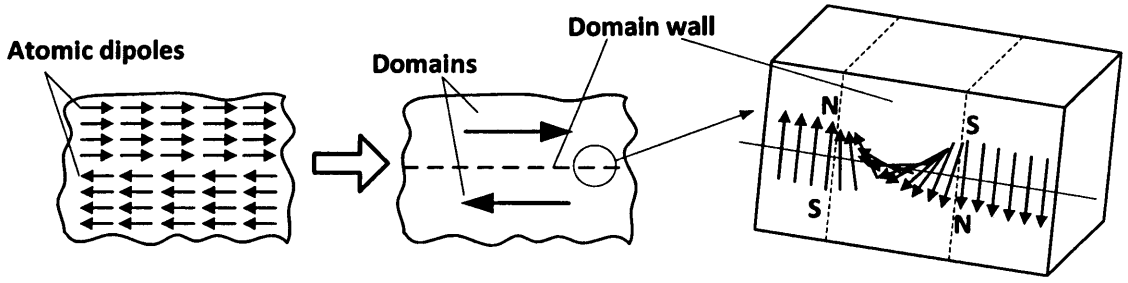

Fig. 2-1 Illustration of domains and domain walls in ferromagnetic materials [*2.1*]

Domains distribute themselves to minimise the magnetostatic energy due to the leakage field during the demagnetisation process as shown in Fig. 2-2. At the demagnetised state, domains re-arrange themselves with narrower domains and flux-closure domains arise to provide return paths for the spontaneous magnetisations of the main domains. The net magnetisation within the material is also zero at this state. The domain walls separating two anti-parallel bar domains are called 180° domain walls. The walls between the main bar domains and the perpendicular flux-closure domains can be classified as 90° domain walls. In iron, only 90° and 180° domain walls exist [*2.1*].

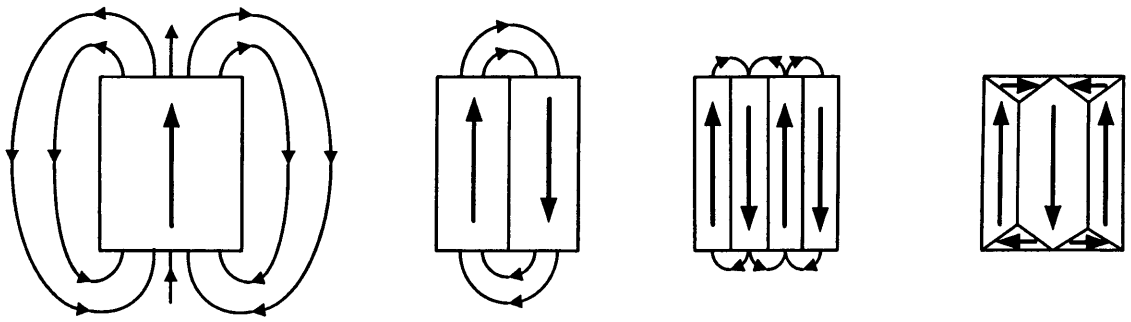

Fig. 2-2 Rearrangement of domains at the demagnetised state due to the energy minimisation [*2.2*]

Magnetisation and magnetic field both contribute to the flux density as follows

$$B=\mu_0(H+M)=\mu_0 H+J \tag{2.4}$$

where $J=\mu_0 M$ is the magnetic polarisation. Susceptibility (χ) defines how well the material responds to the field and can be written as

$$\chi = \frac{M}{H} = \mu_r - 1. \tag{2.5}$$

If an external field H is applied to a demagnetised ferromagnetic material (point ***a*** in Fig. 2-3), the minimum energy condition is altered. The main domain walls move to create magnetostatic energy to counter-balance the energy from the slowly increasing field, so the net magnetisation is not zero (point ***b***). The flux-closure domains are completely wiped out at a higher field and only a single domain exists (point ***c***). If the field continues to increase, the single domain rotates towards the field direction and the magnetisation eventually reaches the saturation M_s (point ***d***). However, the air flux $\mu_0 H$ still contributes to the flux density. After reducing the field to zero, the flux density does not follow the same path as the initial magnetisation curve and the domain walls do not move back to the position at the demagnetised state due to the irreversible magnetisation process (point ***e***). The remaining induction and magnetisation at this point are called *remanent flux density*, B_r and *remanent magnetisation*, M_r respectively. This irreversible magnetisation process is caused by pinning of domain walls due to impurities. An opposed field, called the *coercive force* H_c, is required to reduce the net magnetisation to zero (point ***f***). Further increase of the magnetic field in the opposite direction will again saturate the material. A repeated process from negative to positive saturation creates an area enclosed by B and H, termed a *$B-H$ loop* or *hysteresis loop*. This area is proportional to the energy loss in the material per unit volume per magnetisation cycle, often termed *hysteresis loss*. Apart from impurities, hysteresis loss also depends on grain size, internal stress, prior heat treatment, surface condition and thickness [*2.3*].

The wider the $B-H$ loop, the higher energy is stored and dissipated in the material. Therefore, hard magnetic materials such as permanent magnets have wider $B-H$ loops which indicate store more energy is stored (classified by $H_c > 10$ kA/m). On the other hand, $B-H$ loops of soft magnetic materials such as electrical steel should be narrow to achieve low loss ($H_c < 1$ kA/m). Obviously, an anhysteretic $B-H$ characteristic would be ideal for soft magnetic material because of zero loss. Under AC magnetisation, the $B-H$ characteristic in Fig. 2-3 is wider due to additional magnetic fields from the eddy current and excess losses and the energy loss per

cycle is higher than under the quasi-static condition. These losses are frequency dependent, sometimes referred to *dynamic losses [2.4]*.

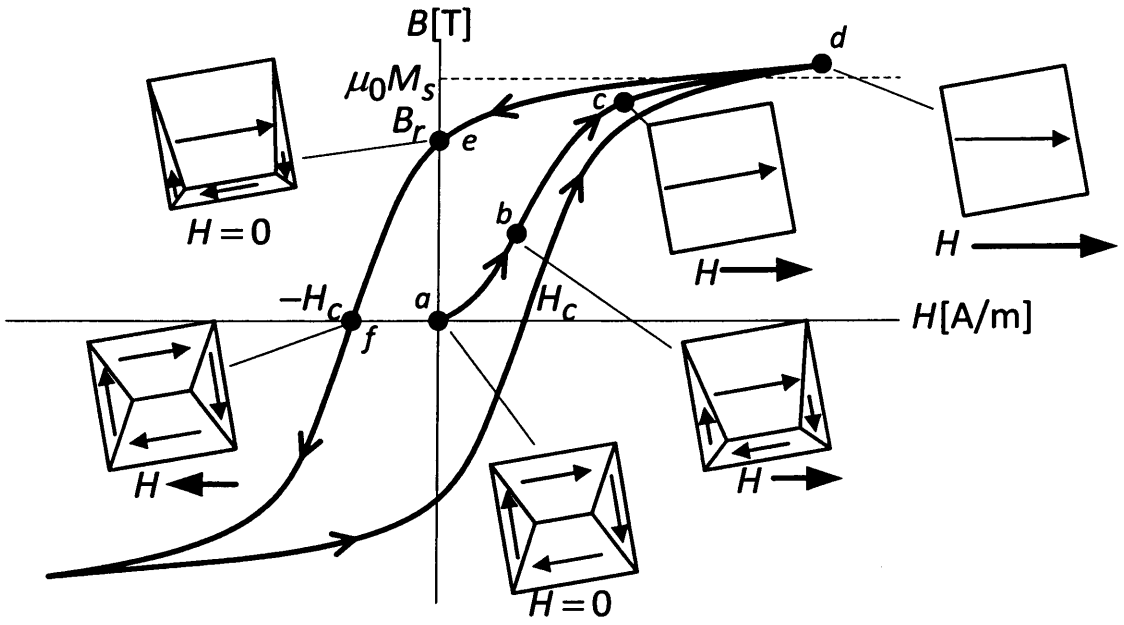

Fig. 2-3 Changes in domain structures during the magnetisation process of a ferromagnetic material

The movements of non-180° walls cause dimensions of a bulk ferromagnetic material to change due to *magnetostriction.* This varies with domain structures, and magnetisation magnitude and direction. High magnetostriction is desirable for materials used in sensors and actuators, but it should be as low as possible in electrical machine and transformer cores since it creates additional vibration and audible noise. A mechanical stress applied to the material also induces the domain structures to change because the energy minimisation is modified by the magnetoelastic energy. So, magnetostriction is a function of external stresses as well as magnetisation. Magnetostriction and stress-induced changes in domain structure are discussed in **Chapters 5** and **9** respectively.

2.3 Electrical Steel

Iron has easy magnetisation directions along the edges of a single crystal (one of the ⟨100⟩ directions) as illustrated by the dipoles pointing along the [100] direction in Fig. 2-4. If the magnetisation direction deviates from the easy axes, there is a torque between the magnetising field and the dipoles. The energy associated with this

torque is called the *crystal anisotropy energy*, E_a. The crystal anisotropy energy of cubic materials can be written as

$$E_a = K_1(\alpha_1^2\alpha_2^2 + \alpha_2^2\alpha_3^2 + \alpha_3^2\alpha_1^2) + K_2\alpha_1^2\alpha_2^2\alpha_3^2 + \ldots, \quad (2.6)$$

where α_1, α_2 and α_3 are the cosines of the magnetisation direction relative to the [100], [010] and [001] directions of the crystal, and K_1 and K_2 are the anisotropy constants [*2.5*]. The higher order terms in (2.6) are sometimes neglected and only the first term is considered if the anisotropy constants of the higher order terms are far less than K_1. However, the easy magnetisation axis can be transformed to the hard axis if K_2 is relatively high enough [*2.6*]. Table 2-2 summarises the magnetisation axes of cubic crystalline material for various ranges of anisotropy constants.

Table 2-2 Magnetisation axes and anisotropy constants of cubic crystalline material [*2.6*]

Anisotropy constants		Magnetisation axes		
		Easy	Medium	Hard
$K_1 > 0$	$-\infty < K_2/K_1 < -9$	⟨111⟩	⟨100⟩	⟨110⟩
	$-9 < K_2/K_1 < -9/4$	⟨100⟩	⟨111⟩	⟨110⟩
	$-9/4 < K_2/K_1 < \infty$	⟨100⟩	⟨110⟩	⟨111⟩
$K_1 < 0$	$-\infty < K_2/\lvert K_1\rvert < 9/4$	⟨111⟩	⟨110⟩	⟨100⟩
	$9/4 < K_2/\lvert K_1\rvert < 9$	⟨110⟩	⟨111⟩	⟨100⟩
	$9 < K_2/\lvert K_1\rvert < \infty$	⟨110⟩	⟨100⟩	⟨111⟩

For iron, $K_1 = 4.8\times10^4$ J/m^3 and $K_2/K_1 = 0.026$. Therefore, the face diagonal (⟨110⟩ directions) and space diagonal (⟨111⟩ directions) are the medium and hard magnetisation axes respectively because of the crystal anisotropy energy.

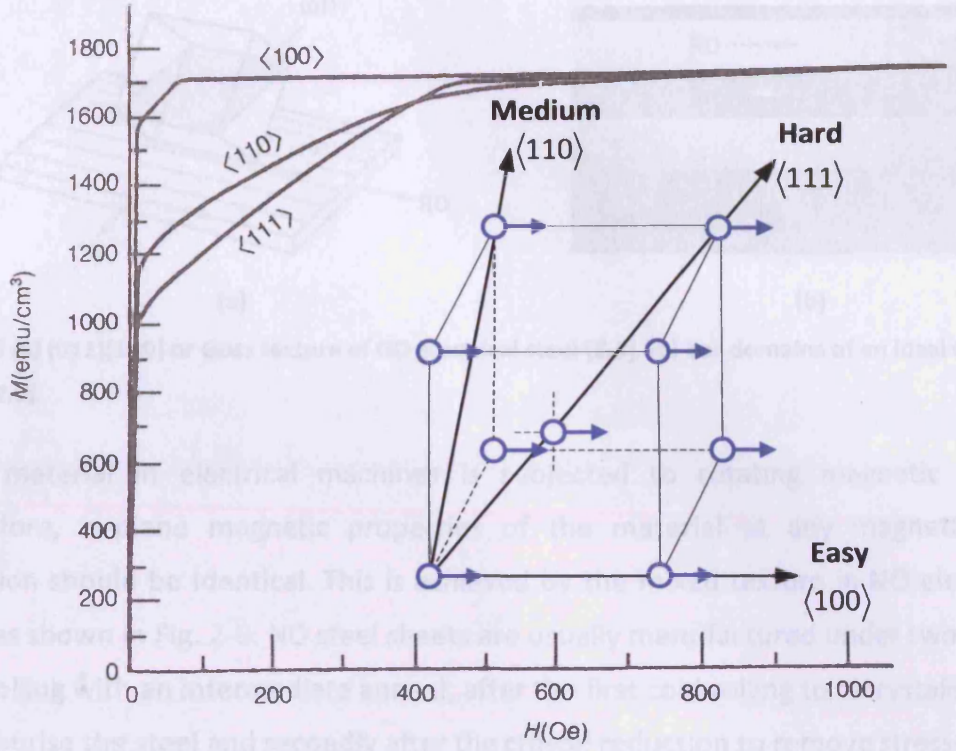

Fig. 2-4 Magnetisation curves of single iron crystal along the ⟨100⟩, ⟨110⟩ and ⟨111⟩ directions (magnetisation of 1 emu/cm^3 = 1000 A/m and magnetic field of 1 Oe = 79.58 A/m) [*2.1*].

For transformer cores and sections of large electrical machine cores, best magnetic properties are desired only for magnetisation along one direction. Grain-oriented (GO) Si-Fe electrical steel with the (011)[100] texture (widely known as Goss texture) shown in Fig. 2-5 (a), invented by Norman Goss in 1933, provides much higher magnetisation close the RD. This is achieved by cold rolling with intermediate anneals, plus a final high temperature anneal, giving magnetically favourable texture due to secondary recrystalisation [*2.2*]. According to Fig. 2-4, the medium and hard directions of this material lie in the plane of the sheet at 90° and 54.7° to the RD respectively. The ideal domain structure of this material is shown in Fig. 2-5 (b). If GO steel is magnetised along the RD, 180° domain wall movement predominates, resulting in low magnetostriction [*2.7*]. However, large magnetostriction occurs due to domain wall rotation if magnetised along the transverse direction (TD) [*2.7*]. Reduction of impurities and grain size optimisation decrease the hysteresis loss, while thinner lamination and higher silicon content to increase resistivity decrease the eddy current loss [*2.3*].

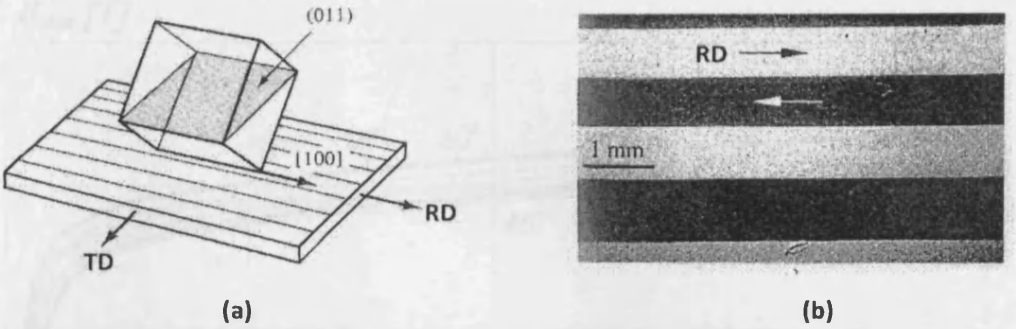

(a) (b)

Fig. 2-5 (a) (011)[100] or Goss texture of GO electrical steel [*2.8*], (b) bar domains of an ideal GO steel [*2.9*].

Core material in electrical machines is subjected to rotating magnetic fields. Therefore, in-plane magnetic properties of the material at any magnetisation direction should be identical. This is achieved by the mixed texture in NO electrical steel as shown in Fig. 2-6. NO steel sheets are usually manufactured under two-stage cold rolling with an intermediate anneal; after the first cold rolling to recrystalise and decarburise the steel and secondly after the critical reduction to remove stresses and to obtain the desired random orientation of grain growth [*2.10*]. The optimal grain size of NO steel depends on the amount of silicon, which ranges from 100 to 200 μm and the loss in NO steel is generally greater than that in GO steel [*2.11*]. There is still inherit anisotropy in its magnetisation characteristics at angles to the RD, but much less pronounced than in GO steel as shown in Fig. 2-7 [*2.11*]. The magnetisation process in NO steel is not well known [*2.9*]. Bulk magnetic and physical properties are usually used to calculate loss and the domain structure is ignored because of its complexity [*2.10*]. Magnetostriction of NO steel is of course difficult to predict from the domain structures unlike in GO steel.

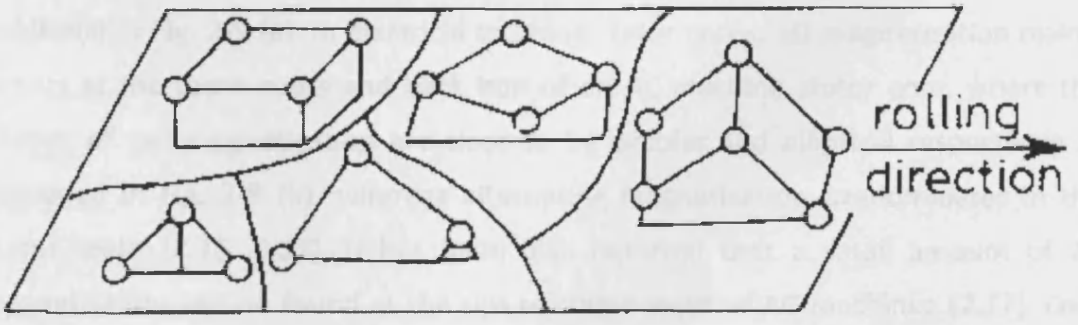

Fig. 2-6 Mixed texture of a silicon-free non-oriented electrical steel [*2.12*]

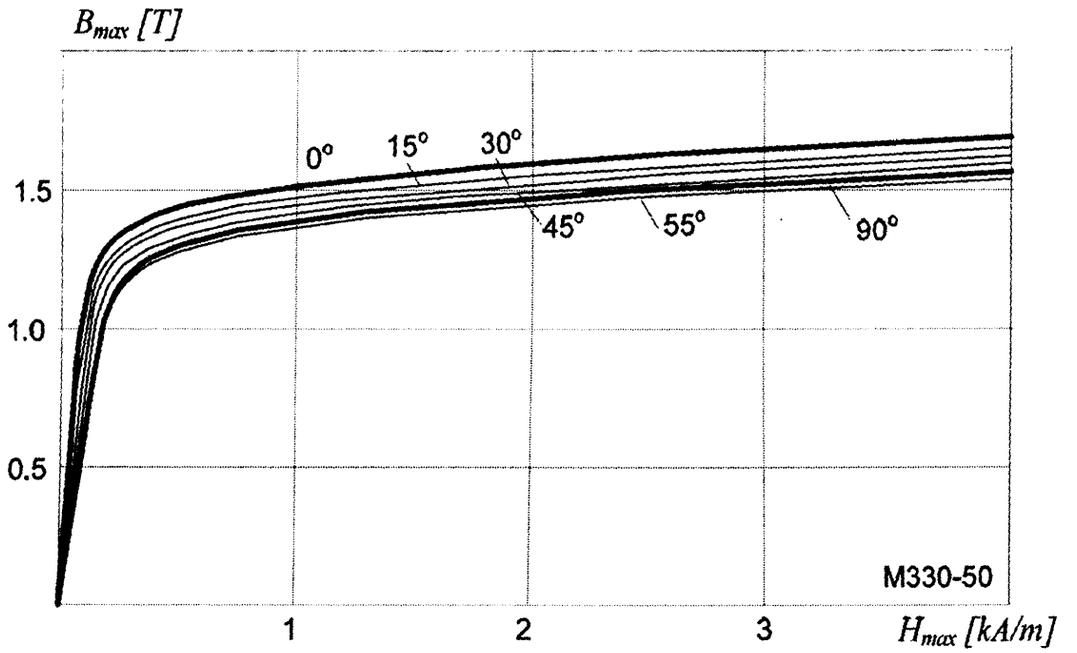

Fig. 2-7 Magnetisation curves of M330-50 NO electrical steel magnetised at angles to the RD [*2.11*]

2.4 2D Magnetisation in Electrical Steel Laminations

In some parts of an electrical machine or transformer core, flux density changes in time and direction as shown in Fig. 2-8 [*2.13, 2.14*]. As a result, the flux density vector rotates and can be projected into orthogonal components. In this thesis, it is called *2D* or *rotational magnetisation*. In contrast, alternating or unidirectional magnetisation changes in magnitude as a function of time, but its direction in the material remains constant [*2.14*].

Alternating magnetisation occurs in the limbs and yokes of a three-phase transformer core, whereas 2D magnetisation mainly occurs at the T joint [*2.15*] as exhibited in Fig. 2-9 (a). In electrical machine stator cores, 2D magnetisation mainly occurs at the tooth roots and back iron of an AC machine stator core, where the shapes of loci magnetisation are close to be circular and elliptical respectively as displayed in Fig. 2-9 (b), whereas alternating magnetisation predominates in the stator teeth [*2.16, 2.17*]. It has been also reported that a small amount of 2D magnetisation can be found at the tips of stator teeth of AC machines [*2.17*]. Core volume carrying 2D flux can be more than 50 % in some rotating machines, but only 2-3 % in transformers [*2.15*]. This phenomenon has been known for many years and widely reported [*2.13-2.19*].

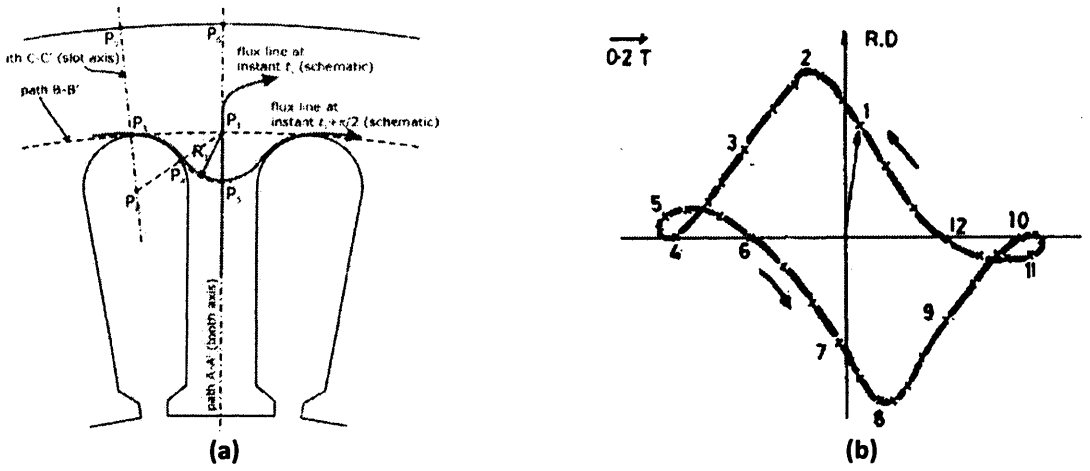

Fig. 2-8 (a) Illustration of a flux line at time instance t_1 and $t_1+\pi/2$ in an induction motor stator core [*2.13*], (b) Magnitude and direction of flux density at the T joint of a three-phase transformer core at 30° intervals in time [*2.14*]

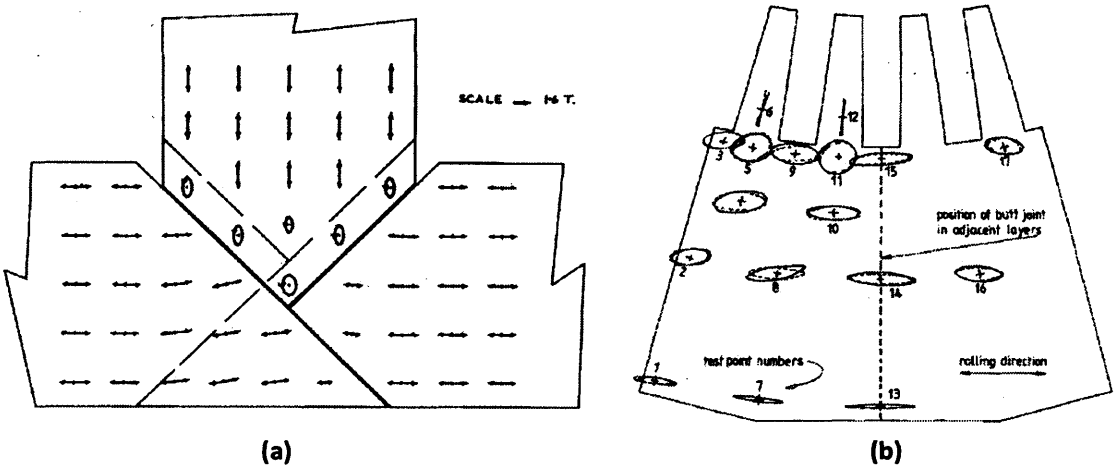

Fig. 2-9 Loci of the 50 Hz component of the flux density: (a) the T joint a three-phase three-limb transformer core [*2.18*], (b) a slice of a turbogenerator core [*2.16*]

Loss under 2D magnetisation at quasi magnetising frequency is greater than under alternating magnetisation in the medium induction range and it drops drastically at higher induction as shown in Fig. 2-10. At low fields, rotational loss arises due to more domain wall motions than that under the alternating field. As discussed in **Section 2.2**, loss under quasi static frequency is only due to the hysteresis component caused by domain wall movement. At high fields, domains under 2D magnetisation become a single domain constantly due to the reduction of active domain walls [*2.15*]. Thus, no loss occurs due to domain wall movement. On the other hand, movement, annihilation and creation of domain walls under quasi static alternating magnetisation change according to the field level and cause the

hysteresis loss. At higher magnetising frequency, rotational loss at saturation does not drop to zero due to the presence of eddy current loss [*2.20*].

In transformer cores, the proportion of the rotational loss is not high, but it can be responsible for more than 50 % of the total core loss in the stator cores of rotating machines [*2.15*]. Magnetostriction of electrical sheets under 2D magnetisation is considerably larger than under alternating magnetisation resulting from complex domain magnetisation processes [*2.21*]. This is discussed in detail in **Chapter 5**.

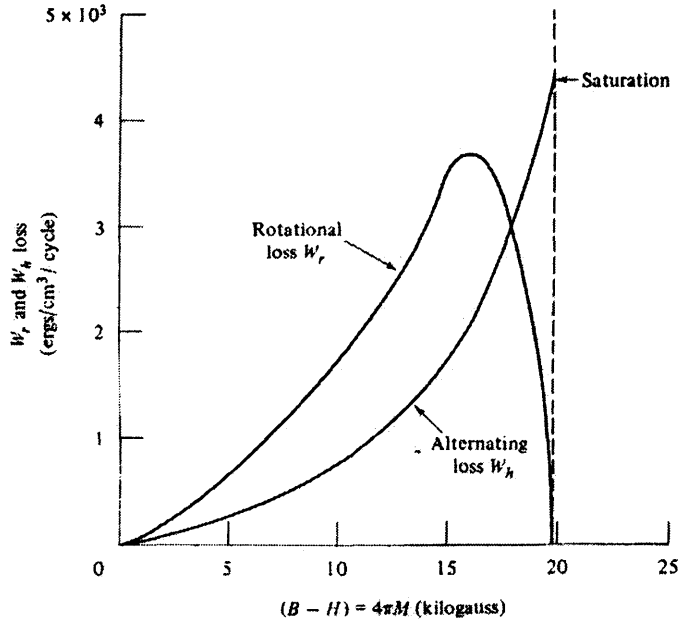

Fig. 2-10 Loss of a 3.13 % SiFe GO steel under rotational and alternating magnetisation at quasi static magnetising frequency (magnetisation of 1 kilogauss = 0.1 T and loss per unit volume of 1 erg/cm³ = 0.1 J/m³) [*2.2*]

2.5 Electrical Steel Subjected to Maxwell forces

The interaction between charges in a body and electric and/or magnetic fields can be expressed by a Maxwell stress tensor, which physically is the set of forces per unit area (stresses) acting on the surface of a body. In electrical machines, core laminations are mainly subjected to magnetic fields. Therefore, the Maxwell stress tensor due to a magnetic field is given as

$$\sigma_{ij}^{M} = \frac{1}{\mu_0}\left(b_i b_j - \frac{1}{2}\delta_{ij}\mathbf{B}^2\right) \tag{2.6}$$

where b_i are b_j the components of the flux density **B**, and δ_{ij} is the Kronecker delta (1 if $i=j$ otherwise 0) [*2.22*]. Components of the Maxwell stress tensor in Cartesian coordinate can be written as

$$\boldsymbol{\sigma}^M = \begin{bmatrix} \sigma_{xx}^M & \sigma_{xy}^M \\ \sigma_{yx}^M & \sigma_{yy}^M \end{bmatrix} = \frac{1}{\mu_0} \begin{bmatrix} \frac{1}{2}\left(b_x^2 - b_y^2\right) & b_x b_y \\ b_y b_x & \frac{1}{2}\left(b_y^2 - b_x^2\right) \end{bmatrix}. \tag{2.7}$$

In electrical machines, flux crosses the air gap between the stator and rotor teeth, where the Maxwell forces occur due to the flux density at the surfaces at the stator and rotor tooth surfaces as illustrated in Fig. 2-11. The tangential force density at the rotor surface is desirable as it produces torque [*2.23*]. Therefore, the vector control and direct torque control techniques of AC machine drives try to generate the resultant stator flux ahead of the rotor flux by 90° for the maximum torque produced [*2.24*]. On the other hand, the forces acting on the stator teeth are harmful since they cause vibration and acoustic noise in the stator core [*2.25*]. The tangential component of the stator tooth flux density is generally ignored [*2.26-2.28*] since it is comparatively lower than the normal component due to high permeability of the core laminations [*2.29*].

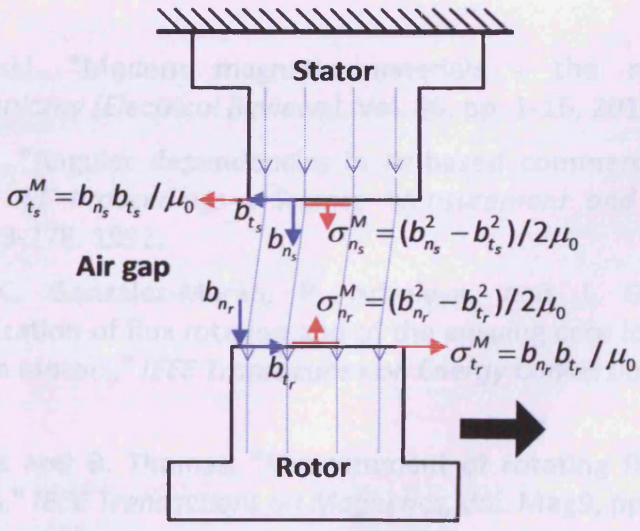

Fig. 2-11 Normal and tangential flux density components of a stator tooth (b_{n_s} and b_{t_s}) and a rotor tooth (b_{n_r} and b_{t_r}), and resultant Maxwell stress components $\sigma_{n_s}^M$, $\sigma_{t_s}^M$, $\sigma_{n_r}^M$ and $\sigma_{t_r}^M$ of a rotating machine

2.6 References for Chapter 2

[*2.1*] D. C. Jiles, *Introduction to Magnetism and Magnetic Materials*, Second edition, Chapman & Hall/CRC, London, 1998.

[*2.2*] B. D. Cullity, *Introduction to Magnetic Materials*, Addison-Wesley, Reading, Massachusetts, 1972.

[*2.3*] T. Moses, "Opportunities for exploitation of magnetic materials in an energy conscious world," *Interdisciplinary Science Reviews*, Vol. 27, pp. 100-113, 2002.

[*2.4*] S. E. Zirka, Y. I. Moroz, P. Marketos, and A. J. Moses, "Viscosity-based magnetodynamic model of soft magnetic materials," *IEEE Transactions on Magnetics*, Vol. 42, pp. 2121-2132, 2006.

[*2.5*] S. Chikazumi, *Physics of Magnetism*, John Wiley & Sons, New York, 1964.

[*2.6*] G. Bertotti, *Hysteresis in Magnetism: For physicists, materials scientists, and engineers*, Academic Press, San Diego, 1998.

[*2.7*] H. J. Stanbury, "The dependence of magnetostriction of grain oriented silicon steel on angle to the rolling direction," *Physica Scripta*, Vol. 39, pp. 538-541, 1989.

[*2.8*] G. E. Fish, "Soft magnetic materials," *Proceedings of the IEEE*, Vol. 78, pp. 947-972, 1990.

[*2.9*] A. Hubert and R. Schäfer, *Magnetic Domains: The analysis of magnetic microstructures*, Springer, Heidelberg, Germany, 1998.

[*2.10*] A. J. Moses, "Electrical steels: past, present and future developments," *IEE Proceedings-A Science Measurement and Technology*, Vol. 137, pp. 233-245, 1990.

[*2.11*] S. Tumánski, "Modern magnetic materials - the review," *Przegląd Elektrotechniczny (Electrical Reviews)*, Vol. 86, pp. 1-15, 2010.

[*2.12*] M. Soinski, "Angular dependencies in Fe-based commercial soft magnetic materials," *IEE Proceedings-A Science Measurement and Technology*, Vol. 139, pp. 273-278, 1992.

[*2.13*] G. Díaz, C. González-Morán, P. Arboleya, and J. Gómez-Aleixandre, "Characterization of flux rotation and of the ensuing core losses in the stator of induction motors," *IEEE Transactions on Energy Conversion*, Vol. 23, pp. 34-41, 2008.

[*2.14*] A. J. Moses and B. Thomas, "Measurement of rotating flux in silicon iron laminations," *IEEE Transactions on Magnetics*, Vol. Mag9, pp. 651-654, 1973.

[*2.15*] A. J. Moses, "Importance of rotational losses in rotating machines and transformers," *Journal of Materials Engineering and Performance*, Vol. 1, pp. 235-244, 1992.

[2.16] G. S. Radley and A. J. Moses, "Apparatus for experimental simulation of magnetic flux and power loss distribution in a turbogenerator stator core," *IEEE Transactions on Magnetics*, Vol. 17, pp. 1311-1316, 1981.

[2.17] G. Díaz, C. González-Morán, P. Arboleya, and J. Gómez-Aleixandre, "Analytical interpretation and quantification of rotational losses in stator cores of induction motors," *IEEE Transactions on Magnetics*, Vol. 43, pp. 3861-3867, 2007.

[2.18] A. Moses and B. Thomas, "The spatial variation of localized power loss in two practical transformer T-joints," *IEEE Transactions on Magnetics*, Vol. 9, pp. 655-659, 1973.

[2.19] T. Kanada, M. Enokizono, and K. Kawamura, "Distributions on localized iron loss of three-phase amorphous transformer model core by using two-dimensional magnetic sensor," *IEEE Transactions on Magnetics*, Vol. 32, pp. 4797-4799, 1996.

[2.20] J. G. Zhu and V. S. Ramsden, "Improved formulations for rotational core losses in rotating electrical machines," *IEEE Transactions on Magnetics*, Vol. 34, pp. 2234-2242, 1998.

[2.21] H. Pfützner and A. Hasenzagl, "Fundamental aspects of rotational magnetostriction," *Nonlinear Electromagnetic Systems*, Vol. 10, pp. 374-379, Edited by A. J. Moses and A. Basak, IOS Press, Amsterdam, 1996.

[2.22] D. J. Griffiths, *Introduction to Electrodynamics*, Third edition, Prentice-Hall International, London, 1999.

[2.23] W. D. Zhu, S. Pekarek, B. Fahimi, and B. J. Deken, "Investigation of force generation in a permanent magnet synchronous machine," *IEEE Transactions on Energy Conversion*, Vol. 22, pp. 557-565, 2007.

[2.24] I. Boldea, "Control issues in adjustable-speed drives," *IEEE Industrial Electronics Magazine*, Vol. 2, pp. 32-50, 2008.

[2.25] P. Vijayraghavan and R. Krishnan, "Noise in electric machines: a review," *IEEE Transactions on Industry Applications*, Vol. 35, pp. 1007-1013, 1999.

[2.26] F. Kako, T. Tsuruta, K. Nagaishi, and H. Kohmo, "Experimental study on magnetic noise of large induction motors," *IEEE Transactions on Power Apparatus and Systems*, Vol. 102, pp. 2805-2810, 1983.

[2.27] F. Ishibashi, K. Kamimoto, S. Noda, and K. Itomi, "Small induction motor noise calculation," *IEEE Transactions on Energy Conversion*, Vol. 18, pp. 357-361, 2003.

[2.28] C. Schlensok, D. van Riesen, M. van der Giet, and K. Hameyer, "Deformation analysis of induction machines by means of analytical and numerical methods," *IEEE Transactions on Magnetics*, Vol. 44, pp. 1498-1501, 2008.

[2.29] P. Krause, O. Wasynczuk, and S. Sudhoff, *Analysis of Electric Machinery and Drive Systems*, Second edition, Wiley-IEEE Press New York, 2002.

Chapter 3

Previous Related Work

Previous related work on the measurement of localised magnetisation conditions in AC machine stator cores, measurement and modelling of 2D magnetostriction of electrical steel laminations, magnetic anisotropy of electrical steel, and deformation, vibration and acoustic noise of AC machines are reviewed in this chapter.

3.1 Measurements of Localised Magnetic Properties in Electrical Machine Cores

In 1981, Radley and Moses [*3.1*] constructed a simulation system of a turbo-generator stator core. The stator core was constructed from slices of core sections cut from GO steel sheets. Several *b* coils were wound in the stator teeth, tooth roots and back iron for measurements of localised flux density, whereas corresponding localised losses were obtained from the initial rate of rise of temperature technique. The experimental setup and an example of measured results are presented in Fig. 3-1. It revealed that unidirectional flux occurs in the stator teeth, whereas circular flux loci are found in the tooth roots and they become elliptical when moving towards the back iron.

Moses and Rahmatizadeh [*3.2*] presented effects of housing stress on iron loss and flux distribution of an induction motor in 1989. A uniform compressive stress was applied to the induction motor stator core to simulate the effects of housing. A critical compressive stress of 2 MPa caused a sharp rise in the core loss.

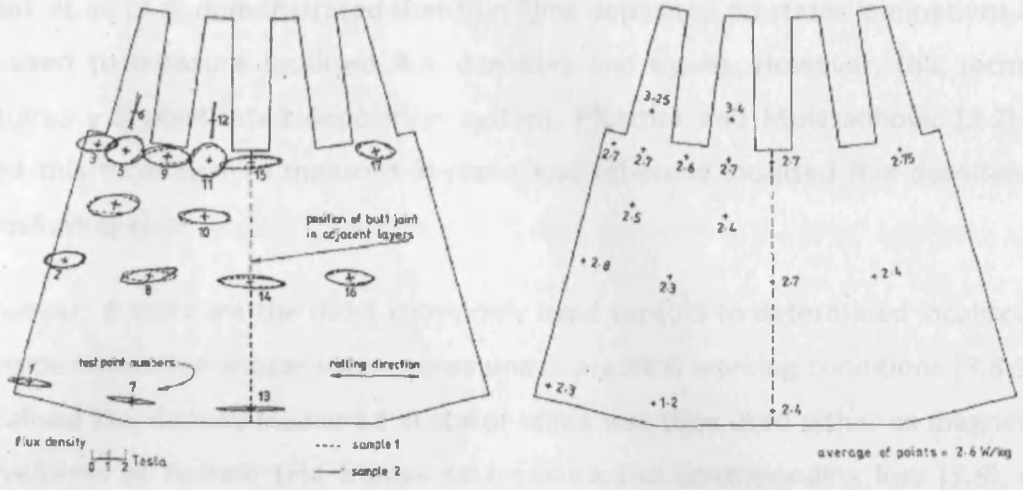

(a) (b)

Fig. 3-1 Simulation of a turbo-generator stator core: (a) the loci of flux density, (b) the resultant specific power loss distribution [3.1].

In 1996, Enokizono et al. [*3.3*] introduced a small localised sensor assembled from orthogonal needle probes and *h* coils to measure components of localised flux density and magnetic field distributed in an induction motor model core and localised losses were subsequently calculated. This measurement technique was also applied to determine localised loss distribution in transformer cores [*3.4, 3.5*]. Two examples of localised magnetic sensors are shown in Fig. 3-2.

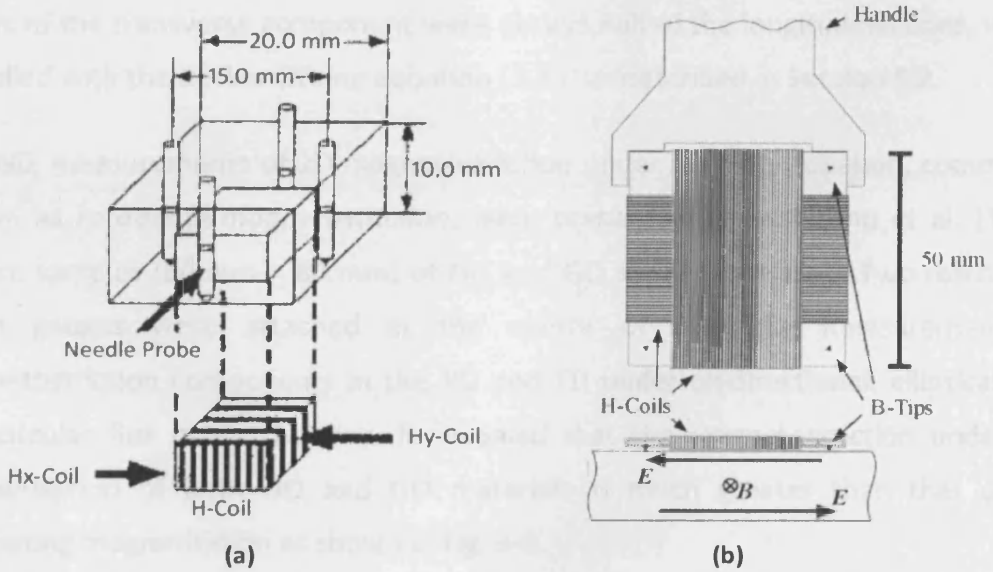

(a) (b)

Fig. 3-2 Localised magnetic sensors based on orthogonal needle probes and *h* coils developed by: a) Enokizono et al [*3.3*], b) Krismanić et al. [*3.5*].

Basak et al. [*3.6*] demonstrated that thin films deposited on stator laminations could be used to measure localised flux densities and losses. However, this technique requires a sophisticated deposition system. Pfützner and Mulasalihovic [*3.7*] then used this technique to measure in-plane and off-plane localised flux densities in a transformer core.

However, *b* coils are the most commonly used sensors to determined localised flux densities induction motor stator cores under practical working conditions [*3.8-3.10*]. Localised flux density measured in stator cores was then used either as magnetising waveforms of Epstein test frames to measure the corresponding loss [*3.8*], or to compare with core flux density calculated from finite element modelling (FEM) [*3.10, 3.11*].

3.2 Measurements and Modelling of 2D Magnetostriction of Electrical Steel Laminations

In-plane 2D magnetostriction of electrical steel sheets became of interest in 1984 when Mapps and White [*3.12*] used a double piezo-electric transducer to measure the longitudinal and transverse magnetostriction components of a single grain of GO steel under alternating magnetisation at 50 Hz parallel to the RD. Peak to peak values of the transverse component were always half of the longitudinal ones, which complied with the Becker-Döring equation [*3.13*] as described in **Section 5.2**.

In 1990, measurements of 2D magnetostriction under 2D magnetisation, commonly known as *rotational magnetostriction*, were presented by Enokizono et al. [*3.14*]. Square samples (80 mm × 80 mm) of NO and GO steels were used. Two resistance strain gauges were attached at the centre of each for measurement of magnetostriction components in the RD and TD under unidirectional, elliptical flux and circular flux magnetisations. It revealed that the magnetostriction under 2D magnetisation of both NO and GO materials is much greater than that under alternating magnetisation as shown in Fig. 3-3.

Since in-plane strain on any surface can be represented as two orthogonal components and a shear component, complete information of the in-plane magnetostriction was obtained from measurement of three components of magnetostrictive strain at angles to the RD of square [*3.15*] and hexagonal samples

[*3.16, 3.17*]. It was found that the direction of maximum magnetostriction does not always follow the magnetisation vector and the magnetisation direction has a significant impact on the magnitude of the magnetostriction [*3.15*]. Pfützner and Hasenzagl [*3.17*] explained that the principal axis of magnetostriction of NO steels rotates with the magnetisation vector, but that of highly grain-oriented (HGO) materials is frozen along the RD as shown in Fig. 3-4. It was also suggested by Pfützner and Hasenzagl [*3.16*] that 2D magnetostriction of GO materials should be characterised under lozenge-like magnetisation patterns, occurring at the T joints of transformer cores.

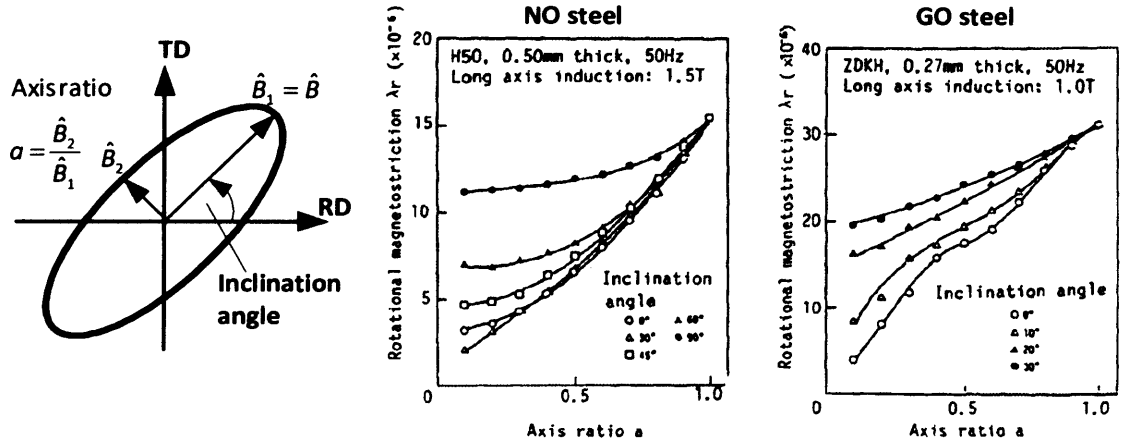

Fig. 3-3 2D magnetisation pattern and resultant magnetostriction along the RD of NO and GO steel [*3.14*]

An attempt was made to use a laser interferometer to measure 2D magnetostriction of electrical steel sheet [*3.18*]. The test bench of the system was flat to allow a laser beam to be reflected by a mirror attached at the centre of the sample. However, the magnetostrictive strains in three different directions could not be simultaneously measured by the single laser head unit, so the laser head had to be rotated at angles to the RD. In addition, the transducer was sensitive to small vibrations due to loud noise in a small room, tramping or knocking on a table, so a sophisticated laboratory was required.

It was surprising that peak to peak magnetostriction of a 230-μm laser-scribed HGO material under 2D magnetisation shown in Fig. 3-5 was found to be greater than 100 μm/m [*3.19*], which was more than 400 % of the saturation magnetostriction of a 3% Si-Fe single crystal [*3.20*].

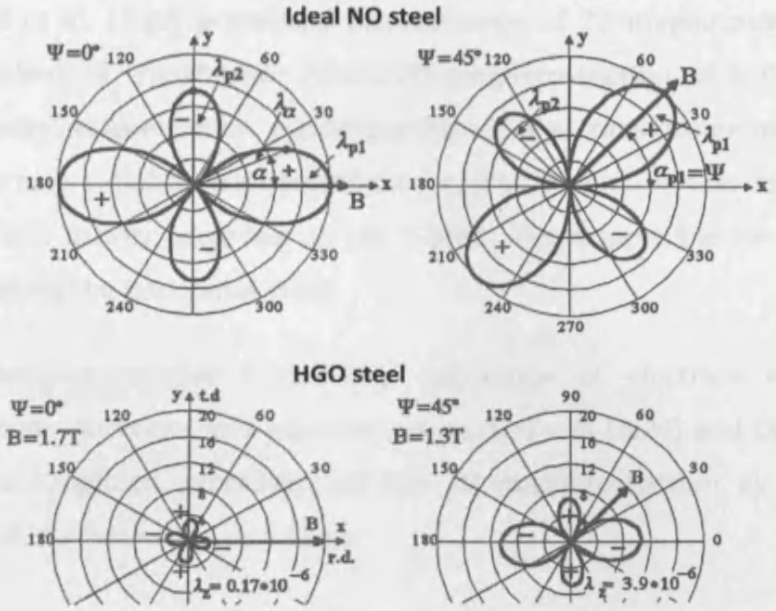

Fig. 3-4 Polar plots of magnetostriction of ideal NO and HGO steels when the magnetisation vector at 0° and 45° to the RD [*3.17*], where the plus (+) and minus (-) denote positive and negative magnetostriction respectively.

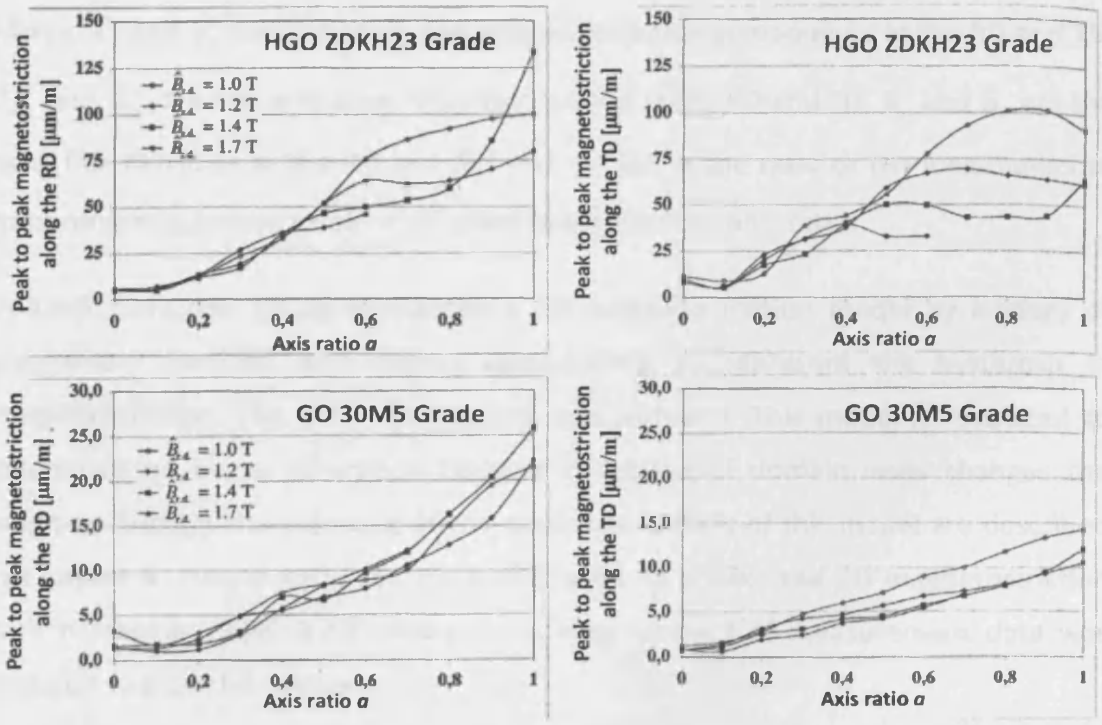

Fig. 3-5 Peak to peak magnetostriction along the RD and TD of HGO and GO steels under 1D and 2D magnetisation, where axis ratio *a* defines the peak flux density along the TD to the RD [*3.19*].

Thanks to the knowledge of the in-plane magnetostriction, the off-plane magnetostriction in the normal direction was estimated based on the assumption of constant in volume [*3.21, 3.22*].

In 2000, Krell et al. [*3.23*] presented the relevance of 2D magnetostriction to the noise generations of transformer cores. 2D magnetostriction of a GO steel was measured under magnetisation conditions found in a transformer model core to calculate the core's global magnetostriction-caused strains. It was found that 2D magnetostriction mainly occurring at the T joint was responsible for 40 % of the global strain along the horizontal yoke.

To include magnetostrictive forces into calculation of electrical machine and transformer core vibrations and acoustic noises, Låftman [*3.24*] and Delaere et al. [*3.25*] used a simplified expression of the 2D magnetostriction as functions of components of magnetisation as follows

$$\lambda_x^* = \lambda_{RD}(\hat{B}_x) - \xi\lambda_{TD}(\hat{B}_y) \tag{3.1}$$

$$\lambda_y^* = \lambda_{TD}(\hat{B}_y) - \xi\lambda_{RD}(\hat{B}_x) \tag{3.2}$$

where λ_x^* and λ_y^* are the predicted magnetostriction components in the RD and TD, λ_{RD} and λ_{TD} are the measured magnetostriction in the RD and TD, $\hat{B}_x$ and $\hat{B}_y$ are the peak flux densities in the RD and TD, and $\xi = 0.5$ is the ratio of the longitudinal to transverse magnetostriction or so-called magnetic Poisson's ratio.

In 1999, Lundgren [*3.18*] introduced a 2D magnetostriction model by analogy of mechanical elasticity with history dependence to represent the hysteresis in magnetostriction. The shear component was included. This model is restricted to magnetisation below saturation because reduction of domain walls changes the magnetostriction characteristic of the materials. Details of this model are described in **Chapter 5**. Neural networks were also used to predict the 2D magnetostriction with hysteresis [*3.26, 3.27*]. However, a large amount of measurement data was required to train the networks.

3.3 Anisotropy in Magnetic Properties of Electrical Steel Laminations and Its Contributions to Performance of Electrical Machines

In 1989, Stanbury [*3.28*] analysed the dependence of magnetostriction of GO materials on angles to the RD. Zero magnetostriction theoretically occurs at 0° and 55° to the RD and the magnetostriction is negative in between this angular range.

From 55° to 90°, the magnetostriction is positive and increases with the magnetisation angle. Fig. 3-6 shows an experimental magnetostriction coefficient of GO steel at angles to the RD. This is due to the switching of domain magnetisation of the Goss texture of this material and magnetostriction coefficient. Further magnetostriction measurements and observed domain patterns confirmed this phenomenon [*3.29, 3.30*].

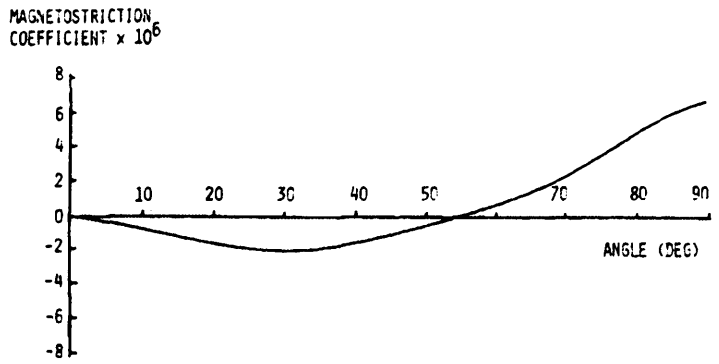

Fig. 3-6 Experimental magnetostriction coefficient of GO steel at angles to the RD [*3.28*]

Shiozaki and Kurosaki [*3.31*] showed that anisotropy in magnetic properties of NO electrical steel sheets depends on material texture resulting from the manufacturing processes. A conventional temper rolling process provided the most isotropic materials, while a process equipped with special hot band annealing and single-reduction cold rolling produced the highest induction NO steels with an anisotropic texture close to the (100)[001] texture. Goss textures were found in the final annealing process that introduced more anisotropy to the materials [*3.32-33*].

Bán and Di Nunzio [*3.34*] investigated crystallographic orientation distribution functions (ODFs) of 1.0%, 1.8% and 3.2% SiFe NO steels with grain size ranging from 10.6 μm to 174.6 μm. From the ODFs, they developed a texture-dependent function $s(\theta)$ calculated from the nearest ⟨100⟩ directions to the sheet plane of each material shown in Fig. 3-7. Hysteresis loss increased linearly with $s(\theta)$, whereas magnetostriction changed with $s^2(\theta)$. This made the magnetostriction highly angular dependence. Their results also showed that grain size did not have an impact on the anisotropy characteristic, unlike the silicon content.

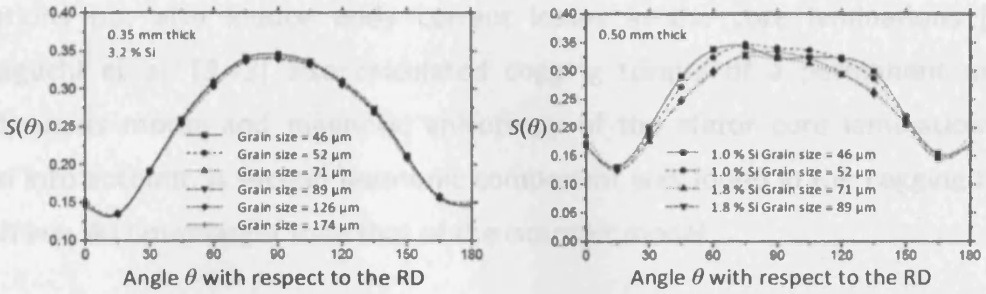

Fig. 3-7 Texture-dependent function $s(\theta)$ calculated from ODFs of NO steels [*3.34*]

Hubert et al. [*3.35*] presented magnetostriction measurements on a commercial 0.50 mm thick 3%Si-Fe NO steel showing highly magnetostrictive anisotropy. An ODF determined experimentally was used to calculate the projection of the closest easy magnetisation axes ⟨100⟩ to the sheet plane, which correlated with the magnetostriction measured at different angles to the RD as shown in Fig. 3-8. The lowest magnetostriction of NO steel with strong Goss texture occurred at angles of 40° to 50° to the RD [*3.36*].

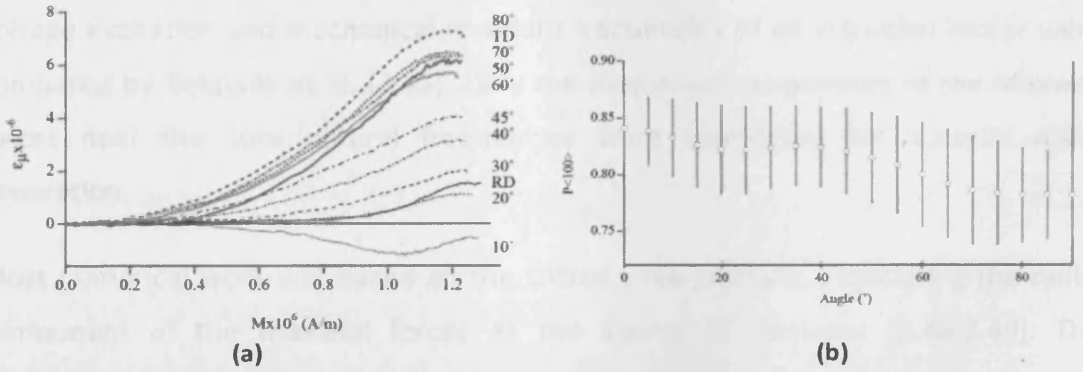

Fig. 3-8 (a) Longitudinal anhysteretic magnetostriction of Epstein strips of a 0.50 mm thick Fe-3% Si NO steel cut at the angles to the RD, (b) projection of the closest ⟨100⟩ directions to the sheet plane [*3.35*]

It is obvious that the anisotropy characterisation method was using strips of electrical steel sheets cut at several angles to the RD magnetised along the strip length [*3.28-3.30, 3.32-3.37*]. Square or disc samples magnetised in 2D magnetisation systems were also proposed by several authors [*3.38-3.40*] to minimise measurement time and a waste of material.

In 1988, Zagradišnik and Hribernik [*3.41*] reported that magnetic anisotropy in NO steel created higher harmonics in the air gap flux of induction motors subsequently causing negative-sequence torque. A similar situation was found in switched reluctance machines that high harmonics in the air gap flux not only cause core

vibrations but also induce eddy current losses in the core laminations [*3.42*]. Yamaguchi et al. [*3.43*] also calculated cogging torque of a permanent magnet synchronous motor and magnetic anisotropy of the stator core laminations was taken into account. A second harmonic component was found in the cogging torque which was 40 times larger than that of the isotropic model.

3.4 Deformation, Vibration and Acoustic Noise of AC Machine Cores

In 1983, Kako et al. [*3.44*] measured stator tooth flux densities of a 6000-V 260-kW induction motor using *b* coils wound on the stator teeth to measure tooth flux density and Maxwell force acting on each tooth was calculated. Frequencies and vibration modes were extracted by the fast Fourier transformation (FFT). They found that the maximum values occur if the frequencies and mode shapes of the Maxwell forces coincided with the natural frequency and vibration mode of the motor core.

The radial component of the Maxwell forces under pulse-width modulated (PWM) voltage excitation and mechanical resonant frequencies of an induction motor were compared by Belmans et al. [*3.45*]. Only the frequency components of the Maxwell forces near the core natural frequencies were considered for acoustic noise generation.

Most numerical work was based on the virtual work principle considering the radial component of the Maxwell forces as the source of vibration [*3.46-3.49*]. The principle of virtual work and mechanical structural analysis are described in **Chapter 4**. Stator cores sometimes were treated as a ring shape with the Maxwell forces normal to the inner surfaces [*3.49, 3.50*] as shown in Fig. 3-9.

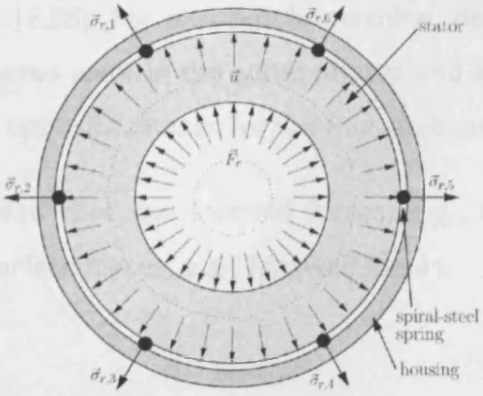

Fig. 3-9 The simplified structure of an induction machine stator core for deformation analysis [*3.49*]

Harmonics of radial Maxwell forces due to discontinuity of the air gap flux, stator and rotor winding space harmonics, rotor eccentricity, and saturation in flux density are conventionally considered as magnetic sources of acoustic noise radiated from induction machines [*3.51*]. The audible noise generated from these sources can be predicted during the design processes using combinations of stator and rotor slot numbers [*3.52, 3.53*].

In electrical machines, Maxwell forces and magnetostriction both cause the stator cores to deform. Låftman [*3.24*] constructed a stator core without a rotor so that the core deformation was mainly due to magnetostriction. Frequency components obtained from a microphone revealed the same spectrum as the Maxwell forces, which meant that the magnetostriction contributed significantly to the core deformation and vibration. Delaere et al. [*3.25*] used the magnetostriction expression in (3.1) and (3.2) to represent nodal magnetostrictive forces together with the Maxwell forces acting on the material surfaces in calculation of deformation and vibration of electrical machines. Mohammed et al. calculated electromagnetic forces generated in a permanent magnet machine [*3.54*] and they found that the magnetostrictive forces were responsible for up to 50 % of the total forces.

In 2002, Vandevelde and Melkebeek [*3.55*] proposed a new approach for modelling deformation in magnetised materials. Apart from magnetostriction, a piece of a magnetised material was stressed by long-range magnetic forces from the other magnetic sources (currents and magnetised materials). An imaginary gap was created along surface $\mathbf{S_1}$ of the material volume of interest $\mathbf{V_1}$ shown in Fig. 3-10 so that the long-range magnetic forces could be written similar from as the Maxwell stress tensor in (2.6). This approach was applied to calculate induction machine stator core deformation [*3.56*]. For a two-pole machine, deformation mode shapes due to the long-range forces were in the same phases and added up to those of the magnetostrictive forces, opposite phases for the four-pole machine.

Choi et al. [*3.57*] reported that the internal forces, e.g., long-range forces, were much smaller than the surface forces, e.g., Maxwell forces.

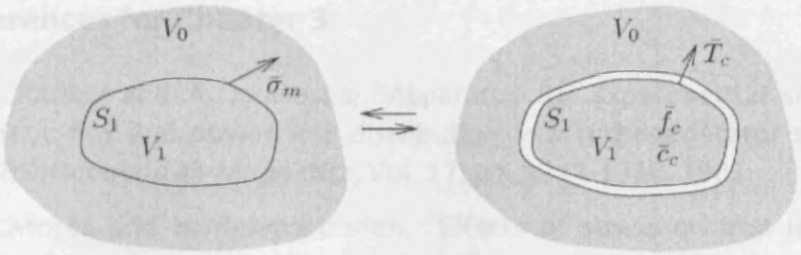

Fig. 3-10 Definition of the long-range magnetic forces [*3.55*]

3.5 Summary

Based on the reviews in **Sections 3.1** to **3.4**, it can be summarised that:

- Textures causes anisotropy in magnetic properties of NO steel and the anisotropy level of the magnetostriction is greater than that of the specific power loss
- 2D magnetisation conditions occur in the tooth root and back iron regions of AC electrical machine stator cores
- Magnetostriction of NO steel under 2D magnetisation is greater than under AC magnetisation
- Magnetostriction of stator core laminations couples with Maxwell forces in the air gap of an AC electrical machine
- Magnetostrictive forces contribute significantly to core deformation, vibration and acoustic noise.

According to the summary above, the following questions arise:

- How does the magnetostrictive anisotropy relate to the 2D magnetostriction?
- How do materials with highly anisotropic magnetostriction behave under practical 2D magnetisation conditions present in AC machine stator cores when subjected to Maxwell stresses?
- Are the radial deformation and vibration and loss distribution uniform if the core material is anisotropic?

3.6 References for Chapter 3

[*3.1*] G. S. Radley and A. J. Moses, "Apparatus for experimental simulation of magnetic flux and power loss distribution in a turbogenerator stator core," *IEEE Transactions on Magnetics*, Vol. 17, pp. 1311-1316, 1981.

[*3.2*] A. J. Moses and H. Rahmatizadeh, "Effects of stress on iron loss and flux distribution of an induction motor stator core," *IEEE Transactions on Magnetics*, Vol. 25, pp. 4003-4005, 1989.

[*3.3*] M. Enokizono, M. Morikawa, K. Kawamura, and J. Sievert, "Distribution of two-dimensional magnetic properties in three-phase induction motor model core," *IEEE Transactions on Magnetics*, Vol. 32, pp. 4989-4991, 1996.

[*3.4*] T. Kanada, M. Enokizono, and K. Kawamura, "Distributions on localized iron loss of three-phase amorphous transformer model core by using two-dimensional magnetic sensor," *IEEE Transactions on Magnetics*, Vol. 32, pp. 4797-4799, 1996.

[*3.5*] G. Krismanić, H. Pfützner, and N. Baumgartinger, "A hand-held sensor for analyses of local distributions of magnetic fields and losses," *Journal of Magnetism and Magnetic Materials*, Vol. 215, pp. 720-722, 2000.

[*3.6*] A. Basak, D. M. Rowe, and F. J. Anayi, "Thin film senses magnetic flux and loss in rotary electric motors," *IEEE Transactions on Magnetics*, Vol. 33, pp. 3382-3384, 1997.

[*3.7*] H. Pfützner and A. Mulasalihovic, "Thin-film technique for interior magnetic analysis of laminated machine cores," *Przegląd Elektrotechniczny (Electrical Reviews)*, Vol. R. 85, pp. 39-42, 2009.

[*3.8*] C. Cester, A. Kedous-Lebouc, and B. Cornut, "Iron loss under practical working conditions of a PWM powered induction motor," *IEEE Transactions on Magnetics*, Vol. 33, pp. 3766-3768, 1997.

[*3.9*] S. Takada, K. Mohri, H. Takito, T. Nomura, and T. Sasaki, "Magnetic losses of electrical iron sheet in squirrel-cage induction motor driven by PWM inverter," *IEEE Transactions on Magnetics*, Vol. 33, pp. 3760-3762, 1997.

[*3.10*] O. Bottauscio, M. Chiampi, and M. Zucca, "Experimental and numerical investigations on rotational fluxes in stator cores of three-phase motors," *IEEE Transactions on Magnetics*, Vol. 38, pp. 3294-3296, 2002.

[*3.11*] L. Dupré, M. De Wulf, D. Makaveev, V. Permiakov, A. Pulnikov, and J. Melkebeek, "Modelling of electromagnetic losses in asynchronous machines," *International Journal for Computation and Mathematics in Electrical and Electronic Engineering (COMPEL)*, Vol. 22, pp. 1051-1065, 2003.

[*3.12*] D. J. Mapps and C. E. White, "Longitudinal and transverse magnetostriction harmonics in (110) [001] silicon-iron," *IEEE Transactions on Magnetics*, Vol. 20, pp. 1566-1568, 1984.

[*3.13*] S. Chikazumi, *Physics of Magnetism*, John Wiley & Sons, New York, 1964.

[*3.14*] M. Enokizono, T. Suzuki, and J. D. Sievert, "Measurement of dynamic magnetostriction under rotating magnetic field," *IEEE Transactions on Magnetics*, Vol. 26, pp. 2067-2069, 1990.

[*3.15*] M. Enokizono, S. Kanao, and G. Shirakawa, "Measurement of arbitrary dynamic magnetostriction under alternating and rotating field," *IEEE Transactions on Magnetics*, Vol. 31, pp. 3409-3411, 1995.

[*3.16*] A. Hasenzagl, B. Weiser, and H. Pfützner, "Magnetostriction of 3%SiFe for 2-D magnetization patterns," *Journal of Magnetism and Magnetic Materials*, Vol. 160, pp. 55-56, 1996.

[*3.17*] H. Pfützner and A. Hasenzagl, "Fundamental aspects of rotational magnetostriction," *Nonlinear Electromagnetic Systems*, Vol. 10, pp. 374-379, Edited by A. J. Moses and A. Basak, IOS Press, Amsterdam, 1996.

[*3.18*] A. Lundgren, *On Measurement and Modelling of 2D Magnetization and Magnetostriction of SiFe Sheets*, PhD Thesis, Royal Institute of Technology, Sweden, 1999.

[*3.19*] C. Krell, K. Kitz, L. Zhao, and H. Pfützner, "Multidirectional magnetostriction of different types of silicon iron materials," *Proceedings of The 16th Soft Magnetic Materials Conference (SMM16)*, Vol. 1, pp. 191-196, Düsseldorf, Germany, September 9-12, 2003.

[*3.20*] J. Shilling and G. Jr. Houze, "Magnetic properties and domain structure in grain-oriented 3% Si-Fe," *IEEE Transactions on Magnetics*, Vol. 10, pp. 195-223, 1974.

[*3.21*] H. Yamaguchi, H. Pfützner, and A. Hasenzagl, "Magnetostriction measurements on the multidirectional magnetization performance of SiFe steel," *Journal of Magnetism and Magnetic Materials*, Vol. 320, pp. E618-E622, 2008.

[*3.22*] D. Wakabayashi, Y. Maeda, H. Shimoji, T. Todaka, and M. Enokizono, "Measurement of vector magnetostriction in alternating and rotating magnetic field," *Przegląd Elektrotechniczny (Electrical Reviews)*, Vol. R. 85, pp. 34-38, 2009.

[*3.23*] C. Krell, N. Baumgartinger, G. Krismanić, E. Leiss, and H. Pfützner, "Relevance of multidirectional magnetostriction for the noise generation of transformer cores," *Journal of Magnetism and Magnetic Materials*, Vol. 215, pp. 634-636, 2000.

[*3.24*] L. Låftman, "Magnetostriction and its contribution to noise in a PWM inverter fed induction machine," *Journal de Physique IV*, Vol. 8, pp. 567-570, 1998.

[*3.25*] K. Delaere, W. Heylen, R. Belmans, and K. Hameyer, "Finite element based expressions for Lorentz, reluctance and magnetostriction forces," *Journal for Computation and Mathematics in Electrical and Electronic Engineering (COMPEL)*, Vol. 20, pp. 20-31, 2001.

[*3.26*] N. Baumgartinger, C. Krell, H. Pfützner, and G. Krismanić, "Application of neural networks for the prediction of multidirectional magnetostriction," *Journal of Magnetism and Magnetic Materials*, Vol. 215, pp. 617-619, 2000.

[*3.27*] T. Hilgert, L. Vandevelde, and J. Melkebeek, "Neural network-based model for dynamic hysteresis in the magnetostriction of electrical steel under sinusoidal induction," *IEEE Transactions on Magnetics*, Vol. 43, pp. 3462-3466, 2007.

[*3.28*] H. J. Stanbury, "The Dependence of Magnetostriction of Grain Oriented Silicon Steel on Angle to the Rolling Direction," *Physica Scripta*, Vol. 39, pp. 538-541, 1989.

[*3.29*] H. Mogi, Y. Matsuo, and T. Kumano, "AC magnetostriction hysteresis and magnetization direction in grain oriented silicon steel," *IEEE Transactions on Magnetics*, Vol. 35, pp. 3364-3366, 1999.

[*3.30*] T. Yamamoto, A. Shiuchi, A. Saito, Y. Okazaki, A. Hasenzagl, and H. Pfützner, "Magnetostriction and magnetic domain structure changes of grain oriented Si-Fe sheets," *Journal de Physique IV*, Vol. 8, pp. 511-514, 1998.

[*3.31*] G. H. Shirkoohi, "Anisotropic dependence of magnetostriction in electrical steels under applied linear stress," *Journal of Magnetism and Magnetic Materials*, Vol. 157, pp. 516-518, 1996.

[*3.32*] M. F. de Campos, F. J. G. Landgraf, I. G. S. Falleiros, G. C. Fronzaglia, and H. Kahn, "Texture evolution during the processing of electrical steels with 0.5% Si and 1.25% Si," *ISIJ International*, Vol. 44, pp. 1733-1737, 2004.

[*3.33*] J. H. R. Page, "Some observations on the magnetic anisotropy of non-oriented 3% Si steels," *IEEE Transactions on Magnetics*, Vol. 20, pp. 1542-1544, 1984.

[*3.34*] G. Bán and P. E. Di Nunzio, "Minimum force model. Effect of crystallographic texture on the magnetostriction and loss characteristics of non-oriented electrical steels," *Journal of Magnetism and Magnetic Materials*, Vol. 254, pp. 265-268, 2003.

[*3.35*] O. Hubert, L. Daniel, and R. Billardon, "Experimental analysis of the magnetoelastic anisotropy of a non-oriented silicon iron alloy," *Journal of Magnetism and Magnetic Materials*, Vol. 254, pp. 352-354, 2003.

[*3.36*] F. Bohn, A. Gündel, F. J. G. Landgraf, A. M. Severino, and R. L. Sommer, "Magnetostriction, Barkhausen noise and magnetization processes in E110 grade non-oriented electrical steels," *Journal of Magnetism and Magnetic Materials*, Vol. 317, pp. 20-28, 2007.

[*3.37*] M. Shiozaki and Y. Kurosaki, "Anisotropy of magnetic properties in non-oriented electrical steel sheets," *Textures and Microstructures*, Vol. 11, pp. 159-170, 1989.

[*3.38*] N. Nencib, S. Spornic, A. Kedouslebouc, and B. Cornut, "Macroscopic anisotropy characterization of SiFe using a rotational single sheet tester," *IEEE Transactions on Magnetics*, Vol. 31, pp. 4047-4049, 1995.

[*3.39*] S. Tumánski, "A method of testing of the plane distribution of anisotropy," *IEEE Transactions on Magnetics*, Vol. 38, pp. 2808-2810, 2002.

[*3.40*] S. Zurek, R. Rygal, and M. Soinski, "Asymmetry of magnetic properties of conventional grain-oriented electrical steel with relation to 2D measurements," *Przegląd Elektrotechniczny (Electrical Reviews)*, Vol. R. 85, pp. 16-19, 2009.

[*3.41*] I. Zagradišnik and B. Hribernik, "Influence of anisotropy of magnetic material on the saturation harmonics in the 3-phase induction motor," *IEEE Transactions on Magnetics*, Vol. 24, pp. 491-494, 1988.

[*3.42*] F. N. Isaac, A. A. Arkadan, and A. El-Antably, "Magnetic field and core loss evaluation of ALA-rotor synchronous reluctance machines taking into account material anisotropy," *IEEE Transactions on Magnetics*, Vol. 34, pp. 3507-3510, 1998.

[*3.43*] S. Yamaguchi, A. Daikoku, and N. Takahashi, "Cogging torque calculation considering magnetic anisotropy for permanent magnet synchronous motors," *International Journal for Computation and Mathematics in Electrical and Electronic Engineering (COMPEL)*, Vol. 23, pp. 639-646, 2004.

[*3.44*] F. Kako, T. Tsuruta, K. Nagaishi, and H. Kohmo, "Experimental study on magnetic noise of large induction motors," *IEEE Transactions on Power Apparatus and Systems*, Vol. 102, pp. 2805-2810, 1983.

[*3.45*] R. J. M. Belmans, D. Verdyck, W. Geysen, and R. D. Findlay, "Electromechanical analysis of the audible noise of an inverter-fed squirrel-cage induction motor," *IEEE Transactions on Industry Applications*, Vol. 27, pp. 539-544, 1991.

[*3.46*] C. G. C. Neves, R. Carlson, N. Sadowski, J. P. A. Bastos, N. S. Soeiro, and S. N. Y. Gerges, "Experimental and numerical analysis of induction motor vibrations," *IEEE Transactions on Magnetics*, Vol. 35, pp. 1314-1317, 1999.

[*3.47*] F. Ishibashi, K. Kamimoto, S. Noda, and K. Itomi, "Small induction motor noise calculation," *IEEE Transactions on Energy Conversion*, Vol. 18, pp. 357-361, 2003.

[*3.48*] D. Mori and T. Ishikawa, "Force and vibration analysis of induction motors," *IEEE Transactions on Magnetics*, Vol. 41, pp. 1948-1951, 2005.

[*3.49*] C. Schlensok, D. van Riesen, M. van der Giet, and K. Hameyer, "Deformation analysis of induction machines by means of analytical and numerical methods," *IEEE Transactions on Magnetics*, Vol. 44, pp. 1498-1501, 2008.

[*3.50*] F. Ishibashi, K. Kamimoto, T. Hayashi, S. Noda, and K. Itomi, "Natural frequency of stator core of small induction motor," *IEE Proceedings-Electric Power Applications*, Vol. 150, pp. 210-214, 2003.

[*3.51*] P. Vijayraghavan and R. Krishnan, "Noise in electric machines: A review," *IEEE Transactions on Industry Applications*, Vol. 35, pp. 1007-1013, 1999.

[*3.52*] M. Hecquet, A. Ait-Hammouda, M. Goueygou, P. Brochet, and A. Randria, "Prediction of the electromagnetic noise of an asynchronous machine using experimental designs," *Mathematics and Computers in Simulation*, Vol. 71, pp. 499-509, 2006.

[*3.53*] J. Le Besnerais, V. Lanfranchi, M. Hecquet, and P. Brochet, "Optimal slot numbers for magnetic noise reduction in variable-speed induction motors," *IEEE Transactions on Magnetics*, Vol. 45, pp. 3131-3136, 2009.

[*3.54*] O. A. Mohammed, T. Calvert, and R. McConnell, "Coupled magnetoelastic finite element formulation including anisotropic reluctivity tensor and magnetostriction effects for machinery applications," *IEEE Transactions on Magnetics*, Vol. 37, pp. 3388-3392, 2001.

[*3.55*] L. Vandevelde and J. A. A. Melkebeek, "Modeling of magnetoelastic material," *IEEE Transactions on Magnetics*, Vol. 38, pp. 993-996, 2002.

[*3.56*] T. G. D. Hilgert, L. Vandevelde, and J. A. A. Melkebeek, "Numerical analysis of the contribution of magnetic forces and magnetostriction to the vibrations in induction machines," *IET Science Measurement & Technology*, Vol. 1, pp. 21-24, 2007.

[*3.57*] H. S. Choi, Y. S. Kim, J. H. Lee, and I. H. Park, "An observation of body force distributions in electric machines," *IEEE Transactions on Magnetics*, Vol. 43, pp. 1861-1864, 2007.

Chapter 4

Stress and Strain Analysis

This chapter covers basic theories of stress and strain, which are used in measurements of magnetostriction, i.e., Young's modulus, Poisson's ratio and analysis of stator core deformation. Definitions, properties, and transformation of stress and strain are presented. Stress-strain relationships and energies associated with strain are discussed. Finite element modelling of stress and strain analysis is also described.

4.1 Stress

Stress is the internal forces reacting to external forces exerted at a body's surface [*4.1*]. Fig. 4-1 (a) depicts a surface slice of a body with infinitesimal thickness in equilibrium when an external force, ΔF is applied at point **Q** over an area, ΔA. The internal force (dashed line), reacting to ΔF, causes stresses normal and tangential to the surface. As the area ΔA becomes smaller and smaller, the *normal* (or direct), σ and *shear* (or tangential), τ stresses are defined as

$$\sigma = \lim_{\Delta A \to 0} \left(\frac{\Delta F_n}{\Delta A} \right) \tag{4.1}$$

$$\tau = \lim_{\Delta A \to 0} \left(\frac{\Delta F_t}{\Delta A} \right) \tag{4.2}$$

where ΔF_n and ΔF_t are the normal and tangential components of ΔF respectively.

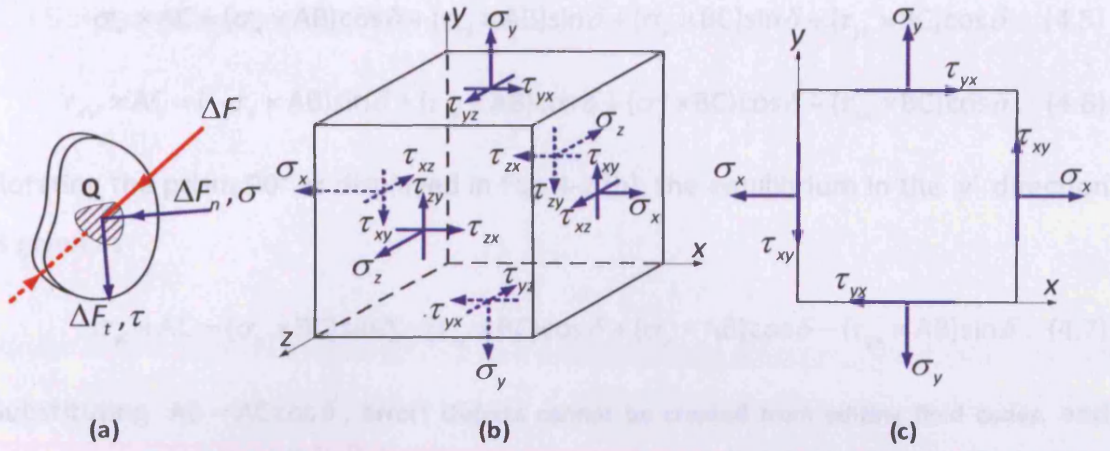

Fig. 4-1 (a) A slice of an equilibrium body with an external force ΔF for stress definition, (b) Stress surface components of a cubic element, and (c) Stress components of the plane stress system

If the point **Q** is infinitesimal and considered as a cube, three stress components act on each surface and the stress components of the opposite surface also act in the opposite direction. For example on the x surface, σ_{xx} or σ_x in the x direction, σ_{xy} or τ_{xy}, and σ_{xz} or τ_{xz} act in the y and z directions as illustrated in Fig. 4-1 (b). The stress tensor ($\boldsymbol{\sigma}$) in the xyz coordinate is given by

$$\boldsymbol{\sigma} = \begin{bmatrix} \sigma_{xx} & \sigma_{xy} & \sigma_{xz} \\ \sigma_{yx} & \sigma_{yy} & \sigma_{yz} \\ \sigma_{zx} & \sigma_{zy} & \sigma_{zz} \end{bmatrix} = \begin{bmatrix} \sigma_x & \tau_{xy} & \tau_{xz} \\ \tau_{yx} & \sigma_y & \tau_{yz} \\ \tau_{zx} & \tau_{zy} & \sigma_z \end{bmatrix}. \tag{4.3}$$

A positive normal stress is termed *tensile* and a negative normal stress *compressive*. The stress tensor is symmetrical and can be superimposed. Therefore, $\tau_{xy} = \tau_{yx}$, $\tau_{xz} = \tau_{zx}$ and $\tau_{yz} = \tau_{zy}$ respectively. If one of the normal stresses (σ_x, σ_y and σ_z) is zero, the system becomes the state of *plane stress* as shown in Fig. 4-1 (c). The plane stress system is adequate for analysis of deformation in AC machine cores due to Maxwell forces mainly created by the in-plane air gap flux at the tips of the stator teeth. Thus, the stress tensor in (4.3) can be simplified to

$$\boldsymbol{\sigma} = \begin{bmatrix} \sigma_{xx} & \sigma_{xy} \\ \sigma_{yx} & \sigma_{yy} \end{bmatrix} = \begin{bmatrix} \sigma_x & \tau_{xy} \\ \tau_{yx} & \sigma_y \end{bmatrix}. \tag{4.4}$$

Another property of the stress tensor is axis transformation. A prism in Fig. 4-2 (a) is cut from Fig. 4-1 (c). If its height along the z direction is unity, the force equilibrium in the x' and y' directions can be written as

$$\sigma_{x'} \times \mathrm{AC} = (\sigma_x \times \mathrm{AB})\cos\delta + (\tau_{xy} \times \mathrm{AB})\sin\delta + (\sigma_y \times \mathrm{BC})\sin\delta + (\tau_{yx} \times \mathrm{BC})\cos\delta \quad (4.5)$$

$$\tau_{x'y'} \times \mathrm{AC} = (-\sigma_x \times \mathrm{AB})\sin\delta + (\tau_{xy} \times \mathrm{AB})\cos\delta + (\sigma_y \times \mathrm{BC})\cos\delta - (\tau_{yx} \times \mathrm{BC})\cos\delta . \quad (4.6)$$

Rotating the prism 90° as displayed in Fig. 4-2 (b), the equilibrium in the y' direction is given as

$$\sigma_{y'} \times \mathrm{AC} = (\sigma_x \times \mathrm{BC})\sin\delta - (\tau_{xy} \times \mathrm{BC})\cos\delta + (\sigma_y \times \mathrm{AB})\cos\delta - (\tau_{yx} \times \mathrm{AB})\sin\delta . \quad (4.7)$$

Substituting $\mathrm{AB} = \mathrm{AC}\cos\delta$, **Error! Objects cannot be created from editing field codes.** and $\tau_{xy} = \tau_{yx}$ into (4.5), (4.6) and (4.7), the generalised stress transformation is expressed as

$$\begin{bmatrix} \sigma_{x'} \\ \sigma_{y'} \\ \tau_{x'y'} \end{bmatrix} = \begin{bmatrix} \cos^2\delta & \sin^2\delta & 2\cos\delta\sin\delta \\ \sin^2\delta & \cos^2\delta & -2\cos\delta\sin\delta \\ -\cos\delta\sin\delta & \cos\delta\sin\delta & \cos^2\delta - \sin^2\delta \end{bmatrix} \cdot \begin{bmatrix} \sigma_x \\ \sigma_y \\ \tau_{xy} \end{bmatrix} \quad (4.8)$$

where $\tau_{x'y'} = \tau_{y'x'}$.

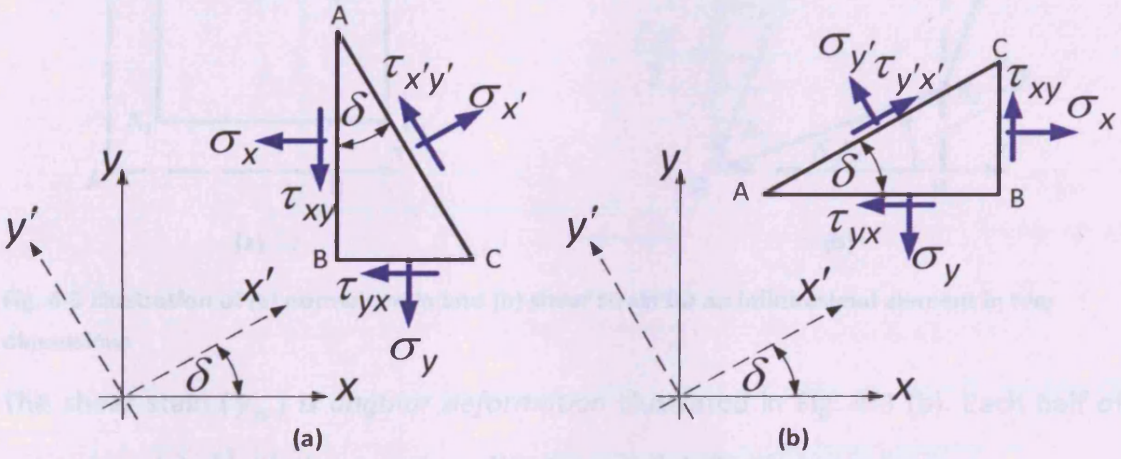

Fig. 4-2 Prisms for determination of axis transformation of the stress tensor: (a) normal and shear stresses is in the x' direction and (b) normal stress is in the y' direction

The principal axis, where the maximum and minimum stresses (σ_1 and σ_2) occurs and the shear stress becomes zero, can be determined in the $x'-y'$ coordinate by setting $\frac{\mathrm{d}\sigma_{x'}}{\mathrm{d}\delta} = 0$, resulting in

$$\tan 2\delta = \frac{2\tau_{xy}}{\sigma_x - \sigma_y} . \quad (4.9)$$

Substituting δ in (4.9) into (4.8) yields

$$\sigma_1, \sigma_2 = \frac{1}{2}(\sigma_x + \sigma_y) \pm \sqrt{\left(\frac{1}{2}(\sigma_x - \sigma_y)\right)^2 + \tau_{xy}^2} \,. \tag{4.10}$$

4.2 Strain

Strain is the relative deformation of a body due to external forces and can be distinguished as *linear* and *shear* strains. If the infinitesimal rectangular **ABCD** in Fig. 4-3 (a) is deformed into the infinitesimal rectangular $\mathbf{A_1B_1C_1D_1}$, the linear strain, also called *direct* or *normal* strain, along the x direction (ε_{xx}) is defined as

$$\varepsilon_{xx} = \lim_{AB \to 0} \left(\frac{A_1B_1 - AB}{AB} \right). \tag{4.11}$$

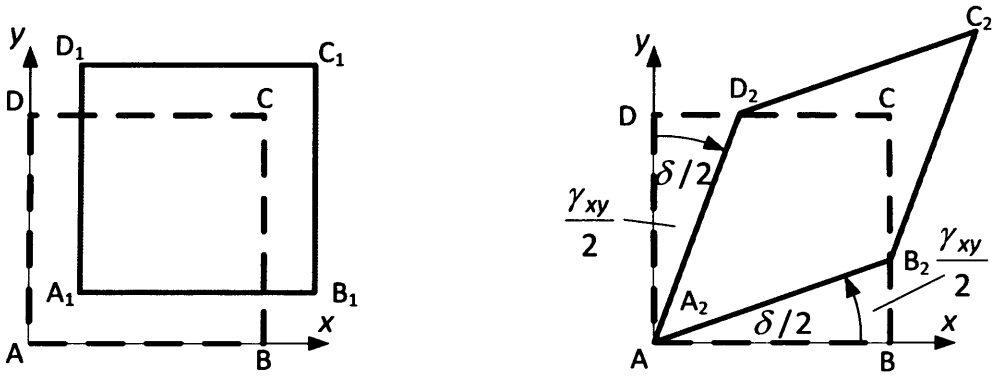

Fig. 4-3 Illustration of (a) normal strain and (b) shear strain for an infinitesimal element in two dimensions

The shear stain (γ_{xy}) is *angular deformation* illustrated in Fig. 4-3 (b). Each half of γ_{xy} is associated with the x and y directions and defined as

$$\gamma_{xy} = \lim_{AB, AD \to 0} \left(B\hat{A}D - B_2\hat{A}_2D_2 \right). \tag{4.12}$$

The strain tensor ($\boldsymbol{\varepsilon}$) in the $x-y$ plane is written as

$$\boldsymbol{\varepsilon} = \begin{bmatrix} \varepsilon_{xx} & \varepsilon_{xy} \\ \varepsilon_{yx} & \varepsilon_{yy} \end{bmatrix} = \begin{bmatrix} \varepsilon_x & \gamma_{xy}/2 \\ \gamma_{yx}/2 & \varepsilon_y \end{bmatrix}. \tag{4.13}$$

The strain tensor possesses similar properties to the stress tensor: symmetry, superposition, and transformation. The strain transformation can be derived from the schematic diagram in Fig. 4-4. The $dx \times dy$ rectangular **OUVW** is deformed into the diamond shape **OU'V'W'.** The diagonal line of **OUVW** is dx' long and the $x'-y'$ coordinate is set along this line. The deformation in the x' and y' can be written as

$$\varepsilon_{x'}dx' = \left(\varepsilon_x dx + \frac{1}{2}\gamma_{xy}dy\right)\cos\delta + \left(\varepsilon_y dy + \frac{1}{2}\gamma_{xy}dx\right)\sin\delta \tag{4.14}$$

$$\frac{1}{2}\gamma_{x'y'}dx' = -\left(\varepsilon_x dx + \frac{1}{2}\gamma_{xy}dy\right)\sin\delta + \left(\varepsilon_y dy + \frac{1}{2}\gamma_{xy}dx\right)\cos\delta . \tag{4.15}$$

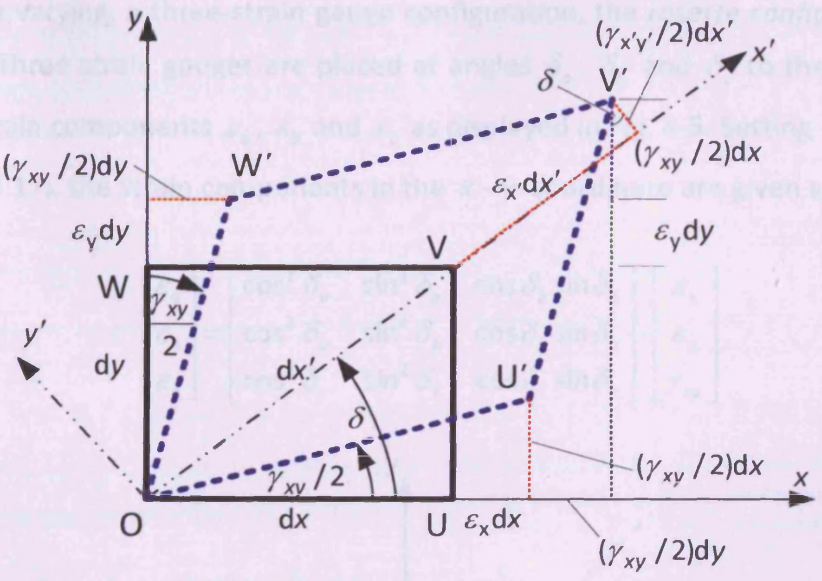

Fig. 4-4 Schematic diagram for illustration of two-dimensional strain transformation

Substituting $dx' = dx/\cos\delta$ into (4.14) and (4.15) and rotating $\varepsilon_{x'}$ to 90° similar to the stress transformation, the generalised strain transformation is given as

$$\begin{bmatrix} \varepsilon_{x'} \\ \varepsilon_{y'} \\ \gamma_{x'y'} \end{bmatrix} = \begin{bmatrix} \cos^2\delta & \sin^2\delta & \cos\delta\sin\delta \\ \sin^2\delta & \cos^2\delta & -\cos\delta\sin\delta \\ -2\cos\delta\sin\delta & 2\cos\delta\sin\delta & \cos^2\delta-\sin^2\delta \end{bmatrix} \cdot \begin{bmatrix} \varepsilon_x \\ \varepsilon_y \\ \gamma_{xy} \end{bmatrix}. \tag{4.17}$$

Setting $\frac{d\varepsilon_{x'}}{d\delta} = 0$ as with stress, the shear strain in the principal axis becomes zero and the maximum and minimum strains (ε_1 and ε_2) are

$$\varepsilon_1, \varepsilon_2 = \frac{\varepsilon_x + \varepsilon_y}{2} \pm \sqrt{\left(\frac{\varepsilon_x - \varepsilon_y}{2}\right)^2 + \left(\frac{\gamma_{xy}}{2}\right)^2} \tag{4.18}$$

and occur at

$$\tan 2\delta = \left(\frac{\gamma_{xy}}{\varepsilon_x - \varepsilon_y}\right). \tag{4.19}$$

Resistance strain gauges are convenient sensors for measurement of in-plane strains. This method is a strain-direct measurement and mounting a strain gauge is straightforward [*4.2*]. It is clearly seen from (4.18) that only two strain sensors are needed for measurement of the in-plane strains if the principal axis is known. If it is unknown or varying, a three-strain gauge configuration, the *rosette configuration*, is necessary. Three strain gauges are placed at angles δ_a, δ_b and δ_c to the x axis to measure strain components ε_a, ε_b and ε_c as displayed in Fig. 4-5. Setting $\varepsilon_{x'} = \varepsilon_a$, ε_b and ε_c in (4.17), the strain components in the $x-y$ coordinate are given as

$$\begin{bmatrix} \varepsilon_a \\ \varepsilon_b \\ \varepsilon_c \end{bmatrix} = \begin{bmatrix} \cos^2\delta_a & \sin^2\delta_a & \cos\delta_a \sin\delta_a \\ \cos^2\delta_b & \sin^2\delta_b & \cos\delta_b \sin\delta_b \\ \cos^2\delta_c & \sin^2\delta_c & \cos\delta_c \sin\delta_c \end{bmatrix} \cdot \begin{bmatrix} \varepsilon_x \\ \varepsilon_y \\ \gamma_{xy} \end{bmatrix}. \tag{4.20}$$

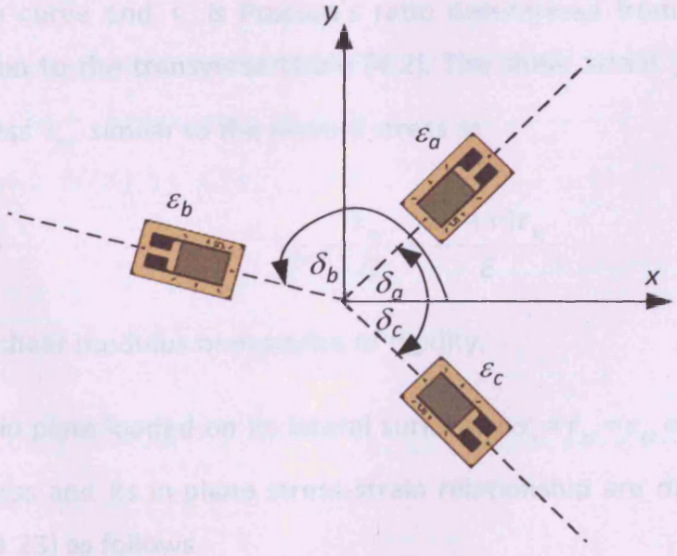

Fig. 4-5 Rosette strain gauge arrangement for measurement of components of in-plane strains

4.3 Linear Stress-strain Relationship

Different materials respond differently to loads. The stress-strain relationship can be *rigid, linear elastic, non-linear-elastic, elastic/strain-hardening, ideal elastic/plastic, linear viscoelastic* or *non-linear viscoelastic* [*4.1*]. For steels, the stress-strain relationship is linear if the stress is below the yield point where a plastic deformation of 0.2 % occurs [*4.3*]. The yield strength of electrical steel normally ranges from 285 to 475 GPa [*4.4, 4.5*]. The maximum stress due to Maxwell forces is $\hat{B}^2/(2\mu_0)$ where $\hat{B}$ is the peak flux density. At saturation ($\hat{B}$ = 2.15 T) [*4.6*], the stress is only 3.5 MPa, much lower than the yield strength. Therefore, the linear elastic relationship is of interest for electrical steel.

If a stress σ_x is applied to a linear elastic material, the corresponding strains ε_x, ε_y and ε_z change according to Hooke's law as follows

$$\varepsilon_x = \frac{\sigma_x}{E} \tag{4.21}$$

$$\varepsilon_y = \varepsilon_z = \frac{-\nu\sigma_x}{E} \tag{4.22}$$

where E is Young's modulus or modulus of elasticity determined from the slope of the stress-strain curve and ν is Poisson's ratio determined from the ratio of the longitudinal strain to the transverse strain [*4.2*]. The shear strain γ_{xy} also responds to the shear stress τ_{xy} similar to the normal stress as

$$\gamma_{xy} = \frac{\tau_{xy}}{G} = \frac{2(1+\nu)\tau_{xy}}{E} \tag{4.23}$$

where G is the shear modulus or modulus of rigidity.

If a body is a thin plate loaded on its lateral surfaces ($\sigma_z = \tau_{xz} = \tau_{yz} = 0$), the system is called *plane stress* and its in-plane stress-strain relationship are directly assembled from (4.21) to (4.23) as follows

$$\begin{bmatrix} \varepsilon_x \\ \varepsilon_y \\ \gamma_{xy} \end{bmatrix} = \frac{1}{E}\begin{bmatrix} 1 & -\nu & 0 \\ -\nu & 1 & 0 \\ 0 & 0 & 2(1+\nu) \end{bmatrix} \cdot \begin{bmatrix} \sigma_x \\ \sigma_y \\ \tau_{xy} \end{bmatrix} \tag{4.24}$$

or

$$\begin{bmatrix}\sigma_x\\ \sigma_y\\ \tau_{xy}\end{bmatrix}=\frac{E}{(1-\nu^2)}\begin{bmatrix}1 & \nu & 0\\ \nu & 1 & 0\\ 0 & 0 & (1-\nu)/2\end{bmatrix}\cdot\begin{bmatrix}\varepsilon_x\\ \varepsilon_y\\ \gamma_{xy}\end{bmatrix}. \tag{4.25}$$

For long bodies such as pipe lines, where the displacements of the end surfaces are prevented ($\varepsilon_z=\gamma_{xz}=\gamma_{yz}=0$), the displacements in the lateral directions are assumed to be independent of the longitudinal direction, z. This is a *plane strain system* and its stress-strain relationship is written as

$$\begin{bmatrix}\sigma_x\\ \sigma_y\\ \tau_{xy}\end{bmatrix}=\frac{E}{(1+\nu)(1-2\nu)}\begin{bmatrix}(1-\nu) & \nu & 0\\ \nu & (1-\nu) & 0\\ 0 & 0 & (1-2\nu)/2\end{bmatrix}\cdot\begin{bmatrix}\varepsilon_x\\ \varepsilon_y\\ \gamma_{xy}\end{bmatrix}. \tag{4.26}$$

The stress-strain relationship in (4.25) and (4.26) can be simplified to

$$\boldsymbol{\sigma}=\mathbf{E}\boldsymbol{\varepsilon} \tag{4.28}$$

where **E** is the stress-strain operator [*4.1*].

4.4 Strain Energy

If a bar of length l and cross-sectional area A is subjected to a uniaxial tension σ_x, the opposed forces F_x at the ends of the bar are $A\sigma_x$ and the length of the bar increases by u due to the product $l\varepsilon_x$. Since $\varepsilon_x=\sigma_x/E$ and $\sigma_y=\sigma_z=0$, F_x can be written as

$$F_x=A\sigma_x=AE\varepsilon_x=\frac{AE}{l}u=k_s u \tag{4.29}$$

where $k_s=AE/l$ is a stiffness coefficient. The total work (W) done by the opposing forces for the linear elastic case is therefore

$$W=\int_0^u F_x\,du=\frac{1}{2}F_x u=\frac{1}{2}\sigma_x\varepsilon_x Al. \tag{4.30}$$

According to the law of energy conversion, W is either stored in the body or dissipated. For elastic materials, W is stored in the body as a form of potential energy, called *strain energy* (W_ε) leading to

$$W_\varepsilon = W \quad . \tag{4.31}$$

The strain energy divided by the bar volume, AL is called *strain energy density* (U_0) expressed as

$$U_0 = \frac{1}{2}\sigma_x \varepsilon_x \, . \tag{4.32}$$

The strain energy density, U_0 is generally written as

$$U_0 = \frac{1}{2}\boldsymbol{\varepsilon}^{\mathrm{T}}\boldsymbol{\sigma} \tag{4.33}$$

where $\boldsymbol{\sigma} = \begin{bmatrix} \sigma_x & \sigma_y & \sigma_z & \tau_{xy} & \tau_{yz} & \tau_{xz} \end{bmatrix}^{\mathrm{T}}$ and $\boldsymbol{\varepsilon}^{\mathrm{T}} = \begin{bmatrix} \varepsilon_x & \varepsilon_y & \varepsilon_z & \gamma_{xy} & \gamma_{yz} & \gamma_{xz} \end{bmatrix}$.

The state of stress and the strain energy density are usually not uniform throughout a body and the total strain energy is derived from the volume integral as follows

$$W_\varepsilon = \int_V U_0 \mathrm{d}V = \iiint U_0 \mathrm{d}x\mathrm{d}y\mathrm{d}z \, . \tag{4.34}$$

4.5 Finite Element Modelling for Plane Elasticity

A structure can be approximately assembled from finite elements (FE) as shown in Fig. 4-6 (a). The elements are triangular or quadrilateral connected at nodes and each element can have more than 3 or 4 nodes such as element **2** and **3**. Nodes at the structure boundary are subjected to different loads and constraints. For instance, nodes between paths **BC** and **CD** are under normal and tangential stresses. Nodes between path **AB** are free to move, whereas those on **AD** are fixed. Displacements of nodes in the x and y direction are represented by u_i and v_i as displayed in Fig. 4-6 (b). The element displacements ($\mathbf{d}_e$) are functional to the nodal displacements ($\mathbf{d}_n$) as follows

$$\begin{bmatrix} u \\ v \end{bmatrix} = \begin{bmatrix} S_1 & 0 & S_2 & 0 & \cdots \\ 0 & S_1 & 0 & S_2 & \cdots \end{bmatrix} \cdot \begin{bmatrix} u_1 \\ v_1 \\ u_2 \\ v_2 \\ \vdots \end{bmatrix} \qquad \text{or} \qquad \mathbf{d}_e = \mathbf{N}\mathbf{d}_n \tag{4.35}$$

where $S_1, S_2, \ldots$ are shape polynomials of elements depending on geometry and node numbers and **N** is the shape function matrix.

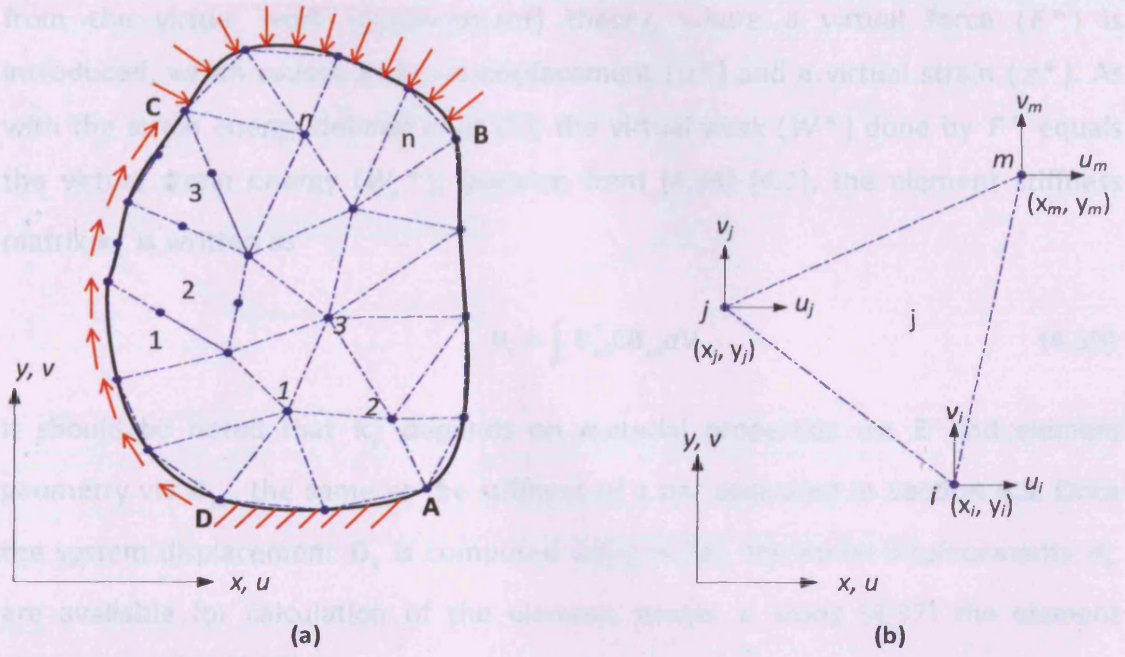

Fig. 4-6 (a) A plane structure assembled from numbers of finite elements (b) a triangular element with 3 nodes and 6 nodal displacements

Element strains ($\boldsymbol{\varepsilon}$) are derived from the element displacements as

$$\begin{bmatrix} \varepsilon_x \\ \varepsilon_y \\ \gamma_{xy} \end{bmatrix} = \begin{bmatrix} \partial/\partial x & 0 \\ 0 & \partial/\partial y \\ \partial/\partial y & \partial/\partial x \end{bmatrix} \cdot \begin{bmatrix} u \\ v \end{bmatrix} \qquad \text{or} \qquad \boldsymbol{\varepsilon} = \partial \mathbf{d}_e . \tag{4.36}$$

Substituting (4.35) into (4.36), the element strains relate to the nodal displacements as follows

$$\boldsymbol{\varepsilon} = \partial \mathbf{N} \mathbf{d}_n = \mathbf{B}_{\varepsilon d} \mathbf{d}_n \tag{4.37}$$

where $\mathbf{B}_{\varepsilon d}$ is the strain-displacement matrix. Nodal displacements eventually formulate the system displacement ($\mathbf{D}_s$). For static problems, $\mathbf{D}_s$ is generally computed from

$$\mathbf{K}_s\mathbf{D}_s = \mathbf{F} \tag{4.38}$$

where $\mathbf{F}$ is the body force matrix and $\mathbf{K}_s$ is the system stiffness matrix assembled from element stiffness matrices ($\mathbf{k}_s$) [*4.7*]. An element stiffness matrix $\mathbf{k}_s$ is obtained from the virtual work (displacement) theory, where a virtual force (F^*) is introduced, which causes a virtual displacement (u^*) and a virtual strain (ε^*). As with the strain energy defined in (4.31), the virtual work (W^*) done by F^* equals the virtual strain energy (W_c^*). Deriving from (4.34) [*4.1*], the element stiffness matrix $\mathbf{k}_s$ is written as

$$\mathbf{k}_s = \int_V \mathbf{B}_{\varepsilon d}^T \mathbf{E}\mathbf{B}_{\varepsilon d} dV . \tag{4.39}$$

It should be noted that $\mathbf{k}_s$ depends on material properties via $\mathbf{E}$ and element geometry via $\mathbf{B}_{\varepsilon d}$, the same as the stiffness of a bar described in **Section 4.3**. Once the system displacement $\mathbf{D}_s$ is computed using (4.38), the nodal displacements $\mathbf{d}_n$ are available for calculation of the element strains $\boldsymbol{\varepsilon}$ using (4.37) the element stresses $\boldsymbol{\sigma}$ using (4.28).

For dynamic problems, where $\mathbf{F} = \mathbf{F}(t)$, damping force ($\mathbf{C}\dot{\mathbf{D}}_s$) and inertia force ($\mathbf{M}\ddot{\mathbf{D}}_s$) are introduced into (4.38) as follows

$$\mathbf{M}_a\ddot{\mathbf{D}}_s + \mathbf{C}\dot{\mathbf{D}}_s + \mathbf{K}_s\mathbf{D}_s = \mathbf{F} \tag{4.40}$$

where $\mathbf{M}_a$ is the mass matrix, $\mathbf{C}$ is the damping matrix, $\dot{\mathbf{D}}_s$ is the system velocity matrix, and $\ddot{\mathbf{D}}_s$ is the system acceleration matrix [*4.7*]. $\mathbf{C}$ is calculated from Rayleigh damping as

$$\mathbf{C} = \alpha_d \mathbf{M}_a + \beta_d \mathbf{K}_s \tag{4.41}$$

where α_d and β_d are chosen from the frequency range of interest as shown in Fig. 4-7 and determined from

$$\begin{bmatrix} \xi_{d1} \\ \xi_{d2} \end{bmatrix} = \begin{bmatrix} 1/2\omega_1 & \omega_1/2 \\ 1/2\omega_2 & \omega_2/2 \end{bmatrix} \cdot \begin{bmatrix} \alpha_d \\ \beta_d \end{bmatrix} \tag{4.42}$$

where ξ_{d1} and ξ_{d2} are the damping factors at frequencies ω_1 and ω_2 respectively. The damping forces $\mathbf{C}\dot{\mathbf{D}}_s$ of most structures are usually small, approximately less than 10 % of $\mathbf{M}_s\ddot{\mathbf{D}}_s$, $\mathbf{K}_s\mathbf{D}_s$ and $\mathbf{F}$, so the damping factor ranges from 0.02 to 0.07 [*4.7*].

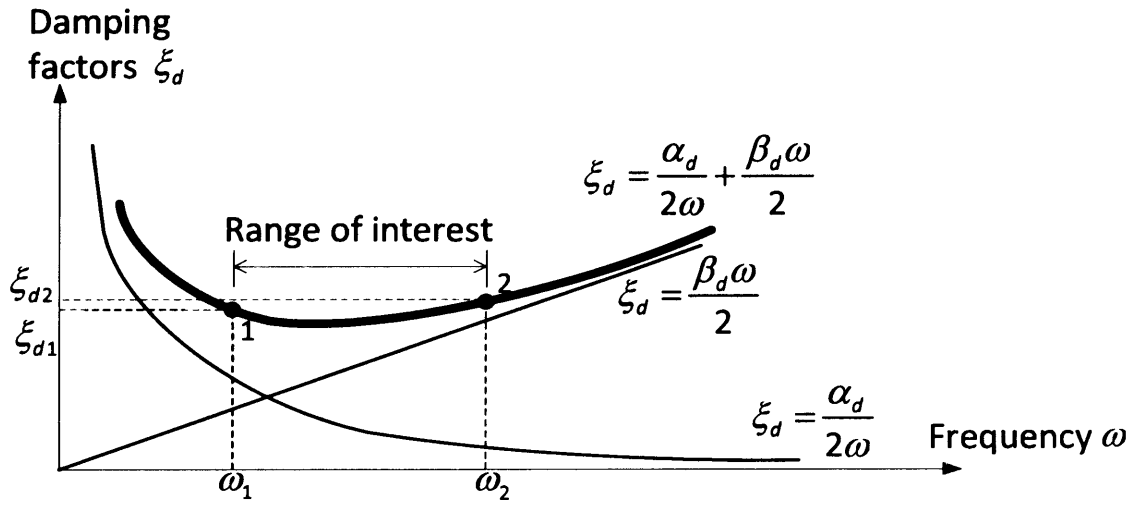

Fig. 4-7 Rayleigh damping specified by frequency range of interest [*4.7*]

4.6 References for Chapter 4

[*4.1*] J. McD. B. Brown, *Introductory Solid Mechanics*, John Wiley & Sons, London, 1973.

[*4.2*] J. S. Rossmann and C. L. Dym, *Introduction to Engineering Mechanics: A continuum approach*, CRC Press, Boca Raton, Florida, 2009.

[*4.3*] D. C. Jiles, *Introduction to the Principles of Materials Evaluation*, CRC Press, Boca Raton, Florida, 2008.

[*4.4*] Cogent™, *Electrical Steel: Grain oriented Unisil Unisil-H*, 2007.

[*4.5*] Cogent™, *Electrical Steel: Non oriented fully processed*, 2007.

[*4.6*] D. C. Jiles, *Introduction to Magnetism and Magnetic Materials*, Second edition, Chapman & Hall/CRC, London, 1998.

[*4.7*] R. D. Cook, *Finite Element Modeling for Stress Analysis*, John Wiley & Sons, New York, 1995.

Chapter 5

Magnetostriction of Electrical Steels and 2D Magnetostriction Model

This chapter begins with basic theory of magnetostriction, leading to the formulation of the modelling of magnetostriction. The magnetostriction of a single crystal under rotating magnetisation is calculated and compared with the measured magnetostriction of GO electrical steel. The magnetostriction of NO electrical steel is discussed and a 2D magnetostriction model is presented. Using such a model shows how the 2D magnetostriction of NO electrical relates to the magnetostrictive anisotropy. Finally, the procedure of parameter identification for such a model is described.

5.1 Basic Theory of Magnetostriction

Magnetostriction (λ) by definition is the resulting strain due to a fractional change in length (Δl) of a ferromagnetic material when there is a change in magnetisation and it is given as

$$\lambda = \frac{\Delta l}{l} \tag{5.1}$$

where l is the length of the material. There are two types of the magnetostriction: firstly, spontaneous magnetostriction due to the transition of a ferromagnetic material from a paramagnetic state at its Curie temperature point to the ferromagnetic state and, secondly, field-induced magnetostriction [*5.1*].

If a ferromagnetic material is heated towards its Curie temperature point, the alignment (magnetisation) within each domain decreases. Above the Curie temperature, the material is paramagnetic so that magnetic moments are in a completely disordered state as shown in Fig. 5-1 (a). When the material is cooled, the formation of magnetic domains from the ordering of the magnetic moments occurs and the material is in a ferromagnetic state. A schematic diagram of the ordering of the magnetic moments is shown in Fig. 5-1 (b). Each domain has spontaneous strain, ε. The spontaneous strain at angle θ from the easy magnetisation axis of the individual domain is expressed as [*5.1*].

$$\varepsilon(\theta) = \varepsilon \cos^2 \theta \,. \tag{5.2}$$

The orientation of the domains is assumed to be random. Thus, the spontaneous magnetostriction (λ_0) is determined from the average of the spontaneous strain of all the domains as

$$\lambda_0 = \int_0^{\frac{\pi}{2}} \varepsilon \cos^2 \theta \sin\theta \, d\theta = \frac{\varepsilon}{3}. \tag{5.3}$$

If the material is magnetised to saturation, all the domains align along the direction of the external magnetic field and the material elongates ε from the paramagnetic state as illustrated in Fig. 5-1 (c). The saturation field-induced magnetostriction λ_s is determined from

$$\lambda_s = \varepsilon - \lambda_0 = \frac{2}{3}\varepsilon \,. \tag{5.4}$$

In a bulk ferromagnetic material, magnetostriction occurs during the rotation of domains. If the external magnetic field is parallel to the 180° domain walls or the easy axis of a single crystal with uniaxial anisotropy, there is no magnetostriction. On the other hand, magnetostriction takes place entirely due to rotation of the domains if the field is perpendicular to the 180° walls or the easy axis of a single crystal. In this case, the magnetisation M at an angle θ to the field is given by

$$M = M_s \cos\theta \,. \tag{5.5}$$

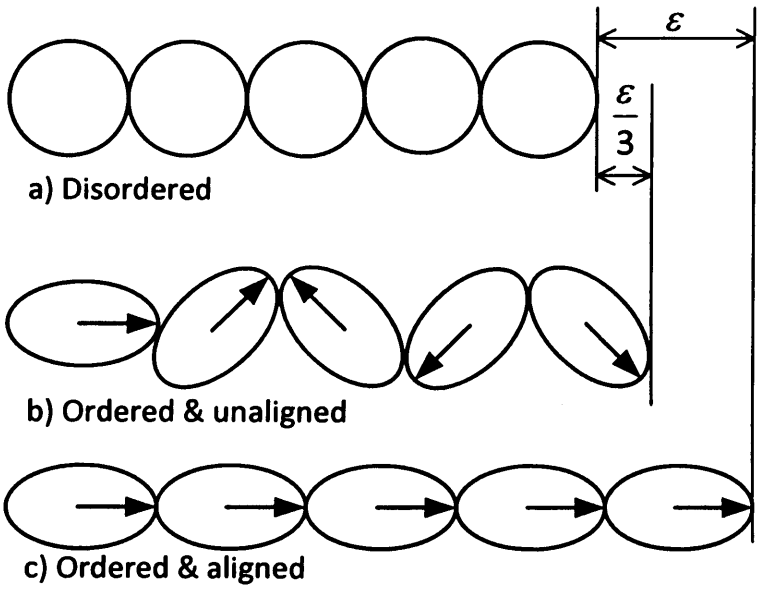

Fig. 5-1 Schematic diagram of the magnetostriction: (a) disordered (paramagnetic) state above the Curie temperature, (b) ferromagnetic, demagnetised state, and (c) ferromagnetic state magnetised to saturation [*5.1*].

The observed magnetostriction along the field direction derived from (5.2) is expressed as

$$\lambda = \frac{3}{2}\lambda_s \cos^2\theta . \tag{5.6}$$

Substituting $\cos\theta$ from (5.5) into (5.6), the bulk magnetostriction is defined as a function of magnetisation in (5.7).

$$\lambda = \frac{3}{2}\lambda_s \left(\frac{M}{M_s}\right)^2 \tag{5.7}$$

If the field makes an angle θ between 0° and 90° to the 180° domain walls, there is no magnetostriction at lower magnetisation because 180° domain wall movement is sufficient to create the net magnetisation. Once the field is high enough to make the walls rotate, magnetostriction occurs [*5.2*]. The relationship between the bulk magnetostriction and the magnetisation at various angles between the direction of the magnetic field and the 180° domain walls is shown in Fig. 5-2.

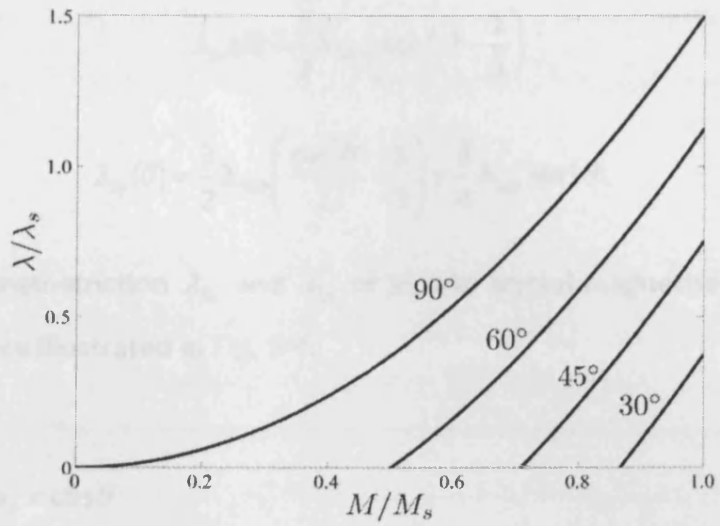

Fig. 5-2 Relation between the bulk magnetostriction and magnetisation at different angles between the direction of the magnetic field and the 180° domain walls [*5.2*]

5.2 Magnetostriction of Electrical Steels under 2D Magnetisation

In some applications such as T joints of transformer cores or the back iron of AC electrical machines, electrical steels are subjected to rotating fields in their plane. Magnetostriction of electrical steels under such magnetising conditions is mainly due to the rotation of domains. For a known domain structure of material such as GO steel with the Goss domain structure shown in Fig. 2-5 (a), the magnetostriction under a rotating field can be predicted from the Becker-Döring equation defining saturation magnetostriction of a single crystal given as

$$\lambda_S = \frac{3}{2}\lambda_{100}\left(\alpha_1^2\beta_1^2 + \alpha_2^2\beta_2^2 + \alpha_3^2\beta_3^2 - \frac{1}{3}\right) + 3\lambda_{111}\left(\alpha_1\alpha_2\beta_1\beta_2 + \alpha_2\alpha_3\beta_2\beta_3 + \alpha_3\alpha_1\beta_3\beta_1\right) \tag{5.8}$$

where λ_{100} and λ_{111} are the saturation magnetostriction values measured along the [100] and [111] axes respectively, and β_1, β_2 and β_3 are the cosines relative to the direction of the observed magnetostriction [*5.2*]. The applied field is assumed to be high enough to saturate the magnetisation in any direction, and it rotates in the (011) plane. The RD and TD are set to be x (β_1=1, $\beta_2=\beta_3$=0) and y (β_1=0, $\beta_2=\beta_3=1/\sqrt{2}$) axes respectively as shown in Fig. 5-3 (a). Thus, saturation magnetostriction along the RD and TD at angle θ with respect to the RD ($\lambda_{Sx}(\theta)$ and $\lambda_{Sy}(\theta)$) can be written as

$$\lambda_{Sx}(\theta)=\frac{3}{2}\lambda_{100}\left(\cos^2\theta-\frac{1}{3}\right) \tag{5.9}$$

$$\lambda_{Sy}(\theta)=\frac{3}{2}\lambda_{100}\left(\frac{\sin^2\theta}{2}-\frac{1}{3}\right)+\frac{3}{4}\lambda_{111}\sin^2\theta. \tag{5.10}$$

Saturation magnetostriction λ_{Sx} and λ_{Sy} of an iron crystal magnetised at θ=0°, 90°, 180° and 270° are illustrated in Fig. 5-4.

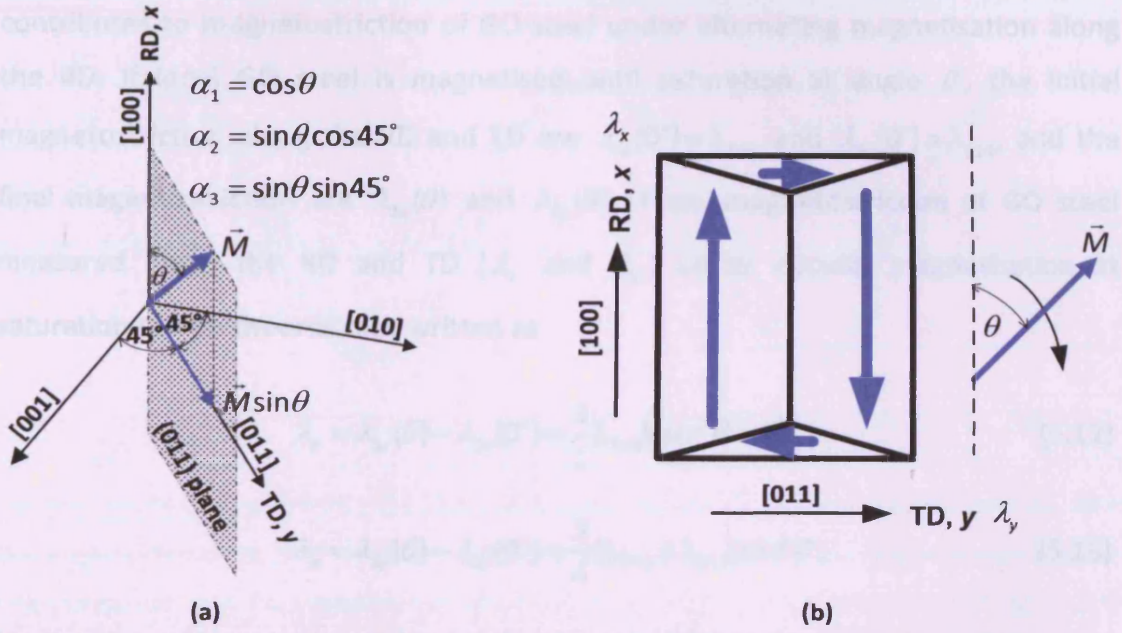

Fig. 5-3 (a) Magnetisation rotating in the (011) plane at angle θ to the [100] direction of an iron crystal, (b) Schematic domain structure of GO electrical steel at the demagnetised state

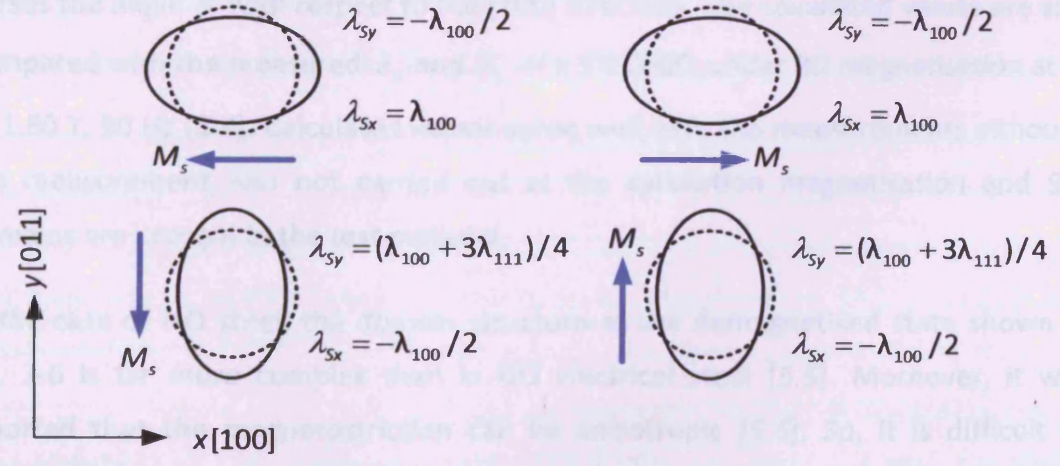

Fig. 5-4 Magnetostriction observed along the [100] and [011] direction of an iron crystal magnetised along the [100], $[\bar{1}00]$, $[0\bar{1}\bar{1}]$ and [011] directions in the (011) plane (The dotted circles are the undeformed shapes and the ellipses are the deformed shapes due to magnetostriction.)

Magnetostriction measured ($\lambda_{measured}$) on a material is a change of magnetostriction before ($\lambda_{initial}$) and after (λ_{final}) magnetisation [*5.3*], which is given by

$$\lambda_{measured} = \lambda_{final} - \lambda_{initial}. \tag{5.11}$$

Magnetostriction of an ideal GO steel (bar domains in Fig. 2-5 (b)) by definition saturates along the RD [*5.3*]. Therefore, λ_{final} and $\lambda_{initial}$ are the same if magnetised singly along the RD. Only fractional numbers of 90° domains exhibited in Fig. 5-3 (b) contributes to magnetostriction of GO steel under alternating magnetisation along the RD. If ideal GO steel is magnetised until saturation at angle θ, the initial magnetostriction along the RD and TD are $\lambda_{Sx}(0^\circ)=\lambda_{100}$ and $\lambda_{Sy}(0^\circ)=\lambda_{111}$, and the final magnetostriction are $\lambda_{Sx}(\theta)$ and $\lambda_{Sy}(\theta)$. Thus, magnetostriction of GO steel measured along the RD and TD (λ_x and λ_y) under circular magnetisation at saturation can be theoretically written as

$$\lambda_x = \lambda_{Sx}(\theta) - \lambda_{Sx}(0^\circ) = \frac{3}{2}\lambda_{100}\left(\cos^2\theta - 1\right) \tag{5.12}$$

$$\lambda_y = \lambda_{Sy}(\theta) - \lambda_{Sy}(0^\circ) = \frac{3}{4}(\lambda_{100} + \lambda_{111})\sin^2\theta. \tag{5.13}$$

Fig. 5-4 shows the calculated λ_x and λ_y of an ideal 3% Si GO steel (λ_{100}=23.7 μm/m and λ_{111}=-4.1 μm/m [*5.3*]) under saturated magnetisation rotating in the (011) plane versus the angle θ with respect to the [100] direction. The calculated values are also compared with the measured λ_x and λ_y of a 3% Si GO under 2D magnetisation at $\hat{B}$ of 1.60 T, 50 Hz [*5.4*]. Calculated values agree well with the measurements although the measurement was not carried out at the saturation magnetisation and 90° domains are present in the test material.

In the case of NO steel, the domain structure at the demagnetised state shown in Fig. 2-6 is far more complex than in GO electrical steel [*5.5*]. Moreover, it was reported that the magnetostriction can be anisotropic [*5.6*]. So, it is difficult to predict the magnetostriction of NO electrical steel from the domain structure [*5.7*]. Assuming domain rotation takes place in NO steel magnetised below saturation due to its random orientation, the bulk magnetostriction varies with b^2. This can be

predicted by using a model based on an analogy of mechanical elasticity which will be explained in the next section.

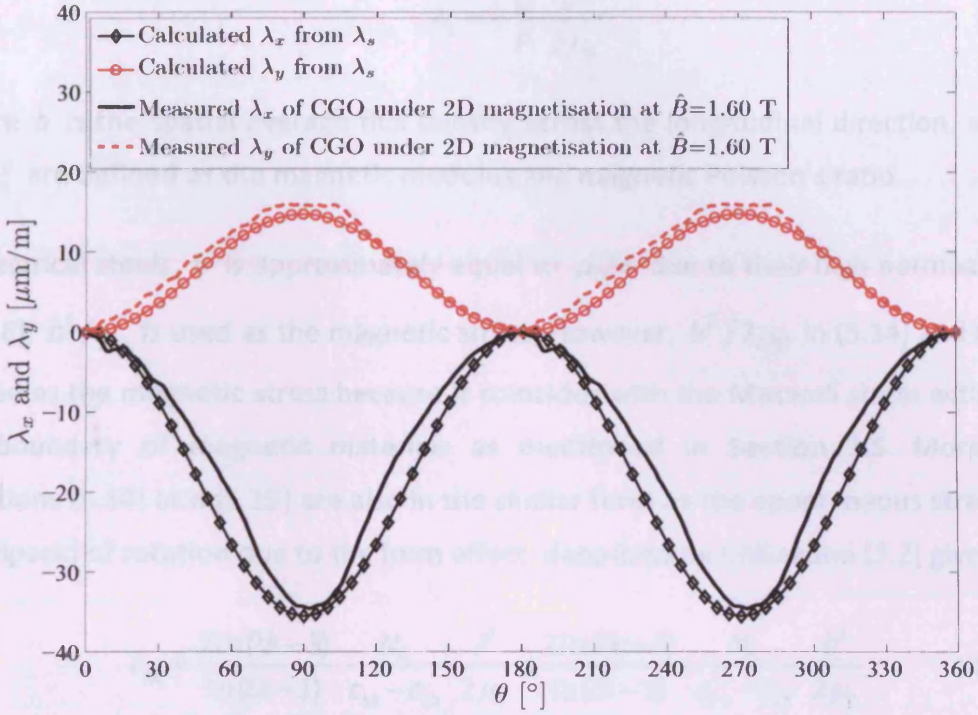

Fig. 5-5 Calculated magnetostriction observed in the [100] and [011] directions (λ_x and λ_y) of a iron single crystal of 3% Si GO steel saturated magnetised at angle θ to the [100] direction (dashed lines) compared with the measured magnetostriction (λ_x and λ_y) along the RD and TD of a 3% Si GO steel under 2D magnetisation at peak flux density of 1.60 T, 50 Hz (solid lines)

5.3 2D Magnetostriction Model for NO Steel

5.3.1 Magnetostriction modelling based on analogy of mechanical elasticity

This model proposed by Lundgren [*5.8*] was used to predict magnetostriction of GO electrical steel under 2D magnetisation. This model is based on a simple linear stress-strain relationship. Longitudinal and transverse strains of an elastic material respond to an applied mechanical stress as described in (4.21) and (4.22). Magnetostriction is the strain due to magnetisation and it varies with the square of magnetisation as in (5.7). Thus, M^2 can be analogous to the mechanical stress, so the longitudinal and transverse magnetostriction ($\lambda_{||}$ and $\lambda_{\perp}$) can be simply modelled as

$$\lambda_{11} = \frac{1}{P} \cdot \frac{b^2}{2\mu_0} \tag{5.14}$$

$$\lambda_{\perp} = -\frac{\xi}{P} \cdot \frac{b^2}{2\mu_0} \tag{5.15}$$

where b is the spatial average flux density across the longitudinal direction, and P and ξ are defined as the magnetic modulus and magnetic Poisson's ratio.

In electrical steels, b is approximately equal to $\mu_0 M$ due to their high permeability. In [*5.8*], b^2/μ_0 is used as the magnetic stress. However, $b^2/2\mu_0$ in (5.14) and (5.15) is used as the magnetic stress because it coincides with the Maxwell stress acting on the boundary of magnetic materials as mentioned in **Section 2.5**. Moreover, equations (5.14) and (5.15) are also in the similar form as the spontaneous strains of an ellipsoid of rotation due to the form effect described by Chikazumi [*5.2*] given as

$$\varepsilon_{xx} = \frac{2\ln(2k-3)}{\ln(2k-1)} \cdot \frac{N_0}{c_{11}-c_{12}} \cdot \frac{J^2}{2\mu_0} \approx \frac{2\ln(2k-3)}{\ln(2k-1)} \cdot \frac{N_0}{c_{11}-c_{12}} \cdot \frac{b^2}{2\mu_0} \tag{5.16}$$

$$\varepsilon_{yy} = \varepsilon_{zz} = -\frac{1}{2}\varepsilon_{xx} \tag{5.17}$$

where ε_{xx}, ε_{yy} and ε_{zz} are the longitudinal, transverse, and normal spontaneous strains of the ellipsoid respectively, N_0 is the initial demagnetisation factor before deformation, c_{11} and c_{12} are the elastic moduli of the single crystal, and k is the ratio of the length to the width of the ellipsoid [*5.2*].

In addition, magnetostriction under alternating magnetisation is generally history dependent, so the plot of magnetostriction against flux density is a butterfly-like shape. This plot is a so-called butterfly loop. Thus, a first order differential equation is added to (5.14) and (5.15) to create the butterfly loop as expressed in (5.18) and (5.19). The width of the loop is controlled by a time constant, τ_m.

$$\tau_m \frac{d\lambda_{11}}{dt} + \lambda_{11} = \frac{1}{P} \cdot \frac{b^2}{2\mu_0} \tag{5.18}$$

$$\tau_m \frac{d\lambda_{\perp}}{dt} + \lambda_{\perp} = -\frac{\xi}{P} \cdot \frac{b^2}{2\mu_0} \tag{5.19}$$

Fig. 5-6 compares the simulated longitudinal magnetostriction under sinusoidal magnetisation at peak flux density of 1.00 T, 50 Hz with P=125 GPa by using the monopoly model in (5.14) and the history dependent model in (5.18). The simulations start from the demagnetised condition and the $\lambda - b$ curve of the history dependent model does not return to their initial value, which is typical in ferromagnetic materials [5.9]. It can be observed that the peak to peak magnetostriction (λ_{pp}) is frequency dependent. Its normalised value decreases as the magnetising frequency (f_m) increases at the rate of $1/\sqrt{(4\pi f_m \tau_m)^2 + 1}$.

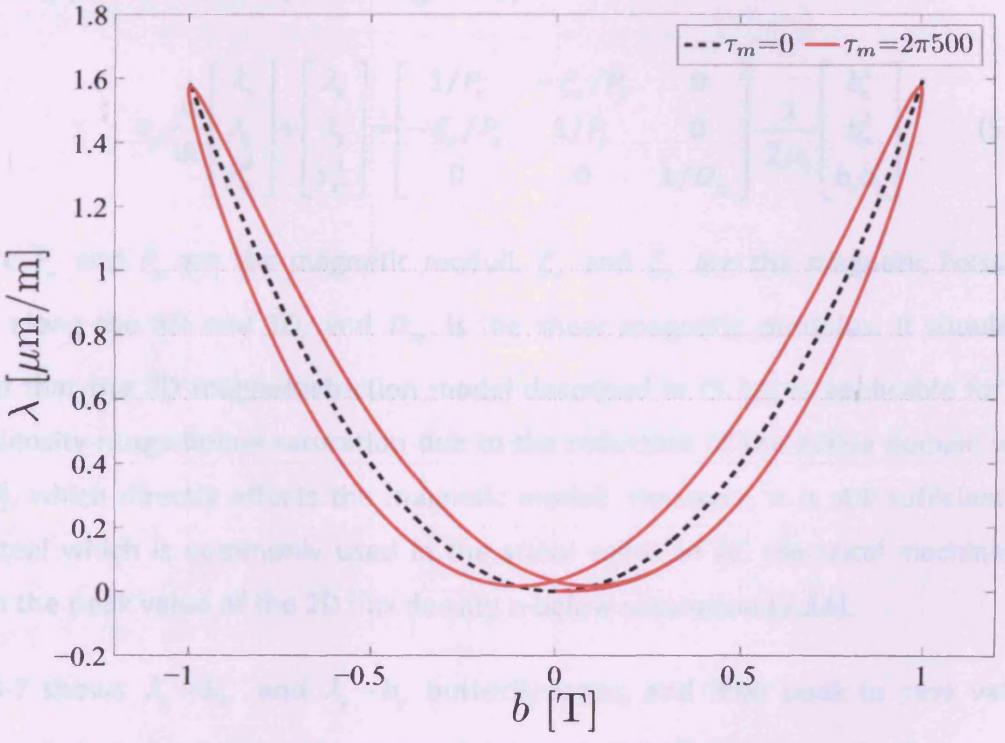

Fig. 5-6 Comparison of simulated longitudinal magnetostriction using the monopoly model in (5.14) and the history-dependent model in (5.18) versus flux density under sinusoidal magnetisation at $\hat{B}$=1.00 T, 50 Hz with P=125 GPa

5.3.2 Magnetostriction model under 2D magnetisation

In the case of 2D magnetisation, there are two components of magnetic induction, creating two components of magnetic stress in the plane of the lamination. By analogy with the in-plane stress/strain relationship in (4.24), and incorporating with the history dependence in (5.13), the magnetostriction of isotropic materials under 2D magnetisation can be modelled as

$$\tau_m \frac{d}{dt}\begin{bmatrix}\lambda_x\\ \lambda_y\\ \gamma^{\lambda}_{xy}\end{bmatrix}+\begin{bmatrix}\lambda_x\\ \lambda_y\\ \gamma^{\lambda}_{xy}\end{bmatrix}=\begin{bmatrix}1/P & -\xi/P & 0\\ -\xi/P & 1/P & 0\\ 0 & 0 & 2(1+\xi)/P\end{bmatrix}\cdot\frac{1}{2\mu_0}\begin{bmatrix}b_x^2\\ b_y^2\\ b_x b_y\end{bmatrix} \quad (5.20)$$

where b_x and b_y are orthogonal components of instantaneous flux density, and γ^{λ}_{xy} is the shear magnetostriction between the RD and TD.

For the case of an anisotropic material, the magnetic modulus and Poisson's ratio in the x direction are not identical to those along the y direction to reflect the anisotropy of the material, which is given by

$$\tau_m \frac{d}{dt}\begin{bmatrix}\lambda_x\\ \lambda_y\\ \gamma^{\lambda}_{xy}\end{bmatrix}+\begin{bmatrix}\lambda_x\\ \lambda_y\\ \gamma^{\lambda}_{xy}\end{bmatrix}=\begin{bmatrix}1/P_x & -\xi_x/P_y & 0\\ -\xi_y/P_x & 1/P_y & 0\\ 0 & 0 & 1/D_{xy}\end{bmatrix}\cdot\frac{1}{2\mu_0}\begin{bmatrix}b_x^2\\ b_y^2\\ b_x b_y\end{bmatrix} \quad (5.21)$$

where P_x and P_y are the magnetic moduli, ξ_x and ξ_y are the magnetic Poisson's ratio along the RD and TD, and D_{xy} is the shear magnetic modulus. It should be noted that the 2D magnetostriction model described in (5.21) is applicable for the flux density range below saturation due to the reduction of the active domain walls [*5.10*], which directly affects the magnetic moduli. However, it is still sufficient for NO steel which is commonly used in the stator cores of AC electrical machines in which the peak value of the 2D flux density is below saturation [*5.11*].

Fig. 5-7 shows $\lambda_x - b_x$ and $\lambda_y - b_y$ butterfly loops, and their peak to peak values ($\lambda_{x_{PP}}$ and $\lambda_{y_{PP}}$) simulated using the model described in (5.21) under the flux density condition of $b_x = \hat{B}\sin(2\pi f_m t)$ and $b_y = \hat{B}\cos(2\pi f_m t)$ where $\hat{B}$=1.30 T, f_m=50 Hz and t is in the range of 0 to 20 ms. Four cases of the parameters as listed in Table 5-1 were used in the simulation to study the effect of magnetostriction anisotropy on the 2D magnetostriction. The $\lambda_x - b_x$ curve is completely overlaid by the $\lambda_y - b_y$ curve in the isotropic case. For case 2, the alternating magnetostriction in the TD is double that along the RD. Not only is the $\lambda_x - b_x$ curve forced away from the $\lambda_y - b_y$ curve, but their peak to peak values are greater than in the isotropic case. The two butterfly loops are far more separated from each other and the values of $\lambda_{x_{PP}}$ and $\lambda_{y_{PP}}$ increase for the higher anisotropic materials in case 3. Comparing case 4 with case 3,

it can be observed that the magnetic Poisson's ratio affects λ_x significantly even though the magnetic moduli are the same.

Table 5-1 Parameters used for simulated magnetostriction under 2D magnetisation

Case	P_x [GPa]	ξ_x	P_y [GPa]	ξ_y	D_{xy} [GPa]	τ_m [ms]
1. Isotropic	300	0.5	300	0.5	$P_x/3$	0.2
2.Less anisotropic	300	0.5	$P_x/2$	0.5	40	0.2
3. Highly anisotropic	300	0.5	$P_x/4$	0.5	40	0.2
4. Highly anisotropic, high transverse magnetostriction	300	1	$P_x/4$	1	40	0.2

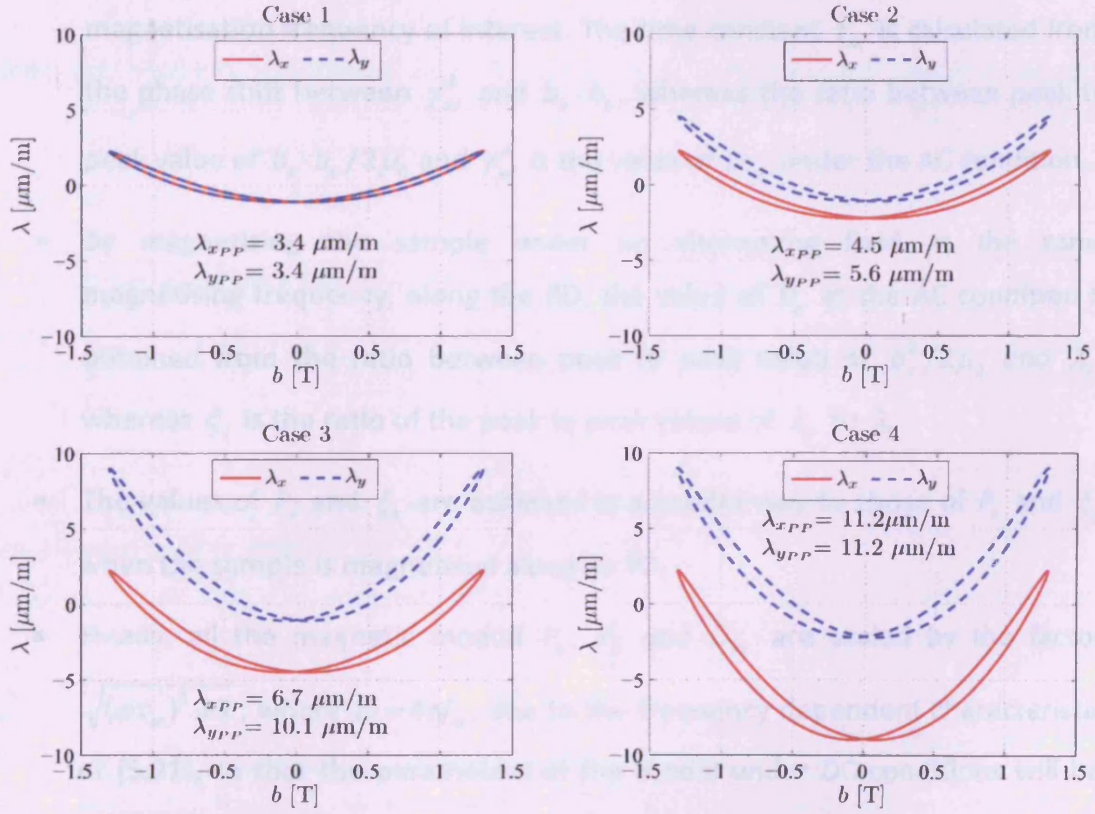

Fig. 5-7 Simulated magnetostriction using the 2D magnetostriction model in (5.21) under 2D magnetisation at $b_x = \hat{B}\sin(2\pi f_m t)$ and $b_y = \hat{B}\cos(2\pi f_m t)$ where $\hat{B}$ =1.30 T, f_m =50 Hz and t is in the range of 0 to 20 ms using parameters in Table 5-1

5.3.3 Identification of parameters for 2D magnetostriction model

The identification of the magnetic moduli, Poisson's ratios and time constant, τ_m requires a 2D magnetising system. This measurement system should be capable of generating both alternating and rotational magnetisation in the plane of electrical steel sheet and the in-plane magnetostriction must be observed in three directions so that the magnetostriction can be transformed to any coordinate as described in **Chapter 4**. The 2D magnetising system is fully explained in **Chapter 6**. The flux density should be kept below the technical saturation value. The identification of the 2D magnetostriction model is obtained as follows:

- Apply a 2D magnetisation (circular flux density loci) to the sample at the magnetisation frequency of interest. The time constant τ_m is calculated from the phase shift between γ_{xy}^{λ} and $b_x \cdot b_y$, whereas the ratio between peak to peak value of $b_x \cdot b_y / 2\mu_0$ and γ_{xy}^{λ} is the value of D_{xy} under the AC condition.
- By magnetising the sample under an alternating field at the same magnetising frequency, along the RD, the value of P_x at the AC condition is obtained from the ratio between peak to peak value of $b_x^2 / 2\mu_0$ and λ_x, whereas ξ_y is the ratio of the peak to peak values of λ_y to λ_x.
- The values of P_y and ξ_x are achieved in a similar way to those of P_x and ξ_y when the sample is magnetised along its TD.
- Finally, all the magnetic moduli P_x, P_y and D_{xy} are scaled by the factor $\sqrt{(\omega\tau_m)^2 + 1}$, where $\omega = 4\pi f_m$, due to the frequency dependent characteristic of (5.21), so that the parameters of the model under DC conditions will be obtained.

5.4 References for Chapter 5

[5.1] D. C. Jiles, *Introduction to Magnetism and Magnetic Materials*, Second edition, Chapman & Hall/CRC, London, 1998.

[5.2] S. Chikazumi, *Physics of Magnetism*, John Wiley & Sons, New York, 1964.

[5.3] J. Shilling and G. Jr. Houze, "Magnetic properties and domain structure in grain-oriented 3% Si-Fe," *IEEE Transactions on Magnetics*, Vol. 10, pp. 195-223, 1974.

[5.4] P. Klimczyk, *Magnetostriction of Grain Oriented Electrical Steels under Two-dimensional Magnetisation*, Unpublished document, Wolfson Centre for Magnetics, Cardiff University, 2009.

[5.5] A. J. Moses, "Electrical steels: past, present and future developments," *IEE Proceedings-A Science Measurement and Technology*, Vol. 137, pp. 233-245, 1990.

[5.6] O. Hubert, L. Daniel, and R. Billardon, "Experimental analysis of the magnetoelastic anisotropy of a non-oriented silicon iron alloy," *Journal of Magnetism and Magnetic Materials*, Vol. 254-255, pp. 352-354, 2003.

[5.7] A. J. Moses, A. Ntatsis, T. Kochmann, and J. Schneider, "Magnetostriction in non-oriented electrical steels: General trends," *Journal of Magnetism and Magnetic Materials*, Vol. 215-216, pp. 669-672, 2000.

[5.8] A. Lundgren, *On Measurement and Modelling of 2D Magnetization and Magnetostriction of SiFe Sheets*, PhD Thesis, Royal Institute of Technology, Sweden, 1999.

[5.9] M. J. Sablik and D. C. Jiles, "Coupled magnetoelastic theory of magnetic and magnetostrictive hysteresis," *IEEE Transactions on Magnetics*, Vol. 29, pp. 2113-2123, 1993.

[5.10] A. J. Moses, "Importance of rotational losses in rotating machines and transformers," *Journal of Materials Engineering and Performance*, Vol. 1, pp. 10, 1992.

[5.11] G. Díaz, C. González-Morán, P. Arboleya, and J. Gómez-Aleixandre, "Analytical interpretation and quantification of rotational losses in stator cores of induction motors," *IEEE Transactions on Magnetics*, Vol. 43, pp. 3861-3867, 2007.

Chapter 6

Magnetisation and Measurement Systems

This chapter describes the magnetisation and measurement systems used in the study of anisotropy of specific power loss, AC permeability, and magnetostriction in Epstein strips of NO electrical steels. The measurement system for measurement of specific power loss and magnetostriction under 2D magnetisation is presented. The system for measurement of Young's modulus and Poisson's ratio of Epstein strips is also explained. Finally, uncertainties of all the measurements in electrical steels are presented.

6.1 System for Measurement of AC Magnetic Properties of Epstein Strips

A computer-controlled system had been developed within the Wolfson Centre for Magnetics providing high accuracy and automatic measurements. It does not require any discrete instrument since a program written in LabVIEW is used to calculate magnetic properties.

Fig. 6-1 displays a schematic diagram of the system. It comprises a personal computer (PC), in which LabVIEW version 8.50 from National Instruments was already installed, a NI PCI-6120 data acquisition (DAQ) card [*6.1*], a power amplifier, a 1 Ω shunt resistor (R_{sh}), and an air-flux compensated single strip tester (SST). A double vertical yoke type shown in Fig. 6-2 (a) is used. Each yoke was made from GO steel and its physical dimensions are detailed in Fig. 6-2 (b). A 250 turn secondary winding (N_2) was wound around a plastic former, while a 865-turn primary winding

(N_1) was wound around the secondary winding. A standard Epstein strip (305 mm long, 30 mm wide) to be tested is placed between the yokes.

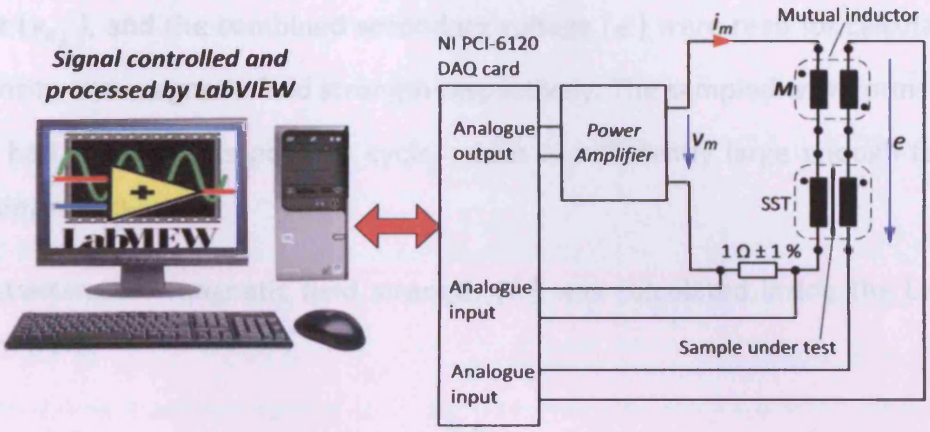

Fig. 6-1 Schematic diagram of computer-controlled AC magnetic property measurement system

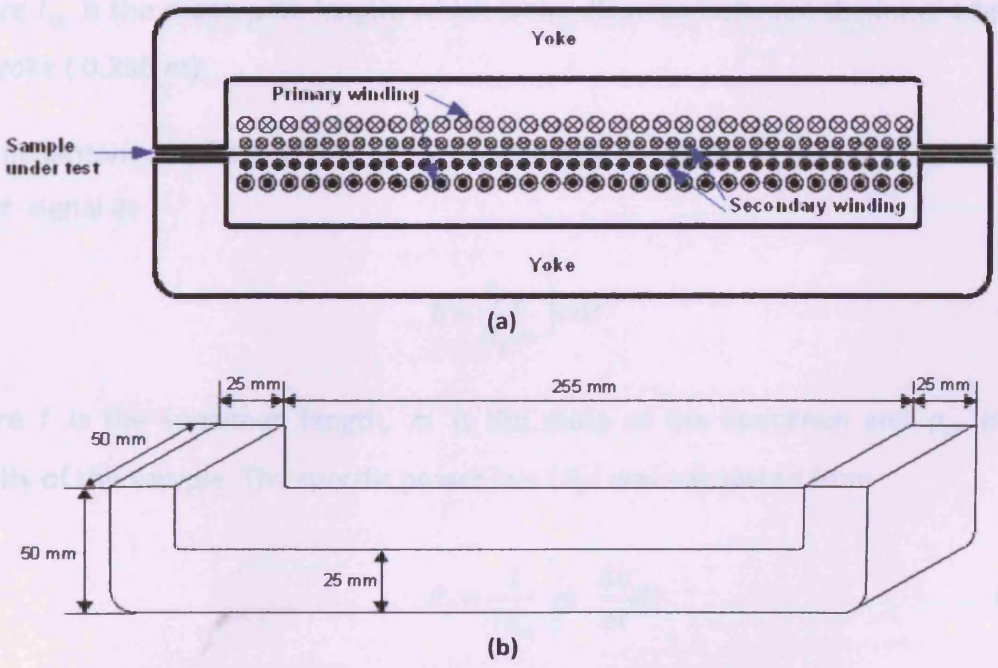

Fig. 6-2 Single strip tester: (a) side view, and (b) physical dimensions of a flux closure yoke

The mutual inductor was used to compensate for the effect of air flux by connecting its primary winding in series with the SST primary winding, while connecting the secondary winding in series opposition with the SST secondary winding. The mutual inductance was adjusted by passing an alternating current through the primary winding in the absence of the test sample until the voltage of the secondary circuit was less than 0.1 % of the SST secondary voltage. Hence, the induced voltage in the combined secondary winding is only due to the flux density in the test sample.

The magnetising voltage was generated by the LabVIEW program via a voltage output of the DAQ card. There were data 20,000 points per magnetisation cycle to make the signal waveform as smooth as possible. The voltage drop across the shunt resistor ($v_{R_{sh}}$), and the combined secondary voltage (e) were read for calculation of flux density and magnetic field strength respectively. The sampled waveforms of $v_{R_{sh}}$ and e had 1,800 points per one cycle, which is sufficiently large enough to avoid quantizing errors.

The instantaneous magnetic field strength (h) was calculated inside the LabVIEW program from

$$h = \frac{N_1 v_{R_{sh}}}{l_m R_{sh}} \tag{6.1}$$

where l_m is the mean path length, which is the distance between the inner edges of the yoke (0.255 m).

The instantaneous flux density (b) was obtained by mean of digital integration of the e signal as

$$b = \frac{l\rho_m}{N_2 m}\int e dt \tag{6.2}$$

where l is the specimen length, m is the mass of the specimen and ρ_m is the density of the sample. The specific power loss (P_s) was calculated from

$$P_s = \frac{1}{T\rho_m}\int_0^T h \cdot \frac{db}{dt} dt \tag{6.3}$$

where T is the magnetising cycle period. The AC relative permeability ($\mu_{r_{AC}}$) of the material was derived from

$$\mu_{r_{AC}} = \frac{\hat{B}}{\mu_0 \hat{H}} \tag{6.4}$$

where $\hat{H}$ is the peak value of magnetic field. $\hat{B}$ and $\hat{H}$ were determined numerically by using the maximum function in LabVIEW.

The control of the flux density waveform was implemented in LabVIEW as shown in Fig. 6-1. A feedback control system was used to control the flux density and secondary induced voltage waveforms to be sinusoidal. The form factor (FF) of the secondary induced voltage was maintained to be 1.111 ± 0.02 %, which is better than the value recommended in [*6.2*]. Fig. 6-3 shows the procedure for each measurement. Firstly, a table of $\hat{B}$ values and the measurement criteria which are the 0.02 % error of $\hat{B}$ and 0.02 % error of the ideal FF of the secondary induced voltage are read. Secondly, a first magnetising waveform is applied to the SST. If the criteria are met, the b and h waveforms will be averaged to minimise random errors and improve repeatability [*6.3*], otherwise the magnetising waveform is adjusted by the feedback algorithm. After averaging, the criteria are re-checked then the measurement data for this point is saved. A spread sheet file is generated if all the values of $\hat{B}$ are measured and the sample is demagnetised by reducing the magnetisation gradually to zero. Fig. 6-4 shows the components of the SST measurement system.

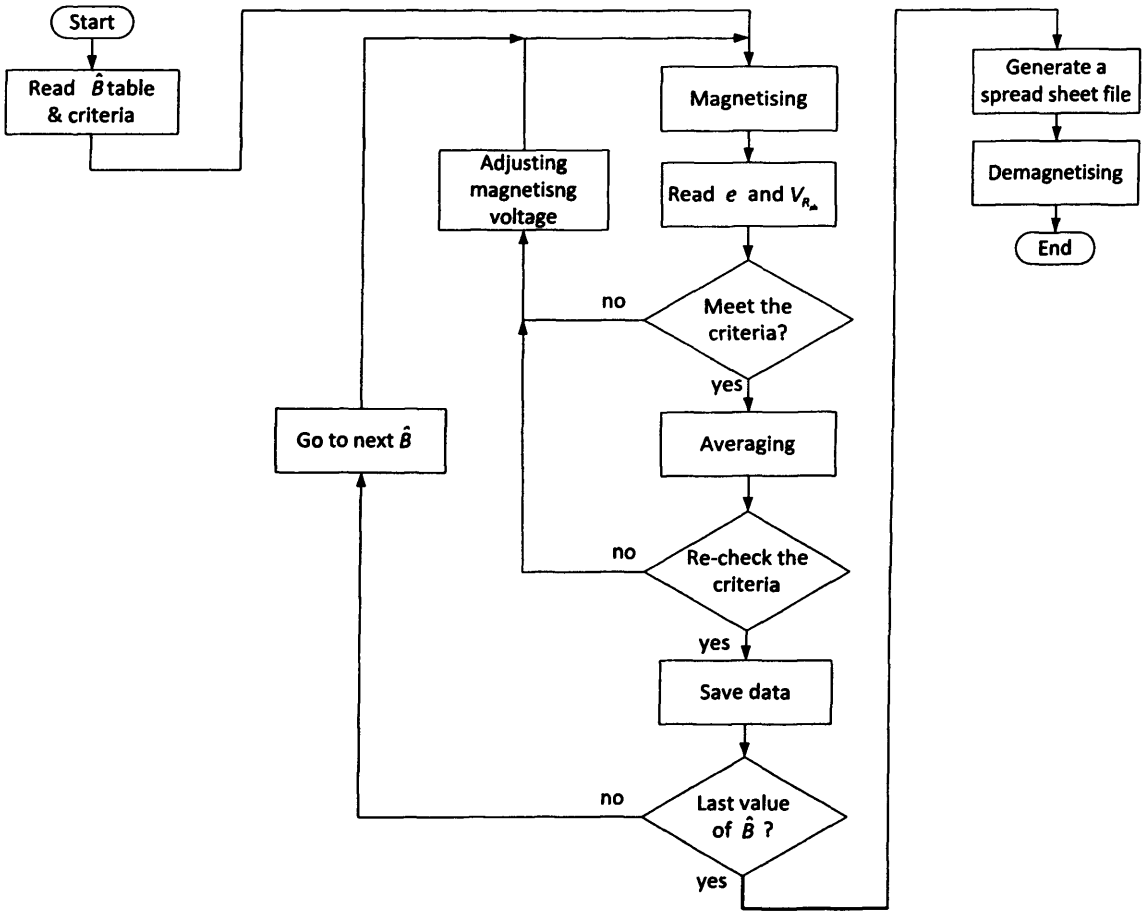

Fig. 6-3 Flowchart showing procedure of each measurement of the single strip tester

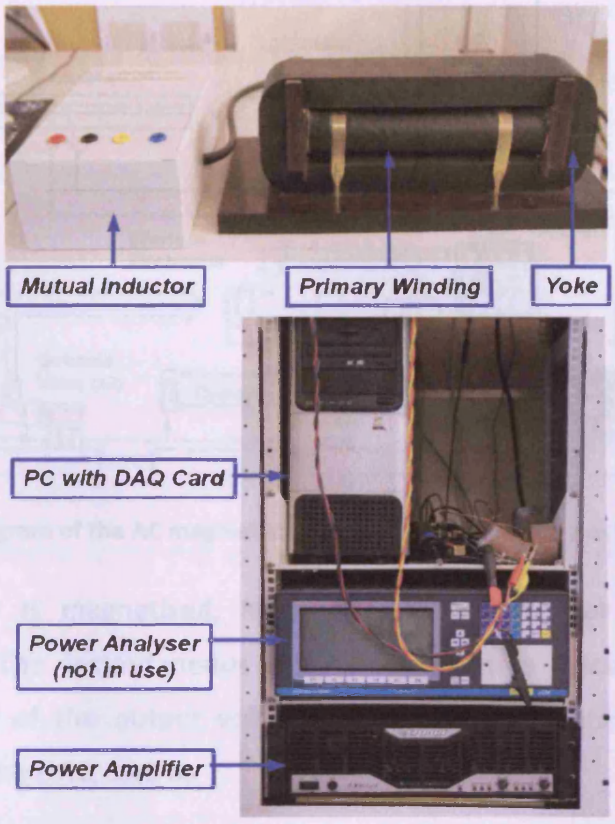

Fig. 6-4 Photographs of components of the single strip tester

6.2 System for Measurement of the AC Magnetostriction of Epstein Strips

Fig. 6-5 shows the schematic diagram of the system for measurement of the AC magnetostriction of Epstein strips. A standard Epstein strip is inserted into a Tufnol former which is enwrapped by the secondary and primary windings. The magnetic circuit is enclosed by a single yoke placed under the sample. The physical dimensions of the yoke are detailed in Fig. 6-6. A mutual inductor is connected with the primary and secondary windings for air flux compensation similar to the SST in Fig. 6-1. The magnetisation control is also the same as for the SST [*6.4*].

One end of the strip is clamped and the other end is attached to an accelerometer, load cell and a pneumatic cylinder. With a stable air supply of approximately 0.7 MPa, the system is capable of applying a range of stress values from 10 MPa to -10 MPa to the sample. The stress σ applied to the sample is automatically controlled by a LabVIEW program via a DAQ card connected to a series of electro-pneumatic and solenoid valves.

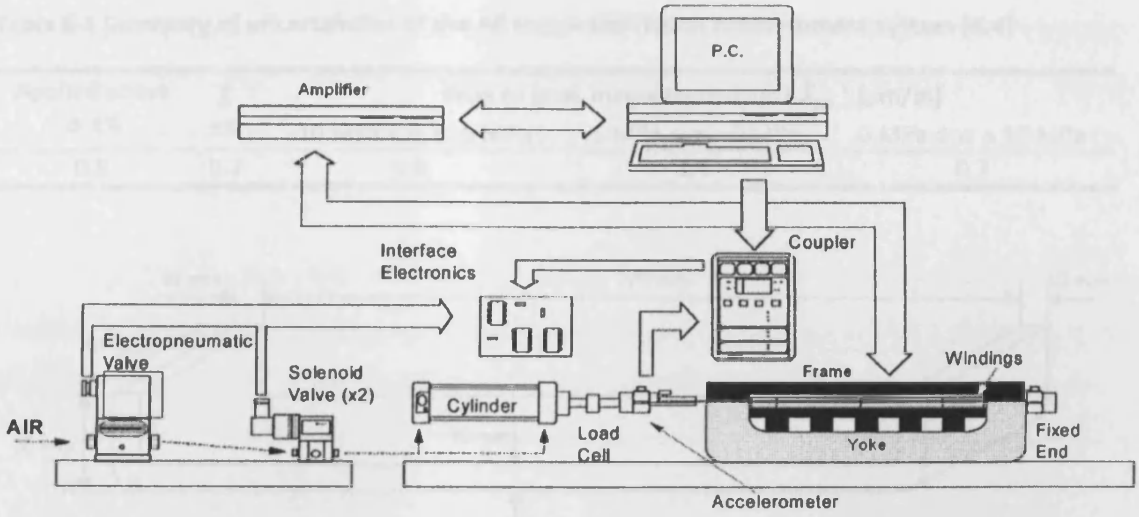

Fig. 6-5 Schematic diagram of the AC magnetostriction measurement system for Epstein strips [*6.4*]

When the sample is magnetised, its free end elongates or contracts due to magnetostriction. The instantaneous magnetostriction is calculated from digital double integration of the output voltage of the accelerometer connected to an analogue input to the DAQ card as

$$\lambda(t) = \frac{1}{k_a l_m} \iint v_a dt + C_a \qquad (6.5)$$

where k_a is the sensitivity of the accelerometer in V/g, v_a is the output voltage of the accelerometer and C_a is the integration constant which can be determined from the relation:

$$\lambda(t) = 0 \qquad \text{at} \qquad h = 0\,. \qquad (6.6)$$

A Kistler 8630C piezoelectric accelerometer was chosen. Its sensitivity (k_a) is 1 V/g ± 5 %, where g is the Earth's gravitational constant (9.80665 m/s^2) [*6.5*] and l_m was taken from the distance between the inner edges of the flux closure yoke which is 0.27 m as seen in Fig. 6-6.

Magnetising frequencies of 50 and 60 Hz were available for this AC magnetostriction measurement system. In fact, the system is able to magnetise up to approximately 500 Hz. However, it is limited due to the measurement range of the accelerometer. The estimated uncertainties of this measurement system are summarised in Table 6-1 [*6.4*]. The system is displayed in Fig. 6-7.

Table 6-1 Summary of uncertainties of the AC magnetostriction measurement system [*6.4*]

Applied stress	$\hat{B}$	Peak to peak magnetostriction (λ_{pp}) [μm/m]		
σ ±%	±%	-10 MPa < σ ≤ -5 MPa	-5 MPa < σ < 0 MPa	0 MPa ≤ σ ≤ 10 MPa
0.9	0.2	1.9	1.4	0.7

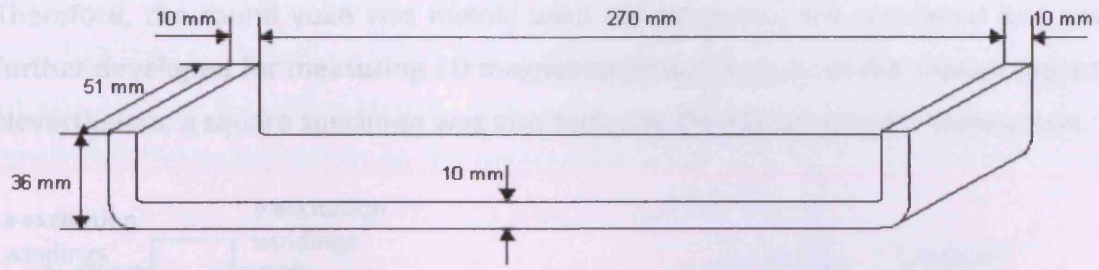

Fig. 6-6 Physical dimensions of the flux closure yoke of the AC magnetostriction measurement system [*6.4*]

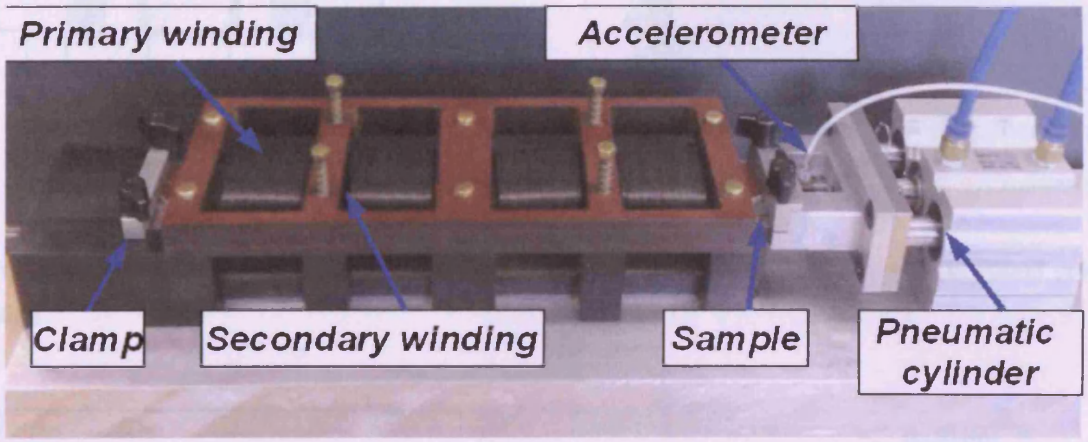

Fig. 6-7 Photograph of components of the AC magnetostriction measurement system [*6.4*]

6.3 2D Magnetisation System for Measurement of Rotational Power Loss and 2D Magnetostriction in Electrical Steel Sheets

6.3.1 Magnetising setups

The 2D magnetisation system was initially developed by Zurek in 2005 [*6.6*] for measurement of rotational loss in electrical steel sheets. This system possesses two magnetising yokes: a round yoke and a planar yoke as displayed in Fig. 6-8. A disc sample with a diameter of 80 mm is suitable for the round yoke (Fig. 6-9 (a)), while the planar yoke accommodates a 90 mm × 90 mm specimen (Fig. 6-9 (b)). One of the advantages of the round yoke is that higher magnetisation can be achieved (approximately up to 2.0 T for NO materials [*6.7*]) but its drawbacks are less field

homogeneity throughout the sample and the difficulty in cutting such a circular shape [*6.8*]. However, the homogeneity of flux density in an area 20 mm × 20 mm at the centre of a 78 mm diameter round sample of 3% NO steel was nearly the same as the flux density at the centre of the sample [*6.9*].

Therefore, the round yoke was mainly used for measuring the rotational loss and further developed for measuring 2D magnetostriction because of the above reasons. Nevertheless, a square specimen was also tested in the planar yoke for comparison.

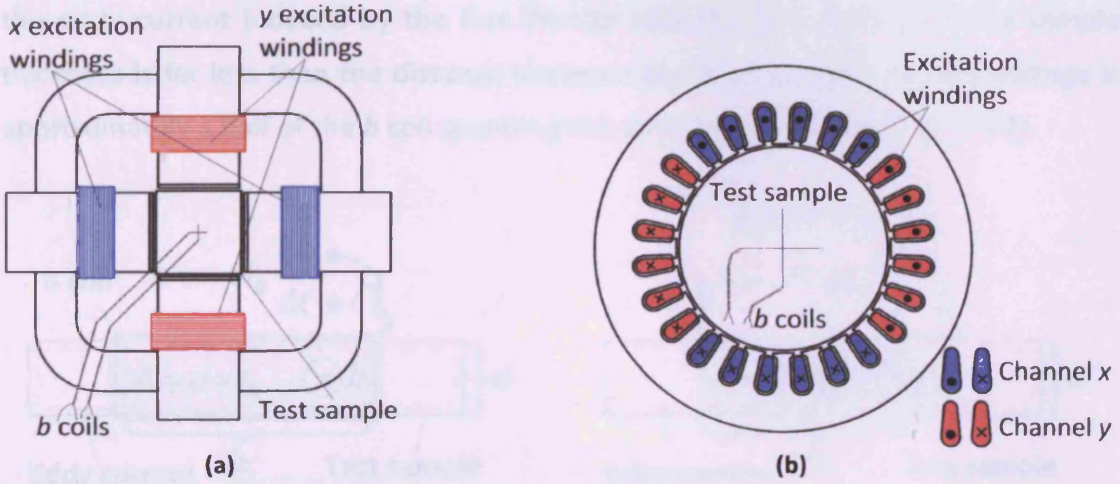

Fig. 6-8 Magnetising yokes for the 2D magnetisation system: (a) planar yoke, and (b) round yoke [*6.6*]

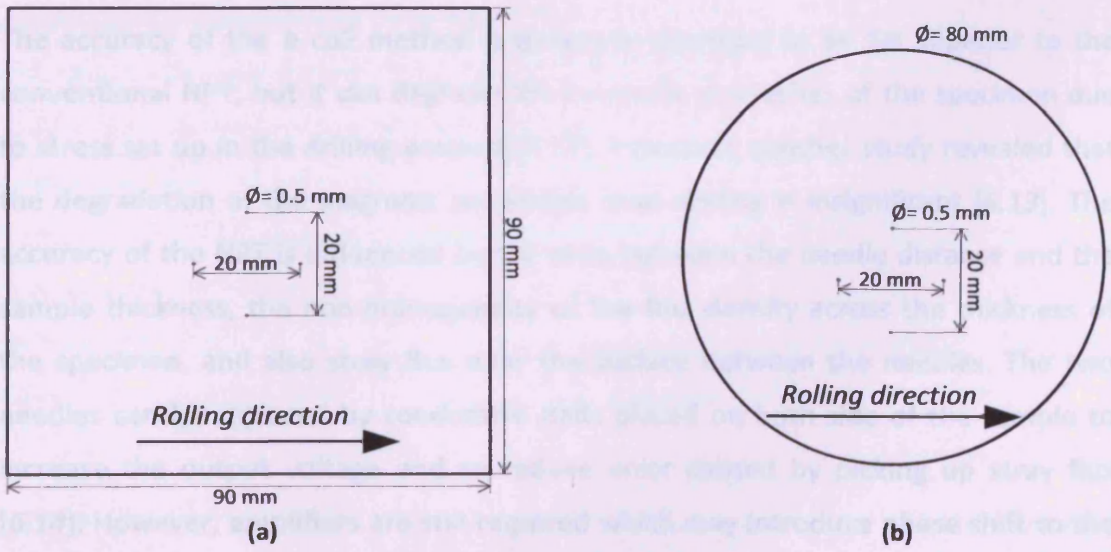

Fig. 6-9 Dimensions of specimens for the 2D magnetisation system: (a) square specimen for the planar yoke, and (b) disc specimen for the round yoke (ø is the diameter.)

6.3.2 Flux density sensors

To detect localised flux density at the centre region of the sample, two techniques can be used: (a) *b* coil technique (also termed as search coils or pick-up coils) and (b) needle probe technique (NPT) as shown in Fig. 6-10 [*6.10*]. The *b* coil technique requires a wire to be threaded through small holes in the specimen to form a search coil. The output voltage of the *b* coil is proportional to the rate of change of the spatial average flux density over the region *A* in Fig. 6-10. The NPT is a non-destructive technique based on the measurement of the potential difference due to the eddy current induced by the flux density between two needles. If the sample thickness is far less than the distance between the two needles, the NPT voltage is approximately a half of the *b* coil spanning the same measured distance [*6.11*].

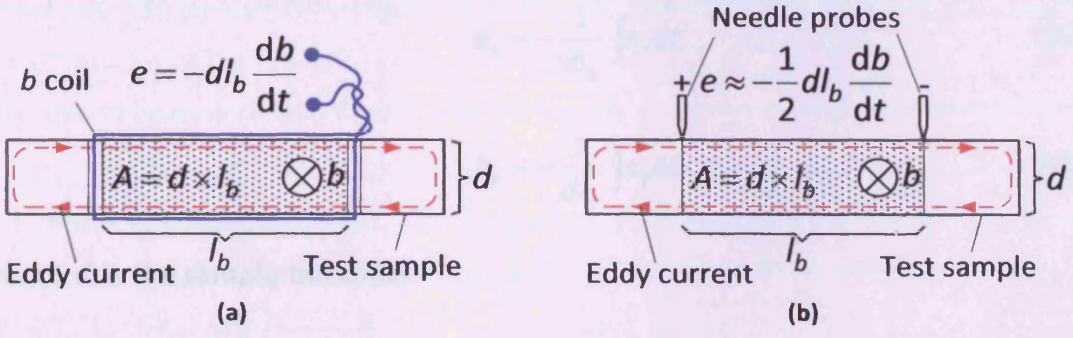

Fig. 6-10 Illustration of the flux density measurement technique: (a) *b* coil technique, and (b) needle probe technique (NPT) [*6.6*]

The accuracy of the *b* coil method is generally accepted to be far superior to the conventional NPT, but it can degrade the magnetic properties of the specimen due to stress set up in the drilling process [*6.12*]. However, another study revealed that the degradation of the magnetic properties from drilling is insignificant [*6.13*]. The accuracy of the NPT is influenced by the ratio between the needle distance and the sample thickness, the non-homogeneity of the flux density across the thickness of the specimen, and also stray flux near the surface between the needles. The two needles can be replaced by conductive pads placed on both side of the sample to increase the output voltage and to reduce error caused by picking up stray flux [*6.14*]. However, amplifiers are still required which may introduce phase shift to the waveforms causing errors in power loss measurement.

Taking measurement accuracy into account, the *b* coil technique was selected for this study. The compromise distance between the two holes is 20 mm since the flux

density is homogeneous and the output voltage is high enough to connect the b coils straight to the DAQ card [*6.6*]. The convenient hole size was 0.50 mm and four holes were drilled through the samples shown in Fig. 6-9 using an electric drill equipped with a precise positioning table. Hence the effective length (l_b) of each search coil was between the edges of the holes, equal to 19.5 mm. An enamelled copper wire of 0.20 mm diameter was threaded through each pair of holes to create loops perpendicular to the RD and TD as shown in Fig. 6-10 (a). The lead wires were twisted before connected to the DAQ card to reduce picking up stray fields. Therefore, the instantaneous flux densities along the RD and TD (b_x and b_y) were obtained by integration of the voltages (e_x and e_y) induced in the orthogonal search coils:

$$b_x = -\frac{1}{dl_b}\int e_x \mathrm{d}t \tag{6.7}$$

$$b_y = -\frac{1}{dl_b}\int e_y \mathrm{d}t \tag{6.8}$$

where d is the sample thickness.

6.3.3 Magnetic field sensors

To calculate the power loss dissipating in the sample, the spatial average $\mathrm{d}b/\mathrm{d}t$ and the tangential component of surface magnetic field h are required [*6.15*]. The spatial average $\mathrm{d}b/\mathrm{d}t$ can be obtained using the b coils described earlier, while h cannot be detected using the magnetising current method used in the Epstein test frame and the SST because of the field uniformity in the test sample. The tangential components of magnetic field at the boundary of two media with different permeability values is identical in each as illustrated in Fig. 6-11 [*6.16*]. Using this theory, the magnetic field components on the sample surface along the RD and TD (h_x and h_y) can be obtained by measuring the tangential components of the magnetic field close to the sample.

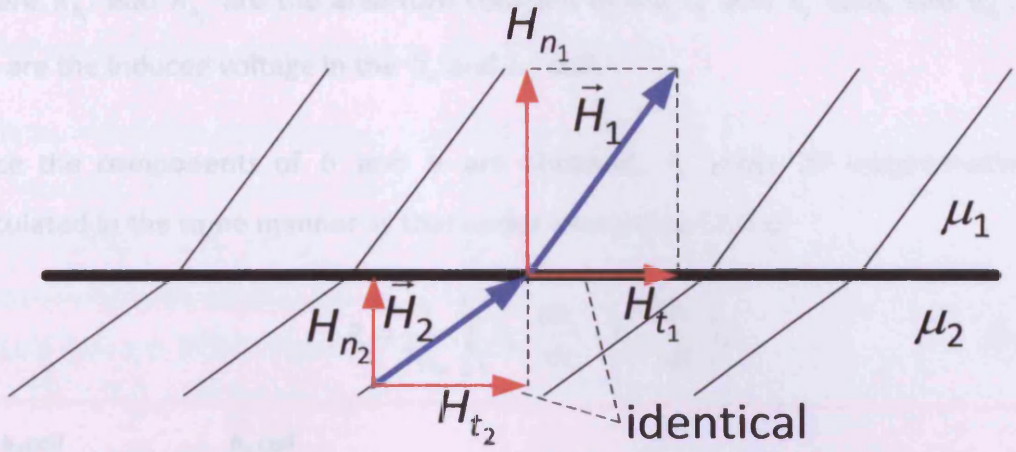

Fig. 6-11 Magnetic field strength vectors at the boundary between two materials with permeability μ_1 and μ_2 showing their equal tangential field components ($H_{t_1} = H_{t_2}$) [6.16]

There are two common methods of measuring the surface magnetic field strength for 2D magnetisation systems: the air coil method (also recognised as *h* coil method) and the Rogowski-Chattock potential (RCP) coil method. It was reported that they provide similar accuracy of measurement and the distance of the *h* coils up to 1.5 mm from the sample surface has insignificant influence on the measurement of power loss [*6.17*]. However, the cross-sectional area of an RCP coil is easily changed when it is bent, which affects the measurement accuracy [*6.15*]. Therefore, it was decided to use orthogonal *h* coils for measuring the surface h_x and h_y.

The h_y coil was wound on a 0.50 mm thick plastic former by an 0.05 mm diameter enamelled copper wire and it was orthogonally enwrapped by the h_x coil with the similar wire as shown in Fig. 6-12 (a). Their lead wires were twisted as for the *b* coils. The final thickness of the coils is 1 mm and the distance from the centre of the coils to the sample surface is about 0.09 mm as displayed in Fig. 6-12 (b). The specifications of the *h* coils are shown in Table 6-2 and **Appendix A** describes the *h* coil calibration process. Thanks to the linear relationship between *b* and *h* in free space, h_x and h_y can be calculated from the induced voltages as

$$h_x = -\frac{1}{\mu_0 K_{h_x}} \int e_{h_x} dt \tag{6.9}$$

$$h_y = -\frac{1}{\mu_0 K_{h_y}} \int e_{h_y} dt \tag{6.10}$$

where K_{h_x} and K_{h_y} are the area-turn constant of the h_x and h_y coils, and e_{h_x} and e_{h_y} are the induced voltage in the h_x and h_y coils.

Once the components of b and h are obtained, P_s under 2D magnetisation is calculated in the same manner as that under alternating field as

$$P_s = \frac{1}{T\rho_m}\int_0^T \left(h_x \cdot \frac{db_x}{dt} + h_y \cdot \frac{db_y}{dt} \right) dt \qquad (6.11)$$

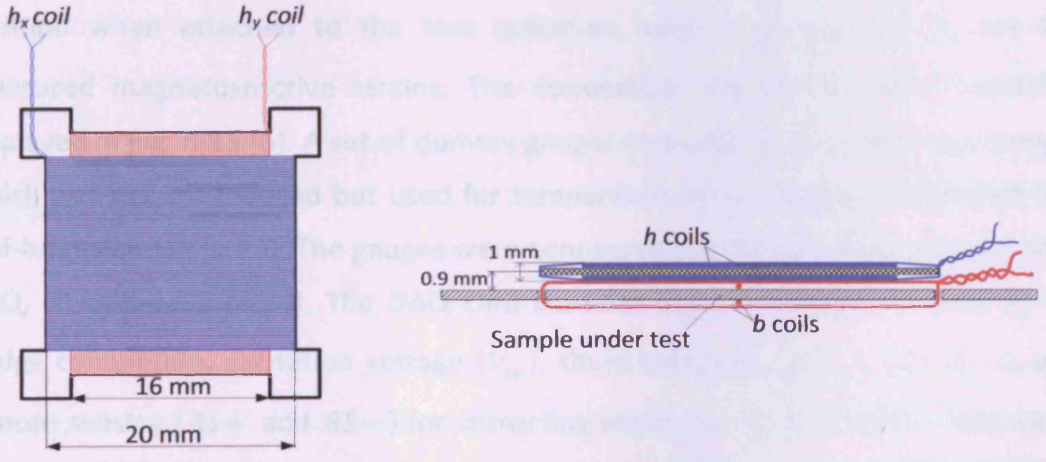

Fig. 6-12 Schematic diagram of orthogonal h coils wound on one plastic former (not scaled): (a) top view, and (b) side view when attached with the sample under test

Table 6-2 Specifications of *h* coils used in the 2D magnetisation system

Coil	Turns	Wire diameter [mm]	Area-turn constant [m^2]	Former size [mm × mm × mm]
h_x	230	0.05	0.003119 ± 0.000057	20 x 16 x 0.5
h_y	230	0.05	0.001989 ± 0.000036	

6.3.4 Sensors for measurement of magnetostriction under 2D magnetisation

Analysis of in-plane magnetostriction under 2D magnetisation requires information of strain components measured in three directions on the surface of the sample. These give magnetostriction components λ_x and λ_y, and the shear magnetostriction between the RD and TD, γ_{xy}^{λ} as described in **Chapter 4**. This contrasts with b and h measurements which require only two orthogonal components. The most convenient method is to use resistance strain gauges due to their accuracy and

simplicity [*6.18, 6.19*]. An optical technique could be used [*6.20*], but it is not cost-effective since three measurement units are required.

Rosette resistance strain gauges from TML model FRA-6-11 were therefore selected to measure the in-plane magnetostriction [*6.21*]. Table 6-3 summarises the specifications. Each gauge was 6 mm long and 2.4 mm wide, which covers approximately 60 surface grains of NO electrical steels having typical grain size of around 100 μm [*6.22*]. The method of strain gauge attachment is fully described in **Chapter 7**. Fig. 6-13 (a) shows the dimensions of the rosette strain gauges and their position when attached to the test specimen, where λ_a, λ_b and λ_c are the measured magnetostrictive strains. The connection diagram of each channel is displayed in Fig. 6-13 (b). A set of dummy gauges were attached to a dummy sample which was not magnetised but used for temperature compensation connected in a half-bridge circuit [*6.23*]. The gauges were connected to a built-in strain gauge bridge DAQ, NI USB-9237 [*6.24*]. The DAQ card contains built-in resistors R_1 and R_2 for bridge completion, excitation voltage (V_{ex}), shunt calibration ($SC+$ and $SC-$), and remote sensing ($RS+$ and $RS-$) for correcting errors due to lead wire resistance. It accommodates four channels to be connected simultaneously. V_{ex} can be set to be 2.5, 3.3, 5 or 10 V at a maximum power of 150 mW. It was set to 2.5 V for three channels of 120 Ω half-bridge circuits due to the limited excitation power.

Table 6-3 Specifications of the FRA-6-11 Rosette resistance strain gauge

Resistance (R_g) [Ω]	Gauge factor (K_g)	Gauge length [mm]	Gauge width [mm]	Package diameter [mm]
120	2.1 ± 1 %	6	2.4	14

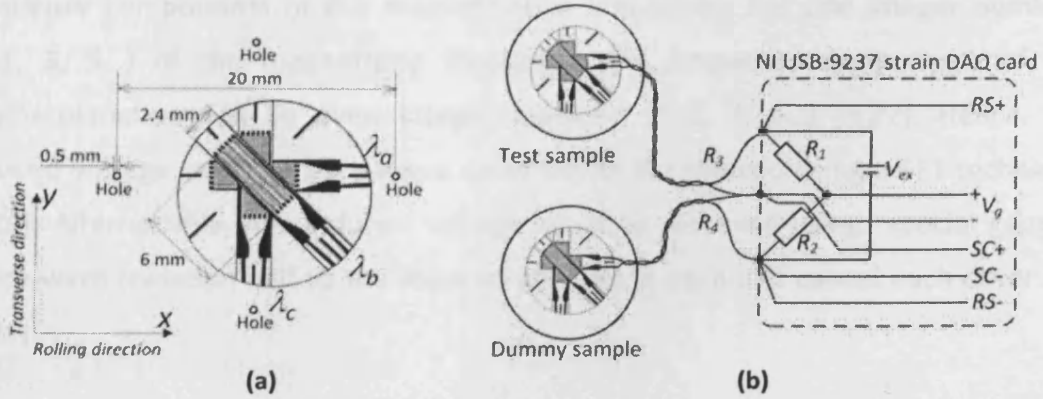

Fig. 6-13 (a) Dimensions of a rosette strain gauge and its position attached to a sample, (b) Connection diagram of an active strain gauge

The bridge output voltage (V_g) changes according to the strain (ε) in the sample as

$$V_g = \frac{1}{4} K_g V_{ex} \varepsilon . \tag{6.12}$$

The nominal full-scale range of this card is ± 25 mV/V. Hence, the measurable range of strain (ε_{range}) is calculated from

$$\frac{V_g}{V_{ex}} = \frac{1}{4} K_g \varepsilon_{range} = \pm 25 \text{mV/V} \tag{6.13}$$

$$\varepsilon_{range} = \pm(4 \times 25 \times 10^{-3})/2.1 = \pm 4.762 \times 10^{-2} \mu\text{m/m} . \tag{6.14}$$

The resolution of the card is 24-bit, so the smallest strain ($\varepsilon_{\min}$) that can be theoretically detected is

$$\varepsilon_{\min} = \frac{(2 \times 4.762 \times 10^{-2})}{(2^{24} - 1)} = 5.68 \times 10^{-3} \ \mu\text{m/m} . \tag{6.15}$$

The resolution of the system is adequate since the magnetostriction of NO steels is in the range of 1 to 15 μm/m at $\hat{B}$=1.5 T, 50 Hz [*6.25*]. Before magnetising the test sample, each strain gauge was automatically calibrated in the LabVIEW program with the internal shunt resistor ($SC+$ and $SC-$ terminal as shown in Fig. 6-13 (b)) to correct errors due to the resistance of the leads to the active gauge and also due to the residual strain [*6.26*].

Although the lead wires of the gauges were twisted, there was still an inevitable problem of voltage induced in the gauges due to a normal flux component. If the frequency components of the magnetisation waveforms are odd integer numbers (n=1, 3, 5...) of the magnetising frequency, the frequency components of the magnetostriction will be even integer numbers (n=2, 4, 6...) [*6.27*]. Hence, the induced voltage in the strain gauges could be easily removed using a FFT technique [*6.28*]. Alternatively, this induced voltage could be removed using special gauges, which were folded in half so the induced voltages in each half cancel each other out [*6.29*].

Once λ_a, λ_b and λ_c signals were acquired and the induced voltages were removed, they were transformed into *x-y* coordinate (λ_x, λ_y and γ_{xy}^{λ}) according to the angle arrangement shown in Fig. 6-13 (a) by using (4.20). λ_x, λ_y and γ_{xy}^{λ} are simply written as

$$\lambda_x = \lambda_a \tag{6.16}$$

$$\lambda_y = \lambda_c \tag{6.17}$$

$$\gamma_{xy}^{\lambda} = \lambda_a - 2\lambda_b + \lambda_c . \tag{6.18}$$

The elongation and contraction (λ_1 and λ_2), occurring along and perpendicular to the principal axis where the shear strain becomes zero, are given as

$$\lambda_1, \lambda_2 = \frac{\lambda_x + \lambda_y}{2} \pm \sqrt{\left(\frac{\lambda_x - \lambda_y}{2}\right)^2 + \left(\frac{\gamma_{xy}^{\lambda}}{2}\right)^2} . \tag{6.19}$$

The angle between the principal axis and the RD is determined from

$$\delta = \frac{1}{2}\tan^{-1}\left(\frac{\gamma_{xy}^{\lambda}}{\lambda_x - \lambda_y}\right). \tag{6.20}$$

6.3.5 Schematic connection and control of the 2D magnetisation system

Fig. 6-14 displays the schematic diagram of the 2D magnetisation system. Two magnetising voltage waveforms, generated by LabVIEW via two voltage outputs of the NI PCI-6052E DAQ card [*6.30*], were connected through a two-channel power amplifier and two isolation transformers for DC signal removal. Two 0.01 Ω shunt resistors were used for measuring the magnetising currents (i_x and i_y). The induced voltages in the *b* coils and the *h* coils and the voltages across the shunt resistors were directly connected to the inputs of the DAQ card for control of the magnetisation and calculation of the specific power loss. Three strain gauges with their dummy gauges as described in **Section 6.3.4** were connected to the NI USB-9237 strain DAQ card to obtain λ_a, λ_b and λ_c.

To synchronise these two DAQ cards, they must share the same conversion clock for the analogue to digital converters (ADCs), which requires an additional expensive chassis for the strain DAQ card allowing access to the conversion clock [*6.31*]. Fortunately, one channel was left from the magnetostriction measurement so it was used to acquire the signal from an extra *b* coil in the RD called e_{x1} as shown in Fig. 6-14. This e_{x1} is exactly the same as e_x used for b_x control and measurement. The integral of e_x and e_{x1} were used as the reference for the signals measured by the NI PCI-6052E DAQ card and NI USB-9237 DAQ card respectively. Therefore, the signals measured by these two DAQ cards had the same reference point. Fig. 6-15 illustrates the synchronisation of the two DAQ cards. It required two 120 Ω resistors to complete the bridge for the 4th channel of the NI USB-9237 DAQ card. The peak value of e_{x1} at $\hat{B}$=2.0 T, 200 Hz for the 0.50 mm thick sample was equivalent to 1.84×10^{-2} μm/m, which is only 39 % of the full-scale range as calculated in (6.14). The sampling frequency of all the measurement inputs was fixed at 50 kHz, the highest sampling rate for the NI USB-9237 DAQ card.

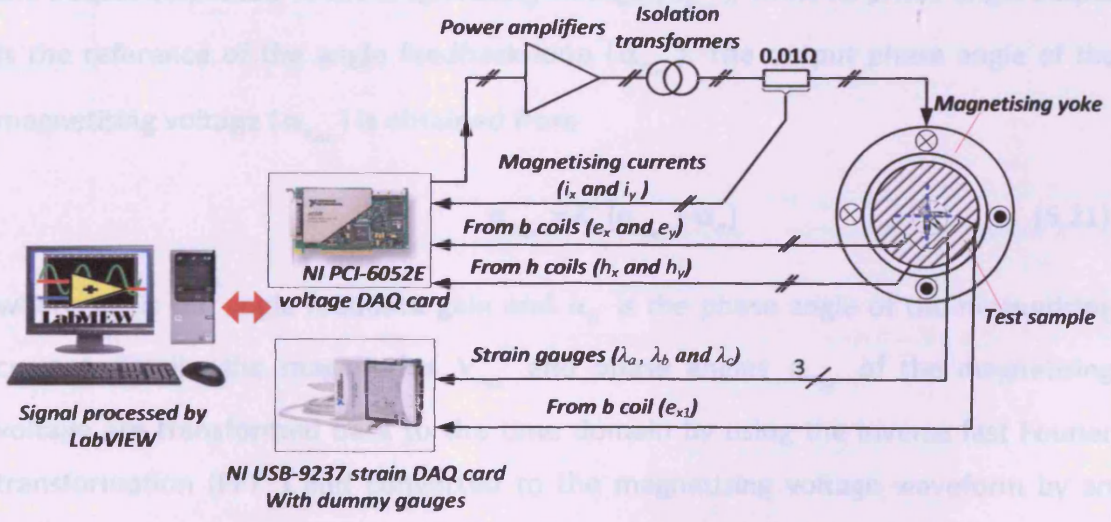

Fig. 6-14 Schematic connection of the 2D magnetisation system

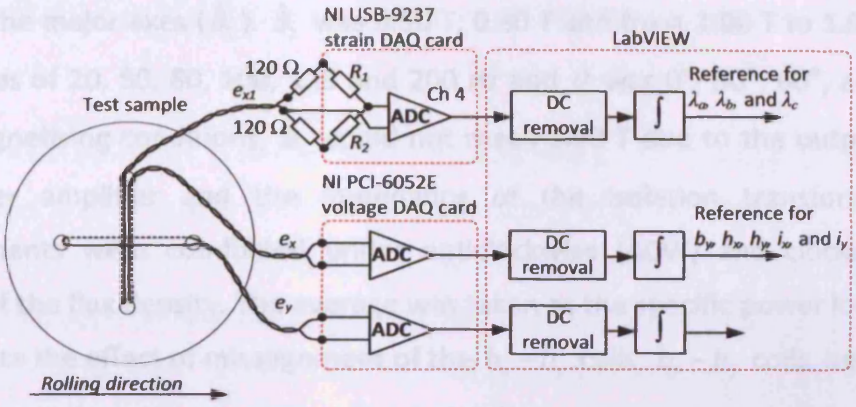

Fig. 6-15 Illustration of signal synchronisation of the 2D magnetisation system measured with the aid of two DAQ cards

b_x and b_y were controlled separately and the control algorithm of each axis implemented in LabVIEW as shown in Fig. 6-16. A cascade feedback control system in the frequency domain was used. The difference between the reference flux density (b_{ref}) and the actual b is converted into the frequency domain by using the FFT. The amplitude output of the FFT is then multiplied with the amplitude gain (K_A) to be the output amplitude of the magnetising voltage ($\mathbf{V}_{n_{out}}$), while its phase angle output is the reference of the angle feedback loop ($\boldsymbol{\alpha}_{n_{ref}}$). The output phase angle of the magnetising voltage ($\boldsymbol{\alpha}_{n_{out}}$) is obtained from

$$\boldsymbol{\alpha}_{n_{out}} = K_{\alpha}(\boldsymbol{\alpha}_{n_{ref}} - \boldsymbol{\alpha}_{n}) \tag{6.21}$$

where K_{α} is the angle feedback gain and $\boldsymbol{\alpha}_n$ is the phase angle of the magnetising current. Finally, the magnitudes $\mathbf{V}_{n_{out}}$ and phase angles $\boldsymbol{\alpha}_{n_{out}}$ of the magnetising voltage are transformed back to the time domain by using the inverse fast Fourier transformation (FFT^{-1}) and converted to the magnetising voltage waveform by an analogue output of the DAQ card. The measurement procedure of this system was also the same as that of the SST shown in Fig. 6-3 but more criteria were applied to this measurement. The criteria of each measurement were $\hat{B}_x$ and $\hat{B}_y$, the total harmonics distortion (THD) of b_x and b_y, and the FF of e_x and e_y all to be within ± 0.50 % of the values for the reference waveforms. The sample was magnetised under circular and elliptical magnetisation as shown in Fig. 6-17. The shape of the flux density loci was controlled by the axis ratio (a) and the angle of the major axis to the RD (θ), where a is the ratio between peak flux density components in the minor

($\hat{B}_2$) and the major axes ($\hat{B}_1$). $\hat{B}_1$ was 0.50 T, 0.80 T and from 1.00 T to 1.90 T at the frequencies of 20, 50, 80, 100, 125 and 200 Hz and θ was 0°, 30°, 60°, and 90°. At some magnetising conditions, $\hat{B}_1$ could not reach 1.90 T due to the output limit of the power amplifier and the impedance of the isolation transformers. The measurements were conducted under anticlockwise (ACW) and clockwise (CW) rotation of the flux density. The average was taken as the specific power loss in order to eliminate the effect of misalignment of the $h_x - h_y$ coils, $b_x - b_y$ coils, between the h coils and the b coils as well as the inter-channel delay of the DAQ [*6.6*]. The measurements were repeated five times (each time the h coils was removed and re-attached) and the average taken. Each measurement took about 4 minutes. Using recorded magnetisation waveforms at each value of $\hat{B}$, the measurement time could be reduced to 1.5 minutes to minimise the strain gauge temperature offset error.

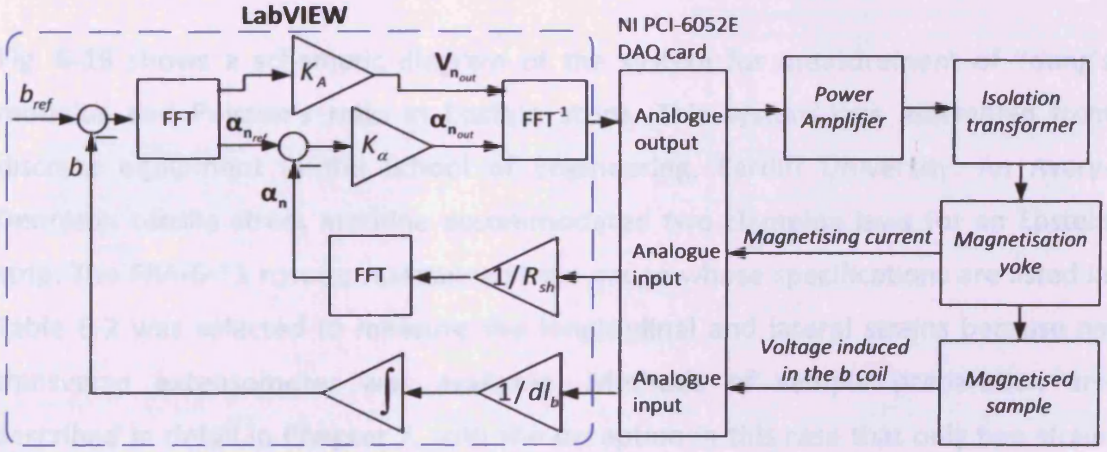

Fig. 6-16 Block diagram showing the feedback control system for an magnetisation axis of the 2D magnetisation system [*6.6*]

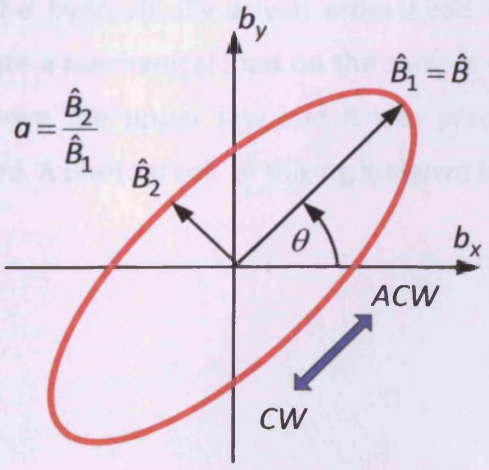

Fig. 6-17 Loci of flux density applied to the test samples of the 2D magnetisation system

6.4 System for Measurement of Young's Modulus and Poisson's Ratio

Young's modulus E of a material can be determined from the slope of the graph of applied longitudinal tensile stress against resulting strain as shown in Fig. 6-18 (a). Poisson's ratio ν is calculated as the ratio between the transverse and longitudinal strains. These two definitions are valid only at stress below the yield strength as depicted in Fig. 6-18 (b). Since it is difficult to determine when the stress-strain curve becomes non-linear, the yield strength is defined as the stress that causes 0.2 % of residual plastic deformation [*6.32*]. The most convenient method of determining E and ν of Epstein strips is using a tensile stress machine. Such a machine was used to apply a longitudinal load to the strip causing a tension along its length and the longitudinal and transverse strains were read by extensometers or resistance strain gauges.

Fig. 6-19 shows a schematic diagram of the system for measurement of Young's modulus and Poisson's ratio in Epstein strips. This system was assembled from discrete equipment in the School of Engineering, Cardiff University. An Avery-Dennison tensile stress machine accommodated two clamping jaws for an Epstein strip. The FRA-6-11 rosette resistance strain gauge whose specifications are listed in Table 6-2 was selected to measure the longitudinal and lateral strains because no transverse extensometer was available. Methods of sample preparation are described in detail in **Chapter 7**, with the exception in this case that only two strain gauges were used, which were aligned with the longitudinal and transverse directions. They were connected to a Vishay 6100 strain gauge data logger in a half bridge circuit [*6.33*]. The hydraulically-driven cross head of the tensile machine moved vertically to create a mechanical load on the sample which was measured by a load cell attached above the upper jaw and it was precisely controlled by the position of the cross head. A photograph of this rig is shown in Fig. 6-20.

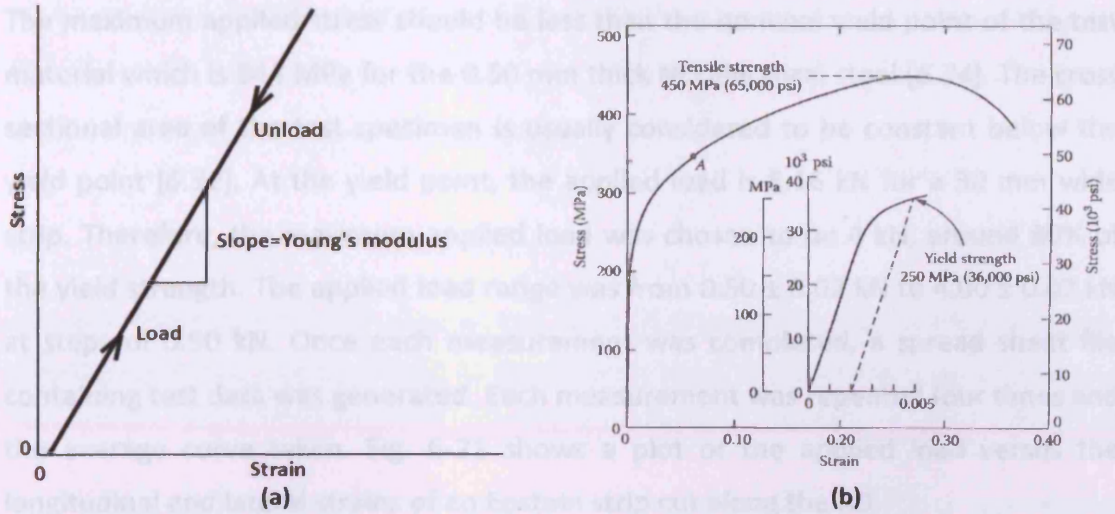

Fig. 6-18 (a) Stress-strain relationship of a material in the plastic range and (b) Plot of stress-strain curve obtained from a tensile test [*6.32*]

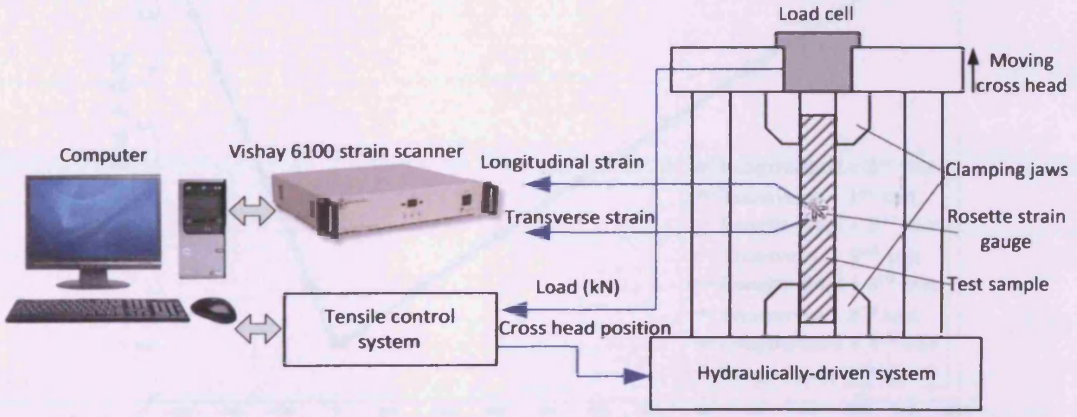

Fig. 6-19 Schematic diagram of the system for measurement of Young's modulus and Poisson's ratio in Epstein samples

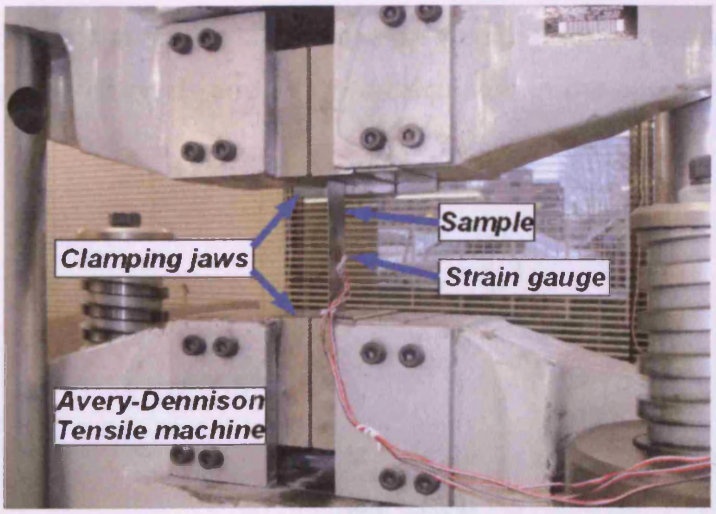

Fig. 6-20 Photograph of a test specimen mounted in the tensile testing machine.

The maximum applied stress should be less than the nominal yield point of the test material which is 344 MPa for the 0.50 mm thick NO electrical steel [*6.34*]. The cross sectional area of the test specimen is usually considered to be constant below the yield point [*6.32*]. At the yield point, the applied load is 5.16 kN for a 30 mm wide strip. Therefore, the maximum applied load was chosen to be 4 kN, around 80% of the yield strength. The applied load range was from 0.50 ± 0.02 kN to 4.00 ± 0.02 kN at steps of 0.50 kN. Once each measurement was completed, a spread sheet file containing test data was generated. Each measurement was repeated four times and the average curve taken. Fig. 6-21 shows a plot of the applied load versus the longitudinal and lateral strains of an Epstein strip cut along the RD.

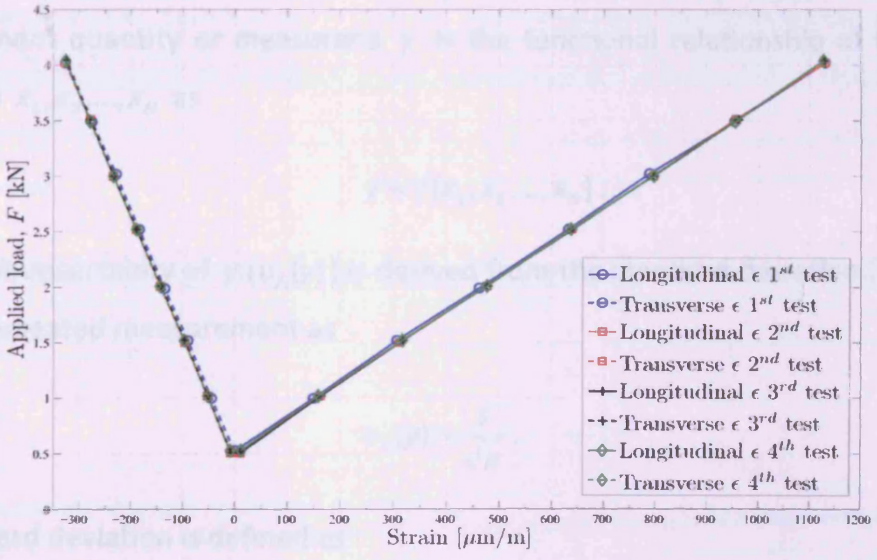

Fig. 6-21 Applied load versus longitudinal and lateral strains of an Epstein strips cut along the RD

There is a non linearity in the load-strain curve in Fig. 6-21 over a load range of 0.50 to 1.50 kN. This was due to the clamping jaws needing some tension to firmly grip the test sample. Therefore, E and ν were calculated in the applied load of 1.50 to 4.00 kN as

$$E = \frac{1}{dw} \cdot \frac{(F_2 - F_1)}{(\varepsilon_{l_2} - \varepsilon_{l_1})} \tag{6.22}$$

and

$$\nu = \left| \frac{(\varepsilon_{\perp_2} - \varepsilon_{\perp_1})}{(\varepsilon_{l_2} - \varepsilon_{l_1})} \right| \tag{6.23}$$

where w is the sample width, F_1 and F_2 are the actual read value of the applied load at 1.50 kN and 4.00 kN, $\varepsilon_{\parallel_1}$, $\varepsilon_{\perp_1}$ and $\varepsilon_{\parallel_2}$, $\varepsilon_{\perp_2}$ are the corresponding longitudinal and transverse strains at F_1 and F_2 respectively.

6.5 Uncertainty in Measurement

The uncertainties of the measurement systems were estimated according to the recommendations given in UKAS M3003 [*6.35*]. Thus, the methodology and all the calculations can be traced back to the uncertainties presented there.

The standard uncertainty is divided into two components; type A uncertainty evaluated by statistical methods and type B evaluated by other means. The measurement quantity or measurand y is the functional relationship of the input quantities $x_1, x_2, \ldots, x_N$ as

$$y = f(x_1, x_2, \ldots, x_N). \tag{6.24}$$

The type A uncertainty of y ($u_A(y)$) is derived from the standard deviation (s) of the n times repeated measurement as

$$u_A(y) = \frac{s}{\sqrt{n}}. \tag{6.25}$$

The standard deviation is defined as

$$s = \sqrt{\frac{\sum_{i=1}^{n}(q_i - \bar{q})^2}{n-1}} \tag{6.26}$$

where q_i is the measured value of y and the averaged value ($\bar{q}$) of y is expressed as

$$\bar{q} = \frac{1}{n}\sum_{i=1}^{n} q_i. \tag{6.27}$$

The type B uncertainty is contributed by the standard uncertainties ($u(x_i)$) of the measurement inputs x_i and is mathematically defined to

$$u_B^2(y)=\left(\frac{\partial y}{\partial x_1}\right)^2 u^2(x_1)+\left(\frac{\partial y}{\partial x_2}\right)^2 u^2(x_2)+\ldots+\left(\frac{\partial y}{\partial x_N}\right)^2 u^2(x_N). \quad (6.28)$$

The partial derivative $\frac{\partial y}{\partial x_i}$ is called the sensitivity coefficient, c_i. Thus, equation (6.28) can be simplified as

$$u_B^2(y)=c_1^2 u^2(x_1)+c_2^2 u^2(x_2)+\ldots+c_N^2 u^2(x_N). \quad (6.29)$$

The evaluation of $u_B(y)$ in (6.28) is useful only if the exact mathematical relation of the measurement is known. In some cases, for instance measurement of magnetic properties, the exact equation is unknown. It is suggested in [*6.35*] to use (6.29) where the sensitivity coefficient, c_i can be experimentally determined from $\Delta y/\Delta x_i$ by varying the value of x_i. Evaluating the uncertainties in the relative values can be more convenient since the coefficients of the measurement relationship will be cancelled out.

Once $u_A(y)$ and $u_B(y)$ have been evaluated, the combined standard uncertainty of y is determined from

$$u(y)=\sqrt{u_A^2(y)+u_B^2(y)}. \quad (6.30)$$

Finally, $u(y)$ is multiplied by the coverage factor, k_{95} to be the expanded uncertainty, $U(y)$ as in (6.31). This k_{95} provides a confidence level at 95% of the normal distribution.

$$U(y)=k_{95}u(y). \quad (6.31)$$

The measured value of y (Y) is then reported as $y=Y\pm U(y)$.

Tables 6-4 to 6-9 provide the estimated uncertainties of $\hat{B}$, P_S, $\hat{H}$ and $\mu_{r_{AC}}$ measured in the SST. The uncertainties of the AC magnetostriction measurement system are summarised in Table 6-10. Tables 6-11 to 6-16 detail the uncertainty evaluation of $\hat{B}_x$, $\hat{B}_y$, P_S, $\lambda_{x_{pp}}$, $\lambda_{y_{pp}}$, $\hat{\lambda}_1$ and $\hat{\lambda}_2$ measured in the 2D magnetisation system. Tables 6-17 and 6-18 detail the uncertainty evaluation of E and ν measurement in Epstein strips. The uncertainty sources obtained from equipment specification sheets were

divided by 2 before used as the sources of uncertainties since these values were supposed to be the expanded uncertainties with k_{95}=2. If the specification sheet were not found, the uncertainty values have been estimated to be a half of their minimum scale divided by $\sqrt{3}$ as a coverage factor of the rectangular distribution. The other contributions, such as the misalignment angle have been estimated from their extreme conditions with the rectangular distribution. **Appendix B** summarises the type A uncertainties of the measurements that have the poorest repeatability.

The number of degrees of freedom (ν_i) is infinity for all the uncertainty sources because it can be any value, whereas ν_i of $u_A(y)$ is $n-1$. The effective number of degrees of freedom (ν_{eff}) of u(y) is derived from the Welch-Satterthwaite equation as follows

$$\nu_{eff} = \frac{u^4(y)}{\sum_{i=1}^{N} \frac{u_i^4(y)}{\nu_i}}. \tag{6.32}$$

This ν_{eff} is eventually used to determine k_{95} from the t-distribution table. ν_{eff} is often infinity where k_{95}=2.

Table 6-4 Uncertainty budget of $\hat{B}$ in 0.50 mm thick Epstein strips of NO sample measured in the SST under sinusoidal magnetisation at 50 Hz

Sources of uncertainty	Value ±%	Probability distribution	Divisor	c_i	u(x_i) ±%	ν_i or ν_{eff}
Accuracy of NI PCI-6120 DAQ	0.050	Normal	2	1	0.0250	∞
Frequency setting	0.010	Normal	2	1	0.0050	∞
Sample mass measurement	0.010	Normal	2	1	0.0050	∞
Sample length measurement	0.100	Rectangular	$\sqrt{3}$	1	0.0577	∞
Density	0.065	Rectangular	$\sqrt{3}$	1	0.0375	∞
Air flux	0.100	Rectangular	$\sqrt{3}$	1	0.0577	∞
Control of $\hat{B}$	0.020	Rectangular	$\sqrt{3}$	1	0.0115	∞
Control of form factor	0.020	Rectangular	$\sqrt{3}$	1	0.0115	∞
Type A uncertainty (repeatability)	0.010	Normal	1	1	0.0100	4
Combined standard uncertainty		Normal			0.0955	∞
Expanded uncertainty U($\hat{B}$)		Normal (k_{95}=2)			0.1910	
Declared uncertainty at the confidence level of 95 %					0.2	

The values in Table 6-4 have been estimated in the following way:

a) Accuracy of NI PCI-6120 DAQ – The accuracy of the voltage measurement range of ± 10 V is ± 4.94 mV [6.1]. Thus, the relative accuracy is 4.94 mV/10 V ×100=0.0494 %, rounded to 0.05 %.

b) Frequency setting – This value was taken from the base clock accuracy of the NI PCI-6120 DAQ card.

c) Sample mass measurement – The mass of the samples was measured using an Avery Berkel FB31 scale with a resolution of 0.01 g and accuracy of ±0.0002 g. Each sample was weighed five times and the expanded uncertainty of all samples was within ± 0.01 %.

d) Sample length measurement – The length of every sample was measured using a metal ruler with a resolution of 0.5 mm. Its uncertainty was assumed as a half of the resolution resulting in 0.082 % of the nominal length of 305 mm. It was truncated to 0.1 %

e) Density – The quoted value in the manufacturer catalogue is 7.70 kg/dm3 [6.34]. The uncertainty is presumably a half of the last digit of the quoted value which is ± 0.005 kg/dm^3. This yields the relative value of 0.065 %.

f) Air flux – The voltage non-common terminals of the secondary circuit was not more than 0.1 % of the secondary winding of the SST by using a mutual inductor to compensate the air flux.

g) Control of $\hat{B}$ and FF – The control algorithm written in LabVIEW was able to maintain the value of $\hat{B}$ and FF of the secondary voltage within ± 0.02 %.

h) Type A uncertainty – The repeatability of $\hat{B}$ measured on the Epstein sample set cut along the RD shown in Table B-1 was found to be the poorest over the entire specimens. Thus, the repeatability of 0.01 % for five times repeated measurements of this sample set covers all the samples.

Table 6-5 Type B uncertainty evaluation of $\hat{H}$ in 0.50 mm thick Epstein strips measured in the SST under sinusoidal magnetisation at 50 Hz

Sources of uncertainty	Value ±%	Probability distribution	Divisor	c_i	$u(x_i)$ ±%	v_i or v_{eff}
Accuracy of NI PCI-6120 DAQ	0.500	Normal	2	1	0.2500	∞
Shunt resistor	1.000	Normal	2	1	0.5000	∞
Mean path length	0.100	Rectangular	$\sqrt{3}$	1	0.0577	∞
Type B uncertainty $u_B(\hat{H})$		Normal	1	1	0.5620	∞

Table 6-6 Type B uncertainty evaluation of P_s in 0.50 mm thick Epstein strips measured in the SST under sinusoidal magnetisation at 50 Hz

Sources of uncertainty	Value ±%	Probability distribution	Divisor	c_i	$u(x_i)$ ±%	v_i or v_{eff}
Frequency setting	0.010	Normal	2	2	0.0100	∞
h measurement	0.562	Normal	1	1	0.5620	∞
b measurement	0.200	Normal	2	2	0.2000	∞
Density	0.065	Rectangular	$\sqrt{3}$	1	0.0375	∞
Type B uncertainty $u_B(P_s)$		Normal	1	1	0.5978	∞

The estimated values in Table 6-5 and 6-6 that have not been described in Table 6-4 were obtained from:

a) Shunt resistor – It was used to measure the magnetising current by mean of the voltage drop across this resistor. The tolerance of this resistor is ±1 % [*6.36*].

b) Mean path length – A metal ruler with a resolution of 0.5 mm was used to measure the length between the inner edges of the flux closure yoke. The nominal length is 255 mm, so the relative uncertainty was 0.25 mm/255 mm ×100=0.098 %, rounded to 0.1 %.

The type B uncertainties of $\hat{H}$ and P_s are combined with the maximum values of the type A uncertainty of the Epstein sample set cut along the RD of the 0.50 mm NO steel as given in Tables B-2 to B-3. This samples set has the poorest repeatability. The calculated uncertainties are therefore valid for all samples. The uncertainties of P_s and $\hat{H}$ are separated into two induction ranges: from 0.10 T to 0.70 T and 0.80 to 1.70 T as summarised in Tables 6-7 and 6-8 respectively. Table 6-9 shows the uncertainties values of $\mu_{r_{AC}}$. Its type B uncertainty was calculated from $u(\hat{B})$ and $u(\hat{H})$

obtained from Tables 6-4 and 6-8 as $u(\mu_{r_{AC}}) = \sqrt{u^2(\hat{B}) + u^2(\hat{H})}$, whereas the type A values were from Tables B-7 and B-8.

Table 6-7 Uncertainty values of P_s in 0.50 mm thick Epstein strips measured in the SST under sinusoidal magnetisation at 50 Hz

Range of $\hat{B}$ [T]	Type A $u_A(P_s)$ ±%	v_i	Type B $u_B(P_s)$ ± %	v_i	Combined $u(P_s)$ ±%	v_{eff}	Expanded $U(P_s)$ (k_{95}=2)	Declared uncertainty at the confidence level of 95 %
0.10 to 0.70	2.0	4	0.5978	∞	2.0874	∞	4.1749	4.5
0.80 to 1.70	0.4	4	0.5978	∞	0.7193	∞	1.4385	1.5

Table 6-8 Uncertainty values of $\hat{H}$ in 0.50 mm thick Epstein strips measured in the SST under sinusoidal magnetisation at 50 Hz

Range of $\hat{B}$ [T]	Type A $u_A(\hat{H})$ ±%	v_i	Type B $u_B(\hat{H})$ ± %	v_i	Combined $u(\hat{H})$ ±%	v_{eff}	Expanded $U(\hat{H})$ (k_{95}=2)	Declared uncertainty at the confidence level of 95 %
0.10 to 0.70	1.5	4	0.5620	∞	1.6769	∞	3.3538	3.5
0.80 to 1.70	0.9	4	0.5620	∞	1.0611	∞	2.1221	2.5

Table 6-9 Uncertainty values of $\mu_{r_{AC}}$ in 0.50 mm thick Epstein strips measured in the SST under sinusoidal magnetisation at 50 Hz

Range of $\hat{B}$ [T]	Type A $u_A(\mu_{r_{AC}})$ ±%	v_i	Type B $u_B(\mu_{r_{AC}})$ ±%	v_i	Combined $u(\mu_{r_{AC}})$ ±%	v_{eff}	Expanded $U(\mu_{r_{AC}})$ (k_{95}=2)	Declared uncertainty at the confidence level of 95 %
0.10 to 0.70	2.1	4	1.609	∞	2.6431	∞	5.2861	5.5
0.80 to 1.70	0.9	4	1.068	∞	1.3949	∞	2.7899	3.0

The uncertainties of the peak to peak values of magnetostriction in the Epstein samples measured in the AC magnetostriction measurement system described in **Section 6.2** are shown in Table 6-10. The uncertainty values in Table 6-1 are considered as type B and the type A uncertainty values are obtained from the measurements as shown in Tables B-5 to B-8 for the worse case scenarios. The values in Table 6-10 are calculated according to the longitudinal stress applied to the sample and are valid over a peak flux density range of 1.00 T ± 0.2 % to 1.70 T ± 0.2 %.

Table 6-10 Uncertainty values of λ_{pp} in 0.50 mm and 0.35 mm thick Epstein strips measured in the AC magnetostriction measurement system under sinusoidal magnetisation at 50 Hz

Range of applied stress	Type A $u_A(\lambda_{pp})$ ±%	v_i	Type B $u_B(\lambda_{pp})$ ±%	v_i	Combined $u(\lambda_{pp})$ ±%	v_{eff}	Expanded $U(\lambda_{pp})$ (k_{95}=2)	Declared uncertainty at the confidence level of 95 %
-10 MPa < σ ≤ -5 MPa	2.5	2	0.85	∞	2.641	∞	5.281	5.5
-5 MPa < σ < 0 MPa	2.2	2	0.70	∞	2.310	∞	4.62	5.0
0 MPa ≤ σ ≤ 10 MPa	4.0	2	0.35	∞	4.015	∞	8.031	8.5

Table 6-11 Uncertainty budget of $\hat{B}_x$ measurement of 0.50 mm and 0.35 mm thick NO steels under 2D magnetisation

Sources of uncertainty	Value ±%	Probability distribution	Divisor	c_i	$u(x_i)$ ±%	v_i or v_{eff}
Accuracy of PCI-6052E DAQ	0.0050	Normal	2	1	0.0025	∞
Thickness of the sample	0.7500	Normal	2	1	0.3750	∞
Width of the b_x coil	0.1100	Normal	2	1	0.0550	∞
Air flux	1.1300	Rectangular	$\sqrt{3}$	1	0.6524	∞
Frequency setting	0.0100	Normal	2	1	0.0050	∞
Misalignment angle	0.0015	Rectangular	$\sqrt{3}$	1	0.0009	∞
Control of b_x	0.5000	Rectangular	$\sqrt{3}$	1	0.2887	∞
Type A uncertainty (repeatability)	0.1300	Normal	1	1	0.1300	9
Combined standard uncertainty		Normal			0.8183	∞
Expanded uncertainty $U(\hat{B}_x)$		Normal (k_{95}=2)			1.6366	
Declared uncertainty at the confidence level of 95 %					2	

Table 6-12 Uncertainty budget of $\hat{B}_y$ measurement of 0.50 mm and 0.35 mm thick NO steels under 2D magnetisation

Sources of uncertainty	Value ±%	Probability distribution	Divisor	c_i	$u(x_i)$ ±%	v_i or v_{eff}
Accuracy of PCI-6052E DAQ	0.0050	Normal	2	1	0.0100	∞
Thickness of the sample	0.7500	Normal	2	1	0.3750	∞
Width of the b_y coil	0.1100	Normal	2	1	0.0550	∞
Air flux	1.1300	Rectangular	$\sqrt{3}$	1	0.6524	∞
Frequency setting	0.0100	Normal	2	1	0.0050	∞
Misalignment angle	0.0130	Rectangular	$\sqrt{3}$	1	0.0075	∞
Control of b_y	0.5000	Rectangular	$\sqrt{3}$	1	0.2887	∞
Type A uncertainty (repeatability)	0.0900	Normal	1	1	0.0900	9
Combined standard uncertainty		Normal			0.8130	∞
Expanded uncertainty $U(\hat{B}_y)$		Normal (k_{95}=2)			1.6259	
Declared uncertainty at the confidence level of 95 %					2	

The values in Tables 6-11 and 6-12 have been estimated in the following way:

a) Accuracy of PCI-6052E – The accuracy of the voltage measurement of the NI PCI-6052E DAQ card is ± 3 LSB and this DAQ card is 16-bit resolution [6.30]. Thus, the relative accuracy is 3/(216)×100=0.005 %.

b) Thickness of the sample – A digital micrometer was used to measure the thickness and its accuracy was 0.0025 mm, which is 0.715 % of the thinnest sample (0.35 mm). A value of 0.75 % was used.

c) Width of the b_x and b_y coils – The distance between the two holes was measured by a digital vernier calliper having accuracy of 0.02 mm. It is 0.1026 % of the nominal value at 19.50 mm. It was truncated to 0.11 %.

d) Air flux – The air flux of the b coils was not compensated. At the highest induction of 1.90 T, it was found that $\hat{H}$ was not greater than 17 kA/m. This value causes $\hat{B}$=21.4 mT in paramagnetic materials, which is less than 1.126 % of all nominal values of b. It was scaled to 1.13 %.

e) Frequency setting – This value was taken from the base clock accuracy of the PCI-6052E DAQ card.

f) Misalignment angle – Fig. 6-22 illustrates the maximum misalignment angle of the b_x and b_y coils. The accuracy of the hole diameter is better than 0.01 mm. The calculation of this error yields 0.0012 % and 0.0123 % for the b_x and b_y coils respectively. The values of 0.0015 % and 0.0130 % were used.

g) Control of b_x and b_y – This is the criteria of $\hat{B}_x$ and $\hat{B}_y$ set in LabVIEW.

h) Type A uncertainty – This value was evaluated from 10 repeated measurements in both ACW and CW directions. Tables B-11 to B-16 summarise the repeatability of $\hat{B}_x$ and $\hat{B}_y$ under circular and elliptical flux loci of the 0.35 mm thick and 0.50 mm thick NO electrical steels. It was found to be not more than 0.13 % and 0.09 % over the entire magnetisation range.

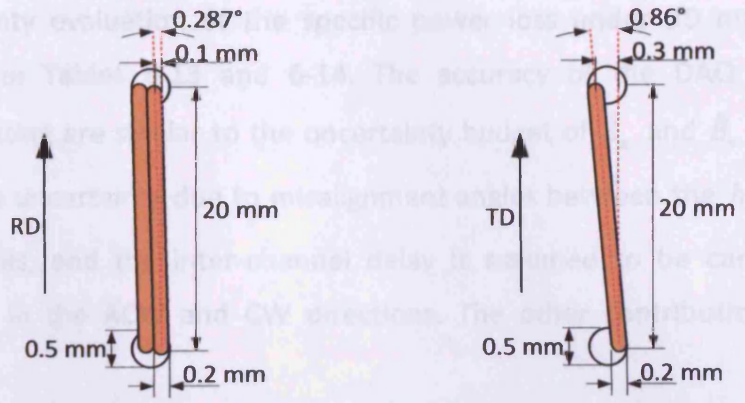

Fig. 6-22 Illustration of misalignment angle estimation of *b* coils (not scaled); (a) in the RD, (b) in the TD

Table 6-13 Uncertainty budget of P_s of the 0.50 thick NO sample under 2D magnetisation

Sources of uncertainty	Value ±%	Probability distribution	Divisor	c_i	$u(x_i)$ ±%	v_i or v_{eff}
Accuracy of PCI-6052E DAQ	0.005	Normal	2	1	0.0025	∞
Frequency setting	0.010	Normal	2	2	0.0100	∞
h_x coil calibration	1.900	Normal	2	1	0.9500	∞
h_y coil calibration	1.900	Normal	2	1	0.9500	∞
b_x measurement	2.000	Normal	2	2	2.0000	∞
b_y measurement	2.000	Normal	2	2	2.0000	∞
Density	0.065	Rectangular	$\sqrt{3}$	1	0.0375	∞
Type A uncertainty (repeatability)	1.000	Normal	1	1	1.0000	4
Combined standard uncertainty		Normal			3.2873	∞
Expanded uncertainty $U(P_s)$		Normal (k_{95}=2)			6.5747	
Declared uncertainty at the confidence level of 95 %					7	

Table 6-14 Uncertainty budget of P_s of the 0.35 thick NO sample under 2D magnetisation

Sources of uncertainty	Value ±%	Probability distribution	Divisor	c_i	$u(x_i)$ ±%	v_i or v_{eff}
Accuracy of PCI-6052E DAQ	0.005	Normal	2	1	0.0025	∞
Frequency setting	0.010	Normal	2	2	0.0100	∞
h_x coil calibration	1.900	Normal	2	1	0.9500	∞
h_y coil calibration	1.900	Normal	2	1	0.9500	∞
b_x measurement	2.000	Normal	2	2	2.0000	∞
b_y measurement	2.000	Normal	2	2	2.0000	∞
Density	0.066	Rectangular	$\sqrt{3}$	1	0.0381	∞
Type A uncertainty (repeatability)	2.6	Normal	1	1	2.6000	4
Combined standard uncertainty		Normal			4.0702	∞
Expanded uncertainty $U(P_s)$		Normal (k_{95}=2)			8.1404	
Declared uncertainty at the confidence level of 95 %					9	

The uncertainty evaluation of the specific power loss under 2D magnetisation is summarised in Tables 6-13 and 6-14. The accuracy of the DAQ card and the frequency setting are similar to the uncertainty budget of $\hat{B}_x$ and $\hat{B}_y$ in Tables 6-11 and 6-12. The uncertainty due to misalignment angles between the h_x and h_y coils, h and b coils, and the inter-channel delay is assumed to be cancelled due to averaging P_s in the ACW and CW directions. The other contributions have been estimated as:

a) Calibration of h_x and h_y coils – The uncertainties of the h_x and h_y coils can be found in Table 6-2, rounded to 1.9 %. Calibration details are fully described in Appendix A.

b) b_x and b_y measurement – These were obtained from the expanded uncertainties in Tables 6-11 and 6-12.

c) Density – The quoted value in the manufacturer catalogue is 7.60 kg/dm^3 for the 0.35 mm thick steel [*6.37*] and 7.70 kg/dm^3 for the 0.50 mm thick material This yields the relative value of 0.065 % and 0.066

d) Type A uncertainty – This value was evaluated from 5 averaged P_s in the ACW and CW direction. It was found to be less than 1 % and 2.6 % for the 0.50 mm and 0.35 mm thick NO electrical steels over the entire magnetisation range.

Table 6-15 Uncertainty budget of $\lambda_{x_{pp}}$ and $\lambda_{y_{pp}}$ of the 0.50 mm and 0.35 mm thick NO steels under 2D magnetisation

Sources of uncertainty	Value ±%	Probability distribution	Divisor	c_i	$u(x_i)$ ±%	v_i or v_{eff}
Accuracy of USB-9237 DAQ	0.050	Normal	2	1	0.0250	∞
Accuracy of shunt calibration resistor of USB-9237 DAQ	0.110	Normal	2	1	0.0550	∞
b_x measurement	2.000	Normal	2	2	2.0000	∞
b_y measurement	2.000	Normal	2	2	2.0000	∞
Homogeneity in flux density	0.050	Rectangular	$\sqrt{3}$	2	0.0577	∞
Gauge factor	1.0000	Normal	2	1	0.5000	∞
Error of gauge factor due to 5°C change of sample temperature	0.050	Normal	2	1	0.0250	∞
Misalignment angle	0.070	Rectangular	$\sqrt{3}$	2	0.0808	∞
Type A uncertainty (repeatability)	5.000	Normal	1	1	5.0000	9
Combined standard uncertainty		Normal			5.7675	∞
Expanded uncertainty $U(\lambda_{x_{pp}})$, $U(\lambda_{y_{pp}})$		Normal (k_{95}=2)			11.5350	
Declared uncertainty at the confidence level of 95 %					12	

Table 6-16 Uncertainty budget $\hat{\lambda}_1$ and $\hat{\lambda}_2$ of the 0.50 mm and 0.35 mm thick NO steels under 2D magnetisation

Sources of uncertainty	Value ±%	Probability distribution	Divisor	c_i	$u(x_i)$ ±%	v_i or v_{eff}
Gain error of USB-9237 DAQ	0.0500	Normal	2	1	0.0250	∞
Accuracy of shunt calibration resistor of USB-9237 DAQ	0.1100	Normal	2	1	0.0550	∞
Offset error of the USB-9237 DAQ	0.0500	Normal	2	1	0.0250	∞
b_x measurement	2.0000	Normal	2	2	2.0000	∞
b_y measurement	2.0000	Normal	2	2	2.0000	∞
Homogeneity in flux density	0.0500	Rectangular	$\sqrt{3}$	2	0.0577	∞
Gauge factor	1.0000	Normal	2	1	0.5000	∞
Error of gauge factor due to 5°C change of sample temperature	0.0500	Normal	2	1	0.0250	∞
Type A uncertainty (repeatability)	5.000	Normal	1	1	5.0000	9
Combined standard uncertainty		Normal			5.76700	∞
Expanded uncertainty $U(\hat{\lambda}_1)$, $U(\hat{\lambda}_2)$		Normal (k_{95}=2)			11.5339 9	
Declared uncertainty at the confidence level of 95 %					12	

The contributions of the type B uncertainties of $\lambda_{x_{pp}}$ and $\lambda_{y_{pp}}$ in Table 6-15 and of $\hat{\lambda}_1$ and $\hat{\lambda}_2$ in Table 6-16 have been estimated in the following way:

a) Gain error of the USB-9237 DAQ card – This error affects the measured strain at room temperature. It can be found in the product specification sheet [6.24].

b) Accuracy of shunt the calibration resistor of the USB-9237 DAQ card – This resistor is used to calibrate the resistance of the gauge lead wires at the beginning of the measurement. Its nominal value is 100 kΩ and the accuracy at room temperature is ± 110 Ω, resulting in ± 0.11 %.

c) Offset error of the USB-9237 DAQ – The error causes a DC shift in the principal strain, but does not affects the peak to peak value of λ. The error at room temperature is 0.05 % [6.24].

d) b_x and b_y measurement – These were obtained from the expanded uncertainties in Tables 6-6 and 6-7. Since magnetostriction is a parabolic function of flux density, the sensitivities, c_i are equal to 2.

e) Homogeneity in flux density – It was found that the flux density 10 mm from the centre of the disc and square sample drops less than 0.05 % of at the centre [6.9].

f) Gauge factor – The uncertainty of K_g is ± 1 % as shown in Table 6-3.

g) Error in gauge factor due to 5°C change of sample temperature – The surface temperature of the sample increases while being magnetised. The magnetising yoke was cooled by an electric fan during the measurements so the temperature change should not be more than 5°C [6.6]. The temperature coefficient of K_g is 0.1% per 10°C. Thus, K_g is expected to vary no more than 0.05% over this temperature range.

h) Misalignment angle – A line was marked between two holes of the b_x coil. The possible misalignment angle is shown in Fig. 6-23. This yields an error of 0.063 %, rounded up to 0.07 %. The measured strain is a parabolic function of the cosine of the misalignment angle. Hence, the sensitivity c_i is equal to 2. This error does not affect $\hat{\lambda}_1$ or $\hat{\lambda}_2$ because any three measured strains in a plane surface can be transformed to the principal strains.

i) Type A uncertainty – The poorest repeatability for all magnetisation conditions and all samples was found to be less than 5 % as shown in Tables B-17 to B-22.

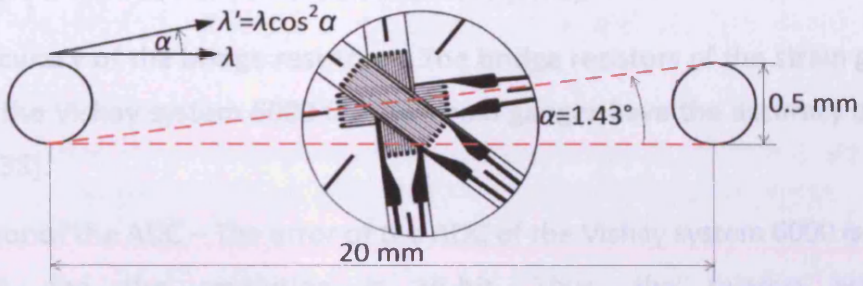

Fig. 6-23 Illustration of misalignment angle estimation the Rosette strain gauge (not scaled)

Table 6-17 Uncertainty budget of measurement of Young's modulus of 0.50 mm thick Epstein strips

Sources of uncertainty	Value ±%	Probability distribution	Divisor	c_i	$u(x_i)$ ±%	v_i or v_{eff}
Accuracy of the strain amplifier	0.0500	Normal	2	1	0.0250	∞
Accuracy of the bridge resistors	0.0100	Normal	2	1	0.0050	∞
Accuracy of ADC	0.0030	Normal	2	1	0.0015	∞
Thickness of the sample	0.5000	Normal	2	1	0.2500	∞
Width of the sample	0.0700	Normal	2	1	0.0350	∞
Gauge factor	1.0000	Normal	2	1	0.5000	∞
Misalignment angle	0.8000	Rectangular	$\sqrt{3}$	2	0.9238	∞
Load measurement	0.7000	Rectangular	$\sqrt{3}$	1	0.4042	∞
Jaw gripping	2.5000	Rectangular	$\sqrt{3}$	1	1.4434	∞
Type A uncertainty (repeatability)	0.6000	Normal	1	1	0.6000	3
Combined standard uncertainty		Normal			1.9428	∞
Expanded uncertainty U(E)		Normal (k_{95}=2)			3.8856	
Declared uncertainty at the confidence level of 95 %					4	

Table 6-18 Uncertainty budget of measurement of Poisson's ratio of of 0.50 mm thick Epstein strips

Sources of uncertainty	Value ±%	Probability distribution	Divisor	c_i	$u(x_i)$ ±%	v_i or v_{eff}
Accuracy of the strain amplifier	0.0500	Normal	2	1	0.0250	∞
Accuracy of the bridge resistors	0.0100	Normal	2	1	0.0050	∞
Accuracy of ADC	0.0030	Normal	2	1	0.0015	∞
Gauge factor	1.0000	Normal	2	1	0.5000	∞
Misalignment angle	0.8000	Rectangular	$\sqrt{3}$	2	0.9238	∞
Type A uncertainty (repeatability)	0.5000	Normal	1	1	0.5000	3
Combined standard uncertainty		Normal			1.1636	∞
Expanded uncertainty U(ν)		Normal (k_{95}=2)			2.3273	
Declared uncertainty at the confidence level of 95 %					2.5	

The uncertainties of the Young's modulus and Poisson's ratio of the Epstein samples detailed in Tables 6-17 and 6-18 have been estimated based on the following:

a) Accuracy of the strain amplifier – The gain of the strain amplifier of the Vishay system 6000 has an resolution of 0.05 % [6.33].

b) Accuracy of the bridge resistors – The bridge resistors of the strain gauge card of the Vishay system 6000 for the strain gauges have the accuracy of ± 0.01 % [6.33].

c) Error of the ADC – The error of the ADC of the Vishay system 6000 is within ± 2 LSB and the resolution is 16-bit. Thus, the relative accuracy is 2/(216)×100=0.003 % [6.33].

d) Width of the sample – The sample width was measured by mean of a digital vernier calliper having an accuracy of 0.02 mm. It is 0.067 % of the nominal value at the nominal value of 30 mm. It was truncated to 0.07 %.

e) Misalignment angle – The samples were cut according to [6.2], so the angle variation should be within ± 5° resulting in ±0.7596 %. It was rounded up to 0.80 %. The sensitivity c_i is equal to 2 due to the parabolic relationship between the measured strain and the cosine of this misalignment angle.

f) Load measurement – No calibration values found, the minimum scale was used instead. At 1.50 k N, the error was estimated to be ± 0.01 kN resulting in ± 0.667 %. The rounded value of 0.7 % was used for the calculation.

g) Jaw gripping – The sample slipped slightly at the start of applying the mechanical load. It was difficult to quantify this effect, so the uncertainty of ± 2.5 % was estimated.

h) Type A uncertainty – The strain measurement of each sample was repeated four times. The repeatability of the Young's modulus and Poisson's ratio of all samples was found to be less than 0.6%.

6.6 References for Chapter 6

[6.1] National Instruments, *DAQ NI 6115/6120 User Manual - Multifunctions devices for PCI/PXI/CompactPCI bus computers*, 2002.

[6.2] BS EN 10280:2001 + A1:2007, *Magnetic Materials - Methods of measurement of the magnetic properties of electrical sheet and strip by means of a single sheet tester*, British Standard, 2007.

[6.3] S. Zurek, P. Marketos, P. I. Anderson, and A. J. Moses, "Influence of digital resolution of measuring equipment on the accuracy of power loss measured in Epstein frame," *Przegląd Elektrotechniczny (Electrical Reviews)*, Vol. R. 83, pp. 50-53, 2007.

[6.4] P. Klimczyk, *AC Magnetostriction Measurement System for Epstein Strip Samples - User manual*, Unpublished document, Wolfson Centre for Magnetics, School of Engineering, Cardiff University, 2009.

[6.5] KISTLER, *8630C & 8636C PiezoBEAM® Accelerometers*, 2008.

[6.6] S. Zurek, *Two-dimensional Magnetisation Problems in Electrical Steels*, PhD Thesis, Cardiff University, United Kingdom, 2005.

[6.7] V. Gorican, A. Hamler, M. Jesenik, B. Stumberger, and M. Trlep, "Unreliable determination of vector B in 2-D SST," *Journal of Magnetism and Magnetic Materials*, Vol. 254-255, pp. 130-132, 2003.

[6.8] N. Nencib, A. Kedous-Lebouc, and B. Cornut, "2D analysis of rotational loss tester," *IEEE Transactions on Magnetics*, Vol. 31, pp. 3388-3390, 1995.

[6.9] M. Jesenik, V. Gorican, M. Trlep, A. Hamler, and B. Stumberger, "Field homogeneity in a two-phase round rotational single sheet tester with one and both side shields," *Journal of Magnetism and Magnetic Materials*, Vol. 254-255, pp. 247-249, 2003.

[6.10] G. Krismanić, "Recent developments and trends in measurements of two-dimensional magnetic properties," *Journal of Electrical Engineering*, Vol. 55, pp. 4, 2004.

[6.11] G. Loisos and A.J. Moses, "Critical evaluation and limitations of localised flux density measurements in electrical steels," *IEEE Transactions on Magnetics*, Vol. 37, pp. 2755-2757, 2001.

[6.12] G. Loisos, *Novel Flux Density Measurement Methods of Examining The Influence of Cutting on Magnetic Properties of Electrical Steels*, PhD Thesis, Cardiff University, United Kingdom, 2002.

[6.13] S. Tumánski and T. Bakon, "Measuring system for two-dimensional testing of electrical steel," *Journal of Magnetism and Magnetic Materials*, Vol. 223, pp. 315-325, 2001.

[6.14] D. Miyagi, Y. Yunoki, M. Nakano, and N. Takahashi, "Study on measurement method of 2 dimensional magnetic properties of electrical steel using diagonal exciting coil," *Przegląd Elektrotechniczny (Electrical Reviews)*, Vol. R. 85, pp. 47-51, 2009.

[6.15] N. F. Astbury, *Industrial Magnetic Testing*, The Institute of Physics, London, 1952.

[6.16] C. T. A. John, *Engineering Electromagnetic Fields and Waves*, International edition, Willey, New York, 1975.

[6.17] J. Xu and J. Sievert, "On the reproducibility, standardization aspects and error sources of the fieldmetric method for the determination of 2D magnetic properties of electrical sheet steel," *Proceedings of The 5th International Workshop on Two-dimensional Magnetization Problems*, Grenoble, France, September, 1997.

[6.18] M. Enokizono, S. Kanao, and G. Shirakawa, "Measurement of arbitrary dynamic magnetostriction under alternating and rotating field," *IEEE Transactions on Magnetics*, Vol. 31, pp. 3409-3411, 1995.

[6.19] A. Hasenzagl, B. Weiser, and H. Pfützner, "Magnetostriction of 3% SiFe for 2-D magnetization patterns," *Journal of Magnetism and Magnetic Materials*, Vol. 160, pp. 55-56, 1996.

[6.20] A. Lundgren, *On Measurement and Modelling of 2D Magnetization and Magnetostriction of SiFe Sheets*, PhD Thesis, Royal Institute of Technology, Sweden, 1999.

[6.21] TML, *FRA-6-11 Strain Gauge Test Data*, 2008.

[6.22] G. Bán and P. E. Di Nunzio, "Minimum force model. Effect of crystallographic texture on the magnetostriction and loss characteristics of non-oriented electrical steels," *Journal of Magnetism and Magnetic Materials*, Vol. 254-255, pp. 265-268, 2003.

[6.23] National Instruments, *Strain Gage Measurement - A tutorial*, 1998.

[6.24] National Instruments, *NI USB-9237 User Guide and Specifications*, 2008.

[6.25] P. Beckley, *Electrical Steels: A handbook for producers and users*, European Electrical Steels, Newport, Wales, 2000.

[6.26] National Instruments, *NI 9237 Calibration Procedure*, 2008.

[6.27] C. G. Kim, H. C. Kim, S. J. Ahn, S. Y. Cha, and S. K. Chang, "Magnetizing angle dependence of harmonics of magnetic induction and magnetostriction in electrical steel," *Journal of Magnetism and Magnetic Materials*, Vol. 215-216, pp. 159-161, 2000.

[6.28] T. Hilgert, L. Vandevelde, and J. Melkebeek, "Application of magnetostriction measurements for the computation of deformation in electrical steel " *Journal of Applied Physics*, Vol. 97, pp. 3, 2005.

[6.29] M. Enokizono, K. Takahashi, and Y. Yamaura, "Development of a new strain gage for measurements of two dimensional magnetostriction," *Journal of Magnetism and Magnetic Materials*, Vol. 196-197, pp. 907-909, 1999.

[6.30] National Instruments, *DAQ PCI-6052E/6053E User Manual*, 1999.

[6.31] National Instruments, *Getting Started with CompactRIO and LabVIEW*, 2008.

[6.32] D. C. Jiles, *Introduction to The Principles of Materials Evaluation*, CRC Press, Boca Raton, Florida, 2008.

[6.33] Vishay, *System 6000 Vishay Micro-measurements*, 2006.

[6.34] ThyssenKrupp Steel, *Power Core® M400-50A NGO Electrical Steel*, 2009.

[6.35] UKAS M3003, *The Expression of Uncertainty and Confidence in Measurement*, 1997.

[6.36] Tyco Electronics, *Aluminium Housed Power Resistors*, 2008.

[6.37] Cogent™ Surahammars Bruks AB, *Typical Data for SURA® M235-35A*, 2008.

Chapter 7

Sample Selection and Preparation

This chapter covers the selection of the materials which were tested in the measurement apparatus described in **Chapter 6**. The methods of sample preparation for all the measurement systems are described here.

7.1 Selection of Test Materials

A fully processed NO electrical steel with a nominal thickness of 0.50 mm [*7.1*] (designated as NO1 in Table 7-1) was mainly used in the study of anisotropy of magnetic properties, AC and 2D magnetostriction, rotational loss, and elastic properties. Another 0.35 mm thick, fully processed NO steel [*7.2*] designated as NO2 in Table 7-1 was selected as a supplementary material to compare its AC and 2D magnetostriction with those of NO1. Density ρ_m and resistivity ρ of the test materials were determined using the method described in [*7.3*]. A standard Epstein sample cut along the RD from each material was tested in the system are described in [*7.4*] and Table 7-2 lists all the instruments. Repeatability tests were carried out 5 times on each sample and the measurement uncertainties of ρ_m and ρ were evaluated based on the procedure in **Section 6.5**. The percentage of silicon (%Si) and aluminium (%Al) content by weight was estimated from the density using [*7.5*]

$$p_m = 7865 - 65 \times (\%Si + 1.7(\%Al)). \qquad (7.1)$$

The nominal density values of NO1 and NO2 quoted in [*7.1, 7.2*] imply the uncertainty of ± 50 kg/m^3 [*7.6*], which should cover the maximum density tolerances

in the production lines of these two materials. However, the uncertainty of ± 2 kg/m^3 in the density measurement stated in Table 7-1 covers only an Epstein sample of each material. Thus, the value of ± 50 kg/m^3 is used as an uncertainty source in the uncertainty evaluation in **Section 6.5**.

According to BS EN 10106:2007 [*7.7*], NO1 and NO2 are graded as M400-50A and M235-35A respectively. The main application of M400-50A grade is stator and rotor cores of medium size rotating machines [*7.1*]. Therefore, NO1 was also used to construct the induction motor model core described in **Chapter 10**.

Table 7-1 Physical properties of the 0.50 mm [*7.1*] and 0.35 mm [*7.2*] thick NO electrical steels

Material Identity	Nominal thickness [mm]	Nominal density [kg/dm^3]	Measured density [kg/m^3]	Measured resistivity [$10^{-7}\Omega$·m]	Estimated silicon and aluminium contents [%]
NO1	0.50	7.70	7,660 ± 2	4.58 ± 0.02	2.5
NO2	0.35	7.60	7,580 ± 2	5.81 ± 0.02	4.0

Table 7-2 List of instruments used in determining density, resistivity and thickness

Measured quantities	Model manufacturer	Measurement range	Resolution	Uncertainty
Sample mass	FB31 Avery Berkel	3.1 kg	0.01 g	±0.0002 g
Sample length	RS600 Metal ruler	600 mm	0.5 mm	±0.2 mm
Sample width	Clarke precision	100 mm	0.1 mm	±0.02 mm
Resistance	Digital vernier calliper Agilent 34420A micro ohmmeter	1 Ω	1 μΩ	(0.0015+0.0002) (% of reading + % of range)

7.2 Preparation of Epstein Specimens

The NO1 steel was cut into Epstein strips, 305 mm long 30 mm wide, from a batch of square sheets, 400 mm × 400 mm by an electric-powered guillotine with a sharp blade. The square sheets had been cut from the same roll of steel to ensure that all Epstein strips had been through the same manufacturing process and had the same chemical composition. Strips were aligned either along the RD or TD or at 10° intervals to the RD for the study of anisotropic properties. Four strips were cut at each angle. No heat treatment is required for Epstein samples of NO steel delivered in the finally annealed state material, except those used in aging tests [*7.7*]. In practice, finally annealed NO steel is normally used without stress relief annealing

[*7.8, 7.9*]. Although the plastic and elastic stresses close to the cut edges of the strips were present [*7.10*], this was assumed to be consistent from sample to sample because of the same shearing force provided by the electric-powered guillotine. Therefore, the as-cut Epstein samples were used in the anisotropy investigation to compare directly with the BS EN 10106:2007 standard [*7.7*]. Three samples were used in the magnetic property and AC magnetostriction measurements and one for the Young's modulus and Poisson's ratio measurements.

Epstein strips of the material NO2 were cut from a 500 mm × 500 mm sheet by electric discharge machining [*7.11*], initially used for a comparison of cutting stress under various techniques carried out by Klimczyk [*7.12*]. The samples were annealed in a nitrogen atmosphere at a temperature of 800° C for 2 hours.

Table 7-3 lists the Epstein samples which were all weighed. The length and the width of the test samples were measured by a precision metal ruler and a digital vernier calliper detailed in Table 7-2.

Table 7-3 List of the test Epstein specimens

Sample identity	Material identity	Angle to the RD θ [°]	Numbers of samples
NO1-00	NO1	0	4
NO1-10	NO1	10	4
NO1-20	NO1	20	4
NO1-30	NO1	30	4
NO1-40	NO1	40	4
NO1-50	NO1	50	4
NO1-60	NO1	60	4
NO1-70	NO1	70	4
NO1-80	NO1	80	4
NO1-90	NO1	90	4
NO2-00	NO2	0	1
NO2-90	NO2	90	1

Rosette resistance strain gauge were attached at the middle of each Epstein sample as described in **Section 6.4** for measurement of Young's modulus (E) and Poisson's ration (ν). A strip was selected from each sample set of NO1-00 to NO1-90 listed in Table 7-2. The insulating coating of each strip was carefully removed using a P220 abrasive paper then acetone was used to clean the strips. Two scratched lines were marked approximately at the centre of the sample by an empty ball-pointed pen with the aid of a precision metal ruler. The top side of the gauge was attached with

transparent adhesive tape then the gauge was positioned on the marked lines with the aid of a magnifying glass as illustrated in Fig. 7-1 (a). Once the gauge was correctly positioned, half of the adhesive tape length was lifted as shown in Fig. 7-1 (b). A drop of the Omega 496 instant adhesive [*7.13*] was spread on the sample over the gauge area. After using a palm to press the gauge on the sample for about 2 minutes, the adhesive tape was carefully removed and the electrical connections were made. The samples with the strain gauges attached were left for 24 hours to allow the bond to firmly set.

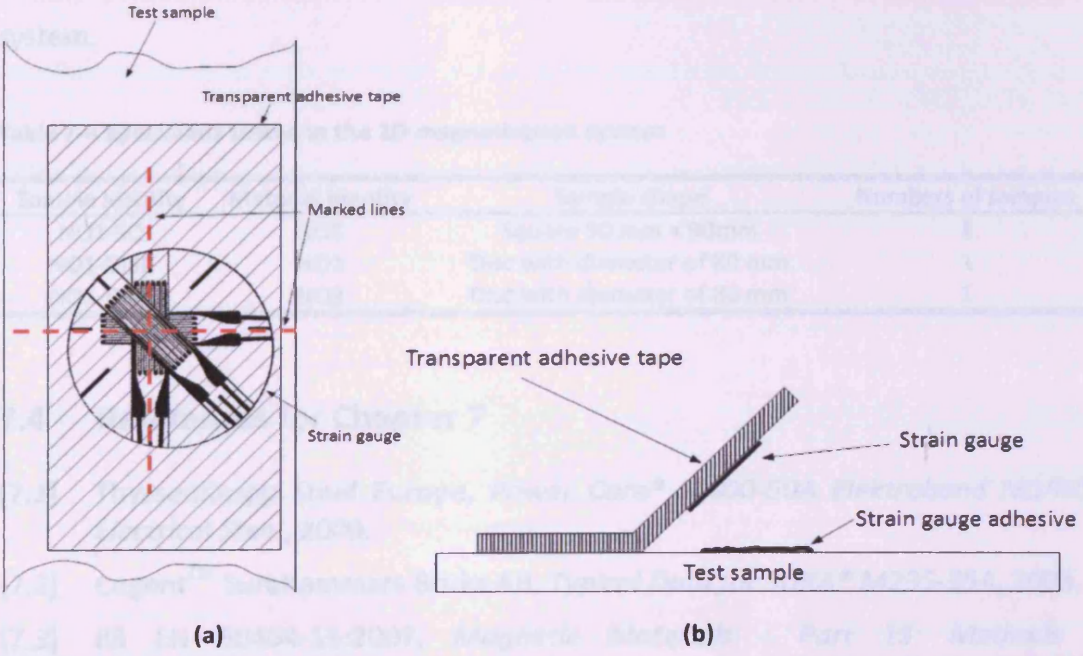

Fig. 7-1 Demonstration of the attachment of a rosette strain gauge (not scaled): (a) top view, and (b) side view

7.3 Preparation of Disc Specimens

The specific power loss (P_s) and magnetostriction under 2D magnetisation were measured on the two grades of NO steel. They were cut into 90 mm × 90 mm square sheets. Four holes for *b* coils with the practically convenient diameter of 0.50 mm were drilled by a high speed drill revolving at about 10,000 rpm. The positions of the holes were marked as in Fig. 6-9 (a). After drilling the holes, the test specimen could be placed into the planar yoke of the 2D magnetisation system shown in Fig. 6-8 (a). A square sample of the NO1 material was tested in the planar yoke. The other square specimens of the NO1 and NO2 materials were stacked between two thick steel plates then a lathe was used to cut them simultaneously into circular samples of

diameter of 80 mm as in Fig. 6-9 (b). All samples were stress relief annealed in nitrogen at 800°C for 2 hours.

After the samples had cooled, a rosette strain gauge was attached at the centre of each as shown in Fig. 6-13 (a). The bonding method was similar to that for the Epstein samples described in **Section 7.3** apart from the fact that position lines were gently marked by a very sharp pencil in order not to deteriorate the stress sensitive magnetic properties. Finally, b_x and b_y coils were wound on each samples as described in **Section 6.3.2**. Table 7-4 lists the samples tested in the 2D magnetisation system.

Table 7-4 Specimens tested in the 2D magnetisation system

Sample identity	Material identity	Sample shape	Numbers of samples
NO1-SQ	NO1	Square 90 mm × 90mm	1
NO1-DISC	NO1	Disc with diameter of 80 mm	1
NO2-DISC	NO2	Disc with diameter of 80 mm	1

7.4 References for Chapter 7

[7.1] ThyssenKrupp Steel Europe, *Power Core® M400-50A Elektroband NO/NGO Electrical Steel*, 2009.

[7.2] Cogent™ Surahammars Bruks AB, *Typical Data for SURA® M235-35A*, 2008.

[7.3] BS EN 60404-13:2007, *Magnetic Materials - Part 13: Methods of measurement of density, resistivity and stacking factor of electrical steel sheet and strip*, British Standard, 2007.

[7.4] J. Leicht, *Magnetic Properties of Electrical Steel under Controlled Magnetisation Conditions*, PhD Thesis, Cardiff University, United Kingdom, 2003.

[7.5] C. Y. Chin and J. H. WErnick, "Soft Magnetic Metallic Materials," *Ferromagnetic Materials*, Vol. 2, Edited by E. P. Wohlfarth, North-Holland Publishing Company, Amsterdam, 1998.

[7.6] L. Kirkup and B. Frenkel, *An Introduction to Uncertainty in Measurement*, Cambridge University Press, Cambridge, England, 1993.

[7.7] BS EN 10106:2007, *Cold rolled non-oriented electrical steel sheet and strip delivered in the fully processed state*, British Standard, 2007.

[7.8] ThyssenKrupp Steel Europe, *Our product. Non Grain Oriented Electrical Steel Power Core®*, 2009.

[7.9] Cogent™, *Electrical Steel: Non oriented fully processed*, 2007.

[7.10] Y. Kurosaki, H. Mogi, H. Fujii, T. Kubota, and M. Shiozaki, "Importance of punching and workability in non-oriented electrical steel sheets," *Journal of Magnetism and Magnetic Materials*, Vol. 320, pp. 2474-2480, 2008.

[7.11] EDM Sales & Services, http://www.edm.co.uk/index.htm

[7.12] P. Klimczyk, *Influence of Cutting Techniques on Magnetostriction Measured in Epstein Strips of Electrical Steel Sheets*, Unpublished document, Wolfson Centre for Magnetics, Cardiff University, 2010.

[7.13] Omega, *SG496 Rapid Cure Strain Gauge Adhesives User's Guides*, 2008.

Chapter 8

Measurements of Magnetostriction, Magnetic and Mechanical Properties of NO Electrical Steels

The experimental results obtained on the 0.50 mm thick and 0.35 mm thick NO steels using the measurement apparatus described in **Chapter 6** are presented in this chapter. Measurements of the anisotropy in specific power loss, AC relative permeability, AC magnetostriction, Young's modulus, and Poisson's ratio of the 0.50 mm thick steel are presented. Experimental measurements of AC magnetostriction under applied stress of the both materials are given.

This chapter also covers the results of the specific power loss and magnetostriction measurements of the 0.50 mm thick and 0.35 mm thick materials under 2D magnetisation. Measured and modelled values of magnetostriction under 2D magnetisation are compared.

Error bars shown in the figures in this chapter indicate the measurement repeatability. The full uncertainties for all measurements are presented in the tables in **Section 6.5**.

8.1 SST Measurements of Specific Power Loss and Relative Permeability of the 0.50 mm Thick NO Electrical Steel

This investigation was carried on Epstein strips of the 0.50 mm NO electrical steel (NO1 material). The SST described in **Section 6.1** was used to measure the specific power loss P_s and AC relative permeability $\mu_{r_{AC}}$ of the sets of the Epstein strips cut at

10° intervals from 0° to 90° with respect to the RD (sample set NO1-00 to NO1-90 in Table 7-2). The preparation of these samples has been previously explained in **Chapter 7**. Three samples from each set were used. Each was singly magnetised under sinusoidal flux density at $\hat{B}$ from 0.10 T ± 0.2 % to 1.70 T ± 0.2 % and magnetisation frequency f_m=50 Hz ± 0.01 %. Each measurement was carried out three times and the average taken. Between measurements each sample was removed then re-inserted into the test system. Details of the evaluation of the measurement uncertainties are described in **Section 6.5**.

The averaged values of the specific power loss versus the angles θ with respect to the RD at peak flux density of 0.50, 1.00, 1.30, 1.50, and 1.70 T are shown in Fig. 8-1. These values were taken from the averaged values of each strip and the spread in each sample set is represented by the error bars. Fig. 8-2 displays the percentage variation of the specific power loss in the Epstein strips cut at angles θ to the RD of the 0.50 mm thick NO steel relative to the averaged power loss of the samples set cut along the RD. The absolute and percentage variations of the AC relative permeability of the Epstein samples cut to the angles θ under the sinusoidal magnetisation measured in the SST are shown in Fig. 8-3 and Fig. 8-4 respectively. The error bars in Figs. 8-1 to 8-4 represent the measurement repeatability of each sample set. The full uncertainties of the specific power loss and AC relative permeability measurement at a confidence level of 95 % of the normal distribution are summarised in Table 8-1.

Table 8-1 Uncertainties in the specific power loss and AC relative permeability measurements at a confidence level of 95 % of the normal distribution

Peak flux density range	Uncertainty of the specific power loss	Uncertainty of the AC relative permeability
0.10 T ± 0.2 % to 0.70 T ± 0.2 %	± 4.5 %	± 5.5 %
0.80 T ± 0.2 % to 1.70 T ± 0.2 %	± 1.5 %	± 3 %

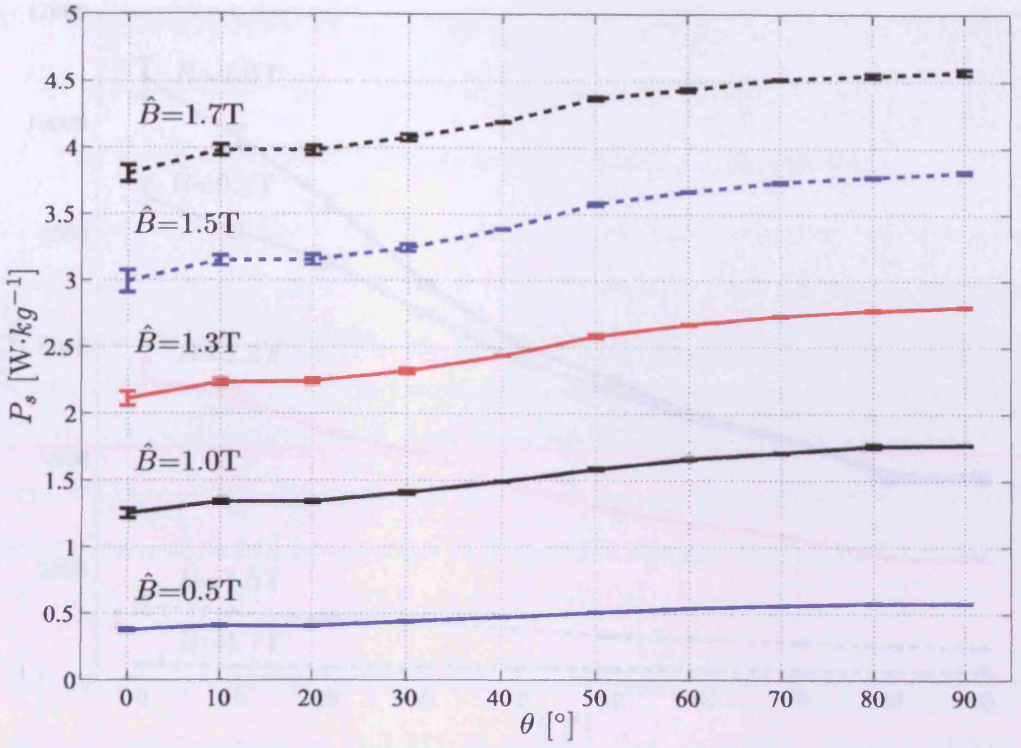

Fig. 8-1 Averaged values of the specific power loss in the Epstein samples of the 0.50 mm thick steel cut at angle θ with respect to the RD at various flux densities

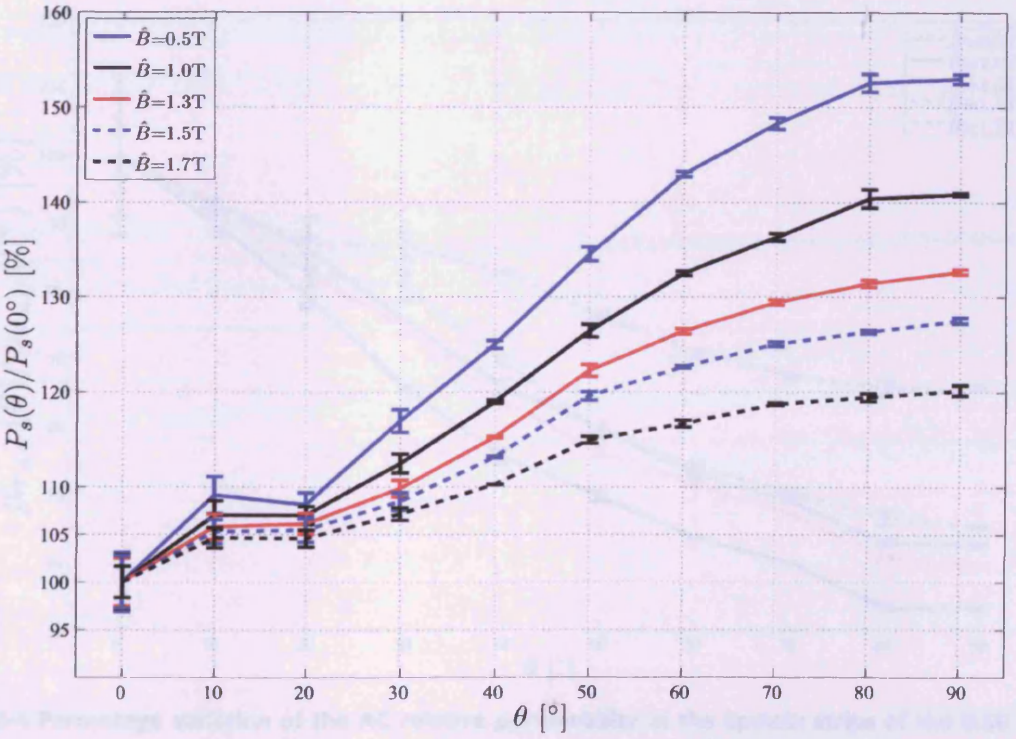

Fig. 8-2 Percentage variation of the specific power loss in the Epstein strips of the 0.50 mm thick steel cut at angle θ relative to that in the sample set cut along the RD at various flux densities

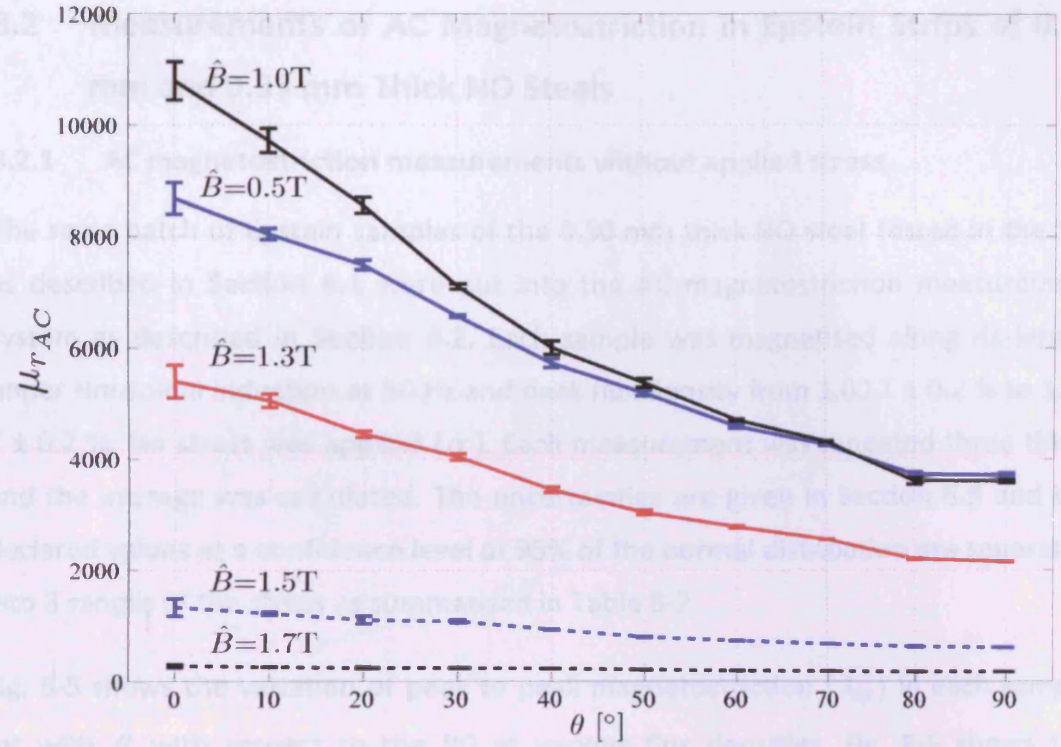

Fig. 8-3 Averaged values of the AC relative permeability in the Epstein samples of the 0.50 mm thick steel cut at angles θ with respect to the RD at various flux densities

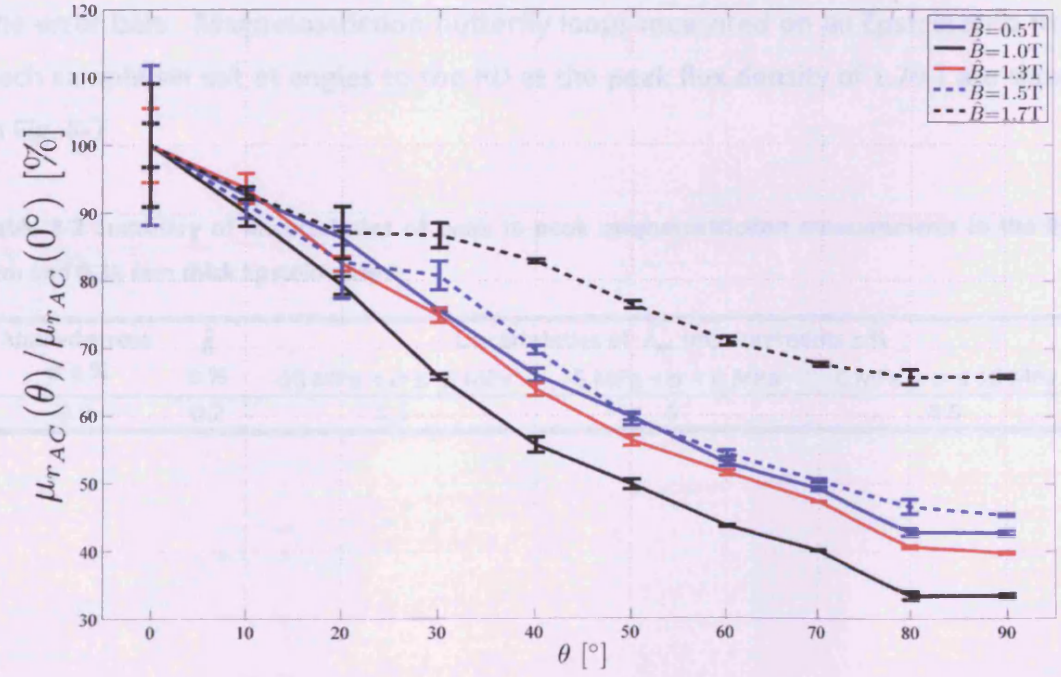

Fig. 8-4 Percentage variation of the AC relative permeability in the Epstein strips of the 0.50 mm thick steel cut at angles θ relative to that in the sample set cut along the RD at various flux densities

8.2 Measurements of AC Magnetostriction in Epstein Strips of 0.50 mm and 0.35 mm Thick NO Steels

8.2.1 AC magnetostriction measurements without applied stress

The same batch of Epstein samples of the 0.50 mm thick NO steel tested in the SST as described in **Section 8.1** were put into the AC magnetostriction measurement system as described in **Section 6.2**. Each sample was magnetised along its length under sinusoidal induction at 50 Hz and peak flux density from 1.00 T ± 0.2 % to 1.70 T ± 0.2 %. No stress was applied (σ). Each measurement was repeated three times and the average was calculated. The uncertainties are given in **Section 6.5** and the declared values at a confidence level of 95% of the normal distribution are separated into 3 ranges of the stress as summarised in Table 8-2.

Fig. 8-5 shows the variation of peak to peak magnetostriction (λ_{pp}) in each sample set with θ with respect to the RD at various flux densities. Fig. 8-6 shows the percentage variation of λ_{pp} in the strips compared to the averaged λ_{pp} in the samples cut along the RD. The measurement repeatability in each set is shown by the error bars. Magnetostriction butterfly loops measured on an Epstein strip from each sample set cut at angles to the RD at the peak flux density of 1.70 T are shown in Fig. 8-7.

Table 8-2 Summary of uncertainties of peak to peak magnetostriction measurements in the 0.50 mm and 0.35 mm thick Epstein strips

Applied stress σ ± %	$\hat{B}$ ± %	Uncertainties of λ_{pp} measurements ± %		
		-10 MPa < σ ≤ -5 MPa	-5 MPa < σ < 0 MPa	0 MPa ≤ σ ≤ 10 MPa
0.9	0.2	5.5	5	8.5

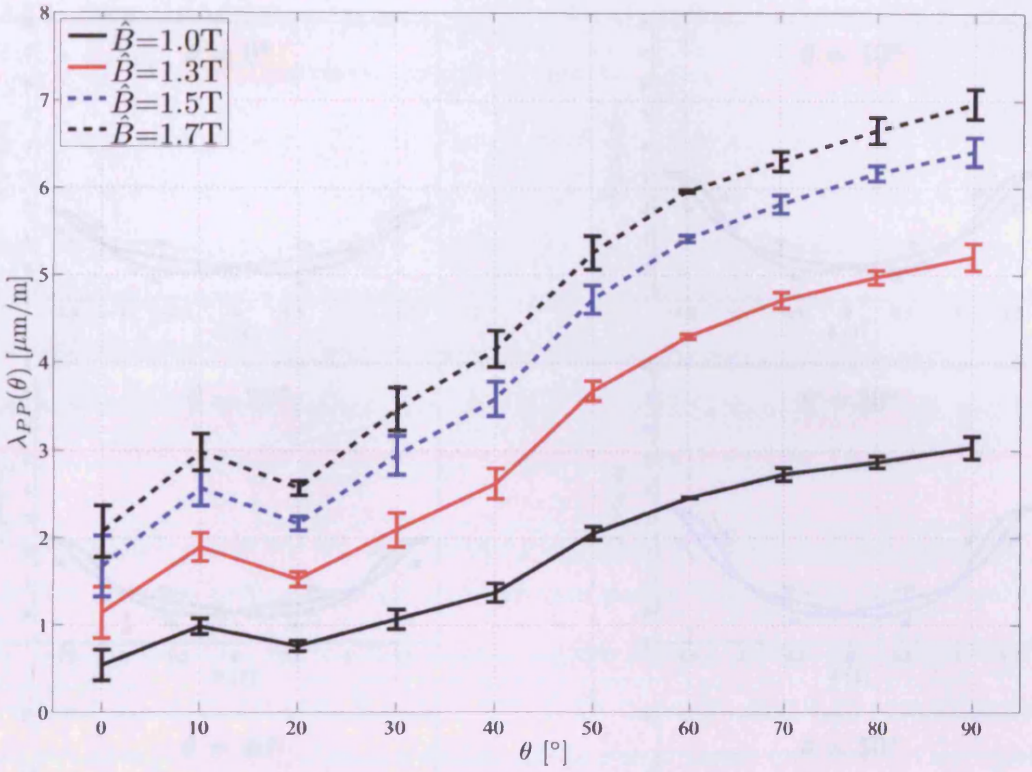

Fig. 8-5 Averaged values of the λ_{pp} in the Epstein strips of the 0.50 mm thick steel cut at angles θ with respect to the RD at various flux densities without applied stress.

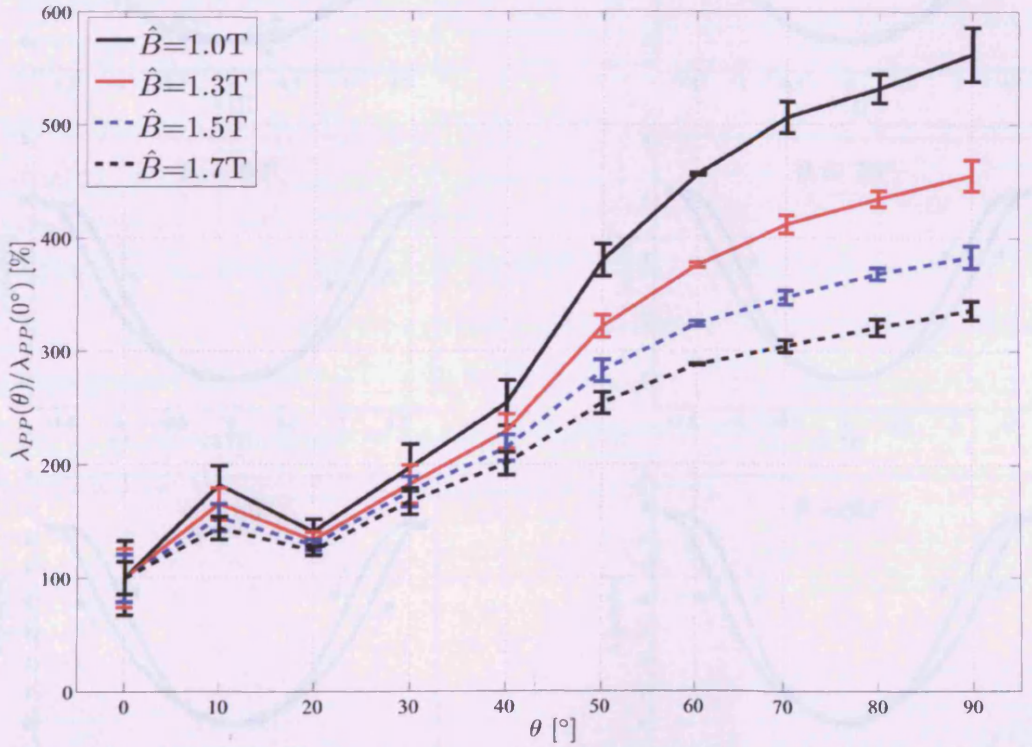

Fig. 8-6 Percentage variation of λ_{pp} in the Epstein strips of the 0.50 mm NO steel cut at angles θ relative to the averaged λ_{pp} of the sample set cut along the RD at various flux densities without applied stress.

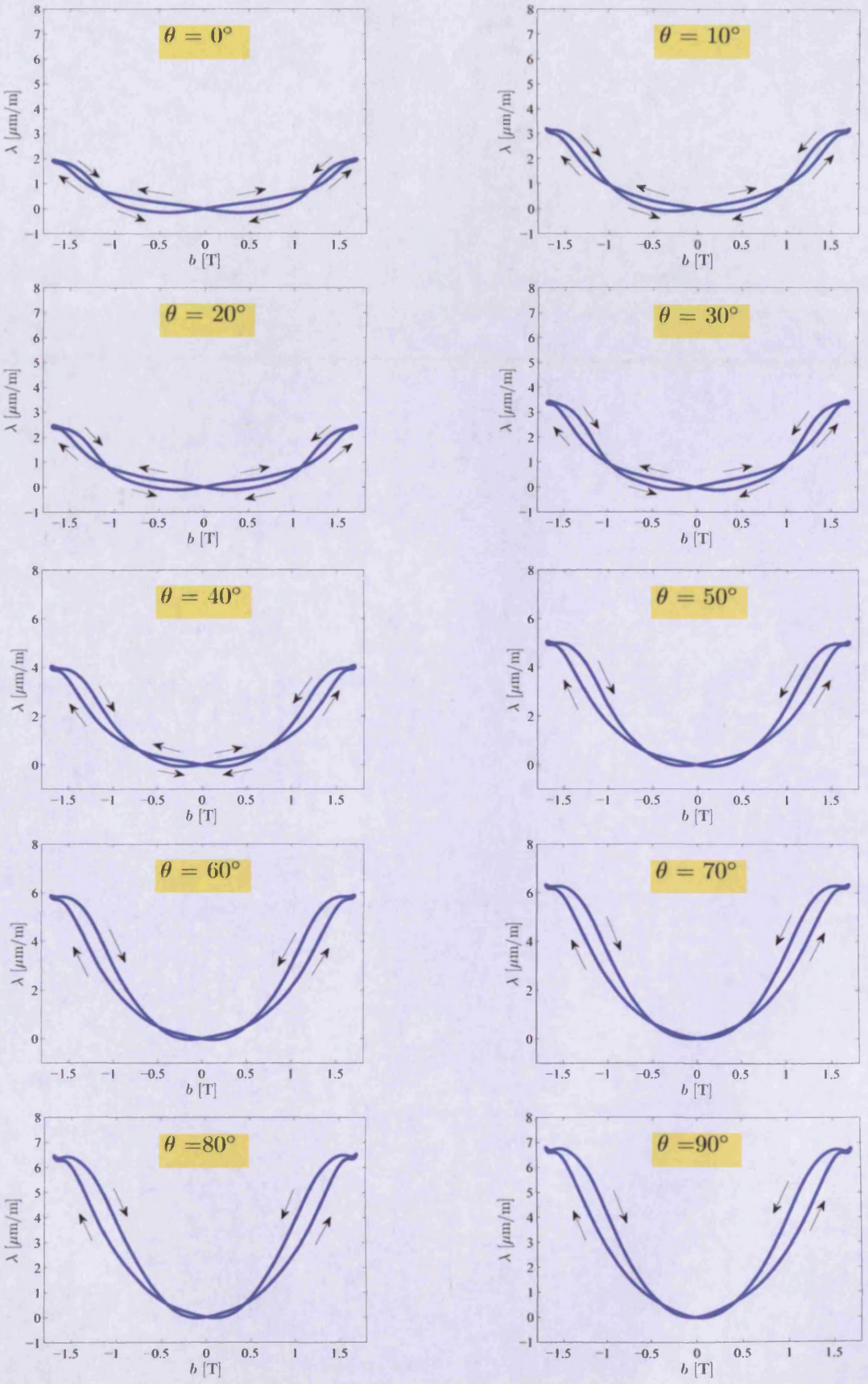

Fig. 8-7 Magnetostriction butterfly loops measured on an Epstein strip of each sample set cut at angles θ under sinusoidal magnetisation at 1.70 T, 50 Hz.

8.2.2 Magnetostriction measurements on the 0.50 mm and 0.35 thick Epstein strips under applied longitudinal stress

The Epstein sample sets of the 0.50 mm thick NO steel cut at 0°, 30°, 60° and 90° with respect to the RD previously used in **Section 8.1** and **Section 8.2.1** were selected for measuring the effect of longitudinal stress on the magnetostriction. The specimens were tested in the AC magnetostriction measurement system. An applied stress of 10 MPa ± 0.9 % to -10 MPa ± 0.9 % was achieved by the pneumatic cylinder attached to one end of the test sample. The sinusoidal magnetisation was set in the range of peak flux densities from 1.00 T ± 0.2 % to 1.50 T ± 0.2 %, 50 Hz.

The test sample could not be magnetised above 1.60 T since the power output of the amplifier was not sufficient under compressive stress. Two Epstein strips of the 0.35 mm thick NO steel were also tested under similar stress and magnetisation conditions to compare with the 0.50 mm thick material. The 0.35 mm thick strips were cut along and perpendicular to the RD as described in **Chapter 7**. Each Epstein strip was tested three times. The sample was removed between each measurement. The uncertainties in λ_{pp} measurements under stress are summarised in Table 8-2. Fig. 8-8 and Fig. 8-9 show the averaged values of λ_{pp} in the 0.50 mm thick 0°, 30°, 60° and 90° samples measured under at $\hat{B}$ = 1.00 T and 1.50 T, versus the applied longitudinal stress of -10 MPa to 10 MPa. The error bars represent the variation of λ_{pp} in each sample set.

The values of λ_{pp} in the 0° and 90° Epstein samples of the 0.35 mm thick steel measured in the AC magnetostriction measurement system under sinusoidal magnetisation at $\hat{B}$ = 1.00 T and 1.50 T, 50 Hz versus applied longitudinal stress of -10 MPa to 10 MPa are shown in Fig. 8-10 and Fig. 8-11 respectively. The error bars here indicate the measurement repeatability in each strip.

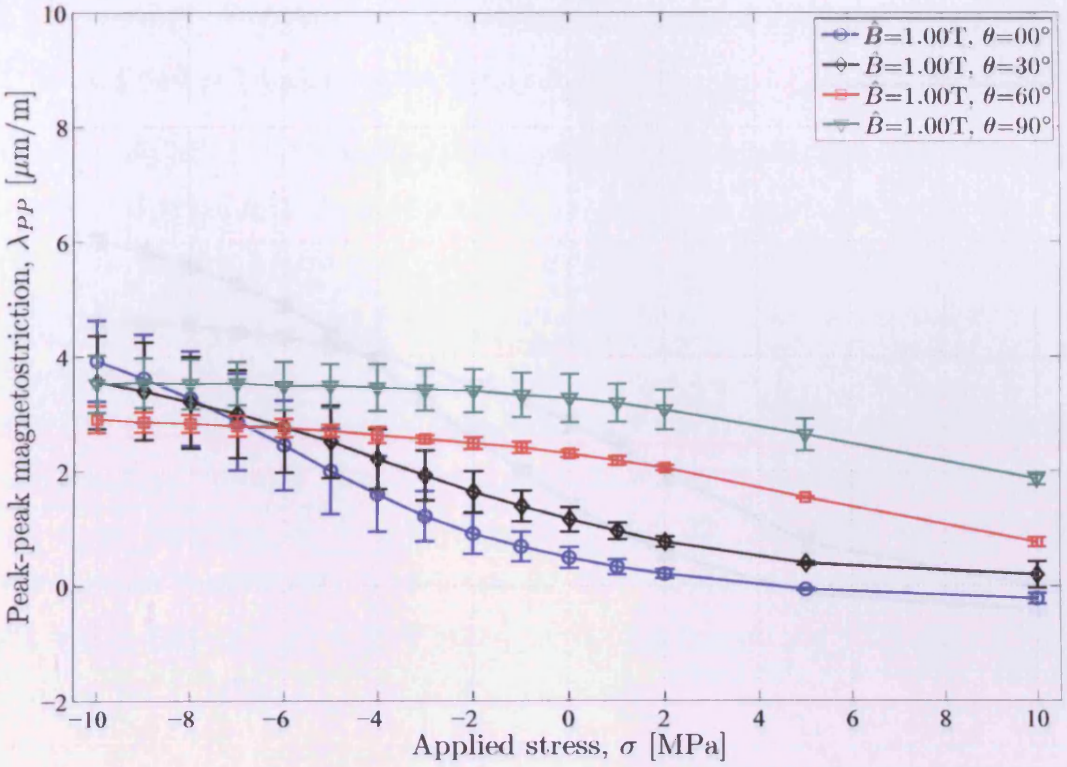

Fig. 8-8 Averaged values of λ_{pp} in the 0.50 mm thick Epstein sample sets cut at 0°, 30°, 60° and 90° to the RD under sinusoidal magnetisation at 1.00 T, 50 Hz versus the applied longitudinal stress.

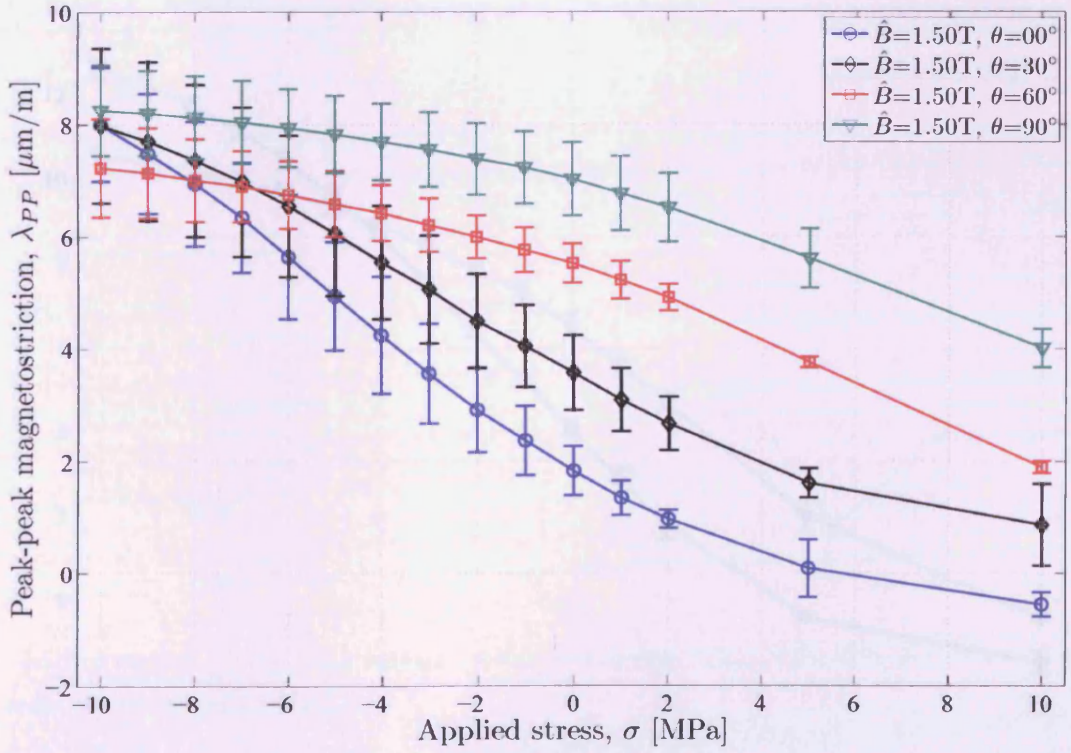

Fig. 8-9 Averaged values of λ_{pp} in the 0.50 mm thick Epstein sample sets cut at 0°, 30°, 60° and 90° to the RD under sinusoidal magnetisation at 1.50 T, 50 Hz versus the applied longitudinal stress.

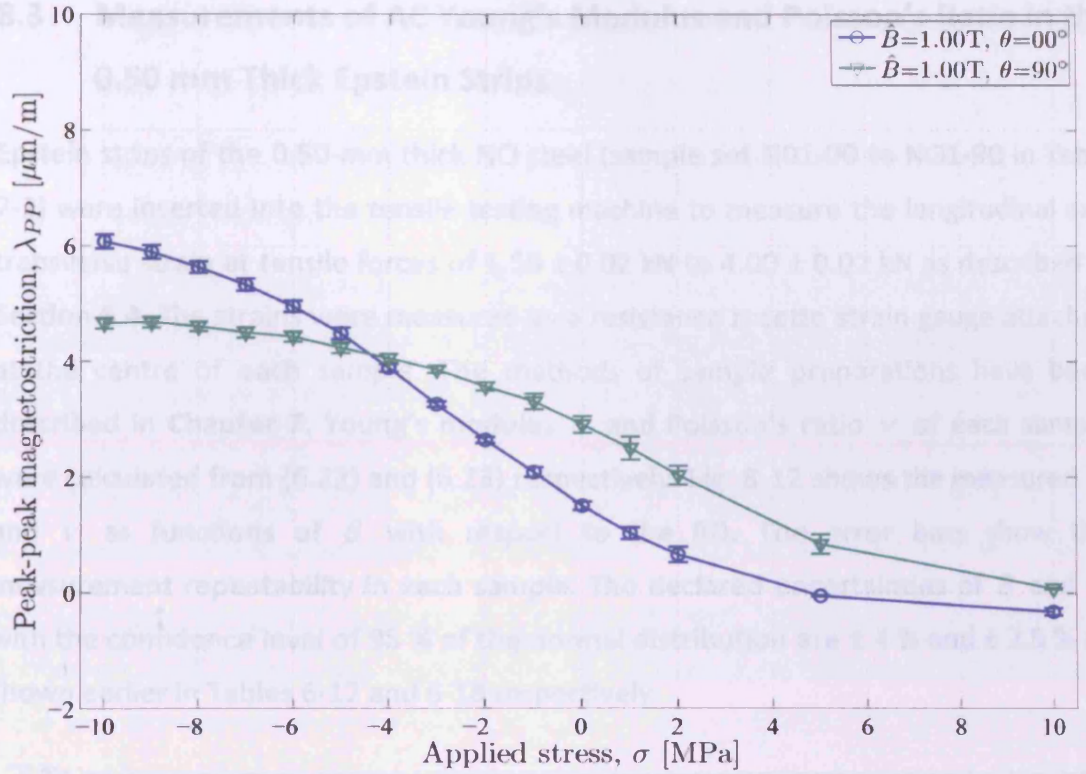

Fig. 8-10 Averaged values of λ_{pp} in the 0.35 mm thick Epstein samples cut at 0° and 90° to the RD under sinusoidal magnetisation at 1.00 T, 50 Hz versus the applied longitudinal stress.

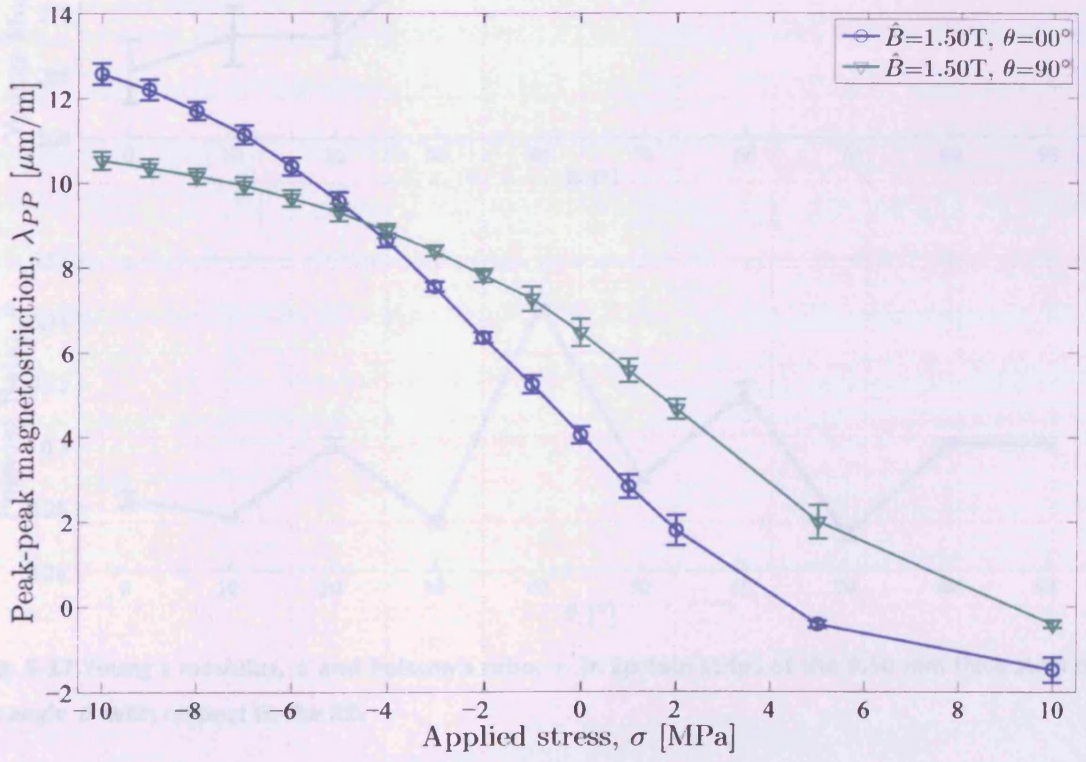

Fig. 8-11 Averaged values of λ_{pp} in the 0.35 mm thick Epstein samples cut at 0° and 90° to the RD under sinusoidal magnetisation at 1.50 T, 50 Hz versus the applied longitudinal stress.

8.3 Measurements of AC Young's Modulus and Poisson's Ratio in the 0.50 mm Thick Epstein Strips

Epstein strips of the 0.50 mm thick NO steel (sample set N01-00 to NO1-90 in Table 7-2) were inserted into the tensile testing machine to measure the longitudinal and transverse strain at tensile forces of 1.50 ± 0.02 kN to 4.00 ± 0.02 kN as described in **Section 6.4**. The strains were measured by a resistance rosette strain gauge attached at the centre of each sample. The methods of sample preparations have been described in **Chapter 7**. Young's modulus E and Poisson's ratio ν of each sample were calculated from (6.22) and (6.23) respectively. Fig. 8-12 shows the measured E and ν as functions of θ with respect to the RD. The error bars show the measurement repeatability in each sample. The declared uncertainties of E and ν with the confidence level of 95 % of the normal distribution are ± 4 % and ± 2.5 % as shown earlier in Tables 6-17 and 6-18 respectively.

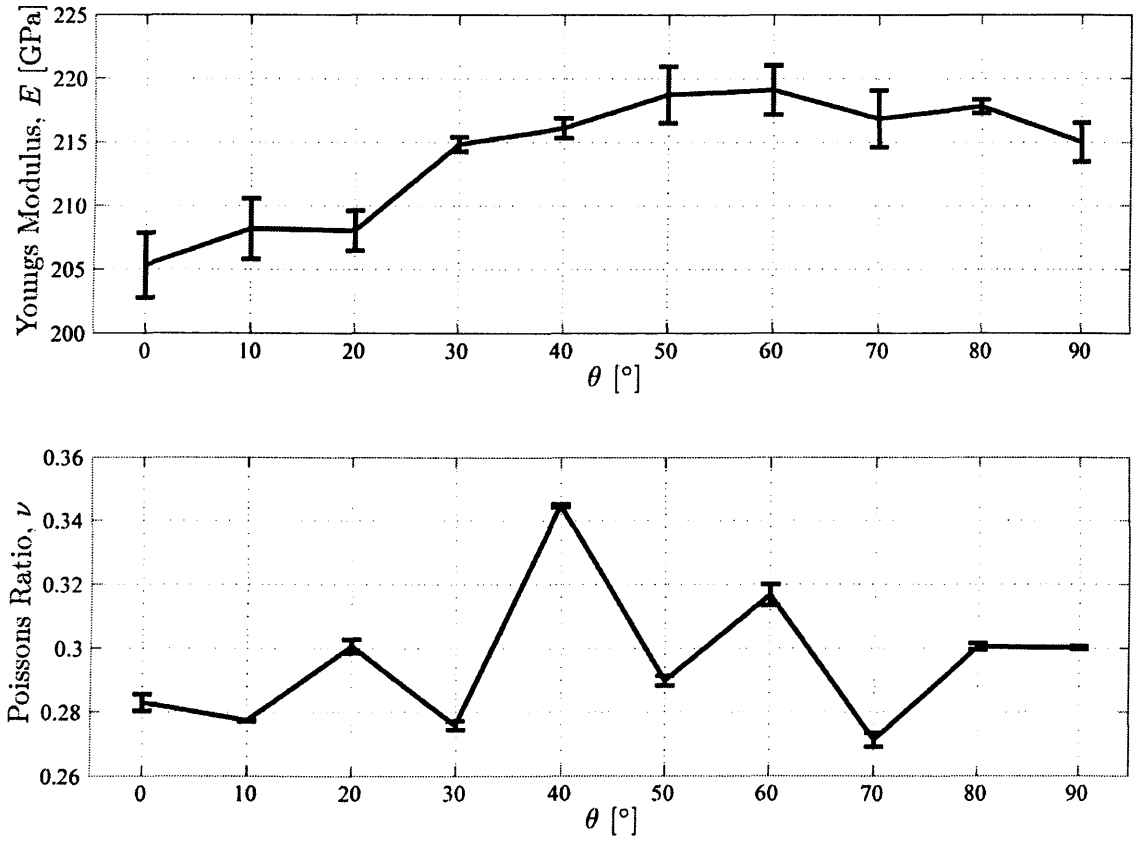

Fig. 8-12 Young's modulus, E and Poisson's ratio, ν in Epstein strips of the 0.50 mm thick steel cut at angle θ with respect to the RD.

8.4 Specific Power Loss and Magnetostriction of 0.50 mm and 0.35 mm Thick Steels under 2D Magnetisation

8.4.1 Justification of magnetising setups for magnetostriction measurement under 2D magnetisation

This test was initially intended to determine the maximum magnetisation range in the planar and round yokes as described in **Section 6.3.1** and also to examine the effect of sample geometry on the 2D magnetostriction measurement. Square and disc samples of the 0.50 mm steel with dimension shown in Fig. 6-9 were tested in the planar and round yokes respectively. They were magnetised under circular magnetisation at the magnetising frequencies f_m of 20, 50, 80, 100, 125 and 200 Hz and each was repeated five times. The maximum peak flux density $\hat{B}$ at 50 Hz and 200 Hz was 1.40 T and 1.00 T respectively for the square sample and 1.90 T and 1.50 T for the disc sample. Peak to peak values of magnetostriction observed in the RD and TD ($\lambda_{x_{pp}}$ and $\lambda_{y_{pp}}$) of the square and disc sample as a function of f_m under circular magnetisation at peak flux densities of 0.50, 0.80 and 1.00 T are shown in Fig. 8-13. The measurement repeatability is indicated by the error bars.

It can be seen that the measured values of magnetostriction of the square sample agree with those of the disc sample. The maximum difference is approximately 1 μm/m at $\hat{B}$ = 0.80 T, f_m = 80 Hz. This can be a sample to sample variation, which was found earlier in the Epstein strips as shown in Fig. 8-5. The sample to sample variation in the Epstein strips was found to be about 0.7 μm/m, which should be less than that in the samples tested in the 2D magnetisation system because of the larger measurement area. Thus, it was decided to use the round yoke and disc samples for power loss and magnetostriction measurements under 2D magnetisation because of the greater magnetisation range.

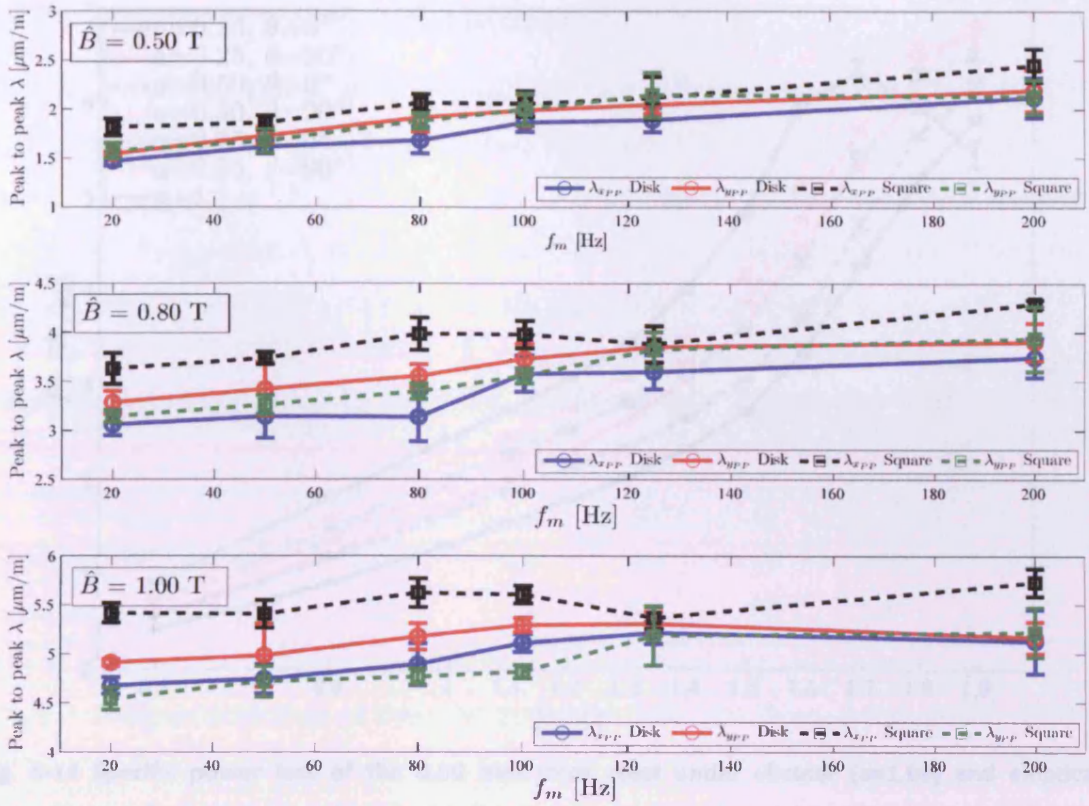

Fig. 8-13 Comparison of $\lambda_{x_{pp}}$ and $\lambda_{y_{pp}}$ in the 0.50 mm thick square and disc samples as a function of f_m under circular magnetisation at peak flux densities of 0.50, 0.80 and 1.00 T

8.4.2 Specific power loss of the 0.50 mm and 0.35 mm thick NO electrical steels under 2D magnetisation at 50 Hz

The specific power losses P_S of the 0.50 mm and 0.35 mm thick steels under circular (α =1) and elliptical flux density loci with the major axis along and perpendicular to the RD as a function of flux density at 50 Hz are displayed in Figs. 8-14 and 8-15 respectively. The average values of P_S measured under ACW and CW field rotation were taken and repeated five times. Between measurements the h coils were removed and re-attached to the sample surface. The measurement repeatability in each magnetisation condition is indicated by the error bars. The peak flux density components $\hat{B}_x$ and $\hat{B}_y$ of both materials were controlled to have the uncertainty of ± 2 % as detailed in Tables 6-11 and 6-12. From this, the uncertainty of the specific power loss measurement was calculated to be ± 7 % and ± 9 % for the 0.50 mm and 0.35 mm thick steels as shown in Tables 6-13 and 6-14 respectively.

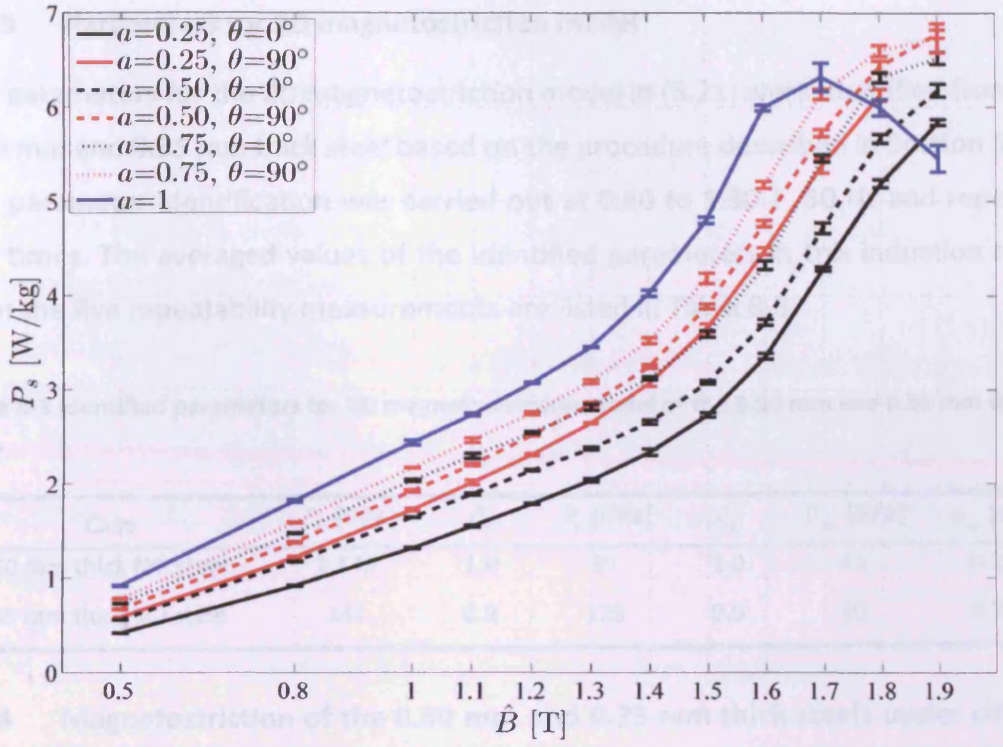

Fig. 8-14 Specific power loss of the 0.50 mm thick steel under circular (α=1.00) and elliptical magnetisation (α=0.25, 0.50 and 0.75) with the major axis along the RD (θ=0°) and the TD (θ=90°), as functions of $\hat{B}$, 50 Hz

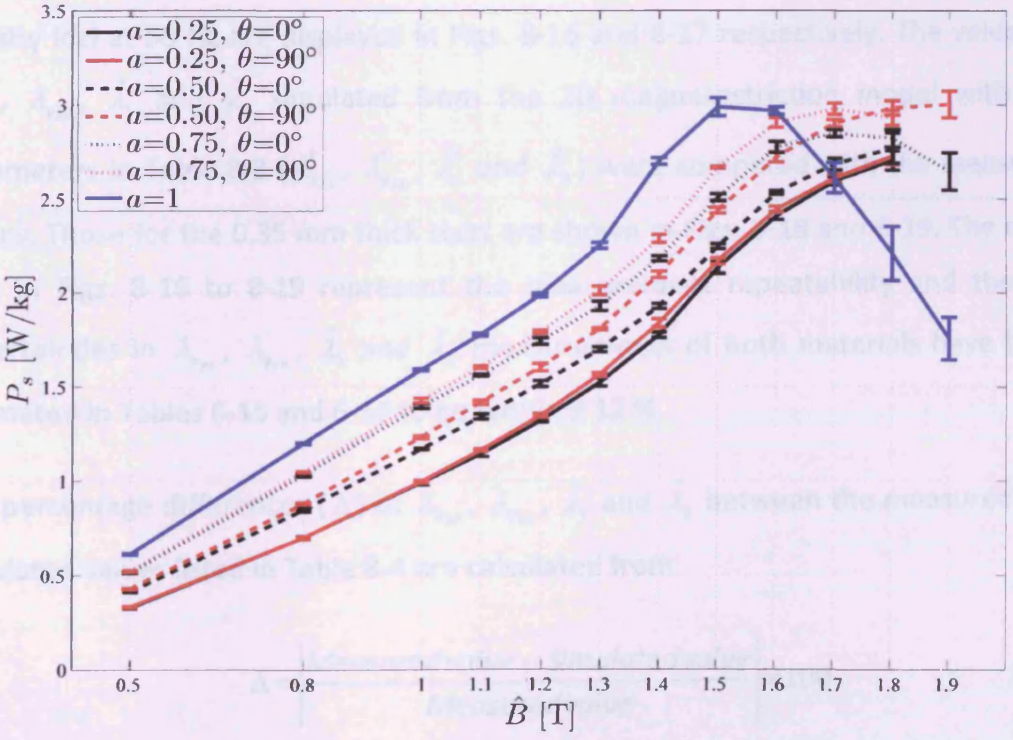

Fig. 8-15 Specific power loss of the 0.35 mm thick steel under circular (α=1.00) and elliptical magnetisation (α=0.25, 0.50 and 0.75) with the major axis along the RD (θ=0°) and the TD (θ=90°), as functions of $\hat{B}$, 50 Hz

8.4.3 Parameters for 2D magnetostriction model

The parameters for the 2D magnetostriction model in (5.21) were identified from the 0.50 mm and 0.35 mm thick steel based on the procedure described in **Section 5.3.3.** The parameter identification was carried out at 0.80 to 1.30 T, 50 Hz and repeated five times. The averaged values of the identified parameters in this induction range from the five repeatability measurements are listed in Table 8-3.

Table 8-3 Identified parameters for 2D magnetostriction model of the 0.50 mm and 0.35 mm thick steel

Case	P_x [GPa]	ξ_x	P_y [GPa]	ξ_y	D_{xy} [GPa]	τ_m [ms]
0.50 mm thick NO steel	2,145	1.0	81	1.0	42	0.17
0.35 mm thick NO steel	141	0.9	128	0.9	40	0.10

8.4.4 Magnetostriction of the 0.50 mm and 0.35 mm thick steels under circular flux density loci at 50 Hz

Peak to peak values of magnetostriction $\lambda_{x_{pp}}$ and $\lambda_{y_{pp}}$, and values of maximum elongation $\hat{\lambda}_1$ and contraction $\hat{\lambda}_2$ of the 0.50 mm thick steel under circular flux density loci at 50 Hz are displayed in Figs. 8-16 and 8-17 respectively. The values of $\lambda_{x_{pp}}$, $\lambda_{y_{pp}}$, $\hat{\lambda}_1$ and $\hat{\lambda}_2$ simulated from the 2D magnetostriction model with the parameters in Table 8-3 ($\lambda^*_{x_{pp}}$, $\lambda^*_{y_{pp}}$, $\hat{\lambda}^*_1$ and $\hat{\lambda}^*_2$) were compared with the measured values. Those for the 0.35 mm thick steel are shown in Figs. 8-18 and 8-19. The error bars in Figs. 8-16 to 8-19 represent the measurement repeatability and the full uncertainties in $\lambda_{x_{pp}}$, $\lambda_{y_{pp}}$, $\hat{\lambda}_1$ and $\hat{\lambda}_2$ measurements of both materials have been estimated in Tables 6-15 and 6-16 to be within ± 12 %.

The percentage differences (Δ) of $\lambda_{x_{pp}}$, $\lambda_{y_{pp}}$, $\hat{\lambda}_1$ and $\hat{\lambda}_2$ between the measured and simulated values listed in Table 8-4 are calculated from

$$\Delta = \left| \frac{Measured\,value - Simulated\,value}{Measured\,value} \right| \times 100 . \qquad (8.1)$$

The measured ($\lambda_x - b_x$ and $\lambda_y - b_y$) and modelled ($\lambda_x^* - b_x$ and $\lambda_y^* - b_y$) butterfly loops of the 0.50 mm and 0.35 mm thick steels under circular magnetisation at 1.30 T are compared in Figs. 8-20 and 8-21 respectively.

If a circular electrical steel sheet with a radius r is considered, the deformation due to magnetostriction can be plotted from

$$r' = r + r \cdot \lambda(\phi, t) \tag{8.2}$$

where $\lambda(\phi,t)$ is the in-plane magnetostriction at a given angle ϕ to the RD and a given time t. This $\lambda(\phi,t)$ is a function of the measured $\lambda_x(t)$, $\lambda_y(t)$ and $\gamma_{xy}^{\lambda}(t)$ defined as

$$\lambda(\phi,t) = \lambda_x(t)\cos^2\phi + \lambda_y(t)\sin^2\phi + \gamma_{xy}^{\lambda}(t)\sin\phi\cos\phi\,. \tag{8.3}$$

Using (8.2), the in-plane deformation plots due to magnetostriction of the 0.50 mm and 0.35 mm thick steels under circular magnetisation at 1.30 and 1.90 T, 50 Hz and the angle between the flux density vector ($\vec{b}$) and the RD of 0°, 45° and 90° are compared in Fig. 8-22.

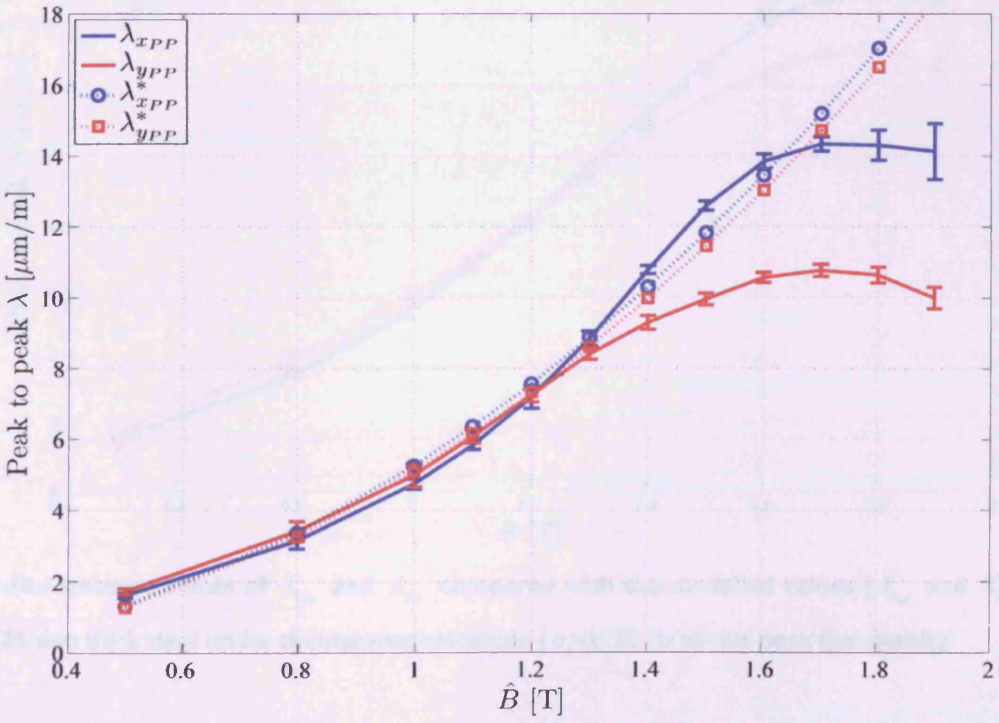

Fig. 8-16 Measured values of $\lambda_{x_{PP}}$ and $\lambda_{y_{PP}}$ compared with the modelled values ($\lambda^*_{x_{PP}}$ and $\lambda^*_{y_{PP}}$) of the 0.50 mm thick steel under circular magnetisation (α =1) 50 Hz versus peak flux density

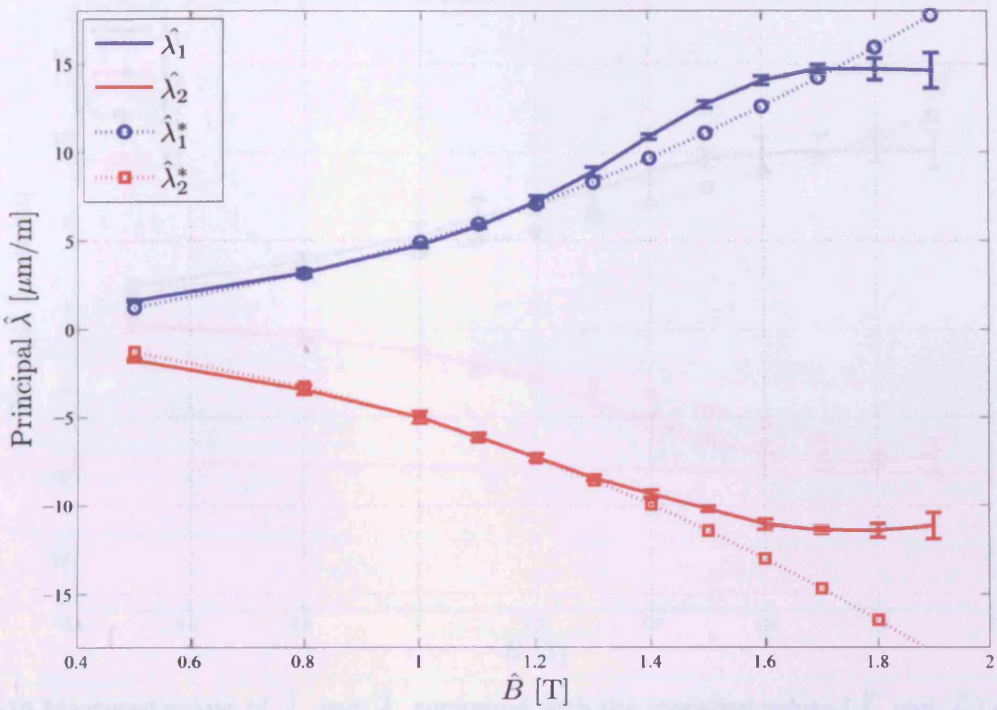

Fig. 8-17 Measured values of $\hat{\lambda}_1$ and $\hat{\lambda}_2$ compared with the modelled values ($\hat{\lambda}_1^*$ and $\hat{\lambda}_2^*$) of the 0.50 mm thick steel under circular magnetisation (σ =1) 50 Hz versus peak flux density

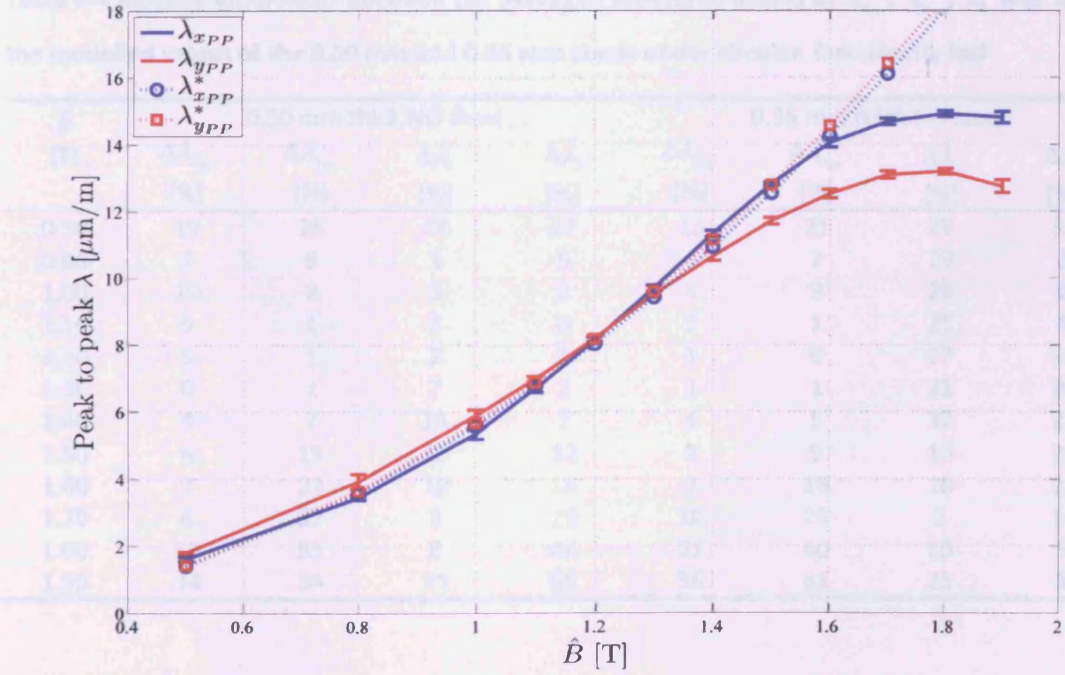

Fig. 8-18 Measured values of $\lambda_{x_{pp}}$ and $\lambda_{y_{pp}}$ compared with the modelled values ($\lambda^*_{x_{pp}}$ and $\lambda^*_{y_{pp}}$) of the 0.35 mm thick steel under circular magnetisation (σ =1) 50 Hz versus peak flux density

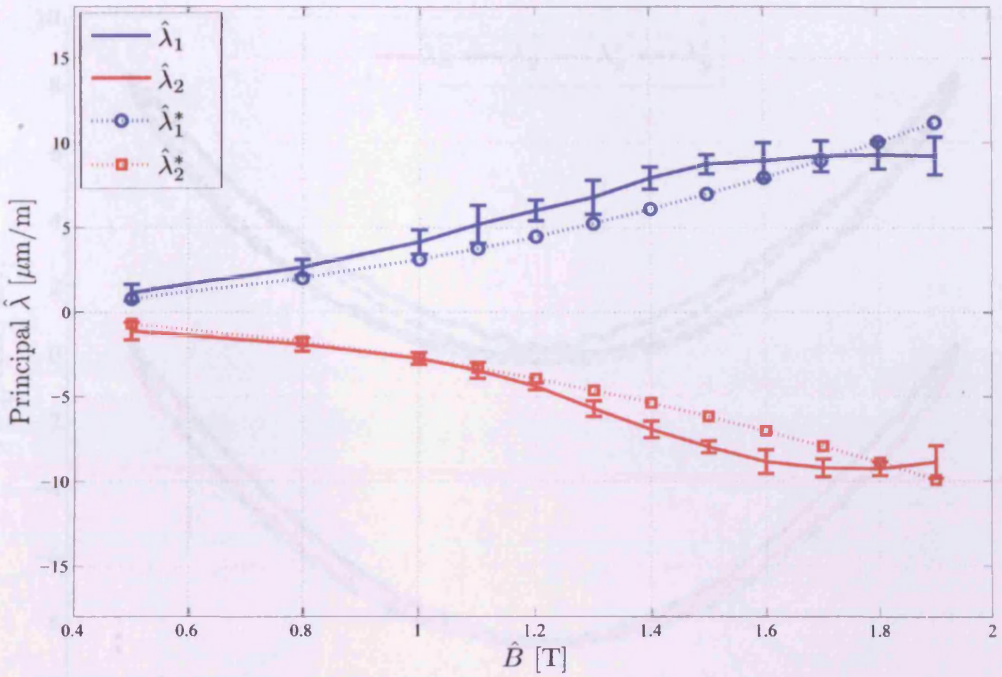

Fig. 8-19 Measured values of $\hat{\lambda}_1$ and $\hat{\lambda}_2$ compared with the modelled values ($\hat{\lambda}_1^*$ and $\hat{\lambda}_2^*$) of the 0.35 mm thick steel under circular magnetisation (α =1) 50 Hz versus peak flux density

Table 8-4 Relative differences between the averaged measured values of $\lambda_{x_{pp}}$, $\lambda_{y_{pp}}$, $\hat{\lambda}_1$ and $\hat{\lambda}_2$ and the modelled values of the 0.50 mm and 0.35 mm steels under circular flux density loci

$\hat{B}$	0.50 mm thick NO steel				0.35 mm thick NO steel			
[T]	$\Delta\lambda_{x_{pp}}$ [%]	$\Delta\lambda_{y_{pp}}$ [%]	$\Delta\hat{\lambda}_1$ [%]	$\Delta\hat{\lambda}_2$ [%]	$\Delta\lambda_{x_{pp}}$ [%]	$\Delta\lambda_{y_{pp}}$ [%]	$\Delta\hat{\lambda}_1$ [%]	$\Delta\hat{\lambda}_2$ [%]
0.50	19	26	24	27	13	21	29	33
0.80	7	5	1	5	4	7	23	3
1.00	10	2	3	2	4	3	24	1
1.10	9	1	2	0	1	1	27	4
1.20	5	1	2	1	1	0	27	10
1.30	0	2	7	2	3	1	21	20
1.40	4	7	11	7	4	5	22	23
1.50	6	15	13	12	2	9	19	23
1.60	3	23	10	18	2	16	10	22
1.70	6	37	3	29	10	25	2	14
1.80	19	55	8	44	21	40	10	5
1.90	34	84	21	65	36	61	25	8

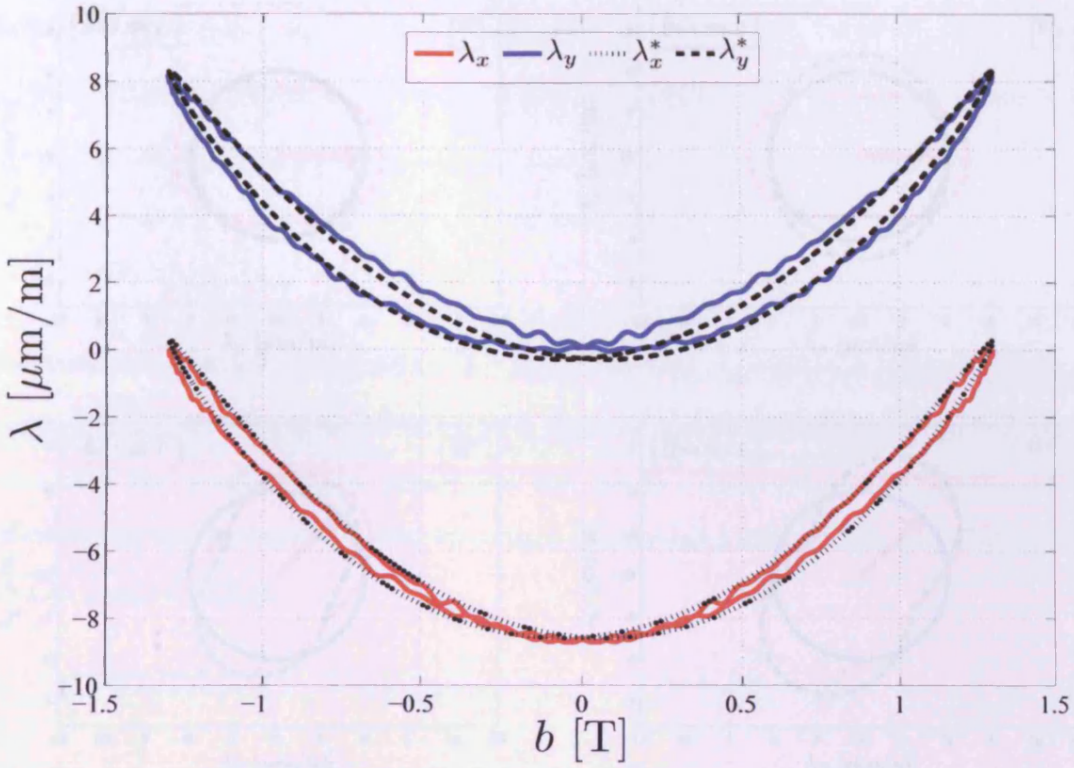

Fig. 8-20 Measured ($\lambda_x - b_x$ and $\lambda_y - b_y$) and simulated ($\lambda_x^* - b_x$ and $\lambda_y^* - b_y$) butterfly loops of the 0.50 mm thick steel under circular magnetisation at 1.30 T, 50 Hz

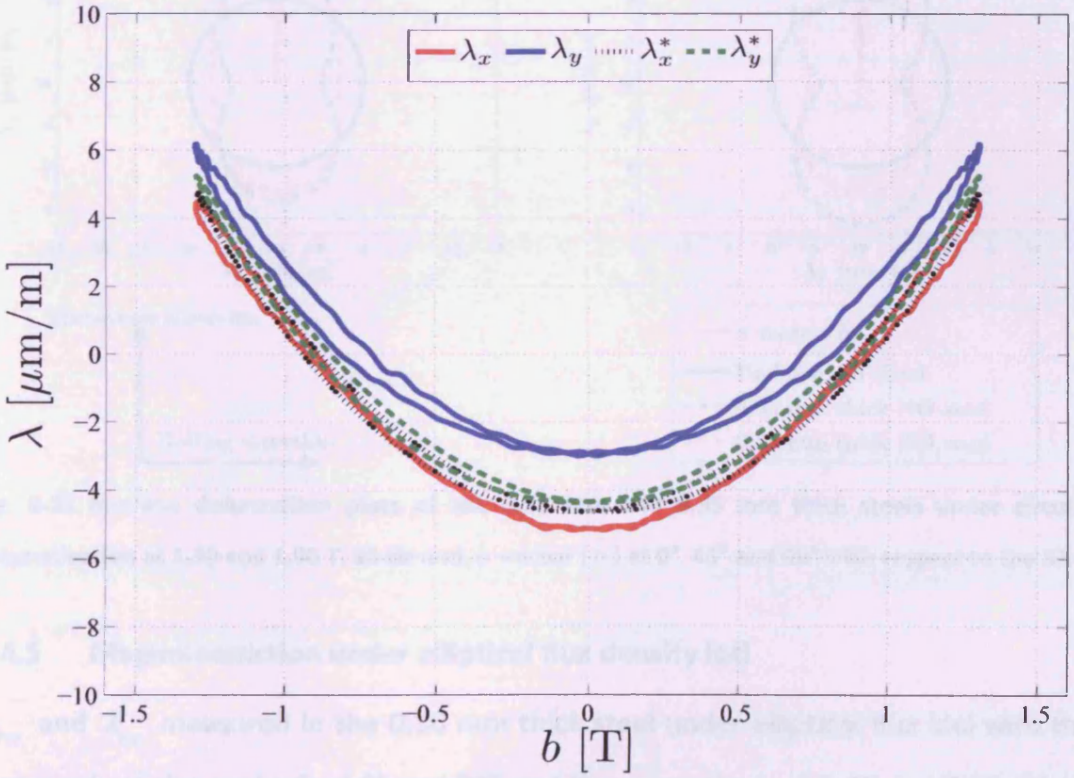

Fig. 8-21 Measured ($\lambda_x - b_x$ and $\lambda_y - b_y$) and simulated ($\lambda_x^* - b_x$ and $\lambda_y^* - b_y$) butterfly loops of the 0.35 mm thick steel under circular magnetisation at 1.30 T, 50 Hz

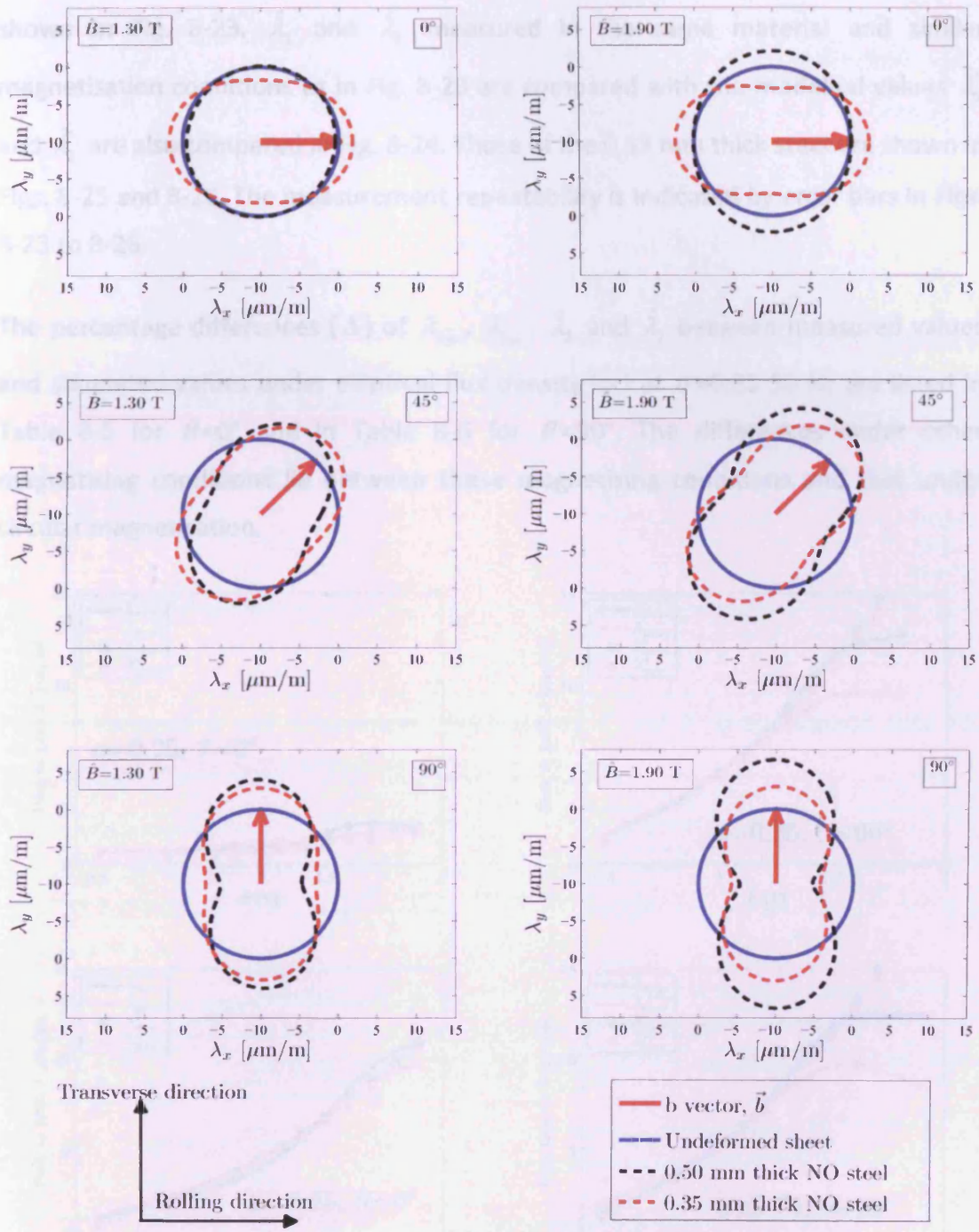

Fig. 8-22 In-plane deformation plots of the 0.50 mm and 0.35 mm thick steels under circular magnetisation at 1.30 and 1.90 T, 50 Hz and b vector ($\vec{b}$) at 0°, 45° and 90° with respect to the RD

8.4.5 Magnetostriction under elliptical flux density loci

$\lambda_{x_{pp}}$ and $\lambda_{y_{pp}}$ measured in the 0.50 mm thick steel under elliptical flux loci with the major axis at the angle θ of 0° and 90° and the axis ratio a of 0.25 and 0.75, 50 Hz are compared with $\lambda^*_{x_{pp}}$ and $\lambda^*_{y_{pp}}$ using the 2D magnetostriction model in (5.21) as

shown in Fig. 8-23. $\hat{\lambda}_1$ and $\hat{\lambda}_2$ measured in the same material and similar magnetisation conditions as in Fig. 8-23 are compared with the modelled values $\hat{\lambda}_1^*$ and $\hat{\lambda}_2^*$ are also compared in Fig. 8-24. Those of the 0.35 mm thick steel are shown in Figs. 8-25 and 8-26. The measurement repeatability is indicated by error bars in Figs. 8-23 to 8-26.

The percentage differences (Δ) of $\lambda_{x_{pp}}$, $\lambda_{y_{pp}}$, $\hat{\lambda}_1$ and $\hat{\lambda}_2$ between measured values and simulated values under elliptical flux density loci at a=0.25 50 Hz are listed in Table 8-5 for θ=0° and in Table 8-6 for θ=90°. The differences under other magnetising conditions lie between these magnetising conditions and that under circular magnetisation.

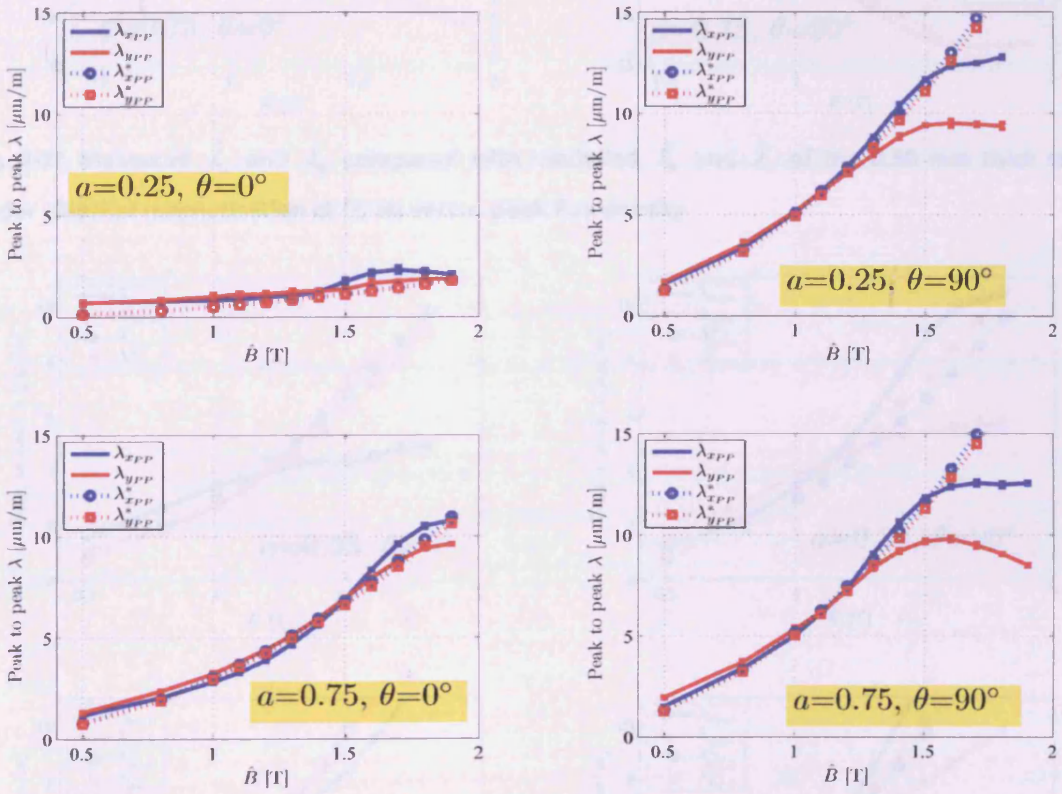

Fig. 8-23 Measured $\lambda_{x_{pp}}$ and $\lambda_{y_{pp}}$ compared with modelled $\lambda^*_{x_{pp}}$ and $\lambda^*_{y_{pp}}$ of the 0.50 mm thick steel under elliptical magnetisation at 50 Hz versus peak flux density

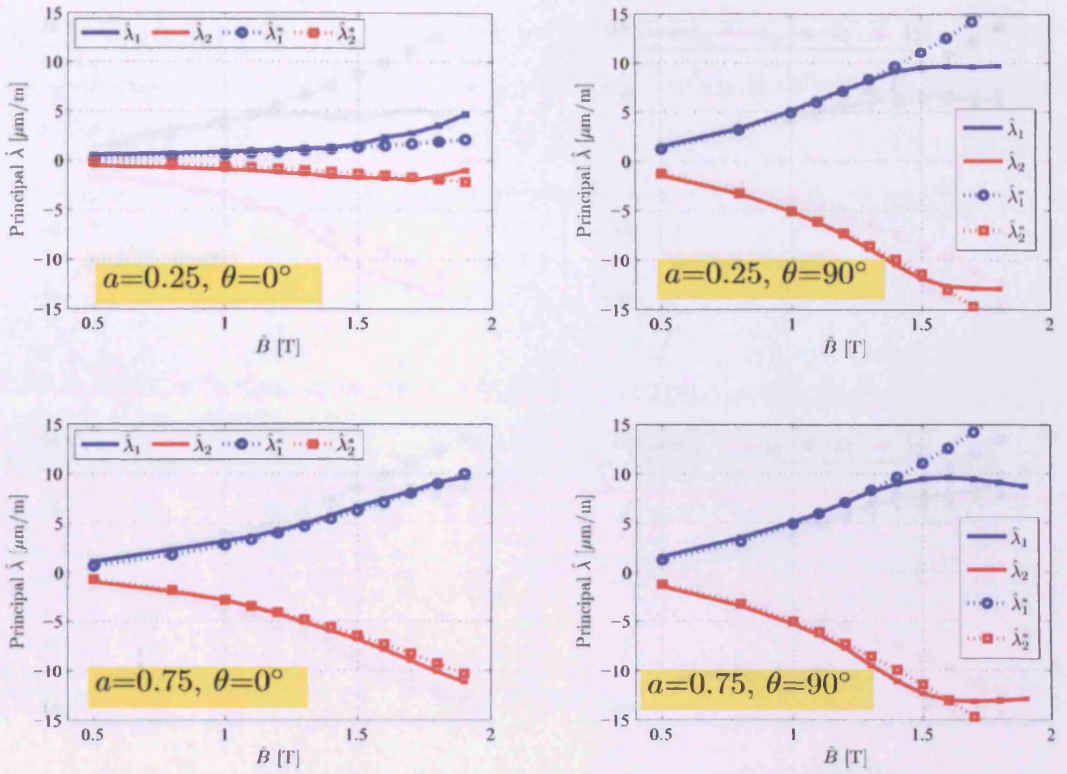

Fig. 8-24 Measured $\hat{\lambda}_1$ and $\hat{\lambda}_2$ compared with modelled $\hat{\lambda}_1^*$ and $\hat{\lambda}_2^*$ of the 0.50 mm thick steel under elliptical magnetisation at 50 Hz versus peak flux density

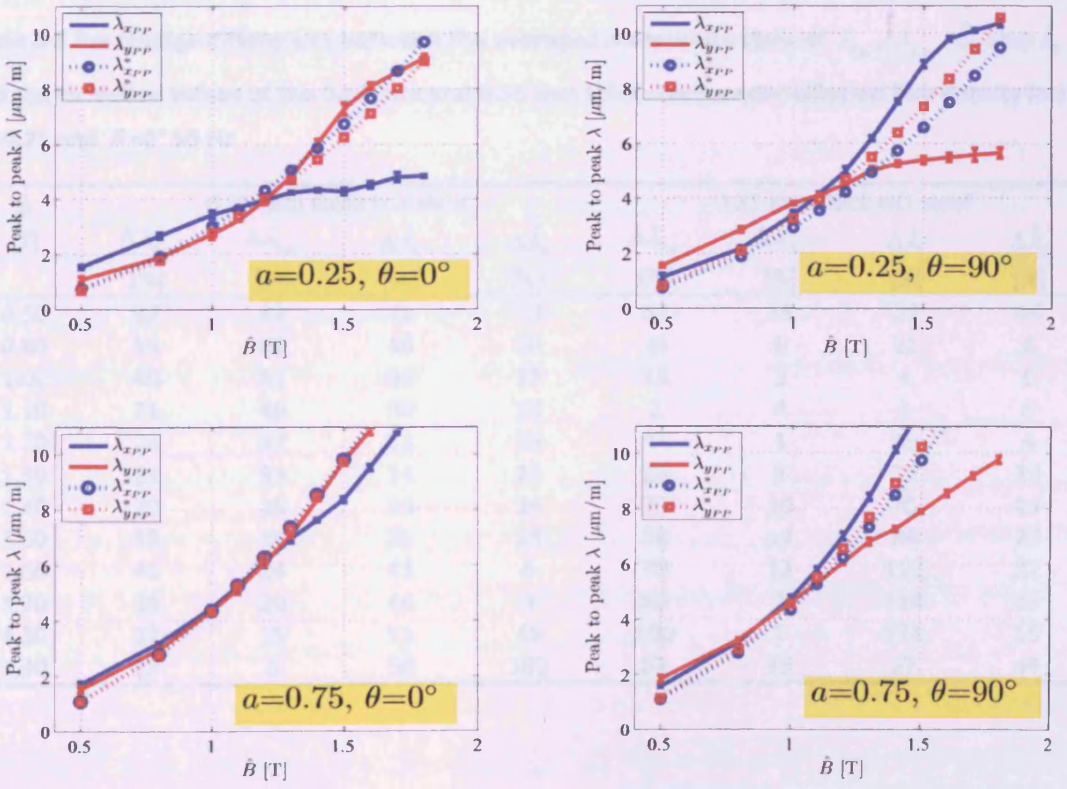

Fig. 8-25 Measured $\lambda_{x_{pp}}$ and $\lambda_{y_{pp}}$ compared with modelled $\lambda_{x_{pp}}^*$ and $\lambda_{y_{pp}}^*$ of the 0.35 mm thick steel under elliptical magnetisation at 50 Hz versus peak flux density

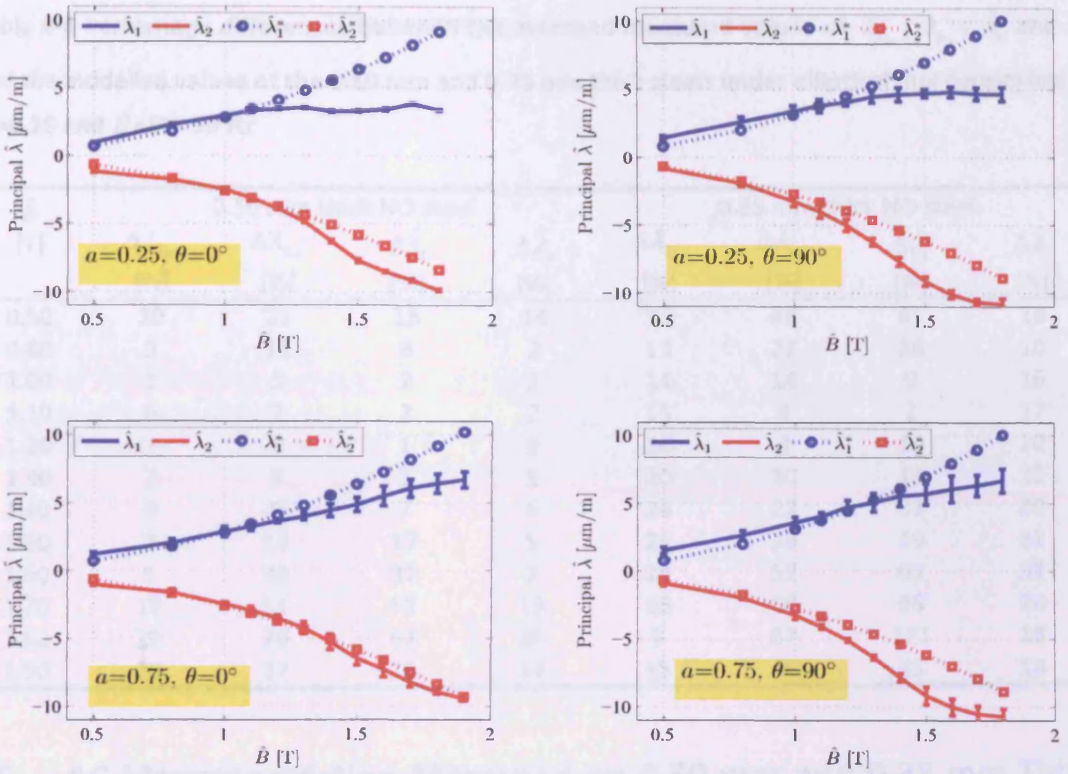

Fig. 8-26 Measured $\hat{\lambda}_1$ and $\hat{\lambda}_2$ compared with modelled $\hat{\lambda}_1^*$ and $\hat{\lambda}_2^*$ of the 0.35 mm thick steel under elliptical magnetisation at 50 Hz versus peak flux density

Table 8-5 Percentage differences between the averaged measured values of $\lambda_{x_{pp}}$, $\lambda_{y_{pp}}$, $\hat{\lambda}_1$ and $\hat{\lambda}_2$ and the modelled values of the 0.50 mm and 0.35 mm thick steels under elliptical flux density loci at a =0.25 and θ=0° 50 Hz

$\hat{B}$	0.50 mm thick NO steel				0.35 mm thick NO steel			
[T]	$\Delta\lambda_{x_{pp}}$ [%]	$\Delta\lambda_{y_{pp}}$ [%]	$\Delta\hat{\lambda}_1$ [%]	$\Delta\hat{\lambda}_2$ [%]	$\Delta\lambda_{x_{pp}}$ [%]	$\Delta\lambda_{y_{pp}}$ [%]	$\Delta\hat{\lambda}_1$ [%]	$\Delta\hat{\lambda}_2$ [%]
0.50	82	82	73	73	52	36	27	44
0.80	59	62	46	50	28	6	21	6
1.00	40	51	32	33	13	2	4	5
1.10	31	46	30	25	2	4	3	0
1.20	26	37	23	25	9	1	19	4
1.30	21	33	24	23	20	3	35	10
1.40	20	25	15	24	36	10	70	19
1.50	35	19	25	18	58	14	94	25
1.60	41	24	41	6	70	12	112	22
1.70	38	20	46	3	80	7	114	18
1.80	27	15	51	45	100	1	171	15
1.90	13	6	58	182	52	36	27	44

Table 8-6 Percentage differences between the averaged measured values of $\lambda_{x_{pp}}$, $\lambda_{y_{pp}}$, $\hat{\lambda}_1$ and $\hat{\lambda}_2$ and the modelled values of the 0.50 mm and 0.35 mm thick steels under elliptical flux density loci at α =0.25 and θ =90° 50 Hz

$\hat{B}$	0.50 mm thick NO steel				0.35 mm thick NO steel			
[T]	$\Delta\lambda_{x_{pp}}$ [%]	$\Delta\lambda_{y_{pp}}$ [%]	$\Delta\hat{\lambda}_1$ [%]	$\Delta\hat{\lambda}_2$ [%]	$\Delta\lambda_{x_{pp}}$ [%]	$\Delta\lambda_{y_{pp}}$ [%]	$\Delta\hat{\lambda}_1$ [%]	$\Delta\hat{\lambda}_2$ [%]
0.50	20	27	16	14	35	48	45	18
0.80	3	11	3	2	13	27	26	10
1.00	1	5	2	2	14	14	9	16
1.10	0	3	2	2	15	4	2	17
1.20	1	0	1	3	16	4	10	20
1.30	2	5	3	5	20	10	16	25
1.40	4	9	7	6	24	22	31	30
1.50	2	18	17	5	26	36	49	32
1.60	5	33	32	2	24	52	65	31
1.70	18	51	51	13	16	68	96	26
1.80	29	70	67	26	9	87	121	18
1.90	20	27	16	14	35	48	45	18

8.5 AC Magnetostriction Measured on 0.50 mm and 0.35 mm Thick Steels Using the 2D Magnetisation System

These measurements were carried out to investigate the differences between magnetostriction measured in Epstein strips and measured in disc samples. In addition, it was to further investigate why the differences between the measured and modelled magnetostriction of the 0.35 mm thick steel under 2D magnetisation are generally higher than those in the 0.50 mm thick material. The magnetisation in the *x* and *y* axes (RD and TD) were controlled to create an AC magnetisation vector at angle θ to the RD using the 2D magnetisation system as shown in Fig. 8-27 and the magnetostriction along the magnetisation direction was calculated from (8.3) by setting $\phi = \theta$. The peak flux density ranged from 0.50 T to 1.80 T at 50 Hz and θ was varied from 0° to 90° at 10 ° intervals. The measurements were repeated five times and the average taken. Peak to peak magnetostriction λ_{pp} measured in the disc samples at 1.00 T, 1.30 T, 1.50 T and 1.70 T, 50 Hz versus the angles with respect to the RD are shown in Fig. 8-28 for the 0.50 mm thick steel and Fig. 8-31 for the 0.35 mm thick steel. Comparisons of λ_{pp} between measured in the Epstein strips and disc samples of both materials are also displayed in Fig. 8-29 and Fig. 8-32 respectively. Fig. 8-30 shows the differences of λ_{pp} measured in the Epstein strips and in the disc sample of the 0.50 mm thick steel measured at $\hat{B}$ = 1.0, 1.30, 1.50 and 1.70 T, 50 Hz

as a function of θ. Repeatability in magnetostriction measurements is indicated by the error bars.

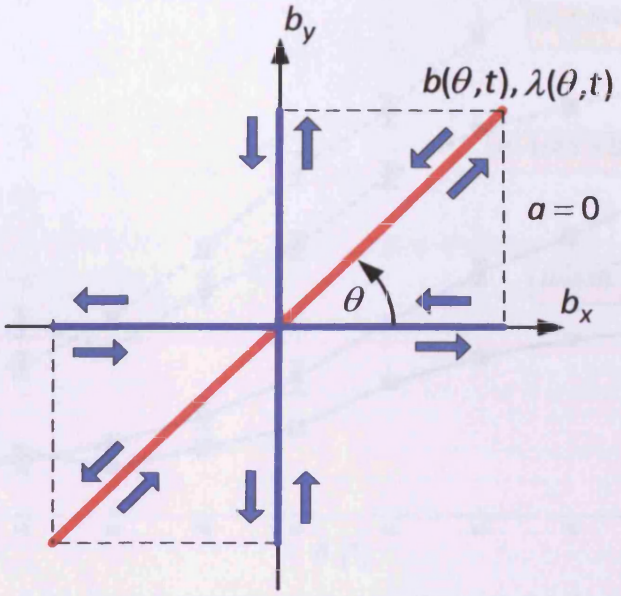

Fig. 8-27 Illustration of control of magnetisation in the 2D magnetisation system to create an AC magnetisation vector at angle θ to the x axis

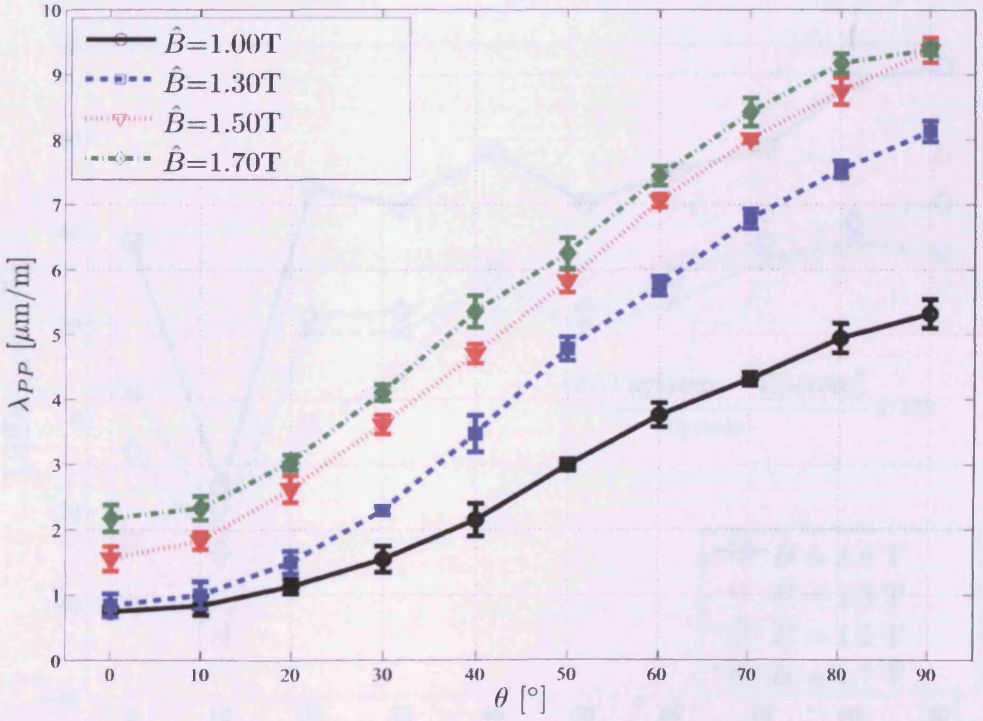

Fig. 8-28 Values of λ_{pp} in the disc sample of the 0.50 mm thick steel under sinusoidal magnetisation at various flux densities, 50 Hz versus the angle θ with respect to the RD

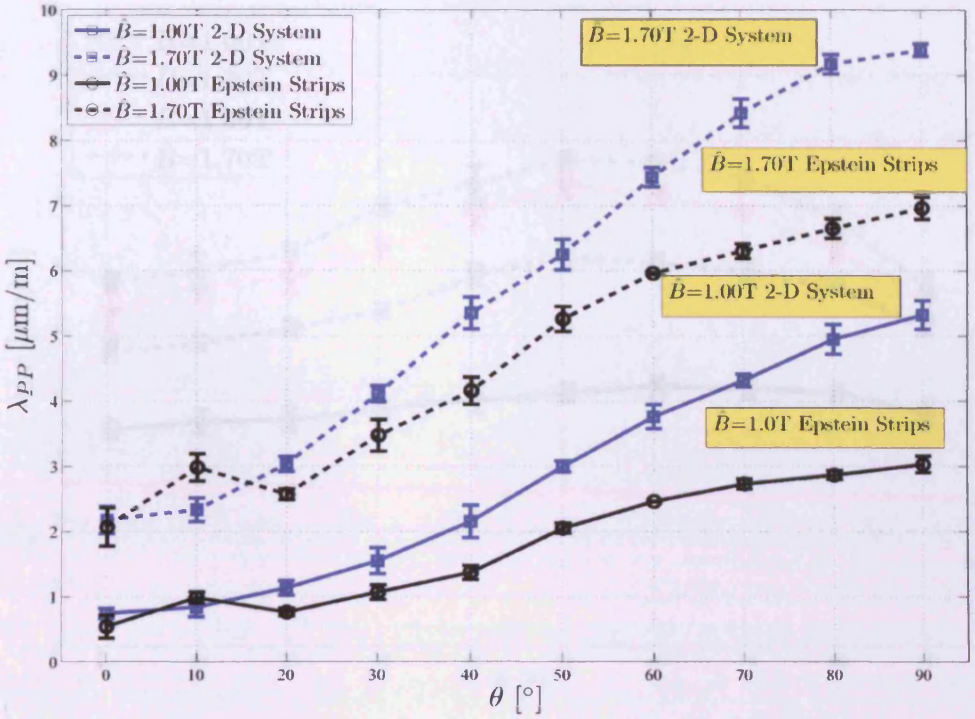

Fig. 8-29 Comparison of λ_{pp} in the Epstein strips and disc sample of the 0.50 mm thick steel measured under sinusoidal magnetisation at 1.00 T and 1.70 T, 50 Hz versus the angle θ with respect to the RD

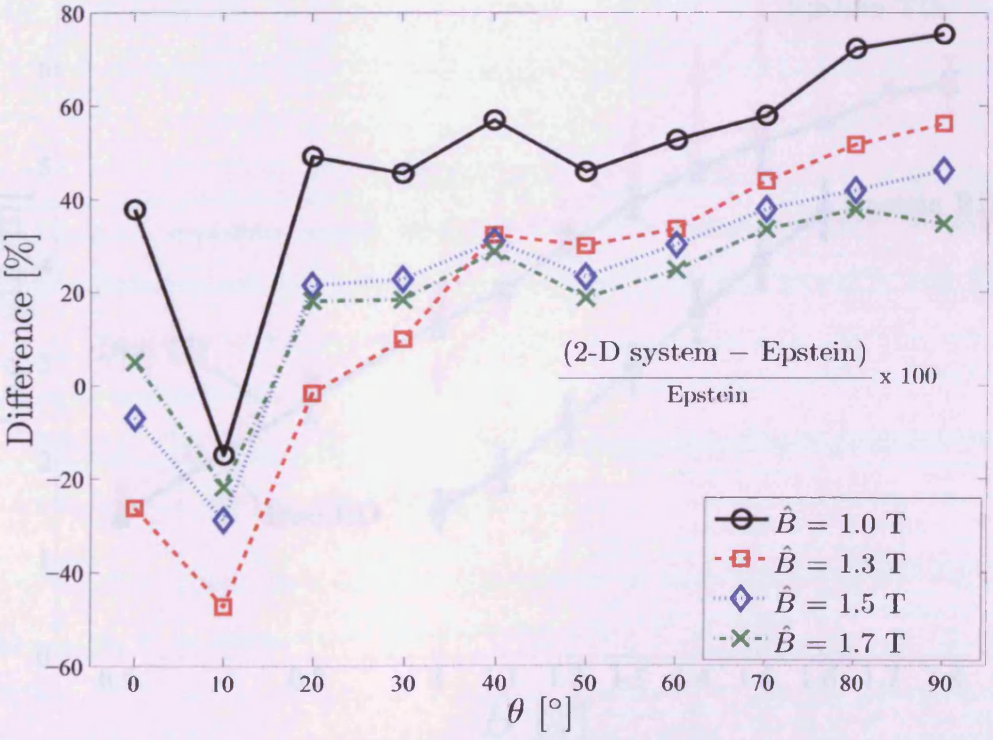

Fig. 8-30 Differences of λ_{pp} in the Epstein strips and disc sample of the 0.50 mm thick steel under sinusoidal magnetisation at various flux densities, 50 Hz versus the angle θ with respect to the RD

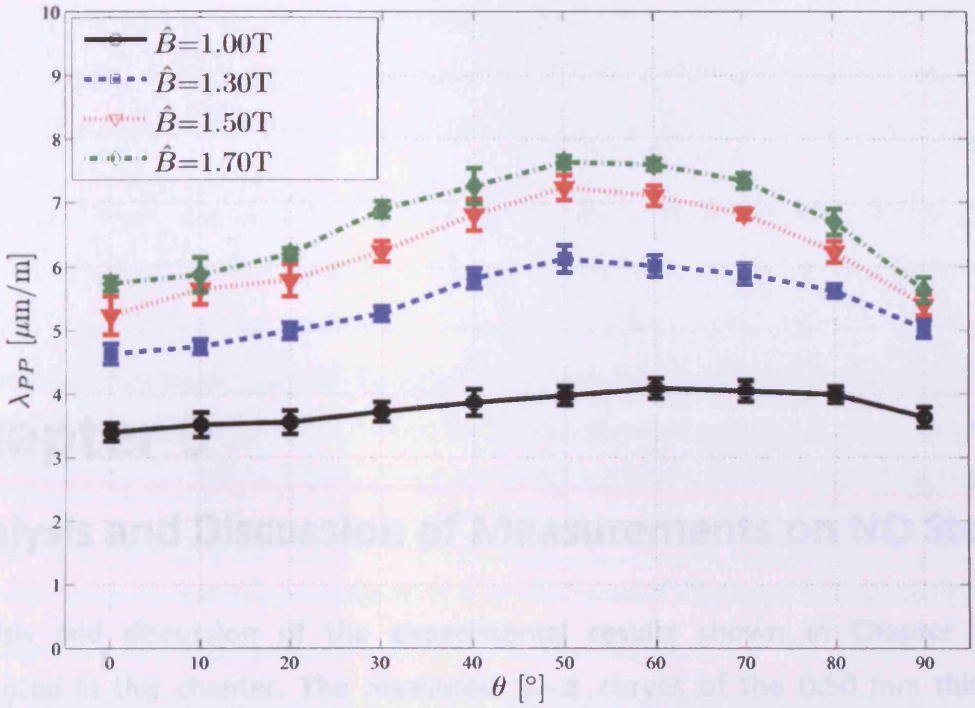

Fig. 8-31 Values of λ_{pp} in the disc sample of the 0.35 mm thick steel under sinusoidal magnetisation at various flux densities, 50 Hz versus the angle θ with respect to the RD

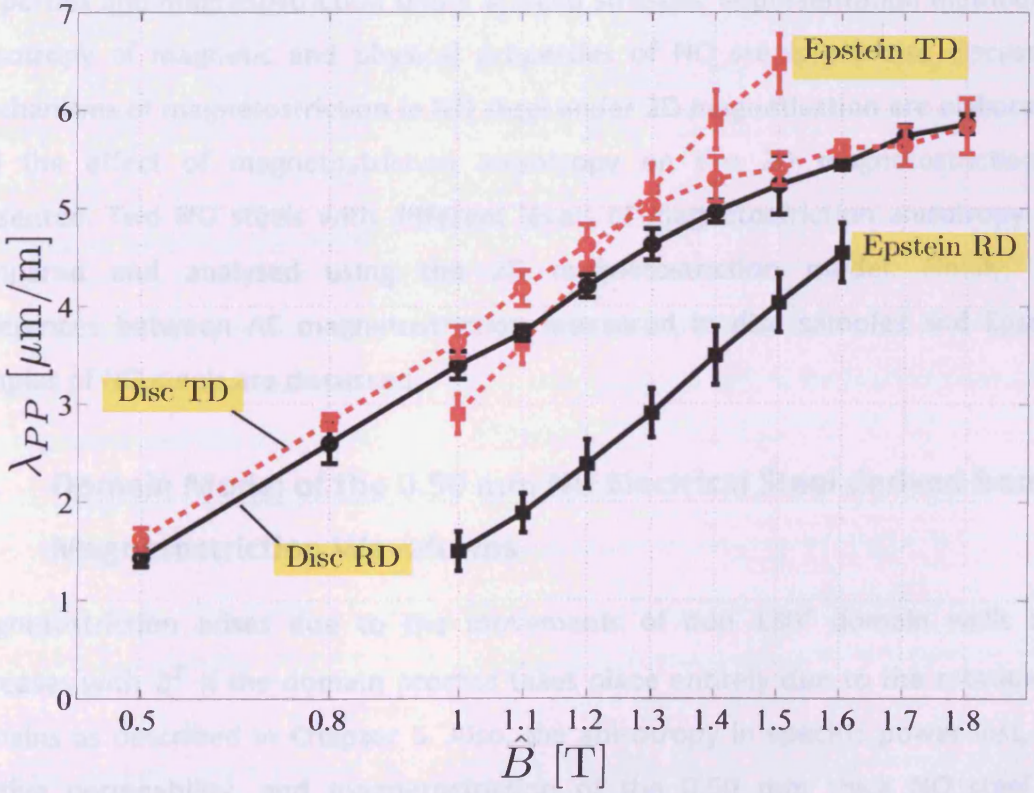

Fig. 8-32 Comparison of λ_{pp} in the Epstein strips cut along the RD and TD and in the disc sample of the 0.35 mm thick steel under sinusoidal magnetisation at 50 Hz as a function of peak flux densities

Chapter 9

Analysis and Discussion of Measurements on NO Steels

Analysis and discussion of the experimental results shown in **Chapter 8** are presented in this chapter. The measured $\lambda - b$ curves of the 0.50 mm thick NO electrical steel are analysed and compared with theories and previous works, leading to an estimation of a domain model for this material. The estimated domain model is then used in the analysis of anisotropies of magnetostriction and magnetic properties and magnetostriction under applied stresses. Representation methods of anisotropy of magnetic and physical properties of NO steels are also discussed. Mechanisms of magnetostriction in NO steel under 2D magnetisation are elaborated and the effect of magnetostriction anisotropy on the 2D magnetostriction is presented. Two NO steels with different levels of magnetostriction anisotropy are compared and analysed using the 2D magnetostriction model. Finally, the differences between AC magnetostriction measured in disc samples and Epstein samples of NO steels are discussed.

9.1 Domain Model of the 0.50 mm NO Electrical Steel derived from Magnetostriction Waveforms

Magnetostriction arises due to the movements of non 180° domain walls and increases with b^2 if the domain process takes place entirely due to the rotation of domains as described in **Chapter 5**. Also, the anisotropy in specific power loss, AC relative permeability, and magnetostriction of the 0.50 mm thick NO steel as displayed in Figs. 8-1, 8-3, and 8-5 are all associated with the domain structures. The $\lambda - b$ curves of the samples cut at different angles to the RD in Fig. 8-7 have

different characteristics due to different domain processes. Thus, an understanding of the domain activities can be obtained from the $\lambda - b$ curves, which eventually leads to development of a domain model.

Fig. 9-1 (a) shows the excursion of magnetostriction with flux density in the positive half of the magnetisation cycle of an Epstein sample of the 0.50 mm NO steel cut parallel to the RD shown in Fig. 8-7. The sample was magnetised under sinusoidal magnetisation at peak flux density of 1.70 T 50 Hz. The $\lambda - b$ curve is also compared with the $b - h$ curve measured in the SST under the same magnetisation conditions displayed in Fig. 9-1 (b). Starting at $b(t)$=0 T, the magnetostriction increases with the flux density linearly until a flux density around 1.2 T marked as region **A**. This induction range is below the knee of the $b - h$ curve. Chikazumi [*9.1*] describes that the linear relationship between the magnetostriction and the flux density is due to the 90° and 180° domain wall motion taking place simultaneously if a crystal of an iron is magnetised along the ⟨100⟩ axes. This also conforms with the bulk magnetostriction of electrical steels presented in [*9.2*]. At the knee of the $b - h$ curve (b=1.2 T) in region **B**, the annihilation of the 180° walls starts and the 90° domain walls rotate towards the magnetisation vector [*9.2*]. As a result, the magnetostriction increases rapidly with flux density. The magnetostriction finally reaches saturation in region **C** and the closest ⟨100⟩ axis is parallel to the magnetisation vector [*9.3*]. The saturation value of magnetostriction at this angle is expected to be 2.0 to 2.5 μm/m.

The domain processes in regions **A** to **C** are also inferred from the fact that the slope between b and h ($\mathrm{d}b/\mathrm{d}h$). $\mathrm{d}b/\mathrm{d}h$ is very high if there is 180° domain wall displacement and the suppression of 90° domain walls in region **A**. $\mathrm{d}b/\mathrm{d}h$ is lower if the 90° wall rotation takes place in regions **B** and **C**. When the flux density drops from its peak value of 1.7 T, the 90° domain walls re-emerge in region **D** [*9.3*] and starts to rotate back (region **E**) at a higher rate. The magnetostriction reaches zero when the flux density decreases to around 0.8 T and swings to a negative value around -0.2 μm/m before returning to the origin when b=0 T. The reformation of the 180° domain walls should occur in this process [*9.3*]. The fast return rate and oscillation of magnetostriction could be due to the anisotropic energy of the grains. This is analogous to a stiff spring which returns to its original position quickly and

oscillates before settling down. The quicker change of magnetostriction from saturation to zero magnetisation than that from zero to saturation magnetisation was also found in the study by Bohn et al [*9.3*] as shown in Fig. 9-2. Moreover, the flux density does not return on the same path on the $b-h$ curve due to the irreversible domain process [*9.4*]. Therefore, the hysteresis in the $\lambda-b$ curve is clearly linked to the hysteresis of the $b-h$ curve as described earlier in [*9.5*].

When the magnetisation direction in Fig. 8-7 deviates from the RD, region **A** where the magnetostriction is proportional to the magnetisation shrinks. On the other hand, region **B** where the magnetostriction is functional to b^2 is wider. This indicates that the domain rotation increases when the magnetisation direction is out of the RD. Domain rotation starts quicker at a lower induction level when the angle between the magnetisation direction to the RD is increasing as illustrated in Fig. 5-2 [*9.1*]. The 180° domain walls in the 0° samples become 90° domain walls for the 90° samples. The magnetostriction in the sample cut at 90° to the RD mostly changes with b^2 as shown in the region **B** in Fig. 9-1 (b). The $b-h$ curve as displayed in Fig. 9-1 (d) has also lower $\mathrm{d}b/\mathrm{d}h$ and requires a higher field to reach 1.7 T. The magnetisation process due to the displacement of 180° domain walls of this sample can be the region **A** in Fig. 9-1 (c) and (d), where the highest $\mathrm{d}b/\mathrm{d}h$ occurs before the $b-h$ curve starts to bend.

Schematic diagrams of the simplified domain model for different magnetisation regimes already explained are shown in Fig. 9-3. At b=0 T, the ratio between the volume fraction of the 90° and 180° domains is simply estimated based on the measurement results of the peak to peak values of magnetostriction, λ_{pp} measured in the samples cut at 0° and 90° to the RD as displayed in Fig. 8-5. It is assumed that the magnetostriction increases linearly with the angle between the magnetising direction and the RD. At $\hat{B}$=1.70 T, the average λ_{pp} of strips cut along the RD is around 2 μm/m, approximately 30 % of λ_{pp} measured in the samples cut along the TD. Therefore, the areas **C** and **D** are assumed to be 30 % of the area **A** and **B** at b=0 T in Fig. 9-3 (a) and Fig. 9-3 (b). To cover the regime **C** in Fig. 9-1 where the magnetostriction approaches saturation, the 180° domains must be slightly mis-oriented from the RD. The sketches of domains for the magnetisation regimes **A**, **B** and **C** in Fig. 9-1 are also illustrated. This estimated domain structure will be used to

explain the magnetostriction measurement under applied stress and under 2D magnetisation.

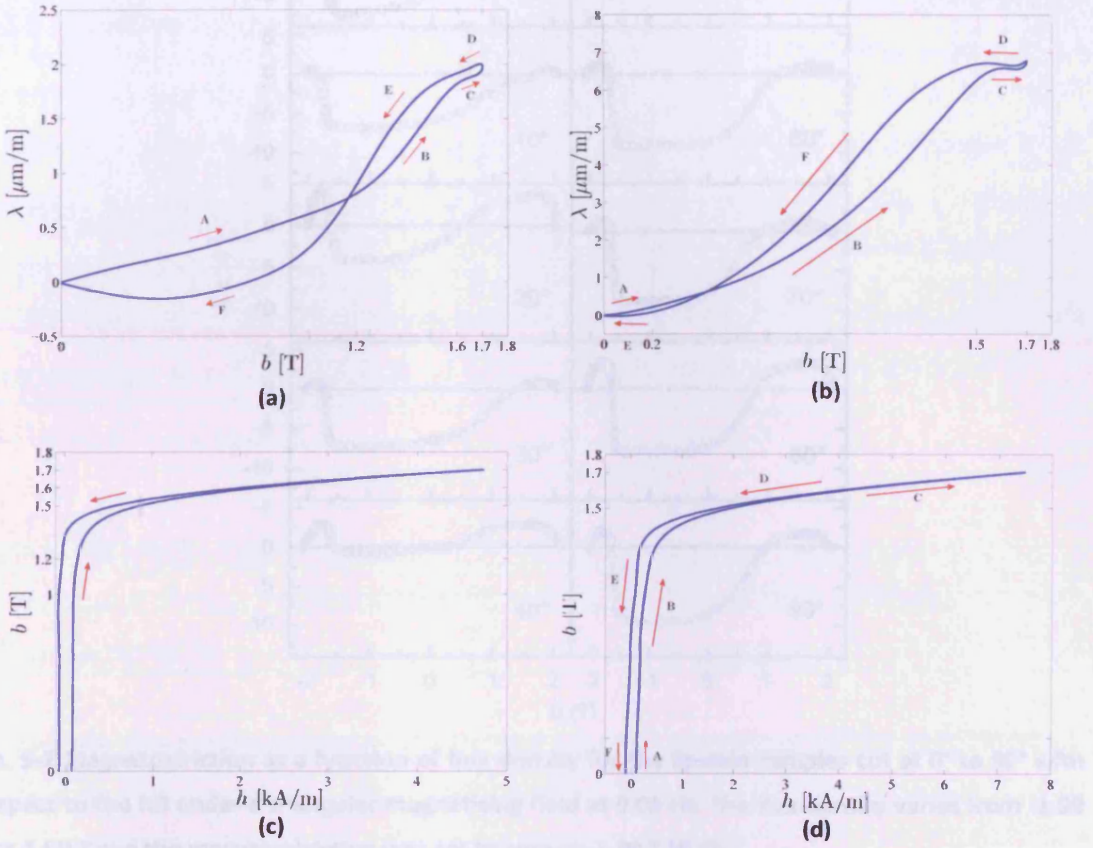

Fig. 9-1 $\lambda - b$ **curves of the 0.50 mm thick Epstein strips cut along: (a) the RD, (b) the TD,** $b - h$ **curves of the 0.50 mm thick Epstein samples cut along: (c) the RD, (d) the TD. All curves were obtained from the tests under sinusoidal magnetisation at peak flux density of 1.70 T, 50 Hz.**

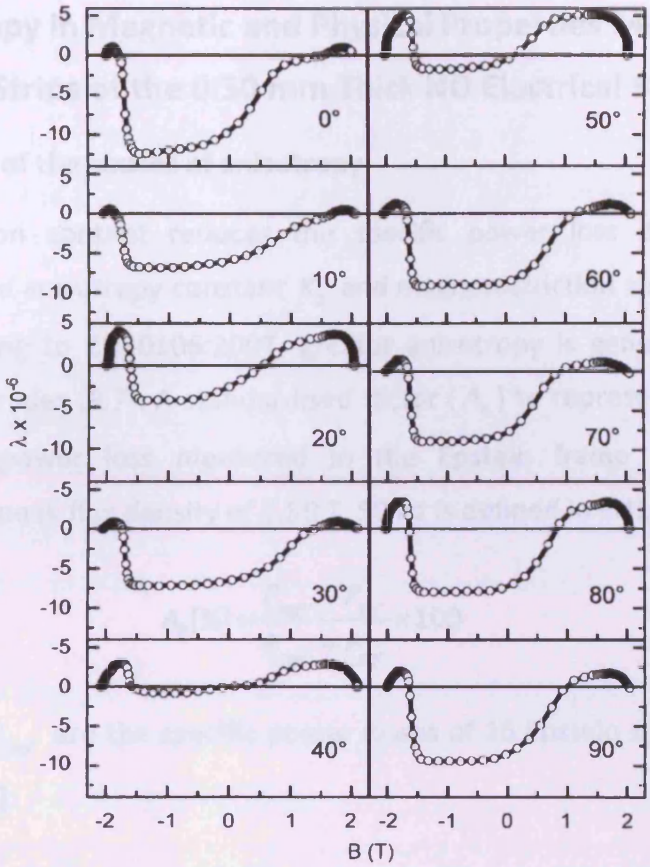

Fig. 9-2 Magnetostriction as a function of flux density for the Epstein samples cut at 0° to 90° with respect to the RD under a triangular magnetising field at 0.05 Hz. The flux density varies from -1.99 T to 1.99 T and the magnetostriction was set to zero at -1.99 T [*9.3*].

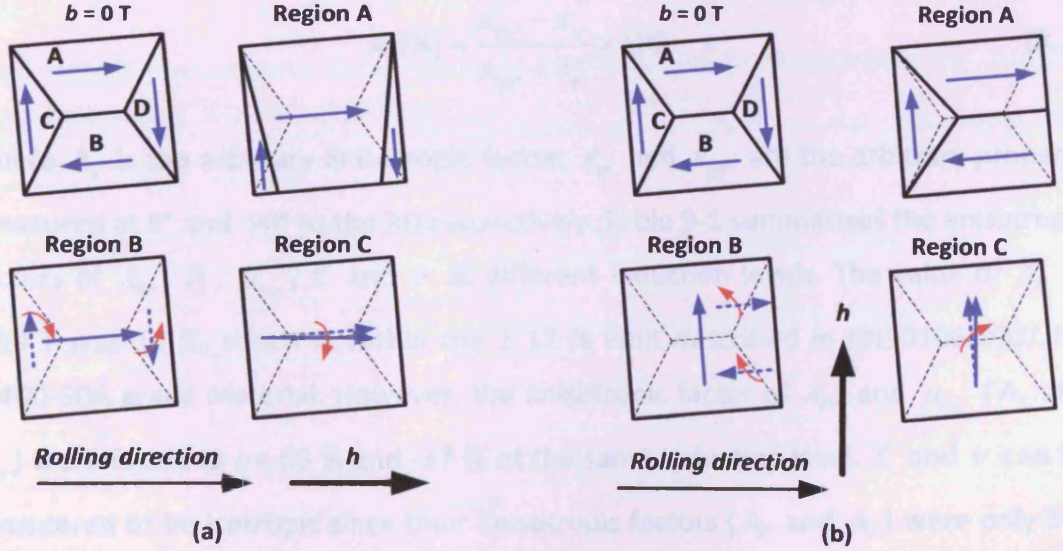

Fig. 9-3 Schematic diagram of the domain model of the 0.50 mm NO steel in different regions of magnetisation (referred to Fig. 9-1): (a) magnetised along the RD, (b) magnetised perpendicular to the RD.

9.2 Anisotropy in Magnetic and Physical Properties Measured in Epstein Strips of the 0.50 mm Thick NO Electrical Steel

9.2.1 Analysis of the causes of anisotropy

Increase in silicon content reduces the specific power loss due to increased resistivity, and the anisotropy constant K_1 and magnetostriction also decrease [*9.6*]. However according to EN10106:2007, greater anisotropy is generally expected in better material grades [*9.7*]. A standardised factor (A_P) to represent the anisotropy in the specific power loss measured in the Epstein frame under sinusoidal magnetisation at peak flux density of 1.50 T, 50 Hz is defined in EN10106:2007 as

$$A_P[\%] = \frac{P_{S90^\circ} - P_{S0^\circ}}{P_{S90^\circ} + P_{S0^\circ}} \times 100 \tag{9.1}$$

where P_{S0° and P_{S90° are the specific power losses of 16 Epstein strips cut at 0° and 90° to the RD [*9.7*].

To analyse the anisotropy in magnetic and physical properties of the test material, the standardised anisotropic factor of the specific power loss in (9.1) is adapted to define the other properties at different magnetisation levels as

$$A_x[\%] = \frac{x_{90^\circ} - x_{0^\circ}}{x_{90^\circ} + x_{0^\circ}} \times 100 \tag{9.2}$$

where A_x is the arbitrary anisotropic factor, x_{0° and x_{90° are the arbitrary property measured at 0° and 90° to the RD respectively. Table 9-1 summarises the anisotropic factors of λ_{PP}, P_S, $\mu_{r_{AC}}$, E and ν at different induction levels. The value of A_P at 1.50 T was 12 %, which is within the ± 12 % limit described in EN10106:2007 for M400-50A grade material. However, the anisotropic factor of λ_{PP} and $\mu_{r_{AC}}$ (A_λ and A_μ) were found to be 60 % and -37 % at the same induction level. E and ν can be considered to be isotropic since their anisotropic factors (A_E and A_ν) were only 3 % and 2 % respectively.

Table 9-1 shows that A_λ, A_P and A_μ are magnetisation dependent. As expected A_λ and A_P decrease as the induction increases, but the change in A_λ with flux density is

comparatively large compared to the change in A_P. This phenomenon can be explained using the simplified domain model in Fig. 9-3. At peak flux density below 1.20 T, the domain activities in the sample cut at 0° to the RD are the movement of the 180° domain walls and the suppression of the 90° domain walls causing the linear change of magnetostriction to the flux density. For the samples cut along the TD, the 90° domains must be rotated in order to achieve the same net magnetisation as in the 0° samples resulting in magnetostriction changes with b^2 and higher specific power loss. As a result, the differences of λ_{pp} and P_s measured along the RD and TD are high. At higher induction, the magnetisation of the samples cut at 0° and 90° to the RD is predominately caused by domain rotation. Hence, the anisotropic factors of λ_{pp} and P_s are lower than those at lower induction.

Table 9-1 Anisotropic factor of peak to peak magnetostriction (A_λ), specific power loss (A_P), AC relative permeability (A_μ) under sinusoidal magnetisation at 50 Hz, and Young's modulus (A_E) and Poisson's ratio (A_ν) of the 0.50 mm thick NO steel

$\hat{B}$ [T]	A_λ [%]	A_P [%]	A_μ [%]	A_E [%]	A_ν [%]
0.50	-	21	-40	3	2
1.00	70	17	-50	3	2
1.30	64	14	-43	3	2
1.50	59	12	-37	3	2
1.70	54	9	-21	3	2

A_P is found to be lower than A_λ and A_μ partly due to the presence of the classical eddy current loss (P_{clas}) which is independence of domain structures of the steel. The loss separation method is used to explain the effect of the classical eddy current loss on the loss anisotropy. According to Bertotti [*9.8*], specific power loss of soft magnetic material can be approximated as a function of peak flux density $\hat{B}$ and magnetising frequency f_m as

$$P_s \approx C_0 \hat{B}^2 f_m + \frac{\pi^2 d^2}{6\rho_m \rho}\left(\hat{B}^2 f_m^2\right) + C_1 (\hat{B} f_m)^{3/2} \tag{9.3}$$

where C_0 and C_1 are the characterised constants of the test material.

The first term in (9.3) is the static hysteresis loss caused by domain wall pinning, residual stress, crystal imperfections, etc. [*9.4*]. The second is the classical eddy

current loss calculated from Maxwell's equations for a perfectly homogeneous material with no domain structure and a linear $b-h$ characteristic. The excess loss, previously called anomalous loss, is the third component in (9.3) and it is assumed to be caused by an excess hysteresis resulting from domain wall motion. The hysteresis and excess loss are dependence of the domain structures, whereas the classical eddy current loss depends on physical properties of the material (thickness, density and resistivity). Resistivity is assumed to be isotropic, and the resistivity in the direction perpendicular to the magnetisation causing the classical eddy current loss does not change with the magnetisation [*9.9*]. Therefore, the classical eddy current loss in the 0° and 90° cut samples are assumed to be identical and their total specific power loss measured along the RD and TD (P_{S0° and P_{S90°) are now expressed as

$$P_{S0^\circ} = P_{DS0^\circ} + P_{clas} \tag{9.4}$$

$$P_{S90^\circ} = P_{DS90^\circ} + P_{clas} \tag{9.5}$$

where P_{DS0° and P_{DS90° are the power loss due to the presence of domain structure consisting of the hysteresis and excess losses in the samples cut along the RD and TD respectively. Substituting (9.4) and (9.5) into (9.1), A_p as a function of the classical eddy current los can be obtained as

$$A_p[\%] = \frac{P_{DS90^\circ} - P_{DS0^\circ}}{P_{DS90^\circ} + P_{DS0^\circ} + \dfrac{\pi^2 d^2}{3\rho_m \rho}\left(\hat{B}^2 f_m^2\right)} \times 100. \tag{9.6}$$

It can be observed from (9.6) that A_p drops at higher induction partly because of the classical eddy current loss. If the classical eddy current loss were removed from the total loss, the anisotropy of the hysteresis and excess loss would be higher than the total loss as compared in Fig. 9-4. For thin gauge materials with high resistivity due to high silicon contents, A_p is expected to be greater than in the lower material grades [*9.7*].

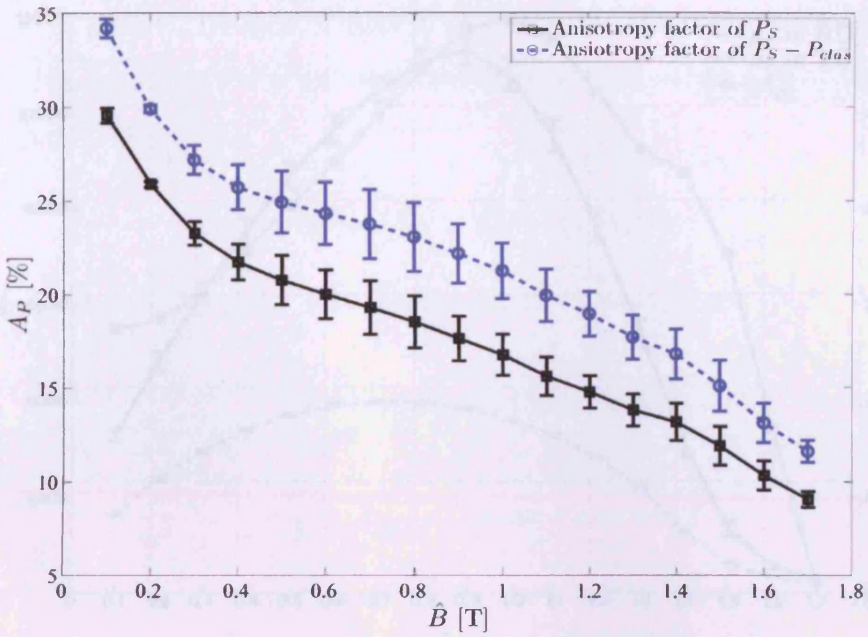

Fig. 9-4 Anisotropic factor of specific power loss of 0.50 mm thick NO steel as a function of peak flux density compared with the anisotropic factor of the specific power loss after the classical eddy current loss is removed. Resistivity of 4.58×10^{-7} Ω·m and density of 7.70 kg/dm^3 shown in Table 7-1 were used to calculate the classical eddy current loss.

A_μ is always negative since the AC relative permeability in the transverse direction is always less than that in the RD. The curve of $|A_\mu|$ as shown in Fig. 9-5 is not monotonous as those of A_P and A_λ due to the intrinsic characteristic of permeability of ferromagnetic materials. The permeability generally increases until the maximum value is reached and then begins to drop at the knee of the $b-h$ curve, where rotation of domain walls starts [*9.1*]. As seen in Fig. 9-5, the AC relative permeability of the samples cut along the TD reaches its peak at lower flux density than that in samples cut along the RD due to lower volume fraction of 180° domains, making the 90° domains rotate. Consequently, the difference in the AC relative permeability of these two sample sets is high resulting in higher $|A_\mu|$. Once the 90° domains of the 0° cut samples begin to rotate, $|A_\mu|$ drops significantly to about 21 % at 1.70 T.

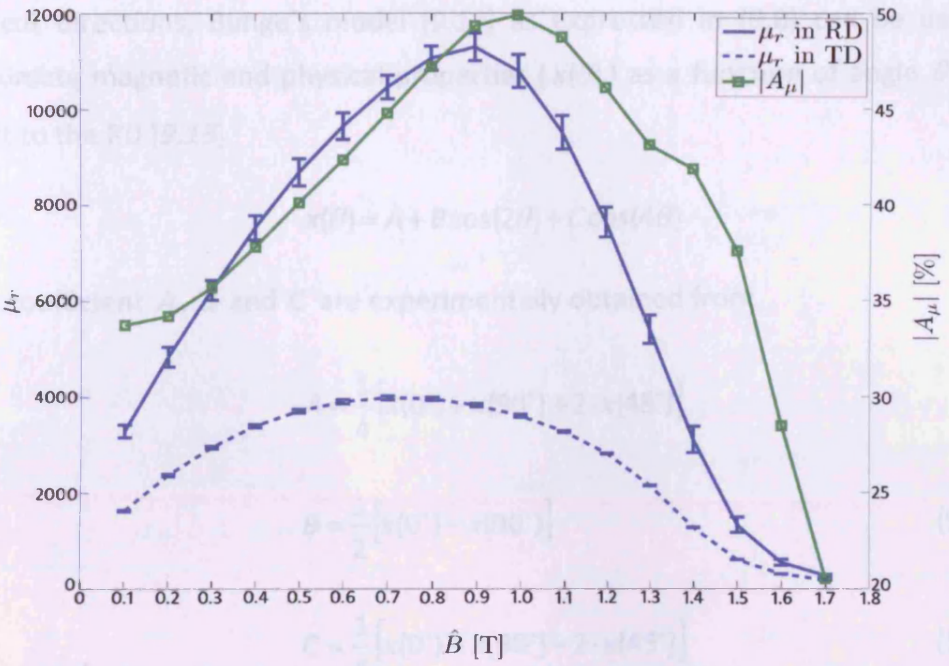

Fig. 9-5 AC relative permeability when magnetised along the RD and TD, and absolute value of anisotropic factor of relative permeability at the magnetisation frequency of 50 Hz

9.2.2 Representation of the anisotropy

The anisotropy factor expressed in (9.2) can precisely represent the anisotropy of electrical steels if the two extreme values of any properties occur along the RD and TD. However, the correct information cannot be obtained if one of the extreme values lies between the RD and TD, for example the NO steel with strong Goss texture in [*9.10*]. To obtain accurate anisotropic properties, a number of samples cut at different angles to the RD were tested and the anisotropic factor defined as

$$A_x[\%] = \frac{X_{MAX} - X_{MIN}}{X_{MAX} + X_{MIN}} \times 100 \qquad (9.7)$$

where X_{MAX} and X_{MIN} are the maximum and minimum value of arbitrary properties.

The newly defined anisotropic factor in (9.7) of Young's modulus and Poisson's ratio were found to be 4 % and 14% respectively. It is clear that the anisotropic factor in (9.7) gives better anisotropic information. However, it is not practical on an industrial scale, so Hribernik and Ambrož [*9.11*] proposed a three-point control method by cutting Epstein strips at 0°, 45° and 90° to the RD. This proposal was based on an observation that the hardest magnetising axis occurs between 45 ° and 55° to the RD for material showing some Goss texture. Combining with the measured values from

three cut directions, Bunge's model [*9.12*] as expressed in (9.8) can be used to approximate magnetic and physical properties ($x(\theta)$) as a function of angle θ with respect to the RD [*9.13*].

$$x(\theta) = A + B\cos(2\theta) + C\cos(4\theta) \tag{9.8}$$

where coefficient A, B and C are experimentally obtained from

$$A = \frac{1}{4}\left[x(0°) + x(90°) + 2 \cdot x(45°)\right] \tag{9.9}$$

$$B = \frac{1}{2}\left[x(0°) - x(90°)\right] \tag{9.10}$$

$$C = \frac{1}{4}\left[x(0°) + x(90°) - 2 \cdot x(45°)\right] \tag{9.11}$$

where $x(0°)$, $x(45°)$ and $x(90°)$ are the measured properties at 0°, 45° and 90° to the RD.

Fig. 9-6 compares the measured and fitted values using Bunge's model of λ_{pp}, P_S, $\mu_{r_{AC}}$ of the 0.50 mm thick steel under sinusoidal magnetisation at 1.50 T 50 Hz, and E and ν. The values of these properties at 45° were not measured but estimated by averaging those at 40° and 50° to the RD. The relative difference ($\Delta x(\theta)$) between the measured $x(\theta)$ and fitted $x_{Bunge}(\theta)$ values at each angle is defined as

$$\Delta x(\theta) = \frac{x(\theta) - x_{Bunge}(\theta)}{x(\theta)} \times 100\,. \tag{9.12}$$

The relative differences between the measured and fitted values of λ_{pp}, P_S, $\mu_{r_{AC}}$, E and ν at different θ shown in Fig. 9-6 are listed in Table 9-2. The estimated values of λ_{pp}, P_S, $\mu_{r_{AC}}$ and E agree with the measured values and the relative errors are within ± 10 %, except for λ_{pp} at 10° to the RD. This could be due to some effects of texture to which magnetostriction is sensitive. The measured values of Poisson's ratio agree with the estimated values and the maximum error is found to be 14 %. Hence, Bunge's model represents the anisotropy in magnetic and physical properties of the NO steel quite well if the variation of the measured values with the angle to

the RD is smooth. Therefore, the three-point control method combined with Bunge's model has a potential to represent the anisotropy of commercial NO electrical steels.

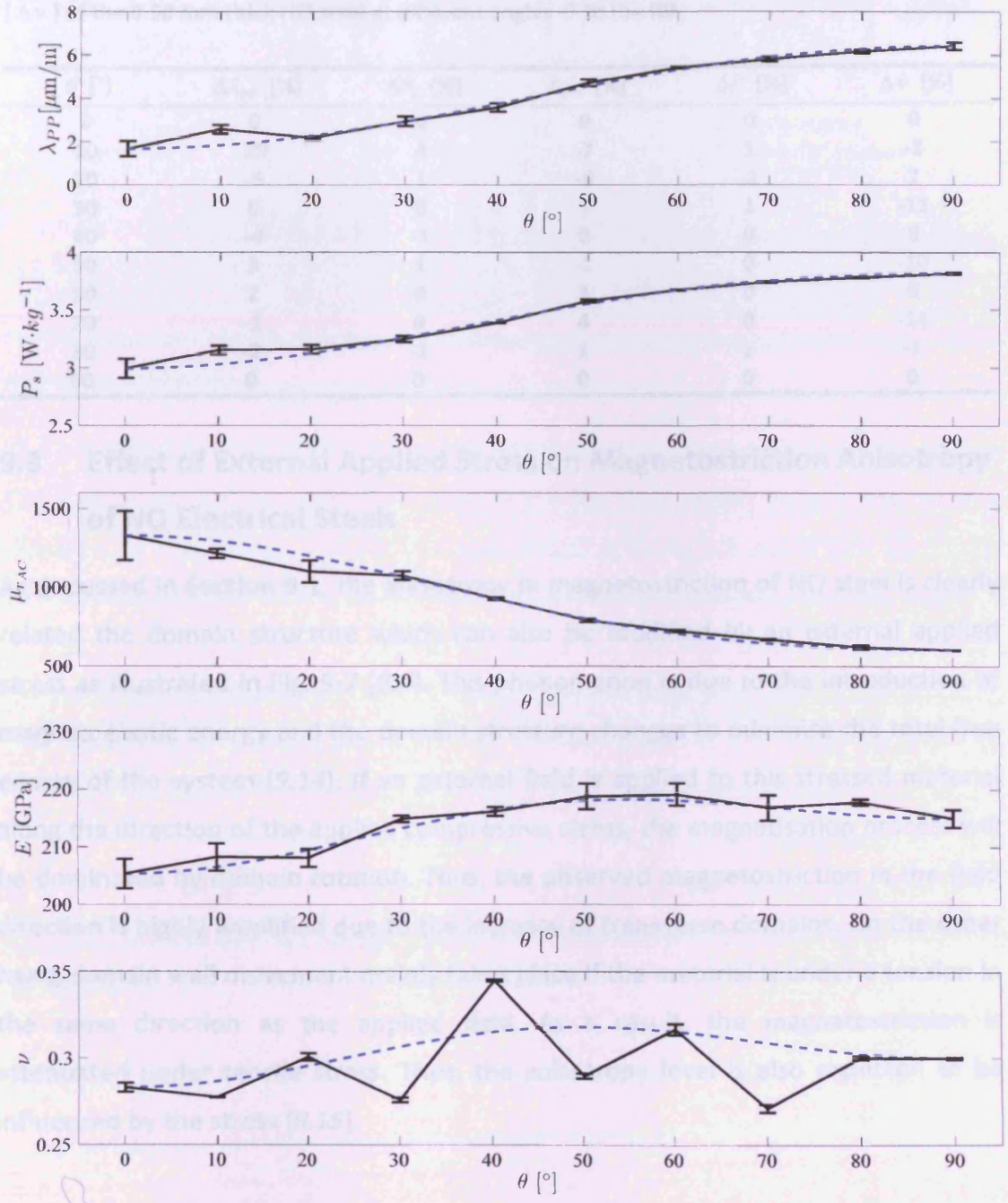

Fig. 9-6 Measured (solid lines with error bars) and estimated (dashed lines) values using Bunge's model of λ_{PP}, P_S, $\mu_{r_{AC}}$ under sinusoidal magnetisation at 1.50 T, 50 Hz, and E and ν of the steel as a function of the angle θ to the RD change

Table 9-2 Relative differences between the measured and estimated values using Bung's model of peak to peak magnetostriction ($\Delta\lambda_{pp}$), specific power loss (ΔP_S), AC relative permeability ($\Delta\mu_r$) under sinusoidal magnetisation at 1.50 T, 50 Hz, and Young's modulus (ΔE) and Poisson's ratio ($\Delta\nu$) of the 0.50 mm thick NO steel at different angles θ to the RD

θ [°]	$\Delta\lambda_{pp}$ [%]	ΔP_S [%]	$\Delta\mu_r$ [%]	ΔE [%]	$\Delta\nu$ [%]
0	0	0	0	0	0
10	29	4	-7	1	-3
20	-5	1	-9	-1	2
30	0	0	1	1	-11
40	-4	-1	0	0	9
50	3	1	-1	0	-10
60	2	0	3	0	0
70	-2	0	4	0	-14
80	-2	-1	1	1	-1
90	0	0	0	0	0

9.3 Effect of External Applied Stress on Magnetostriction Anisotropy of NO Electrical Steels

As discussed in **Section 9.1**, the anisotropy in magnetostriction of NO steel is clearly related the domain structure which can also be modified by an external applied stress as illustrated in Fig. 9-7 [*9.4*]. This phenomenon is due to the introduction of magnetoelastic energy and the domain structure changes to minimise the total free energy of the system [*9.14*]. If an external field is applied to this stressed material along the direction of the applied compressive stress, the magnetisation process will be dominated by domain rotation. Thus, the observed magnetostriction in the field direction is highly amplified due to the increase of transverse domains. On the other hand, domain wall movement mainly takes place if the material is under a tension in the same direction as the applied field. As a result, the magnetostriction is attenuated under tensile stress. Thus, the anisotropy level is also expected to be influenced by the stress [*9.15*].

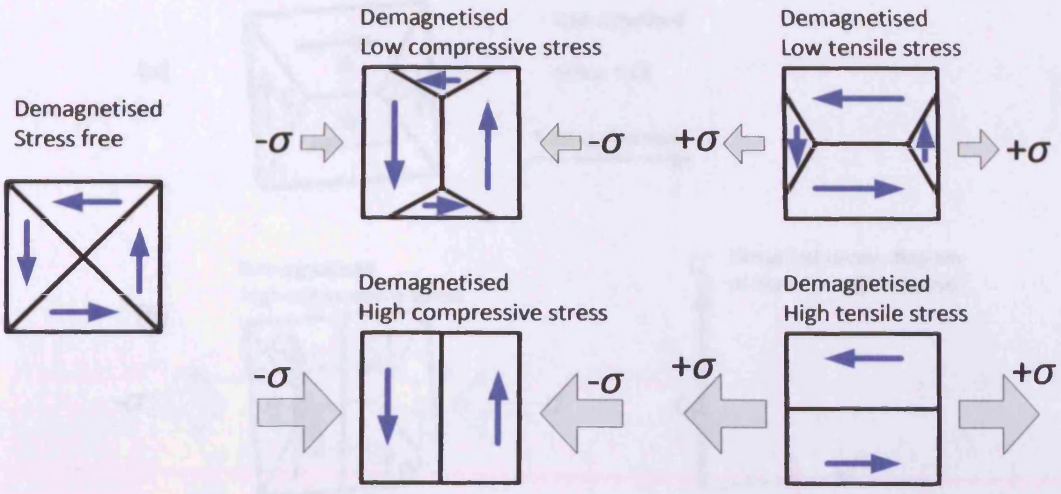

Fig. 9-7 Schematic diagrams of demagnetised domain structure stress free and under applied tensile and compressive stress

The simplified domain model estimated based on the $\lambda - b$ curves in **Section 9.1** at the unstressed and demagnetised state of the NO steel mainly used in this study is displayed in Fig. 9-8 (a). The domain magnetisation vectors **A** and **B** that align close to the RD are comparatively larger than the domain magnetisation vector **C** and **D**. If a large compressive stress is applied along the RD, the new domain magnetisation vector **C'** will be formulated from the close domain magnetisation vectors **A**, **C** and the vectors **B**, **D** creating the vector **D'** perpendicular to the stress direction as illustrated by the schematic diagram in Fig. 9-8 (b). The schematic diagram in Fig. 9-8 (c) shows the new domain magnetisation vectors **A'** and **B'** emerging from **A, C** and **B, D** due to a large tension applied along the RD. Simplified vector diagrams of the domain magnetisation for stress applied at 30°, 60° and 90° to the RD are also shown in Fig. 9-9.

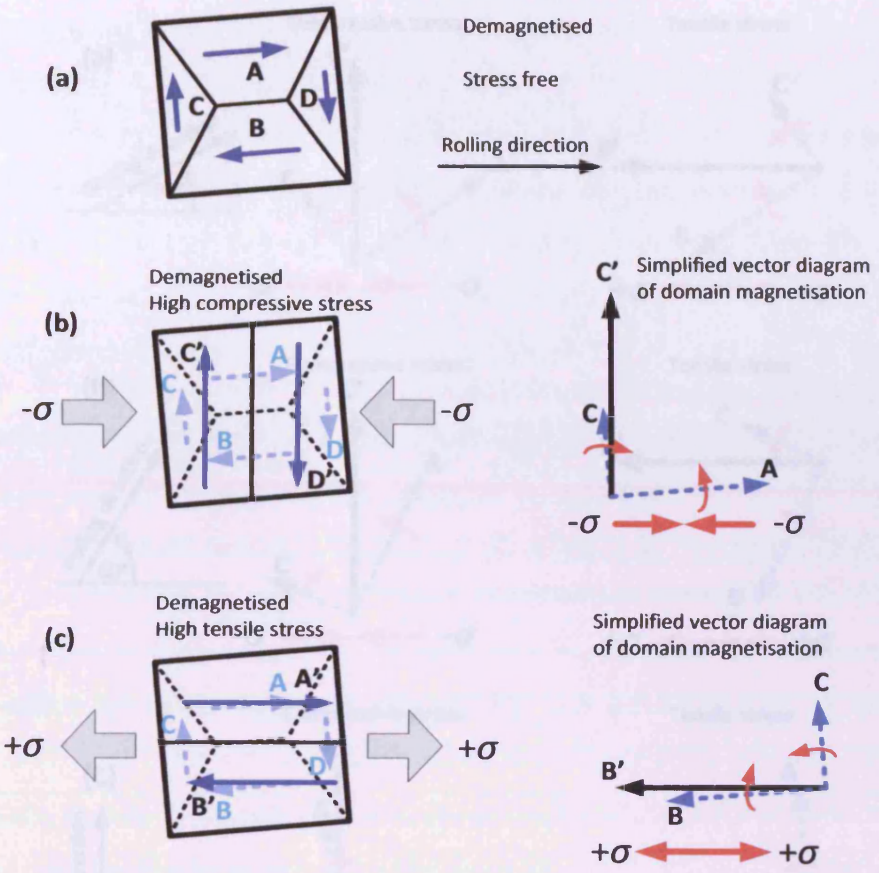

Fig. 9-8 Schematic diagrams of simplified domain structure of the 0.50 mm thick NO steel: (a) in demagnetised state, stress free, (b) with applied large compressive stress along the RD and (c) with applied large tensile stress along the RD

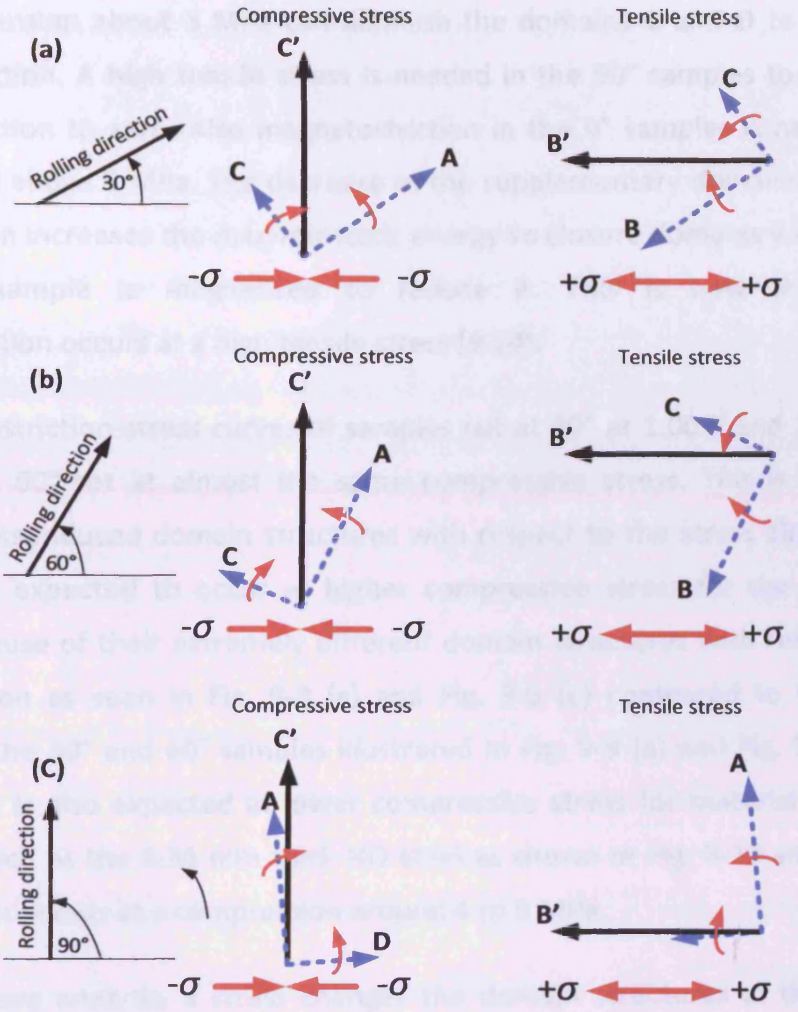

Fig. 9-9 Schematic diagrams of the magnetisation vector change in the 0.50 mm thick NO steel with applied compressive and tensile stress along at: (a) 30°, (b) 60° and (c) 90° with respect to the RD

As expected, magnetostriction in the samples cut at 0° to the RD is much more affected by the compressive stress than in the samples cut at 90° as shown in Fig. 8-8 and Fig 8-9. This is because the large domains **A** and **B** are moved to be perpendicular to the compression for the 0° samples, creating higher magnetostriction when the field is applied. For the 90° samples, the domain magnetisation vectors **A** and **B** are already close to 90° to the magnetisation and stress direction as shown in Fig. 9-9 (c) and the compression slightly changes the domain structure. This can be observed in Fig. 8-8 where the magnetostriction in the samples cut at 90° is virtually unchanged by the compressive stress at 1.00 T.

It is expected that the magnetostriction in the 0° samples will reach zero at a lower applied tensile stress than the samples cut at other angles to the RD because the smaller domain vectors **C** and **D** disappear easily. It can be seen in Fig. 8-8 and Fig. 8-

9 that the tension about 5 MPa can diminish the domains **C** and **D** to cause zero magnetostriction. A high tensile stress is needed in the 90° samples to reduce the magnetostriction to zero. Also magnetostriction in the 0° samples is negative at a tensile stress above 5 MPa. The decrease of the supplementary domains **C** and **D** at higher tension increases the magnetostatic energy so closure domains will re-appear when the sample is magnetised to reduce it. This is how the negative magnetostriction occurs at a high tensile stress [*9.14*].

The magnetostriction-stress curves of samples cut at 30° at 1.00 T and 1.50 T cross those of the 60° set at almost the same compressive stress. This is due to the identical stress-induced domain structures with respect to the stress direction. This cross over is expected to occur at higher compressive stress for the 0° and 90° samples because of their extremely different domain structures with respect to the stress direction as seen in Fig. 9-8 (c) and Fig. 9-9 (c) compared to the domain structure of the 30° and 60° samples illustrated in Fig. 9-9 (a) and Fig. 9-9 (b). This phenomenon is also expected at lower compressive stress for material with lower anisotropy such as the 0.35 mm thick NO steel as shown in Fig. 8-10 and Fig. 8-11. The cross over occurs at a compression around 4 to 5 MPa.

From the above analysis, a stress changes the domain structures of the material, which subsequently affects the level of anisotropy. For example, if a tension is applied along the TD of the 0.50 mm NO steel until the large domains **A** and **B** decrease to balance with the small domains **C** and **D**, the anisotropy is expected to decrease. On the other hand, the anisotropy can also be decreased if a compressive stress is applied along the RD. The change in magnetostriction anisotropy can be observed in samples cut at 0° under compressive stress and in samples cut at 90° under tension in Fig. 8-8 and Fig. 8-9. Although NO steels used in AC machine stator cores are subjected to very complex stresses such as static compressive stress due to the frame housing [*9.16*] and dynamic tensile stress due to Maxwell force in the air gap [*9.17*], this analysis is fundamental to understand magnetostriction under complex stress conditions.

9.4 Magnetostriction of NO Steels under 2D Magnetisation

9.4.1 Analysis of 2D magnetostriction using a simple domain model

Magnetostriction of the 0.50 mm and 0.35 mm thick steels under circular magnetisation are found to be higher than under alternating magnetisation measured either in the Epstein strips or disc samples. These results agree with previous works in [*9.18-9.20*]. However, no clear conclusion has been drawn. The schematic of the simple domain structure shown in Fig. 9-10 is used to describe the mechanism of the 2D magnetostriction. This diagram simplifies the domain structure of the ideal isotropic NO steel having identical magnetostriction in any magnetising direction. The RD and TD of this material are designated as x and y axes. Starting at the demagnetised state, magnetostriction λ_x and λ_y are set to be zero. Magnetising this material to saturation in the RD causes $\lambda_x = \lambda_s$ and, $\lambda_y = -\lambda_s/2$ based on the assumption that the transverse magnetostriction is half of the longitudinal component. On the other hand, $\lambda_x = -\lambda_s/2$ and $\lambda_y = \lambda_s$ when magnetising the material to saturation along the TD. The maximum and minimum values of λ_x and λ_y are found to be $\lambda_{x_{MAX}} = \lambda_{y_{MAX}} = \lambda_s$ and $\lambda_{x_{MIN}} = \lambda_{y_{MIN}} = -\lambda_s/2$ respectively. Thus, the maximum values of $\lambda_{x_{PP}}$ and $\lambda_{y_{PP}}$ ($\lambda_{x_{PPMAX}}$ and $\lambda_{y_{PPMAX}}$) are calculated from the difference between their maximum and minimum values as

$$\lambda_{x_{PPMAX}} = \lambda_{x_{MAX}} - \lambda_{x_{MIN}} = 3\lambda_s/2 \tag{9.13}$$

$$\lambda_{y_{PPMAX}} = \lambda_{y_{MAX}} - \lambda_{y_{MIN}} = 3\lambda_s/2\,. \tag{9.14}$$

The values of $\lambda_{x_{PPMAX}}$ and $\lambda_{y_{PPMAX}}$ agree closely with the magnetostriction theory described in (5.7) if only domain rotation takes place.

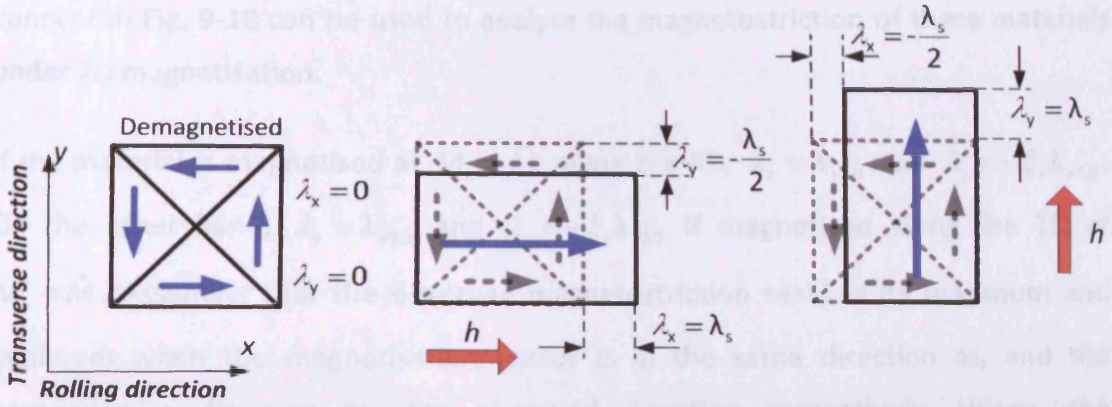

Fig. 9-10 Schematic diagrams of domain structure of an ideal, demagnetised, isotropic NO steel. The material is saturated along the RD and TD.

It can be seen in Fig. 9-10 that the negative magnetostriction is caused by the magnetisation in the TD. If the magnetostriction is assumed to vary with the square of the magnetisation and hysteresis is absent in the $\lambda - b$ curve, λ_x and λ_y can be estimated as

$$\lambda_x = \lambda_s \left(\frac{M_x}{M_s}\right)^2 - \frac{1}{2}\lambda_s \left(\frac{M_y}{M_s}\right)^2 \tag{9.14}$$

$$\lambda_y = \lambda_s \left(\frac{M_y}{M_s}\right)^2 - \frac{1}{2}\lambda_s \left(\frac{M_x}{M_s}\right)^2 \tag{9.15}$$

where M_x and M_y are the magnetisation in the RD and TD respectively.

Based on the simplified expressions in (9.14) and (9.15), the trajectories of λ_x and λ_y can be plotted according to the trajectory of magnetisation starting from the demagnetised state as illustrated in Fig. 9-11. It can be seen that the $\lambda_x - M_x$ curve is in the same position as the $\lambda_y - M_y$ curve for the ideal isotropic material if the initial trajectory **A** is neglected. The peak to peak, maximum and minimum values of both λ_x and λ_y are proved to be the same, which are $3\lambda_s/2$, λ_s, and $-\lambda_s/2$ respectively. This analysis can be applied for 2D magnetostriction at lower magnetisation levels by replacing λ_s with λ_{1D}, where λ_{1D} is the magnetostriction under one-dimensional magnetisation at a given induction level if the material is isotropic and the transverse magnetostriction is always half of the longitudinal value. However, magnetostriction of the 0.50 mm thick NO steel is found to be anisotropic as seen in **Section 8.2**. The

concept in Fig. 9-10 can be used to analyse the magnetostriction of these materials under 2D magnetisation.

If the material is magnetised at $M_x = \hat{M}$ along the RD, $\lambda_x = \lambda_{x1D}$ and $\lambda_y = -\xi_y \lambda_{x1D}$. On the other hand, $\lambda_y = \lambda_{y1D}$ and $\lambda_x = -\xi_x \lambda_{y1D}$ if magnetised along the TD at $M_y = \hat{M}$. Assuming that the observed magnetostriction reaches its maximum and minimum when the magnetisation vector is in the same direction as, and the perpendicular direction to, the observed direction respectively. Hence, the trajectories of λ_x and λ_y corresponding to the magnetisation vector starting from the demagnetised state and rotating anticlockwise are shown in Fig. 9-12. In the regime **A1** in Fig. 9-12, it is assumed that the movement of 180° domain walls and the suppression of the 90° domain walls causes λ_x to increase linearly with M_x as described in **Section 9-1**. The magnetisation along the RD causes the maximum in λ_x and minimum in λ_y. The maximum λ_y and minimum λ_x occur when the magnetisation is along the TD. The peak to peak values of magnetostriction $\lambda_{x_{PP}}$ and $\lambda_{y_{PP}}$ for this case are

$$\lambda_{x_{PP}} = \lambda_{x_{MAX}} - \lambda_{x_{MIN}} = \lambda_{x1D} + \xi_x \lambda_{y1D} \tag{9.16}$$

$$\lambda_{y_{PP}} = \lambda_{y_{MAX}} - \lambda_{y_{MIN}} = \lambda_{y1D} + \xi_y \lambda_{x1D}. \tag{9.17}$$

Fig. 9-12 and (9.16), (9.17) demonstrate how the anisotropy in magnetostriction affects the 2D magnetostriction. If λ_{y1D} is higher than λ_{x1D}, $\lambda_x - M_x$ will be separated from $\lambda_y - M_y$ into the negative region. The values of ξ_x and ξ_y also cause $\lambda_{x_{PP}}$ and $\lambda_{y_{PP}}$ under circular magnetisation to be higher than the AC peak to peak magnetostriction λ_{PP} under unidirectional magnetisation at the same induction.

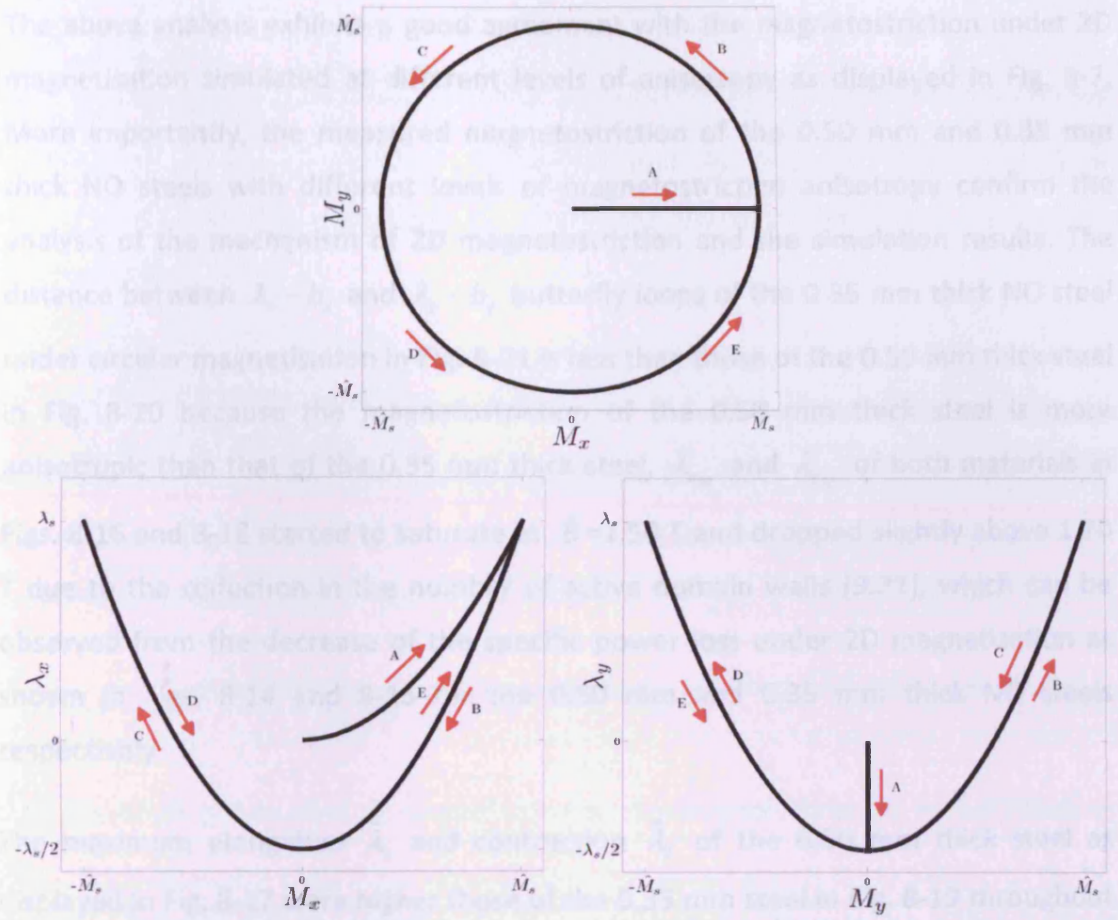

Fig. 9-11 Trajectories of λ_x and λ_y of ideal NO steel corresponding to the trajectory of the magnetisation starting from the demagnetised state until saturation then rotating in the anticlockwise direction

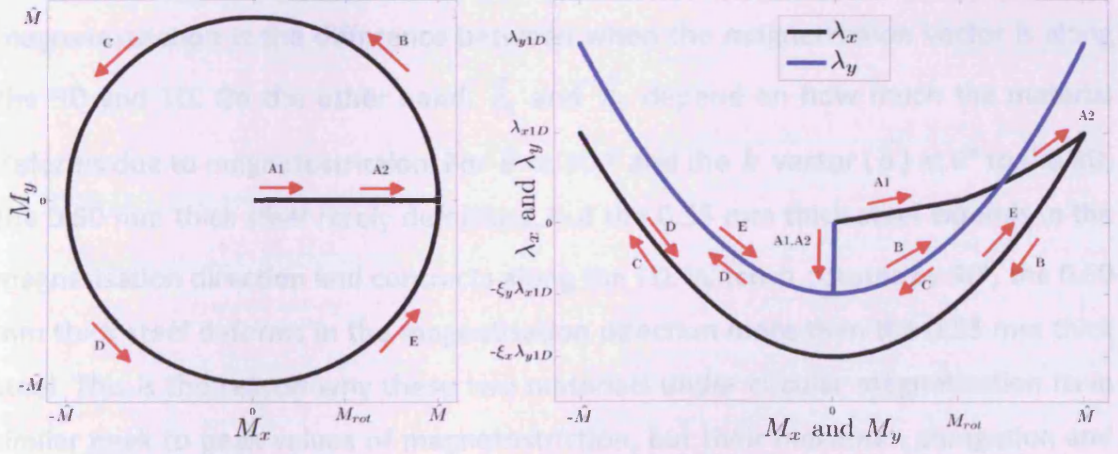

Fig. 9-12 Trajectories of λ_x and λ_y of a magnetostrictively anisotropic NO steel corresponding to the trajectory of the magnetisation starting from the demagnetised state then rotating in anticlockwise direction

The above analysis exhibits a good agreement with the magnetostriction under 2D magnetisation simulated at different levels of anisotropy as displayed in Fig. 5-7. More importantly, the measured magnetostriction of the 0.50 mm and 0.35 mm thick NO steels with different levels of magnetostriction anisotropy confirm the analysis of the mechanism of 2D magnetostriction and the simulation results. The distance between $\lambda_x - b_x$ and $\lambda_y - b_y$ butterfly loops of the 0.35 mm thick NO steel under circular magnetisation in Fig. 8-21 is less than those of the 0.50 mm thick steel in Fig. 8-20 because the magnetostriction of the 0.50 mm thick steel is more anisotropic than that of the 0.35 mm thick steel. $\lambda_{x_{PP}}$ and $\lambda_{y_{PP}}$ of both materials in Figs. 8-16 and 8-18 started to saturate at $\hat{B}$=1.50 T and dropped slightly above 1.70 T due to the reduction in the number of active domain walls [*9.21*], which can be observed from the decrease of the specific power loss under 2D magnetisation as shown in Figs. 8-14 and 8-15 for the 0.50 mm and 0.35 mm thick NO steels respectively.

The maximum elongation $\hat{\lambda}_1$ and contraction $\hat{\lambda}_2$ of the 0.50 mm thick steel as displayed in Fig. 8-17 were higher those of the 0.35 mm steel in Fig. 8-19 throughout the magnetisation range. This phenomenon is directly related to the maximum and minimum values of λ_x and λ_y, which can be observed in the $\lambda_x - b_x$ and $\lambda_y - b_y$ curves in Figs. 8-20 and 8-21. The in-plane deformation plots in Fig. 8-22 illustrate the difference of $\hat{\lambda}_1$ and $\hat{\lambda}_2$ in both materials. The peak to peak value of 2D magnetostriction is the difference between when the magnetisation vector is along the RD and TD. On the other hand, $\hat{\lambda}_1$ and $\hat{\lambda}_2$ depend on how much the material deforms due to magnetostriction. For $\hat{B}$=1.30 T and the b vector ($\vec{b}$) at 0° to the RD, the 0.50 mm thick steel rarely deformed, but the 0.35 mm thick steel extends in the magnetisation direction and contracts along the TD. When $\vec{b}$ rotates by 90°, the 0.50 mm thick steel deforms in the magnetisation direction more than the 0.35 mm thick steel. This is the reason why these two materials under circular magnetisation have similar peak to peak values of magnetostriction, but their maximum elongation and contraction values are different. Interestingly, at $\hat{B}$=1.30 T, 45°, the deformation curve of the 0.50 mm thick steel stays close to the TD, while that of the 0.35 mm thick steel followed $\vec{b}$. This shows the strong anisotropy in magnetostriction of the 0.50 mm thick steel. Surprisingly, the 0.50 mm thick steel extends in the direction

perpendicular to the magnetisation vector at $\hat{B}$=1.90 T, 0° and it causes $\lambda_{y_{pp}}$ to be lower than $\lambda_{x_{pp}}$ as can be observed in Fig. 8-18. This could be due to the fact that the material did not have enough time to recover from the large deformation when $\vec{b}$ was at 90° and this phenomenon would not be expected under quasi-static magnetisation.

Although the saturation magnetostriction of the two materials differs, their AC components ($\lambda_{x_{pp}}$ and $\lambda_{y_{pp}}$) are the same below saturation induction. This indicates that their AC components of 2D magnetostriction ($\lambda_{x_{pp}}$ and $\lambda_{y_{pp}}$) are not only due to the saturation magnetostriction at a given induction, but the ratios between the longitudinal and transverse magnetostriction (ξ_x and ξ_y) also affect $\lambda_{x_{pp}}$ and $\lambda_{y_{pp}}$.

9.4.2 Analysis of 2D magnetostriction of NO steels using a 2D magnetostriction model

The identified parameters P_x and P_y for the 2D magnetostriction model listed in Table 8-3 reflect the anisotropy level of each material. The time constant τ_m of the 0.50 mm thick steel is higher than that of the 0.35 mm thick steel, which can be observed in the butterfly loops of the 0.50 mm thick steel in Fig. 8-20 which are wider than those of the 0.35 mm thick material in Fig. 8-21. The hysteresis in $\lambda - b$ curve is also connected to the hysteresis in $b - h$ curve [*9.5*], which can be confirmed by the fact that the specific power loss of the 0.50 mm thick material is generally higher than that of the 0.35 mm thick steel.

It is very interesting that the magnetic Poisson's ratios ξ_x and ξ_y of both materials were found to greater than the theoretical value of 0.5 [*9.4*]. This result also corresponds to the findings of Hubert et al [*9.22*], who measured longitudinal and transverse magnetostriction of Epstein strips of a 3% SiFe NO steel. Their results showed that the transverse magnetostriction was even greater than the longitudinal value. This theoretical value was derived from an ellipsoid of a ferromagnetic material based on the assumption of constant volume. The saturation magnetostriction of a single crystal in (5.8) is used to prove that the transverse magnetostriction is not always half of the longitudinal value. If the crystal is magnetised to saturation along the x direction ([100] α_1=1, $\alpha_2 = \alpha_3$=0), the

observed magnetostriction in the x axis (β_1=1, $\beta_2=\beta_3$=0) is $\lambda_x=\lambda_{100}$ and in the y axis (β_1=0, $\beta_2=\beta_3=1/\sqrt{2}$) is half of the λ_x ($\lambda_y=-\lambda_{100}/2$) as illustrated in Fig. 5-4. However, $\lambda_x=-\lambda_{100}/2$ and $\lambda_y=\lambda_{100}/4+3\lambda_{111}/4$ if magnetised along the y direction ([011] α_1=0, $\alpha_2=\alpha_3=1/\sqrt{2}$). Thus for the Goss textured material, the transverse magnetostriction is half of the longitudinal value if magnetised along the RD. However for NO steels with random orientation, it is possible for the transverse magnetostriction to be more than half of the longitudinal value.

The simulated magnetostriction of the 0.50 mm thick steel under circular and elliptical magnetisation agrees well with the measured values at peak flux densities from 0.80 to 1.40 T as shown in **Section 8.4.4** of **Chapter 8**. The differences between the measured and modelled magnetostriction are within 10 % as shown in Tables 8-4 to 8-6 except for those under elliptical magnetisation at a=0.25, θ=0°, where the measured magnetostriction was very low leading to large percentage differences. The accuracy of the 2D magnetostriction model for the 0.35 mm thick material is lower than that of the 0.50 mm thick steel due to the fact that its in-plane magnetostriction profile as shown in Fig. 8-31 is more complex. This is discussed in the next section. The reduction of active domain walls affects the values of the parameters of the 2D magnetostriction model. Although this 2D magnetostriction model is limited to a certain induction range, it is useful for describing the relevance of magnetostriction anisotropy to the 2D magnetostriction.

The flux density b_x and b_y in the 2D magnetisation system are controlled and expressed as

$$b_x=\hat{B}_x\sin\omega t \tag{9.18}$$

$$b_y=\hat{B}_y\sin(\omega t\pm\delta). \tag{9.19}$$

$\hat{B}_x$ and $\hat{B}_y$ as a function of $\hat{B}$, a, and θ are given by

$$\hat{B}_x=\hat{B}\sqrt{\cos^2\theta+a^2\sin^2\theta} \tag{9.20}$$

$$\hat{B}_y=\hat{B}\sqrt{a^2\cos^2\theta+\sin^2\theta}. \tag{9.21}$$

The ± sign in (9.19) is for defining the rotating direction of the flux density vector and the phase angle δ of the b_y is obtained from

$$\delta = \tan^{-1}\left(\frac{a}{\tan\theta}\right) + \tan^{-1}(a\tan\theta). \tag{9.22}$$

Substituting (9.18) and (9.19) into the 2D magnetostriction model in (5.21), λ_x and λ_y under 2D magnetisation can be written as

$$\tau_m \frac{d\lambda_x}{dt} + \lambda_x = \frac{1}{4\mu_0}\left(\frac{1}{P_x}\cdot\hat{B}_x^2 - \frac{\xi_x}{P_y}\cdot\hat{B}_y^2\right) - \frac{1}{4\mu_0}\left(\frac{1}{P_x}\cdot\hat{B}_x^2\cos 2\omega t - \frac{\xi_x}{P_y}\cdot\hat{B}_y^2\cos 2(\omega t \pm \delta)\right) \tag{9.23}$$

$$\tau_m \frac{d\lambda_y}{dt} + \lambda_y = \frac{1}{4\mu_0}\left(\frac{1}{P_y}\cdot\hat{B}_y^2 - \frac{\xi_y}{P_x}\cdot\hat{B}_x^2\right) - \frac{1}{4\mu_0}\left(\frac{1}{P_y}\cdot\hat{B}_y^2\cos 2(\omega t \pm \delta) - \frac{\xi_y}{P_x}\cdot\hat{B}_x^2\cos 2\omega t\right). \tag{9.24}$$

Under circular flux density (a =1), $\hat{B}_x = \hat{B}_y = \hat{B}$ and δ =90°. λ_x and λ_y will be

$$\tau_m \frac{d\lambda_x}{dt} + \lambda_x = \frac{\hat{B}^2}{4\mu_0}\left(\frac{1}{P_x} - \frac{\xi_x}{P_y}\right) - \frac{\hat{B}^2}{4\mu_0}\left(\frac{1}{P_x} + \frac{\xi_x}{P_y}\right)\cos 2\omega t \tag{9.25}$$

$$\tau_m \frac{d\lambda_y}{dt} + \lambda_y = \frac{\hat{B}^2}{4\mu_0}\left(\frac{1}{P_y} - \frac{\xi_y}{P_x}\right) + \frac{\hat{B}^2}{4\mu_0}\left(\frac{1}{P_y} + \frac{\xi_y}{P_x}\right)\cos 2\omega t. \tag{9.26}$$

The first terms on the right hand side of (9.25) and (9.26) create the DC components of λ_x and λ_y ($\lambda_{x_{DC}}$ and $\lambda_{y_{DC}}$). For isotropic materials, $P_x = P_y$ and $\xi_x = \xi_y$ resulting in $\lambda_{x_{DC}} = \lambda_{y_{DC}}$. Thus, the $\lambda_x - b_x$ curve is overlaid by the $\lambda_y - b_y$ curve, which can be seen in the simulation shown in Fig. 5-7 and the analytical trajectories of magnetostriction in Fig. 9-11. The difference between $\lambda_{x_{DC}}$ and $\lambda_{y_{DC}}$ is expressed as

$$\lambda_{x_{DC}} - \lambda_{y_{DC}} = \frac{\hat{B}^2}{4\mu_0}\left(\frac{1+\xi_y}{P_x} - \frac{1+\xi_x}{P_y}\right). \tag{9.27}$$

Using the parameters in Table 8-3, the value of $\lambda_{x_{DC}}$ - $\lambda_{y_{DC}}$ is -8 μm/m for the 0.50 mm thick steel with high magnetostriction anisotropy and -0.4 μm/m for the 0.35 mm thick steel with low magnetostriction anisotropy at 1.30 T. This shows how the

magnetostriction anisotropy affects the distance between the $\lambda_x - b_x$ and $\lambda_y - b_y$ curves.

Neglecting the time constant τ_m, $\lambda_{x_{pp}}$ and $\lambda_{y_{pp}}$ can be derived from the AC component of (9.25) and (9.26) as follows

$$\lambda_{x_{pp}} = \frac{\hat{B}^2}{2\mu_0}\left(\frac{1}{P_x} + \frac{\xi_x}{P_y}\right) \tag{9.28}$$

$$\lambda_{y_{pp}} = \frac{\hat{B}^2}{2\mu_0}\left(\frac{1}{P_y} + \frac{\xi_y}{P_x}\right). \tag{9.29}$$

The expressions for $\lambda_{x_{pp}}$ and $\lambda_{y_{pp}}$ in (9.28) and (9.29) are similar to (9.16) and (9.17) obtained analytically. Up to this point, it is very interesting that the ratios between the transverse and longitudinal magnetostriction are the important factors for the magnetostriction under circular magnetisation. If ξ_x and ξ_y are set to be the theoretical value of 0.5, $\lambda_{x_{pp}}$ and $\lambda_{y_{pp}}$ under circular magnetisation can be roughly estimated from the measured magnetostriction in Epstein strips cut along and perpendicular to the RD using (9.16) and (9.17). Moreover, ξ_x and ξ_y, and the magnetostrictive anisotropy also create large deformation due to the greater expansion of $\lambda_{x_{DC}} - \lambda_{y_{DC}}$ as expressed in (9.27). From (9.27), the behaviour of magnetostriction under circular flux density is easily predicted from the anisotropy in magnetostriction and vice versa.

For the 0.50 mm thick NO steel under elliptical flux loci, $\lambda_{x_{pp}}$, $\lambda_{y_{pp}}$, $\hat{\lambda}_1$ and $\hat{\lambda}_2$ were found to be sensitive to both the axis ratio a and the angle θ to the RD as displayed in Fig. 8-23 and Fig. 8-24. The impact of θ becomes less prominent at higher axis ratios. On the other hand, the increase of the axis ratio from 0.25 to 1.00 (circular flux) at θ=90° has a very marginal impact on $\lambda_{x_{pp}}$, $\lambda_{y_{pp}}$, $\hat{\lambda}_1$ and $\hat{\lambda}_2$ compared to those at θ=0°. It shows that b_y has a more significant effect on the magnetostriction than b_x, due to the magnetostrictive anisotropic property of the material [*9.23*]. For the isotropic 0.35 mm thick steel under elliptical flux loci, only the axis ratio a has a strong influence on $\lambda_{x_{pp}}$ and $\lambda_{y_{pp}}$ in Fig. 8-25, and $\hat{\lambda}_1$ and $\hat{\lambda}_2$ in Fig. 8-26.

The 2D magnetostriction model also can be used to explain how the anisotropy in magnetostriction influences the values under elliptical flux loci. Only the two extreme angles to the RD (θ=0° and θ=90°) are considered. For θ=0°, substituting $b_x = \hat{B}\sin\omega t$ and $b_y = a\hat{B}\sin(\omega t \pm 90°)$ obtained from (9.18) to (9.22) into (5.21), the peak to peak magnetostriction $\lambda_{x_{PP}}$ and $\lambda_{y_{PP}}$, and the difference $\lambda_{x_{DC}} - \lambda_{y_{DC}}$ are given by

$$\lambda_{x_{PP}} = \frac{\hat{B}^2}{2\mu_0}\left(\frac{1}{P_x} + \frac{\xi_x}{P_y}\cdot a^2\right) \tag{9.30}$$

$$\lambda_{y_{PP}} = \frac{\hat{B}^2}{2\mu_0}\left(\frac{1}{P_y}\cdot a^2 + \frac{\xi_y}{P_x}\right) \tag{9.31}$$

$$\lambda_{x_{DC}} - \lambda_{y_{DC}} = \frac{\hat{B}^2}{4\mu_0}\left(\frac{1+\xi_y}{P_x} - \frac{1+\xi_x}{P_y}\cdot a^2\right). \tag{9.32}$$

Again substituting $b_x = a\hat{B}\sin\omega t$ and $b_y = \hat{B}\sin(\omega t \pm 90°)$ into (5.21), $\lambda_{x_{PP}}$, $\lambda_{y_{PP}}$ and $\lambda_{x_{DC}} - \lambda_{y_{DC}}$ under elliptical flux loci at θ=90° can be now written as

$$\lambda_{x_{PP}} = \frac{\hat{B}^2}{2\mu_0}\left(\frac{1}{P_x}\cdot a^2 + \frac{\xi_x}{P_y}\right) \tag{9.33}$$

$$\lambda_{y_{PP}} = \frac{\hat{B}^2}{2\mu_0}\left(\frac{1}{P_y} + \frac{\xi_y}{P_x}\cdot a^2\right) \tag{9.34}$$

$$\lambda_{x_{DC}} - \lambda_{y_{DC}} = \frac{\hat{B}^2}{4\mu_0}\left(\frac{1+\xi_y}{P_x}\cdot a^2 - \frac{1+\xi_x}{P_y}\right). \tag{9.35}$$

The peak to peak magnetostriction values along the major and minor axes remains unchanged for the isotropic material if θ is varied. This can be observed from $\lambda_{x_{PP}}$ at θ=0° in (9.30) equal to $\lambda_{y_{PP}}$ at θ=90° in (9.34), and $\lambda_{y_{PP}}$ at θ=0° in (9.31) equal to $\lambda_{x_{PP}}$ at θ=90° in (9.33) if $P_x = P_y = P$ and $\xi_x = \xi_y = \xi$. The measured $\lambda_{x_{PP}}$ and $\lambda_{y_{PP}}$ of the 0.35 mm thick steel under elliptical flux loci in Fig. 8-25 confirm this analysis. Also, the absolute value of $\lambda_{x_{DC}} - \lambda_{y_{DC}}$ at θ=0° is the same as at θ=90°, which implies

that the maximum elongation $\hat{\lambda}_1$ and contraction $\hat{\lambda}_2$ are not affected by θ as confirmed by the results in Fig. 8-26.

For the 0.50 mm thick steel having high anisotropy in magnetostriction, $P_x >> P_y$. Thus, $\lambda_{x_{PP}}$, $\lambda_{y_{PP}}$ and $\lambda_{x_{DC}} - \lambda_{y_{DC}}$ at θ=0° in (9.30) to (9.32) can be approximated as

$$\lambda_{x_{PP}} \approx \frac{\hat{B}^2}{2\mu_0} \cdot \frac{\xi_x}{P_y} \cdot a^2 \tag{9.36}$$

$$\lambda_{y_{PP}} \approx \frac{\hat{B}^2}{2\mu_0} \cdot \frac{1}{P_y} \cdot a^2 \tag{9.37}$$

$$\lambda_{x_{DC}} - \lambda_{y_{DC}} \approx -\frac{\hat{B}^2}{4\mu_0} \frac{1+\xi_x}{P_y} \cdot a^2 \tag{9.38}$$

The approximations of $\lambda_{x_{PP}}$ and $\lambda_{y_{PP}}$ at θ=0° in (9.36) and (9.37) agree well with the measured values given in Fig. 8-23, indicating that the increase of b_y via the axis ratio a strongly influences magnetostriction. The measured maximum deformation at θ=0° in Figs. 8-24 is confirmed by the approximation of $\lambda_{x_{DC}} - \lambda_{y_{DC}}$ in (9.38).

The approximations of $\lambda_{x_{PP}}$, $\lambda_{y_{PP}}$, $\lambda_{x_{DC}} - \lambda_{y_{DC}}$ of the 0.50 mm thick steel under elliptical magnetisation at θ=90° in (9.39) to (9.41) show that the magnetostriction is mainly driven by b_y regardless b_x [*9.23*], confirming the measurement results in Fig. 8-23 and Fig. 8-24.

$$\lambda_{x_{PP}} \approx \frac{\hat{B}^2}{2\mu_0} \frac{\xi_x}{P_y} \tag{9.39}$$

$$\lambda_{y_{PP}} \approx \frac{\hat{B}^2}{2\mu_0} \frac{1}{P_y} \tag{9.40}$$

$$\lambda_{x_{DC}} - \lambda_{y_{DC}} \approx -\frac{\hat{B}^2}{4\mu_0} \frac{1+\xi_x}{P_y} \tag{9.41}$$

The angular-dependence of magnetostriction under elliptical magnetisation at a given axis ratio a is due to the increase of b_y at the higher value of θ, which can be

observed in the normalised plots of $\hat{B}_x$ and $\hat{B}_y$ as displayed in Fig. 9-13. The impact of θ is expected to be more pronounced at the lower value of a.

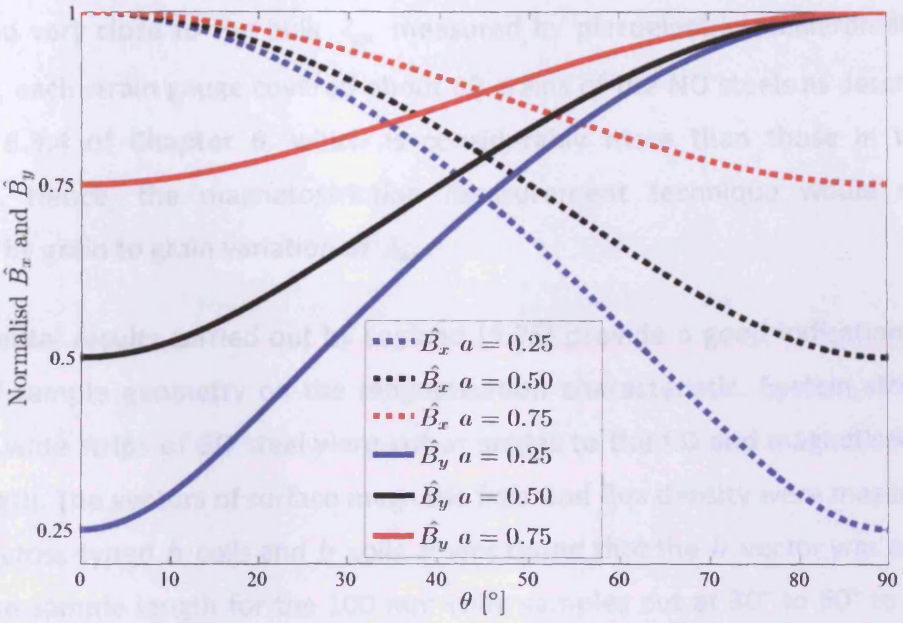

Fig. 9-13 Normalised values of $\hat{B}_x$ and $\hat{B}_y$ of the elliptical flux density loci at axis ratios a =0.25, 0.50 and 0.75, as a function of θ between the major axis of the elliptic and the RD.

9.5 Analysis of AC Magnetostriction of NO Steels Measured in the 2D Magnetisation System

The peak to peak values of AC magnetostriction λ_{pp} of the 0.50 mm thick NO steel measured in the 2D magnetisation system have the same trend as those measured in Epstein strips as compared in Fig. 8-29, apart from those at 10° where λ_{pp} and specific power loss rose. Metallurgical techniques such as electron back-scattered diffraction can be used to determine the crystallographic texture to explain this phenomenon but is not an objective of this thesis. Furthermore, the differences between λ_{pp} measured in the two systems are generally increased with the magnetising direction, but decreased with the magnitude of magnetisation as displayed in Fig. 8-30. There are two possible attributions that cause these differences: magnetostriction measurement techniques and sample shape.

It is apparent that λ_{pp} measured in an Epstein strip is the *bulk* magnetostriction that averages over its length, while λ_{pp} measured in the disc sample is the localised value. The difference between the bulk and localised magnetostriction in Epstein

strips of conventional GO electrical steel was studied by Anderson et al [*9.24*]. For the stress free condition, it showed that localised λ_{pp} at three different positions of the Epstein strips measured by 20 mm long resistance strain gauges were almost the same and very close to the bulk λ_{pp} measured by piezoelectric accelerometers. In addition, each strain gauge covered about 60 grains of the NO steels as described in **Section 6.3.4** of **Chapter 6**, which is considerably more than those in the GO material. Hence, the magnetostriction measurement technique would not be affected by grain to grain variation of λ_{pp}.

Experimental results carried out by Layland [*9.25*] provide a good indication of the effect of sample geometry on the magnetisation characteristic. Epstein strips and 100 mm wide strips of GO steel were cut at angles to the RD and magnetised along their length. The vectors of surface magnetic field and flux density were measured by mean of cross-typed *h* coils and *b* coils. It was found that the *h* vector was at 30° to 40° to the sample length for the 100 mm wide samples cut at 30° to 60° to the RD and this angle decreased at higher magnetisation as shown in Fig. 9-14. However, the *b* vector stayed closely to the longitudinal direction. This phenomenon was not found in the samples cut along the RD and Epstein strips cut at any angle. This was explained by the presence of the demagnetisation field (H_d) occurring along the RD of larger samples and it varies with the sample size [*9.26*]. Sample geometry and magnetic anisotropy have an important influence on the magnetisation characteristic. Long and narrow sample shape such as Epstein strips overshadow the magnetostatic energy (E_N) due to the magnetic ansiotropy, so the easy magnetisation axis is along the sample length. On the other hand, the magnetic anisotropy overwhelms the sample shape in wider samples, causing the easy magnetisation axis to be along the RD.

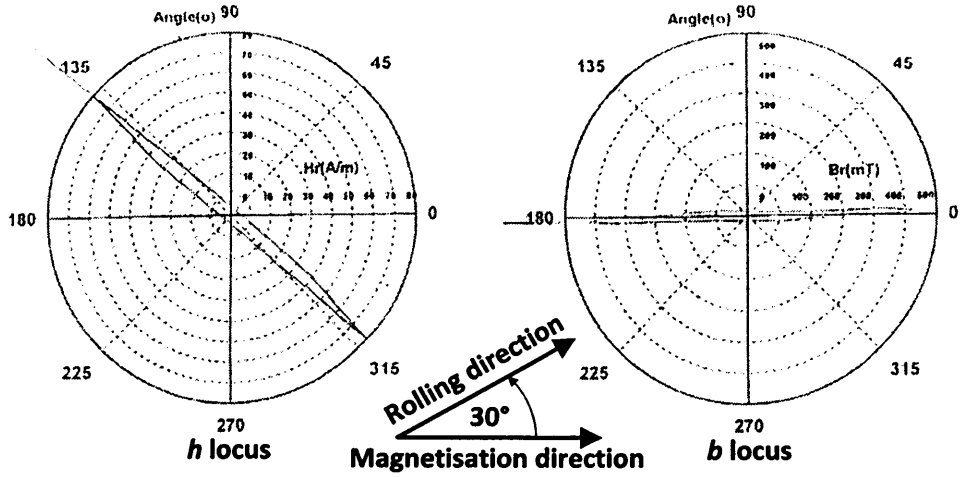

Fig. 9-14 Polar plots of magnetic field and flux density loci of a 100 mm wide GO strip cut at 30° with respect to the RD under sinusoidal magnetisation along the strip length at 0.65 T, 50 Hz [*9.26*].

Chikazumi [*9.1*] describes the effect of sample geometry on magnetostriction using an ellipsoid of rotation magnetised along its length shown in Fig. 9-15 (a). The demagnetisation factor, N_d initially occurs along the longitudinal axis. The total energy (E_{total}) of this system is

$$E_{total} = E_N + E_{elastic} \tag{9.42}$$

where $E_{elastic}$ is the elastic energy. To minimise the total energy, N_d should be decreased to reduce E_N by elongating the ellipsoid. As a result, spontaneous magnetostriction ε_{xx} is increased and ε_{yy} and ε_{zz} are decreased as given in (5.16) and (5.17) respectively. This phenomenon is called the form effect and it is not negligible if N_d is high. Measurement results in **Section 8.1** indicate that the RD of the 0.50 mm thick steel is favoured, quite similar to GO steel in [*9.25*]. Thus, the 0.50 mm thick disc can be equivalent to an ellipse displayed in Fig. 9-15 (b) due to its magnetic anisotropy. The magnetostatic energy due to the magnetic anisotropy is highest when magnetised along the TD. Thus, rise of magnetostriction along the TD due to the form effect is much larger than that along the RD. This is indicated by the difference in λ_{pp} along the RD shown in Fig. 8-30 is lower than the other angles. On the other hand, the 0.35 mm thick steel is quite isotropic and there is no explicit easy magnetisation direction in the disc form. As a result, its geometry dependent magnetostriction is more complicated than that of the 0.50 mm thick steel.

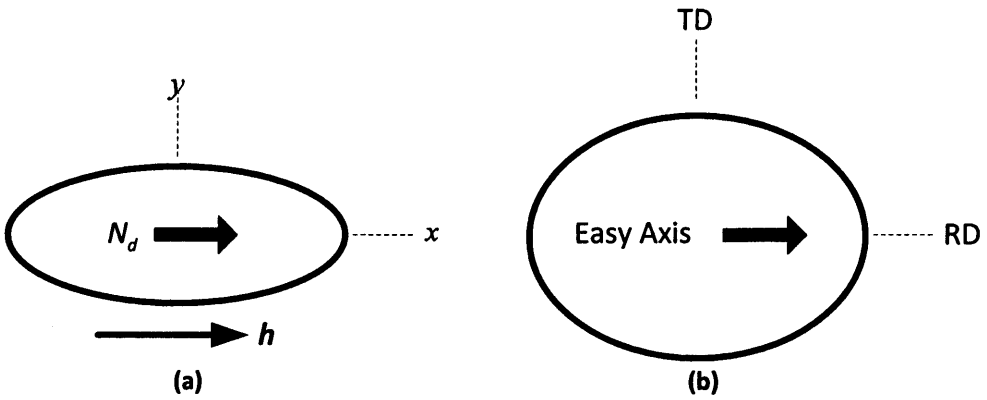

Fig. 9-15 (a) Demagnetisation factor in an ellipsoid of rotation [*9.1*], (b) Equivalent shape of the 0.50 mm disc sample due to the magnetic anisotropy

The measurements of λ_{pp} on the 0.35 mm thick steel displayed in Fig. 8-31 reveal its magnetostrictive anisotropy as the maximum value of λ_{pp} occurred at around 50° to 60° to the RD at any induction. This indicates that the anisotropy factor defined in (9.2) cannot represent the angular characteristic of the magnetostriction. The three-point control method incorporated with Bunge's model as described in **Section 9.2.2** is more suitable for this angular characteristic.

The Identification of parameters for the 2D magnetostriction model was carried out when magnetised along the RD and TD, where two extreme values of magnetostriction are expected. However, the maximum magnetostriction does not lie in either of these directions unlike that of the 0.50 mm thick material. As a result, the differences between the measured and simulated magnetostriction of this material under 2D magnetisation were found to be higher than the 0.50 mm thick material. The difference between the maximum and minimum magnetostriction is higher than between magnetostriction measured along and perpendicular to the RD, causing the distance between the measured $\lambda_x - b_x$ and $\lambda_y - b_y$ curves to be higher than the modelled $\lambda_x^* - b_x$ and $\lambda_y^* - b_y$ as shown in Fig. 8-21. This is the reason why the measured maximum elongation $\hat{\lambda}_1$ and contraction $\hat{\lambda}_2$ in Fig. 8-19 are greater than the modelled values $\hat{\lambda}_1^*$ and $\hat{\lambda}_2^*$.

9.6 References for Chapter 9

[*9.1*] S. Chikazumi, *Physics of Magnetism*, John Wiley & Sons, New York, 1964.

[*9.2*] G. Bán, "Model to evaluate the AC-DC magnetostriction characteristics of SiFe electrical steels," *Journal of Magnetism and Magnetic Materials*, Vol. 254-255, pp. 324-327, 2003.

[*9.3*] F. Bohn, A. Gündel, F. J. G. Landgraf, A. M. Severino, and R. L. Sommer, "Magnetostriction, Barkhausen noise and magnetization processes in E110 grade non-oriented electrical steels," *Journal of Magnetism and Magnetic Materials*, Vol. 317, pp. 20-28, 2007.

[*9.4*] D. C. Jiles, *Introduction to Magnetism and Magnetic Materials*, Second edition, Chapman & Hall/CRC, London, 1998.

[*9.5*] M. J. Sablik and D. C. Jiles, "Coupled magnetoelastic theory of magnetic and magnetostrictive hysteresis," *IEEE Transactions on Magnetics*, Vol. 29, pp. 2113-2123, 1993.

[*9.6*] T. Moses, "Opportunities for exploitation of magnetic materials in an energy conscious world," *Interdisciplinary Science Reviews*, Vol. 27, pp. 100-113, 2002.

[*9.7*] BS EN10106:2007, *Cold Rolled Non-oriented Electrical Steel Sheet and Strip Delivered in The Fully Processed State*, British Standard, 2007.

[*9.8*] G. Bertotti, "General properties of power losses in soft ferromagnetic materials," *IEEE Transactions on Magnetics*, Vol. 24, pp. 621-630, 1988.

[*9.9*] R. M. Bozorth, *Ferromagnetism*, John Wiley & Sons - IEEE Press, New York, 1993.

[*9.10*] M. Emura, M. F. de Campos, F. J. G. Landgraf, and J. C. Teixeira, "Angular dependence of magnetic properties of 2% silicon electrical steel," *Journal of Magnetism and Magnetic Materials*, Vol. 226-230, pp. 1524-1526, 2001.

[*9.11*] B. Hribernik and D. Ambrož, "Proposal of a new anisotropy quality evaluation of nonoriented magnetic steel sheets," *IEEE Transactions on Magnetics*, Vol. 26, pp. 266-269, 1990.

[*9.12*] H. -J. Bunge, *Texture Analysis in Material Science - Mathematical methods*, Butterworths, London, 1982.

[*9.13*] M. F. de Campos, "Anisotropy of steel sheets and consequence for Epstein test:I Theory," *Proceedings of IMEKO XVIII World Congress Metrology for a Sustainable Development*, Rio de Janeiro, Brazil, September 17-22, 2006.

[*9.14*] J. Shilling and G. Jr. Houze, "Magnetic properties and domain structure in grain-oriented 3% Si-Fe," *IEEE Transactions on Magnetics*, Vol. 10, pp. 195-223, 1974.

[*9.15*] T. Yamasaki, S. Yamamoto, and M. Hirao, "Effect of applied stresses on magnetostriction of low carbon steel," *NDT & E International*, Vol. 29, pp. 263-268, 1996.

[*9.16*] K. Yamamoto, E. Shimomura, K. Yamada, and T. Sasaki, "Effects of external stress on magnetic properties in motor cores," *Electrical Engineering in Japan*, Vol. 123, pp. 15-22, 1998.

[*9.17*] F. Kako, T. Tsuruta, K. Nagaishi, and H. Kohmo, "Experimental study on magnetic noise of large induction motors," *IEEE Transactions on Power Apparatus and Systems* Vol. PAS-102, pp. 2805-2810, 1983.

[*9.18*] M. Enokizono, T. Suzuki, and J. D. Sievert, "Measurement of dynamic magnetostriction under rotating magnetic field," *IEEE Transactions on Magnetics*, Vol. 26, pp. 2067-2069, 1990.

[*9.19*] C. Krell, K. Kitz, L. Zhao, and H. Pfützner, "Multidirectional magnetostriction of different types of silicon iron materials," *Proceedings of The 16th Soft Magnetic Materials Conference (SMM16)*, Vol. 1, pp. 191-196, Düsseldorf, Germany, September 9-12, 2003.

[*9.20*] D. Wakabayashi, Y. Maeda, H. Shimoji, T. Todaka, and M. Enokizono, "Measurement of vector magnetostriction in alternating and rotating magnetic field," *Przegląd Elektrotechniczny (Electrical Reviews)*, Vol. R. 85, pp. 34-38, 2009.

[*9.21*] A. J. Moses, "Importance of rotational losses in rotating machines and transformers," *Journal of Materials Engineering and Performance*, Vol. 1, pp. 10, 1992.

[*9.22*] O. Hubert, L. Daniel, and R. Billardon, "Experimental analysis of the magnetoelastic anisotropy of a non-oriented silicon iron alloy," *Journal of Magnetism and Magnetic Materials*, Vol. 254-255, pp. 352-354, 2003.

[*9.23*] S. Somkun, A. J. Moses, P. I. Anderson, and P. Klimczyk, "Magnetostriction anisotropy and rotational magnetostriction of a nonoriented electrical steel," *IEEE Transactions on Magnetics*, Vol. 46, pp. 302-305, 2010.

[*9.24*] P. I. Anderson, A. J. Moses, and H. J. Stanbury, "Evaluation of magnetostriction measurement techniques," *Non Linear Electromagnetic Systems*, Vol. 10, Edited by V. Kose and J. Sievert, IOS Press, Amsterdam, 1998.

[*9.25*] N. J. Layland, *Study of Flux and Field Distribution in Electrical Steels*, MSc Thesis, University of Wales College Cardiff, United Kingdom, 1994.

[*9.26*] A. J. Moses, "Measurement and analysis of magnetic fields on the surface of grain-oriented silicon steel sheet," *Journal de Physique IV*, Vol. 08, pp. Pr2-561-Pr2-565, 1998.

Chapter 10

Localised Flux Density and Localised Deformation Measurement and Simulation Systems of Induction Motor Cores

This chapter covers design, construction and preliminary testing of an induction motor model core for measurements of localised flux densities and deformation. A system for measurement of magnetostriction under magnetisation conditions present in the motor model core is described. Finite element modelling for simulation of core deformation is also discussed.

10.1 Design and Construction of an Induction Motor Model Core

10.1.1 Core geometry and stator winding selection

Fig. 10-1 shows a cross section of the stator and rotor cores of the 200L/M IEC frame size induction motor model. The outer diameter of the stator core was 320 mm, close to typical of 30 to 37-kW induction motors [*10.1*]. For this core size, it was practically convenient to attach strain gauges for measurement of localised deformation. The core had 36 stator slots and teeth. Each stator tooth was 10° apart so that tooth deformation could be directly compared with the magnetostriction measured in the Epstein presented in **Chapter 8**. The rotor had 40 slots and no rotor windings were present. Thus, the core was approximately under the no-load condition. The stator and rotor slots were partly-closed providing a better magnetic circuit than open slots [*10.2*].

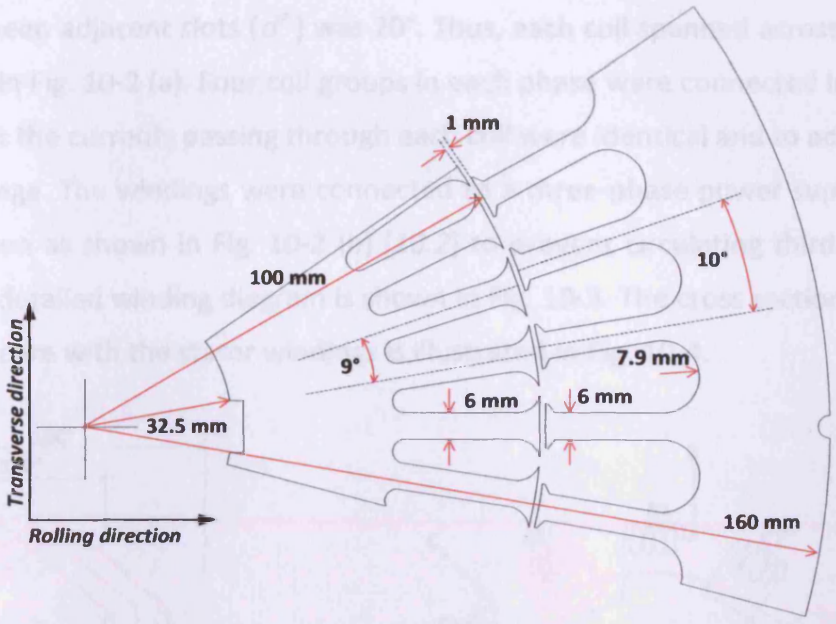

Fig. 10-1 Cross section of the stator and rotor core of the induction motor model

The 2-pole induction motor is rarely used in industry except for high speed applications due to its long return flux path increasing core loss. Also, its long stator windings results in high copper loss and stator leakage inductance [*10.3*]. Four-pole machines are optimum for most industrial applications because of wider constant torque range than other pole configurations [*10.3*]. In addition, the Maxwell force in the air gap acting on stator teeth is a function of time and space and its space cycle completes within $\phi_e/2$ [*10.4*], where ϕ_e is the electrical angle given by

$$\phi_e = p\phi_m \tag{10.1}$$

where p is the number of pole pairs of the stator windings, and ϕ_m is the mechanical or physical angle of the motor core. Thus, a 4-pole stator winding was selected since a quarter of the stator core was sufficient to observe the localised deformation covering a space cycle of the Maxwell force and the physical angle range of 0° to 90 ° with respect to the RD.

A double-layer lap winding, most frequently used in induction motor stator windings [*10.2*], was selected for the model core. The number of coils equalled the slot numbers. There were 12 coil groups derived from the multiplication between the phase numbers and pole numbers, and each consisted of 3 coils as shown in Fig. 10-2. The coil pitch (p°) of 120° was chosen because of its high efficiency for the 36-slot 4-pole motors when operated under PWM voltage excitations [*10.5*]. The electrical

angle between adjacent slots (d°) was 20°. Thus, each coil spanned across 6 slots as illustrated in Fig. 10-2 (a). Four coil groups in each phase were connected in series to ensure that the currents passing through each coil were identical and to achieve high phase voltage. The windings were connected to a three-phase power supply in star configuration as shown in Fig. 10-2 (b) [*10.2*] to prevent circulating third harmonic current. A detailed winding diagram is shown in Fig. 10-3. The cross sectional view of the motor core with the stator windings is illustrated in Fig. 10-4.

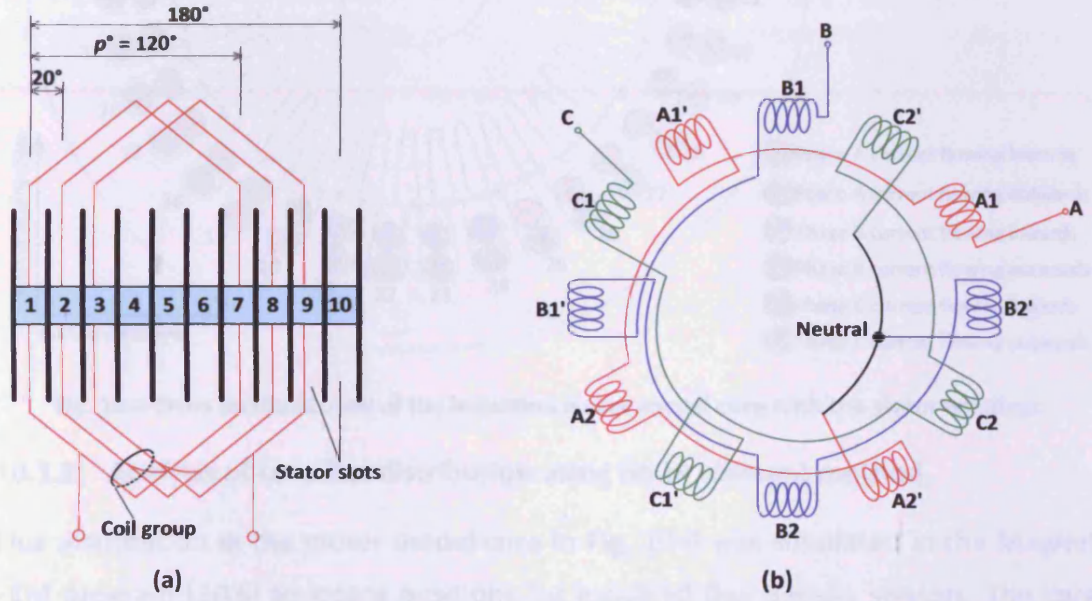

Fig. 10-2 (a) Illustration of coil group and coil pitch for the 36 slot 4 pole induction machine, (b) Connection diagram of the coil groups in star series configuration

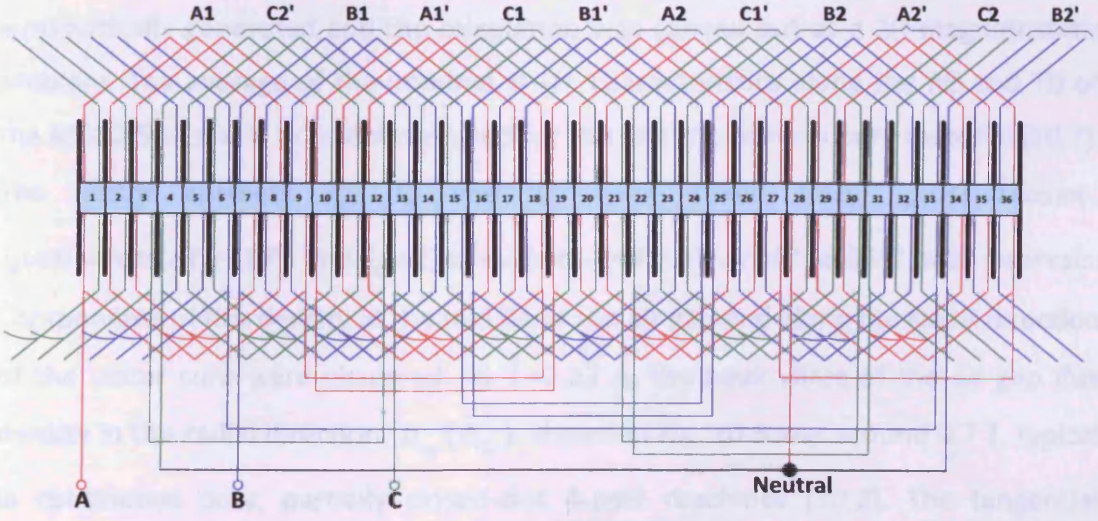

Fig. 10-3 Stator winding of the 36-slot 4-pole 3-phase induction machines with coil pitch of 120° and connected in star series configuration

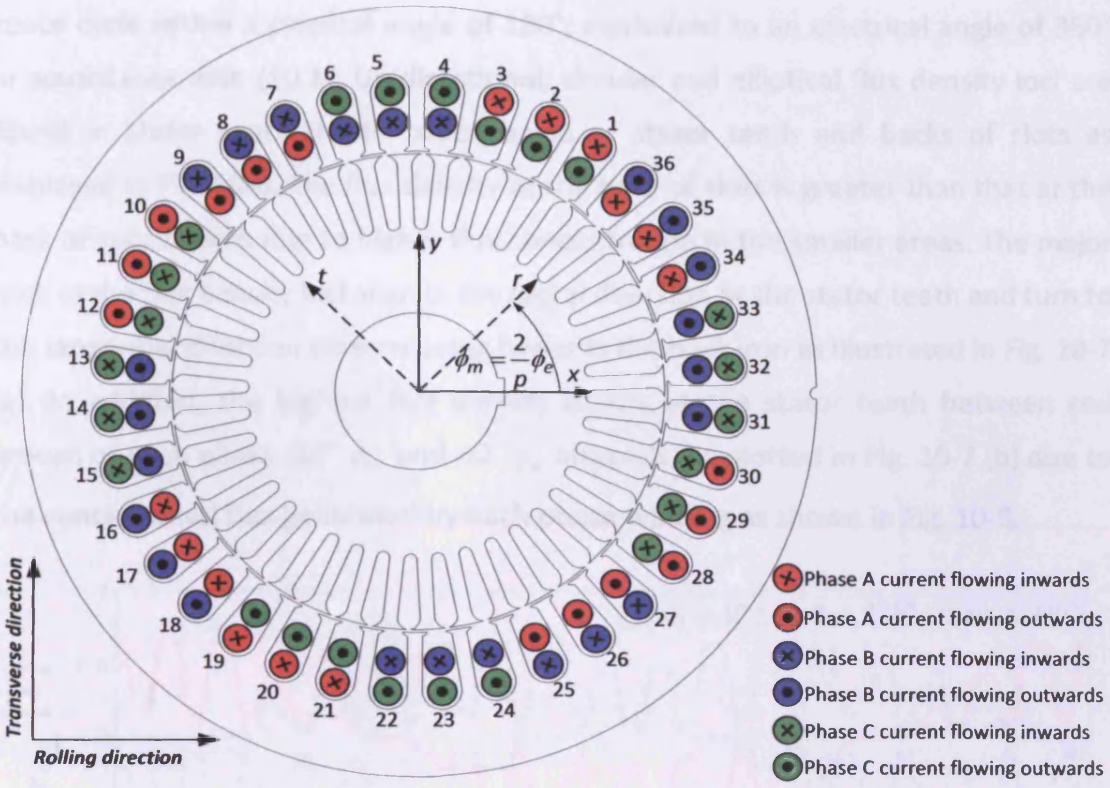

Fig. 10-4 Cross sectional view of the induction motor model core with the stator windings

10.1.2 Analysis of core flux distribution using finite element method

Flux distribution in the motor model core in Fig. 10-4 was simulated in the MagNet FEM program [*10.6*] to locate positions for localised flux density sensors. The core stack was 10 mm thick equivalent to 20 laminations of 0.50 mm thick steels and the turn number of each coil of the stator winding was 60. The meshes were automatically generated and the calculation was carried out as a 2D magnetostatic problem. The average of the nominal $B-H$ characteristics along the RD and TD of the M400-50A grade NO steel was used for the stator and rotor core material [*10.7*]. The stator currents I_A, I_B and I_C were taken from $i_A(\omega t)=\hat{I}\cos\omega t$, $i_B(\omega t)=\hat{I}\cos(\omega t-120^\circ)$ and $i_C(\omega t)=\hat{I}\cos(\omega t-240^\circ)$ at ωt =0° to 355° at 5° intervals. Components of flux density at the middle of the air gap and along the radial direction of the stator core were observed. At $\hat{I}$ =2.22 A, the peak value of the air gap flux density in the radial direction, $b_{r_{ag}}$ ($\hat{B}_{r_{ag}}$) shown in Fig. 10-5 was around 0.7 T, typical in continuous duty, partially closed-slot 4-pole machines [*10.2*]. The tangential component of the air gap flux density ($b_{t_{ag}}$) is comparatively lower than $b_{r_{ag}}$ because of high permeability in the stator and rotor cores. The air gap flux completes one

space cycle within a physical angle of 180°, equivalent to an electrical angle of 360° in accordance with (10.1). Unidirectional, circular and elliptical flux density loci are found in stator teeth, tooth roots, backs of stator teeth and backs of slots as displayed in Fig. 10-6. The flux density at the back of slots is greater than that at the back of stator teeth due to higher flux concentration in the smaller areas. The major axes of the flux density loci align in the radial direction at the stator teeth and turn to the tangential direction when moving towards the back iron as illustrated in Fig. 10-7 (a). In addition, the highest flux density occurs at the stator teeth between coil groups of each phase (30° ϕ_m and 60° ϕ_e intervals) as plotted in Fig. 10-7 (b) due to the concentrated flux generated by each phase winding as shown in Fig. 10-8.

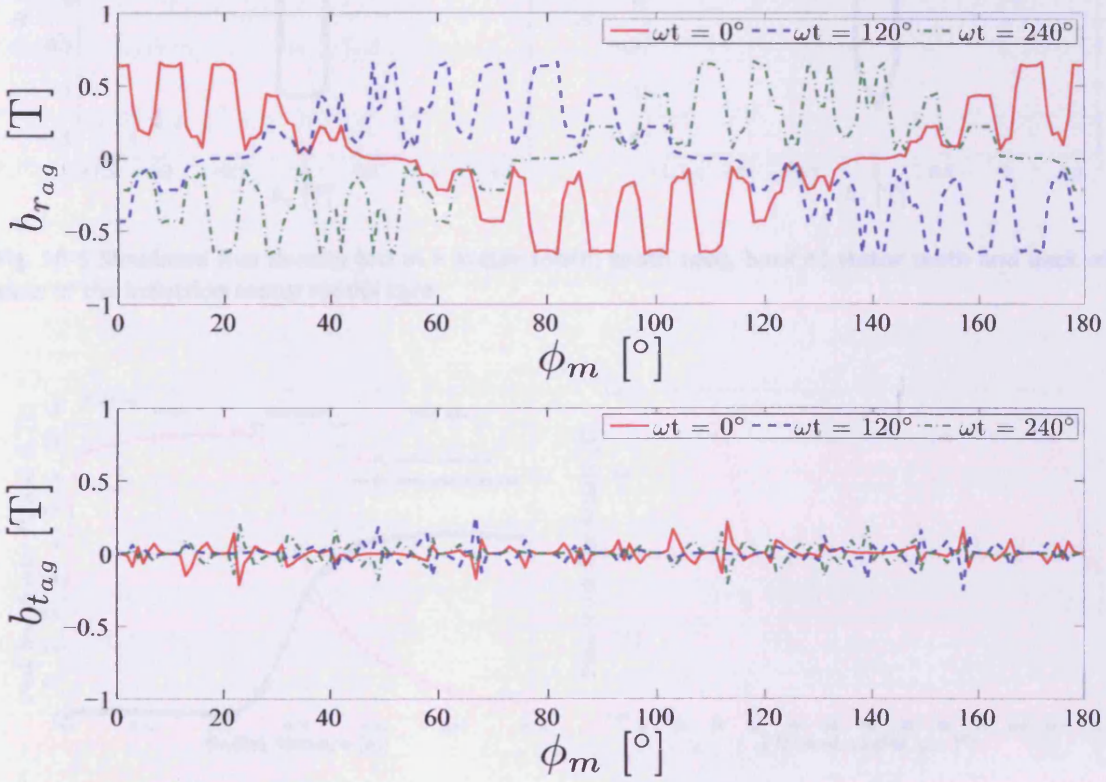

Fig. 10-5 Simulated radial and tangential components of air gap flux density of the induction motor model core at peak phase current of 2.22 A

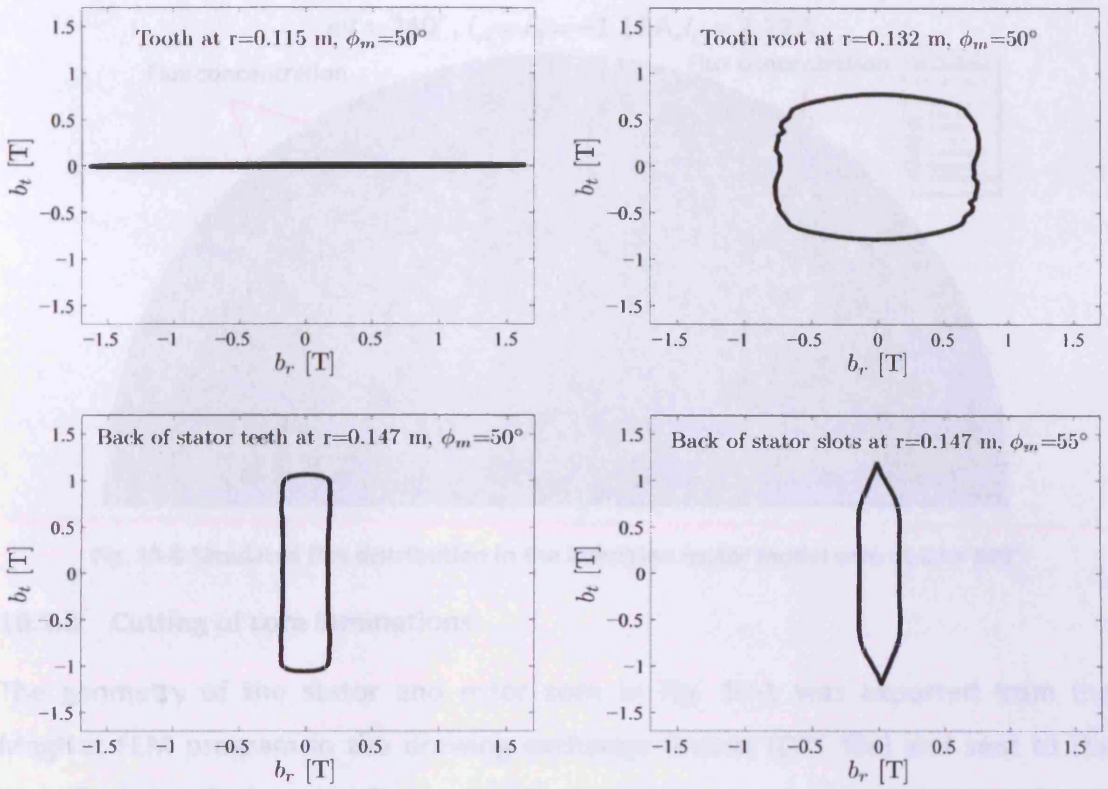

Fig. 10-6 Simulated flux density loci in a stator tooth, tooth root, back of stator teeth and back of slots of the induction motor model core

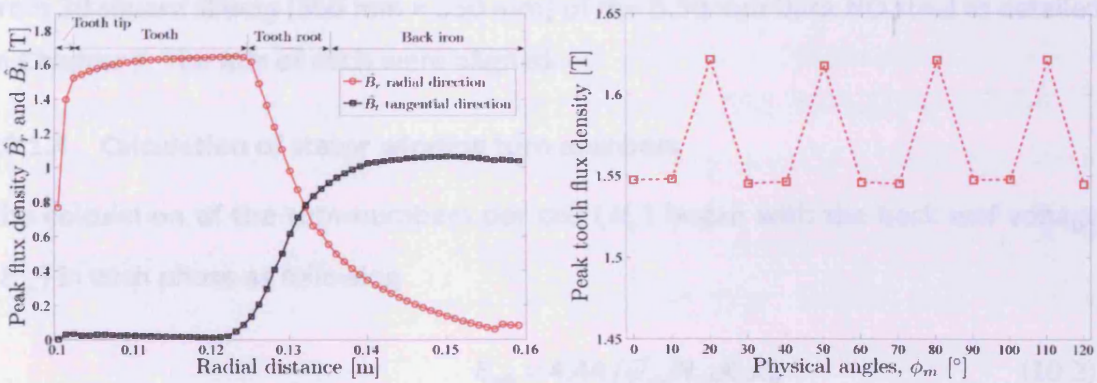

(a) **(b)**

Fig. 10-7 Simulated flux density of the induction motor model core at peak phase current of 2.22 A (a) radial and tangential components of flux density along the tooth at ϕ_m = 50°, (b) averaged tooth flux density at various ϕ_m

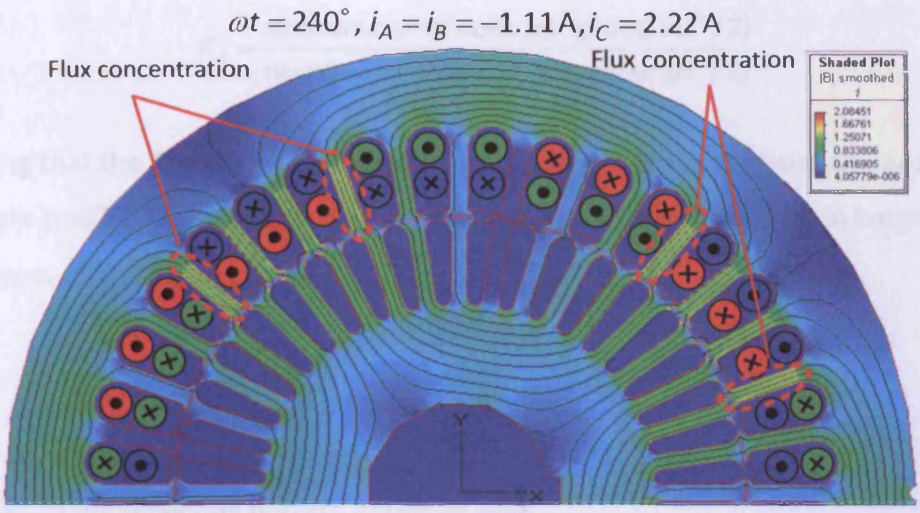

Fig. 10-8 Simulated flux distribution in the induction motor model core at ωt = 240°

10.1.3 Cutting of core laminations

The geometry of the stator and rotor core in Fig. 10-1 was exported from the MagNet FEM program in the drawing exchange format (DXF file) and sent to the Manufacturing Engineering Centre (MEC), Cardiff University to be cut by an electric discharge machine, whose best cutting roughness is 0.2 μm [*10.8*]. Cutting stress due to this technique is negligible [*10.9*]. Thirty stator and rotor laminations were cut from 30 square sheets (350 mm × 350 mm) of the 0.50 mm thick NO steel as detailed in **Chapter 7**. The RDs of each were aligned.

10.1.4 Calculation of stator winding turn numbers

The calculation of the turn numbers per coil (N_c) began with the back emf voltage (E_{ph}) in each phase as following

$$E_{ph} = 4.44 f \overline{\psi}_{ag} N_{ph} K_p K_d \tag{10.2}$$

where f is the supply frequency, $\overline{\psi}_{ag}$ is the average flux under each pole, N_{ph} is the turn numbers in series per phase, K_p and K_d are the pitch and distribution factors of the stator winding given by

$$K_p = \sin\frac{p^\circ}{2} \tag{10.3}$$

$$K_d = \frac{\sin(\text{number of coils per group} \times d^\circ/2)}{\text{number of coils per group} \times \sin(d^\circ/2)}. \quad (10.4)$$

Assuming that the flux under each pole is sinusoidally distributed and the area under each pole is $\pi DL/2p$, where D and L are the inner diameter and axial length of the stator core, $\overline{\psi}_{ag}$ is expressed as

$$\overline{\psi}_{ag} = \frac{2}{\pi}\hat{B}_{ag} \cdot \frac{\pi DL}{2p} = \frac{2\hat{B}_{ag}DL}{2p} \quad (10.5)$$

where $\hat{B}_{ag}$ is the peak flux density in the air gap.

Twelve coils were connected in series resulting in $N_{ph} = 12 \times N_c$. If L = 10 mm (20 laminations of 0.50 mm thick steels), the relationship between E_{ph} and N_c is

$$E_{ph} = 2.21 \times \hat{B}_{ag} \times N_c. \quad (10.6)$$

In practice, the 60 turn stator windings wound from 1 mm diameter class H enamelled copper wires could be easily inserted into the stator slots. The nominal phase voltage about 95 V provides $\hat{B}_{ag}$ =0.7 T using (10.6). The stator windings could carry up to 3.65 A, determined from the maximum current density of 4.65 A/mm^2 as this motor model core was well ventilated [*10.2*]. According to the FEM simulations, the RMS magnetising current was expected to be less than 2 A. Thus, the design margin of the stator windings was over 40 %.

10.1.5 Sensors for measurement of localised flux density and localised deformation

The *b* coil technique described in **Section 6.3.2** was chosen for measurement of localised flux densities in the stator core because of better accuracy and higher output voltage than the conventional needle probe technique when the measuring distance is not comparatively larger than the lamination thickness. Three regions of the stator core, distinguished by shapes of flux loci, were of interest: stator teeth for unidirectional flux loci, tooth roots for circular flux loci and stator back iron for elliptical flux loci. Fig. 10-9 shows the position and dimension of the *b* coils in the stator core. Three groups of single-turn, orthogonal *b* coils for detecting induced voltages due to the flux in the radial and tangential directions at the back iron,

named **YA**, **YB** and **YC** and other three groups at the tooth roots, named **RA**, **RB** and **RC**, were wound on a single lamination subsequently placed at the centre of the core stack. Thanks to physical and electrical similarity between two opposite sides of the stator core, coil groups **RA**, **RB** and **RC** were located 180° away from **YA**, **YB** and **YC** in order not to disturb flux distribution due to the holes of b coils. Each coil was wound from 0.152 mm diameter (SWG 38) enamelled copper wire through the 0.3 mm holes drilled by a 10,000 revolutions per minute drill. Each coil group spanned the teeth between coil groups of the stator windings, where most flux concentration occurs as shown earlier in **Section 10.1.2**. Components of flux density were calculated in the same way as for the disc sample using (6.7) and (6.8). Defining the terminology, for example the radial and tangential components of the flux density at point **1** of the **YA** group are called as $b_{r_{YA1}}$ and $b_{t_{YA1}}$ respectively.

After stacking 20 laminations together, single-turn b coils were wound around each stator tooth covering from the RD to TD. This coil group was named as **T** and the radial flux density in each tooth is called $b_{r_{T0}}$ to $b_{r_{T9}}$ as shown in Fig. 10-9. Three single-turn b coils, b_A, b_B and b_C, were wound around the back iron for measurement of the average back iron flux densities (b_A, b_B and b_C) at the centre of a coil group of each phase winding. An additional b coil, b_{A1} was wound at the same position as b_A coil. b_{A1} and b_A were used as the reference signals for the strain gauge and voltage DAQ cards as described in **Section 6.3.5**. Lead wires of all the b coils were twisted to minimise the voltage induced from the stray field, and connected with 25-way D-sub miniature connectors according to their coil groups [*10.10*]. Two 25-turn coils wound on two rotor teeth and connected in series were used to generate a reference flux for determination of the polarities of the b coils as illustrated in Fig. 10-9.

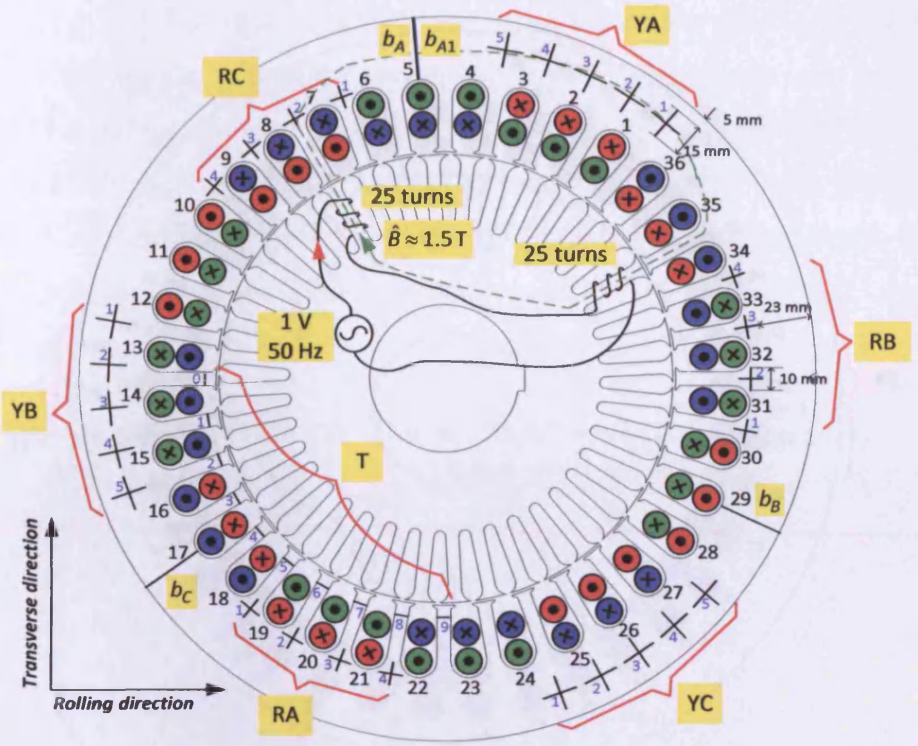

Fig. 10-9 Physical dimensions and locations of b coils in the induction motor model core

Rosette resistance strain gauges from Omega engineering model SGD-3/350-LY11 [*10.11*] listed in Table 10-1 were attached on the top lamination of the stator pack for measuring localised strains. The active area of each gauge was 1.70 mm wide and 3.00 mm long and they were encapsulated in an area of 7.10 mm by 7.10 mm. The gauges were located at the same relative positions as the orthogonal b coils wound on the middle lamination as shown in Fig. 10-10. Unidirectional resistance strain gauges from Omega engineering model SGD-5/350-LY11 [*10.12*] as listed in Table 10-1 with a grid 3.20 mm wide by 4.50 mm long were stuck on the stator teeth wound by the **T** group b coils as shown in Fig. 10-10 for measurement of stator tooth deformation at angles to the RD. The strain gauge attachment method followed the procedure described in **Section 7.2**.

The measured strains were transformed into the radial–tangential $(r-t)$ directions and the RD and TD $(x-y)$ coordinate using (4.17). The strain components in the radial and tangential directions and shear strain in this coordinate for example at point **1** of **YA** group are called $\varepsilon_{r_{YA1}}$, $\varepsilon_{t_{YA1}}$ and $\varepsilon_{rt_{YA1}}$ respectively.

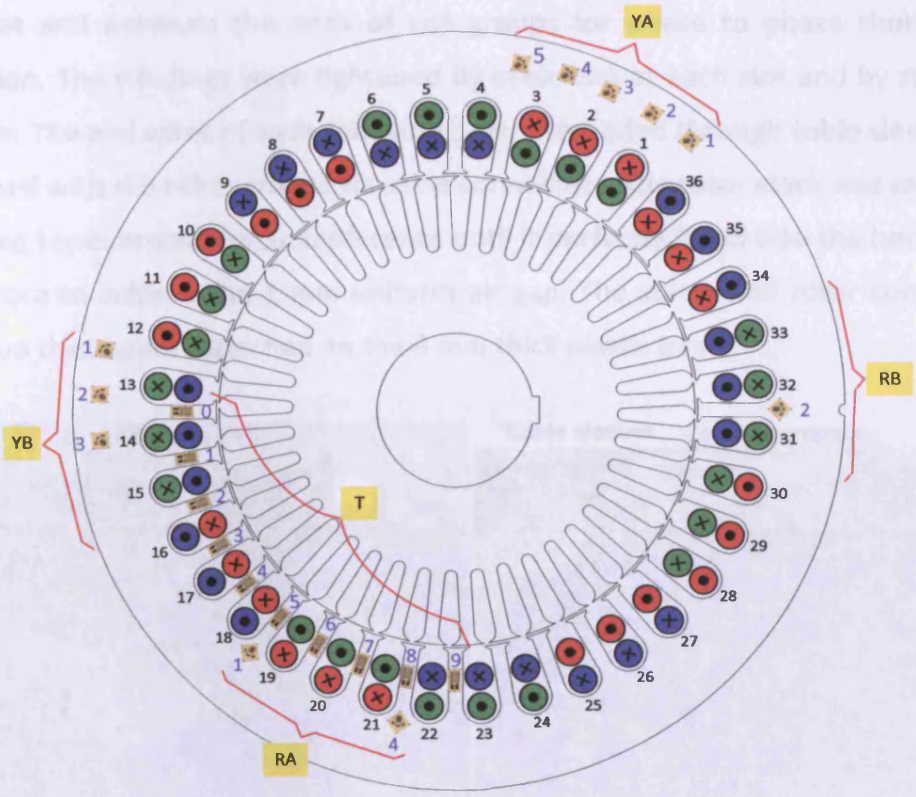

Fig. 10-10 Locations of resistance strain gauges attached on the top lamination of the induction motor model core

Table 10-1 Specifications of the strain gauges for measurement of localised deformation in the induction motor model core

Model	Number of Gauges	Nominal resistance, R_g	Gauge factor, K_g	Gauge dimension		Package dimension	
				Width [mm]	Length [mm]	Width [mm]	Length [mm]
SGD-3/350-LY11	3	350 Ω	1.99 ± 0.40 %	3.00	1.70	7.10	7.10
SGD-5/350-LY11	1	350 Ω	2.00 ± 0.35 %	4.50	3.20	5.20	9.80

10.1.6 Assembly of the induction motor model core

Twenty stator laminations were stacked together, where the lamination with *b* coils and that with strain gauges were placed in the middle and on the top of the pack respectively. The tips of the stator teeth were tightened by plastic cable ties as shown in Fig. 10-11 to prevent the top lamination bending due to the off-plane flux [*10.13*]. The back iron of the stator core was clamped by two 1 mm thick plastic plates with four sets of 8 mm bolts and nuts for adjusting the clamping pressure. The top piece of the plastic clamps was earlier engraved by an electric drill at positions relative to the strain gauges for preventing the gauges from damage. Before installing the stator windings, each slot was insulated by a piece of insulated paper. Insulating papers were also placed between the top and bottom winding layer of

each slot and between the ends of coil groups for phase to phase short circuit protection. The windings were tightened by cable ties at each slot and by strings at the ends. The end wires of each coil groups were threaded through cable sleeves and connected with the other groups via cable connectors. The rotor stack was wound by insulating tapes around its circumference until it perfectly fitted into the bore of the stator core to achieve the 1 mm uniform air gap. The stator and rotor cores were placed on the support attached on the 3 mm thick plastic base.

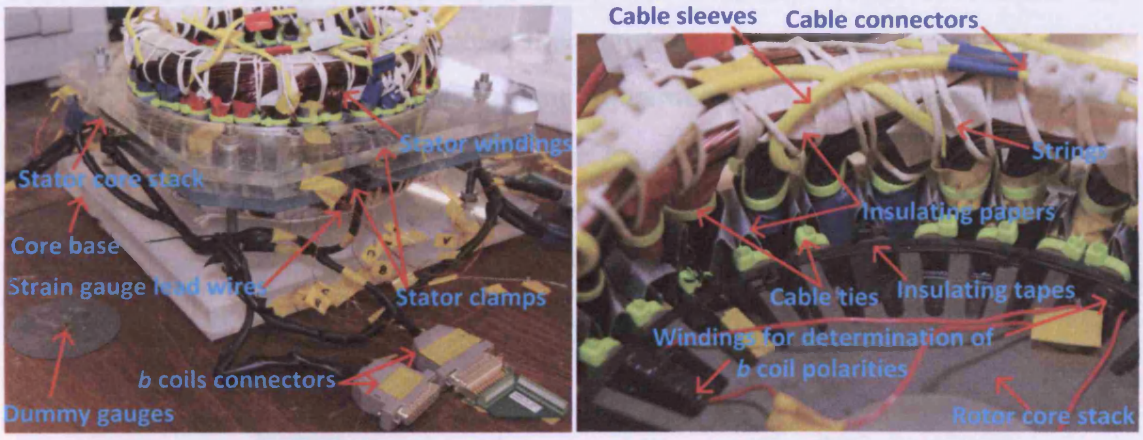

Fig. 10-11 Photographs of components of the induction motor model core

10.1.7 System for measurement of localised flux densities and deformation in the induction motor model core

Fig. 10-12 shows the connection diagram of the system for measurement of localised flux densities and deformation. Three single-phase variable autotransformers connected in star configuration were used to reduce the voltage of a three-phase 50-Hz power supply from line to line voltage (V_{LL}) of 400 V to 165 V, equivalent to a phase voltage (V_{ph}) of 95 V, where the peak air gap flux density was typically 0.7 T. The three-phase stator windings of the motor core were connected to the output of the variable transformers via the Yokogawa WT1600 power meter [*10.14*] in a three-phase four-wire configuration for measurement of the stator voltages, currents and input power.

The b_A, b_B and b_C coils were permanently connected to the NI PCI-6052E voltage DAQ card [*10.15*] for monitoring the average back iron flux density. The other signals connected with the NI PCI-6052E DAQ card were from a set of orthogonal b coils or three b coils at the stator teeth for measurement of localised flux densities. A

program written in the LabVIEW environment was used for calculation of the flux densities from the measured induced voltages. Strain gauges at the measurement points corresponding to the localised b coils were connected to the NI USB-9237 built-in strain gauge DAQ card [*10.16*] in a half-bridge configuration with a set of dummy gauges attached on an unmagnetised circluar sheet cut from the same core material for bridge completion and temperature compensation. The b_{A1} coil was also connected with the strain gauge DAQ card to synchronise signals measured by both DAQ cards using the technique described in **Section 6.3.5**. Therefore, the reference point (t = 0) of the localised flux density and deformation measurements was at $b_A(0) = 0$. The calibration and offset adjustment of the strain gauges, and the removal of the voltage induced in the strain gauges were obtained by the methods described in **Section 6.3.4**. Each measurement was repeated five times and each was averaged over 50 cycles to minimise random noises. All the measurements were carried out at room temperature.

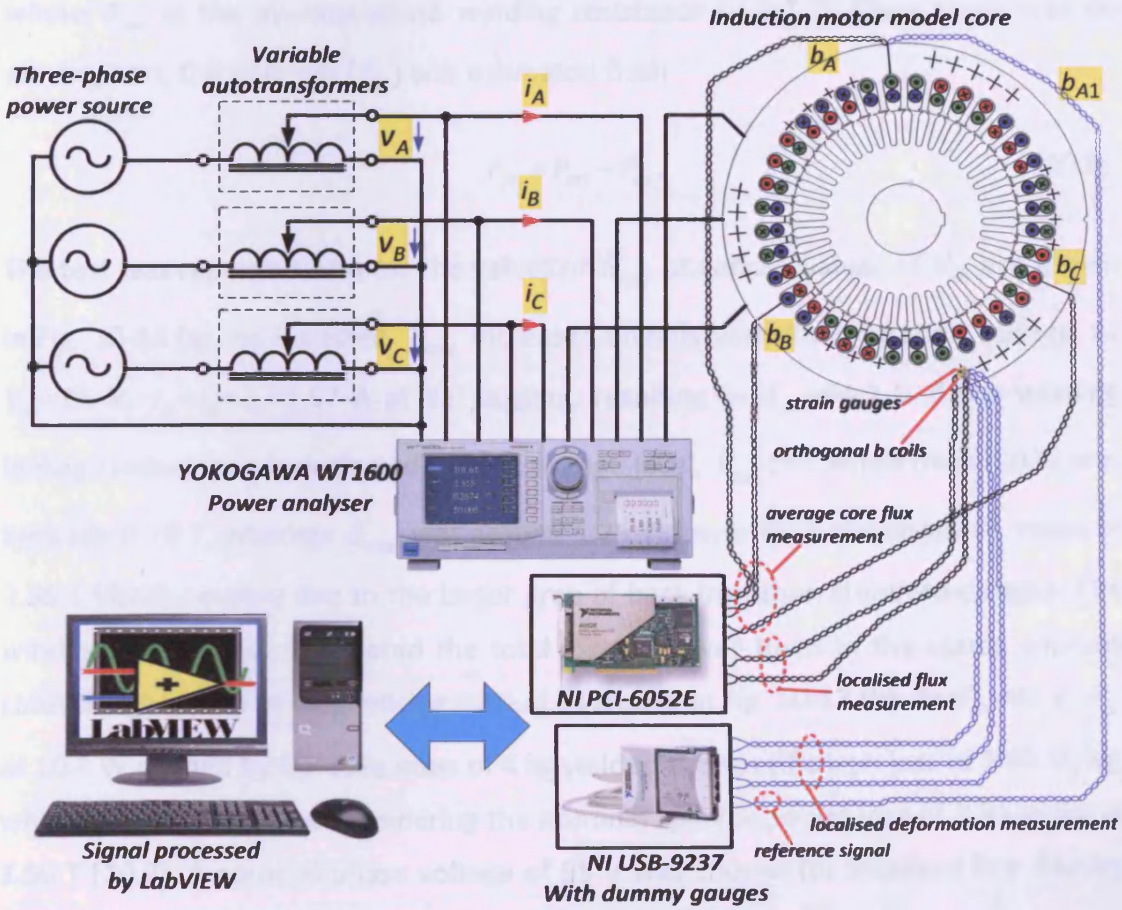

Fig. 10-12 Connection diagram of the system for measurement of localised flux density and core deformation

10.1.8 Preliminary test of the induction motor model core

The model core was initially tested under sinusoidal excitation at nominal phase voltage of 10 to 100 V, using the system in Fig. 10-12. The average peak value of back iron flux density ($\hat{B}_{core}$) was determined from

$$\hat{B}_{core} = (\hat{B}_A + \hat{B}_B + \hat{B}_C)/3 \tag{10.7}$$

where $\hat{B}_A$, $\hat{B}_B$ and $\hat{B}_C$ are the peak value of back iron flux densities. The RMS stator currents (I_A, I_B and I_A), total loss (P_{tot}), power factor, reactive power and apparent power were measured. Resistance of each phase winding measured by an ohm meter [*10.17*] at the room temperature was very close to each other. Thus, the winding copper loss (P_{cu}) was calculated from

$$P_{cu} = (I_A^2 + I_B^2 + I_C^2)R_{sw} \tag{10.8}$$

where R_{sw} is the average phase winding resistance of 6.7 Ω, Since there was no moving part, the iron loss (P_{fe}) was estimated from

$$P_{fe} = P_{tot} - P_{cu}. \tag{10.9}$$

The test was repeated 3 times. The values of $\hat{B}_{core}$ at various values of V_{ph} are shown in Fig. 10-13 (a). As expected, $\hat{B}_{core}$ increased linearly with the excitation voltage. At V_{ph}=95 V, $I_A = I_B = I_A$=1.57 A at 83° lagging, resulting in E_{ph}=94.2 V if the winding leakage inductance is neglected. At this voltage level, $\hat{B}_{ag}$ calculated from (10.6) was typically 0.70 T, whereas $\hat{B}_{core}$ was around 1.25 T, lower than the common value of 1.30 T [*10.2*] possibly due to the larger area of back iron than standard designs. The winding copper loss dominated the total loss as fewer turns in the stator winding caused high values of magnetising current as shown in Fig. 10-13 (b). At V_{ph}=95 V, P_{fe} of 10.4 W divided by the core mass of 4 kg yielded the specific iron loss of 2.60 W/kg, which is a realistic value considering the nominal specific power loss of 3.31 W/kg at 1.50 T [*10.7*]. A nominal phase voltage of 95 V was chosen for localised flux density and deformation measurements because of the peak air gap flux density.

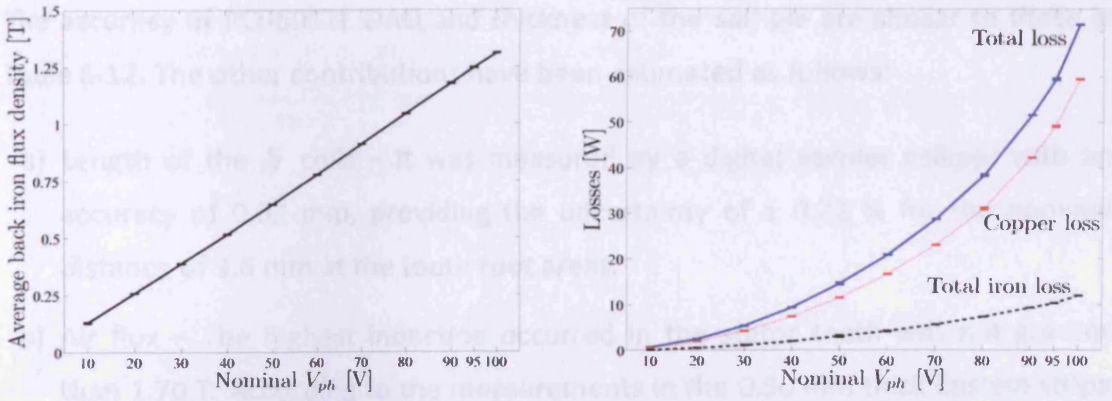

Fig. 10-13 Preliminary test results of the induction motor model core at different values of stator phase voltage: (a) average back iron flux density and (b) total loss, stator winding copper loss, and total iron loss

10.1.9 Uncertainties in localised flux density and deformation measurements

The evaluation of uncertainties in localised flux density and deformation measurements was carried out following the procedure in **Section 6.5.** The tooth root region was selected due to the smallest area of the *b* coils and lowest flux density as shown in Fig. 10-7 (a). Thus, the estimated uncertainties in this region should cover the other parts of the core.

Table 10-2 Uncertainty budget of peak flux density measurements of the induction motor model core

Sources of uncertainty	Value ±%	Probability distribution	Divisor	c_i	$u(x_i)$ ±%	v_i or v_{eff}
Accuracy of PCI-6052E DAQ	0.0050	Normal	2	1	0.0025	∞
Thickness of the sample	0.7500	Normal	2	1	0.3750	∞
Width of the *b* coils	0.2200	Normal	2	1	0.1100	∞
Air flux	0.6000	Rectangular	$\sqrt{3}$	1	0.3464	∞
Frequency variation	1.0000	Rectangular	$\sqrt{3}$	1	0.5774	∞
Misalignment angle	0.0110	Rectangular	$\sqrt{3}$	1	0.0064	∞
Stator voltages	0.5000	Normal	2	1	0.2500	∞
Type A uncertainty (repeatability)	0.4000	Normal	1	1	0.4000	4
Combined standard uncertainty		Normal			0.9103	∞
Expanded uncertainty $U(\hat{B})$		Normal (k_{95} =2)			1.8206	
Declared uncertainty at the confidence level of 95 %					2	

The accuracy of PCI-6052E DAQ and thickness of the sample are similar to those in Table 6-12. The other contributions have been estimated as follows:

a) Length of the b coils – It was measured by a digital vernier calliper with an accuracy of 0.02 mm, providing the uncertainty of ± 0.22 % for the nominal distance of 9.6 mm at the tooth root areas.

b) Air flux – The highest induction occurred in the stator teeth was not greater than 1.70 T. According to the measurements in the 0.50 mm thick Epstein strips at 1.70 T in **Chapter 8**, $\hat{H}$ was lower than 8 kA/m in any magnetising direction. This value caused $\hat{B}$=10 mT in paramagnetic materials, which was less than 0.6 % of 1.70 T.

c) Frequency variation – The National Grid guarantees the power frequency within ± 1 % [*10.18*].

d) Misalignment angle – Based on Fig 6-22, the misalignment angles of the b coils in the tooth root regions were estimated to be within ± 0.85°, resulting in a ± 0.11 % difference from the measurement direction.

e) Stator voltages– The largest uncertainty of the stator voltages was evaluated from the accuracy of the power meter [*10.14*] and repeatability measurements to be within ± 0.5 % at the confidence level of 95 % of the normal distribution.

f) Type A uncertainty – This value was evaluated from 5 repeated measurements. Peak values of flux density at all measurement points were within ± 0.4 %

The uncertainty estimation of peak to peak values of the components of the localised deformation in Table 10-3 is similar to that of $\lambda_{x_{PP}}$ and $\lambda_{y_{PP}}$ in Table 6-15 apart from the stator voltages and gauge factor. The stator voltages were considered as the controlled input variables instead of b_x and b_y in Table 6-15. The ± 0.4 % accuracy of the SGD-3/350-LY11 strain gauge listed in Table 10-1 was used as a source of the uncertainty.

Table 10-3 Uncertainty budget of peak to peak values of the radial and tangential components of the localised deformation in the induction motor model core

Sources of uncertainty	Value ±%	Probability distribution	Divisor	c_i	$u(x_i)$ ±%	v_i or v_{eff}
Accuracy of USB-9237 DAQ	0.050	Normal	2	1	0.025	∞
Accuracy of shunt calibration resistor of USB-9237 DAQ	0.110	Normal	2	1	0.055	∞
Stator voltages	0.500	Normal	2	2	0.500	∞
Gauge factor	0.400	Normal	2	1	0.200	∞
Error of gauge factor due to 5°C change of sample temperature	0.050	Normal	2	1	0.025	∞
Misalignment angle	0.070	Rectangular	$\sqrt{3}$	2	0.081	∞
Type A uncertainty (repeatability)	2.800	Normal	1	1	2.800	4
Combined standard uncertainty		Normal			2.853	∞
Expanded uncertainty $U(\varepsilon_{PP})$		Normal (k_{95}=2)			5.706	
Declared uncertainty at the confidence level of 95 %					6	

10.2 System for Measurements of Magnetostriction and Specific Power Loss in the 0.50 mm Thick NO Steel under Magnetisation Conditions Present in the Induction Motor Model Core

The 2D magnetisation system described in **Section 6.3** was used for measurement of magnetostriction and specific power loss of the 0.50 mm thick disc sample under magnetisation conditions present in the induction motor model core. The waveforms of b_r and b_t at each point of the motor model core had been measured and recorded using the system shown in Fig. 10-12. The averaged waveforms over five repeated measurements were used. Since the 2D system controls and measures the flux density components in the RD and TD (b_x and b_y), b_r and b_t were then transformed to the x and y axes corresponding to the angular position of the orthogonal b coils using

$$\begin{bmatrix} b_x \\ b_y \end{bmatrix} = \begin{bmatrix} \cos\phi_m & -\sin\phi_m \\ \sin\phi_m & \cos\phi_m \end{bmatrix} \cdot \begin{bmatrix} b_r \\ b_t \end{bmatrix}. \tag{10.10}$$

The reference point (t=0) of the 2D system was the zero-crossing point of the positive slope of the b_x signal. However, most b_x waveforms obtained from (10.10) did not cross zero at t=0. For instance, b_x at point **YA1** ($b_{x_{YA1}}$) crosses zero at

$t \approx 14.5$ ms as shown in Fig. 10-14 (b). Therefore, the b_x and b_y waveforms were simultaneously shifted to the zero-crossing point of b_x before feeding into the 2D system. The shifted $b_{x_{YA1}}$ and $b_{y_{YA1}}$ waveforms were named $b_{x_{YA1}}^{acw0}$ and $b_{y_{YA1}}^{acw0}$ corresponding to the rotation direction as displayed in Fig. 10-14 (c). In addition, the measurement of the specific power loss must be performed under the ACW and CW field rotating directions as discussed in **Section 6.3.5**. Thus, the b_x and b_y waveforms were also reversed and shifted. The reversed and shifted $b_{x_{YA1}}$ and $b_{y_{YA1}}$ ($b_{x_{YA1}}^{cw0}$ and $b_{y_{YA1}}^{cw0}$) are displayed in Fig. 10-14 (d). It can be seen in Fig. 10-15 (b) to (c) that the loci of $b_{x_{YA1}} - b_{y_{YA1}}$, $b_{x_{YA1}}^{acw0} - b_{y_{YA1}}^{acw0}$ and $b_{x_{YA1}}^{cw0} - b_{y_{YA1}}^{cw0}$ were similar in shape but different in starting points and rotating directions.

The peak values and THD of b_x and b_y, and FF of $\mathrm{d}b_x/\mathrm{d}t$ and $\mathrm{d}b_y/\mathrm{d}t$ in the sample were controlled within ± 1 % of the reference b_x and b_y. The specific power loss was averaged from the measurements in the ACW and CW field rotation. The repeatability tests were carried out five times. Each time, the h coils were removed and re-attached to the sample. Measured components of flux density and magnetostriction along the x and y axes in the disc sample were finally transformed back to the original radial and tangential components.

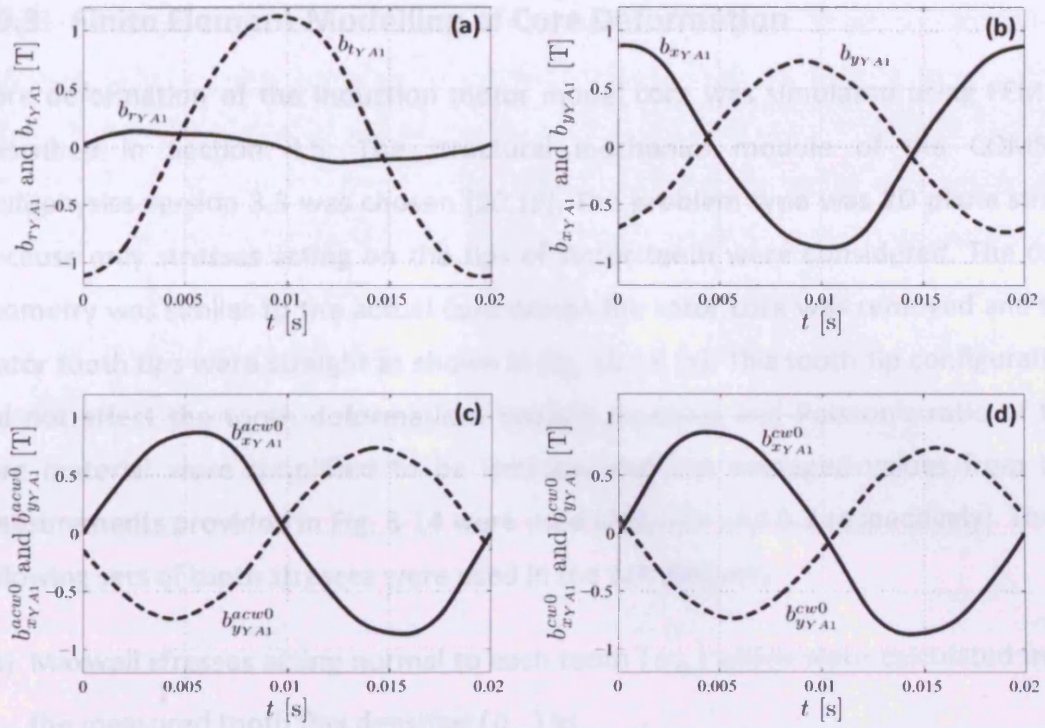

Fig. 10-14 Components of flux density at point YA1 of the induction motor model core: (a) radial and tangential components, (b) components in the RD and TD ($b_{x_{YA1}}$ and $b_{y_{YA1}}$), (c) shifted $b_{x_{YA1}}$ and $b_{y_{YA1}}$, and (d) reversed and shifted $b_{x_{YA1}}$ and $b_{y_{YA1}}$. Note that (c) and (d) were used as the reference signals of the 2D magnetisation system in the ACW and CW field rotation directions.

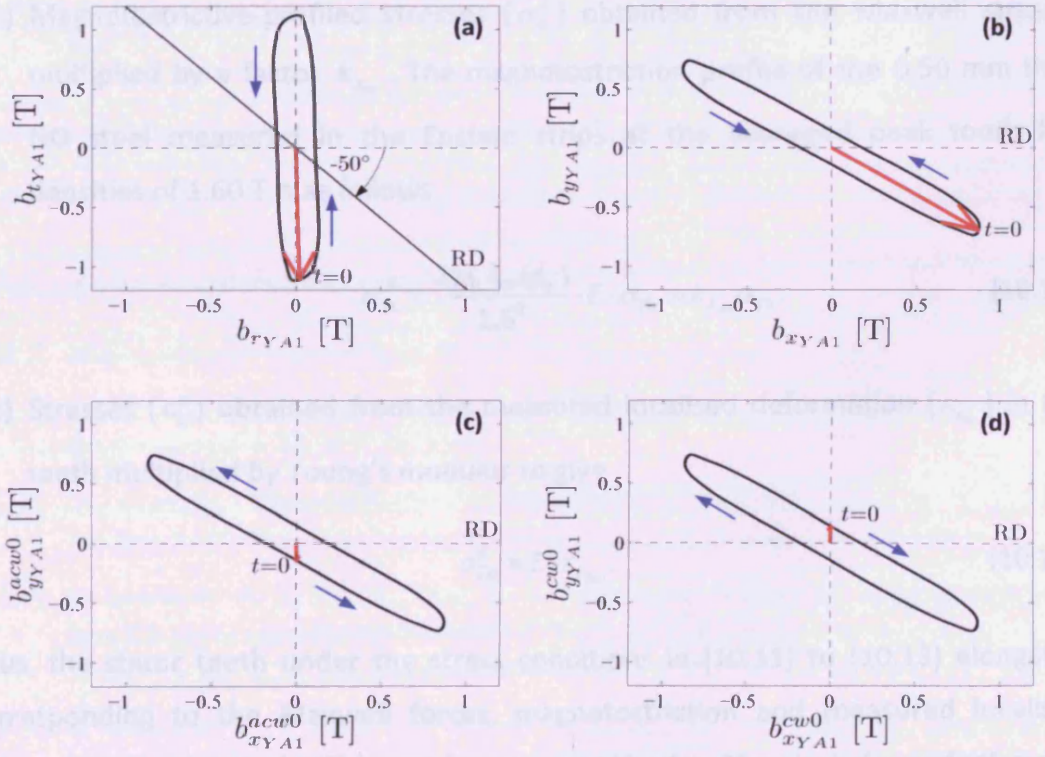

Fig. 10-15 Flux density loci at point YA1 in the core: (a) along the $r-t$ coordinate, (b) along the $x-y$ coordinate, (c) in the $x-y$ coordinate with shifted $b_{x_{YA1}}$ and $b_{y_{YA1}}$, and (d) reversed and shifted $b_{x_{YA1}}$ and $b_{y_{YA1}}$ in the $x-y$ coordinate

10.3 Finite Element Modelling of Core Deformation

Core deformation of the induction motor model core was simulated using FEM as described in Section 4.5. The structural mechanics module of the COMSOL multiphysics version 3.3 was chosen [*10.19*]. The problem type was 2D plane stress because only stresses acting on the tips of stator teeth were considered. The core geometry was similar to the actual core except the rotor core was removed and the stator tooth tips were straight as shown in Fig. 10-16 (a). This tooth tip configuration did not affect the tooth deformation. Young's modulus and Poisson's ratio of the core material were simplified to be isotropic and the averaged values from the measurements provided in Fig. 8-14 were used (214 GPa and 0.3 respectively). Three following sets of tooth stresses were used in the calculations;

a) Maxwell stresses acting normal to each tooth (σ_{Tn}) which were calculated from the measured tooth flux densities ($b_{r_{Tn}}$) as

$$\sigma_{Tn} = \frac{b_{r_{Tn}}^2}{2\mu_0}. \tag{10.11}$$

b) Magnetostrictive-profiled stresses (σ_n^{λ}) obtained from the Maxwell stresses multiplied by a factor $k_{\lambda_{pp}}$. The magnetostriction profile of the 0.50 mm thick NO steel measured in the Epstein strips at the averaged peak tooth flux densities of 1.60 T is as follows

$$\sigma_{Tn}^{\lambda} = \frac{2\mu_0 \lambda_{pp}(\phi_m)}{1.6^2} \cdot E \cdot \sigma_{Tn} = k_{\lambda_{pp}} \sigma_{Tn}. \tag{10.12}$$

c) Stresses (σ_n^{ϵ}) obtained from the measured localised deformation ($\varepsilon_{r_{Tn}}$) in the teeth multiplied by Young's modulus to give

$$\sigma_{Tn}^{\varepsilon} = E \cdot \varepsilon_{r_{Tn}}. \tag{10.13}$$

Thus, the stator teeth under the stress conditions in (10.11) to (10.13) elongated corresponding to the Maxwell forces, magnetostriction and measured localised deformation respectively. The problems were solved in the time dependent mode with a time step of 20 μs. Thus, there were 1001 data points in one electrical cycle. The structure oscillated at about 4 kHz without material damping setting, but the

measured localised deformation waveforms shown in **Chapter 12** are smooth. Thus, damping factors were required to eliminate these high frequency components. Rayleigh damping shown in Fig. 4-7 was used and the frequency of interest was set between 25 Hz and 2 kHz. The damping factors of both frequencies were selected at 0.05, which lay in the damping range of most structures (0.02 to 0.07) as described in **Section 4.4**. So, the mass damping parameter α_d and stiffness damping parameter β_d calculated from (4.42) were put into the core material (15.52 s^{-1} and 7.9 μs respectively). As a result, the high frequency components were removed from simulated waveforms, for example the displacement along the *x* direction at point **1** shown Fig. 10-16 (b).

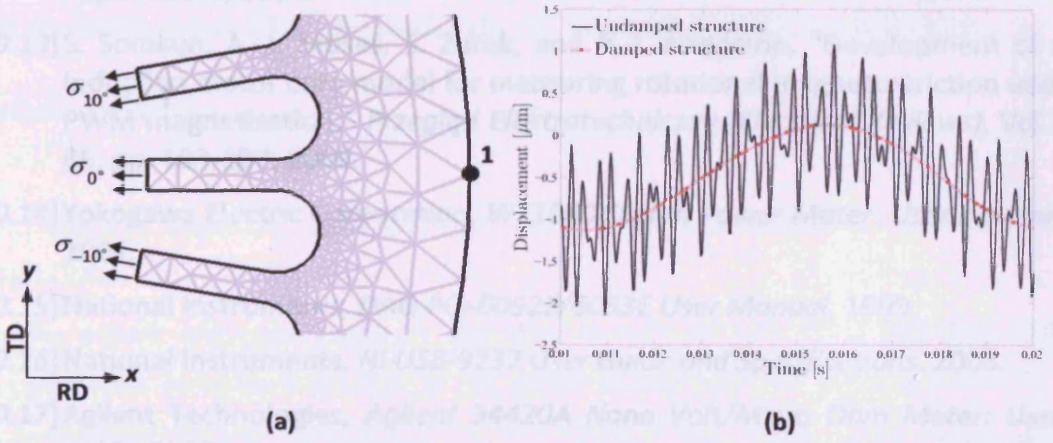

Fig. 10-16 (a) A section of the induction motor model stator core assembled from 6,570 triangular elements with a Maxwell stress acting on the normal direction of each stator tooth, (b) Comparison of displacements at point 1 in Fig. 10-16 (a) along the *x* direction with/without material damping

10.4 References for Chapter 10

[*10.1*] ABB, *Low and High Voltage Process Performance Motors*, 2006.

[*10.2*] C. S. Siskind, *Induction Motors: Single-phase and polyphase*, McGraw-Hill Book Company, New York, 1958.

[*10.3*] M. J. Melfi, "Optimum pole configuration of variable speed AC induction motors," *IEEE Industry Applications Magazine*, Vol. 3, pp. 15-20, 1997.

[*10.4*] S. Somkun, A. J. Moses, and P. I. Anderson, "Effect of magnetostriction anisotropy in nonoriented electrical steels on deformation of induction motor stator cores," *IEEE Transactions on Magnetics*, Vol. 45, pp. 4744-4747, 2009.

[*10.5*] R. Deshmukh, *Voltage Harmonics Analysis and Efficiency of Three-phase Induction Motor with Change in Coil Pitch of The Stator Winding*, PhD Thesis, Cardiff University, United Kingdom, 2006.

[10.6] Infolytica Corporation, *An Introduction to MagNet for Static 2D Modeling*, 2007.

[10.7] ThyssenKrupp Steel Europe, *Power Core® M400-50A Elektroband NO/NGO Electrical Steel*, 2009.

[10.8] Manufacturing Engineering Centre (MEC) Cardiff University, http://www.mec.cf.ac.uk/services/?view=edm&style=plain

[10.9] N. Takahashi, H. Morimoto, Y. Yunoki, and D. Miyagi, "Effect of shrink fitting and cutting on iron loss of permanent magnet motor," *Journal of Magnetism and Magnetic Materials*, Vol. 320, pp. e925-e928, 2008.

[10.10] FCI, *D-sub Crimp Connector*, 2008.

[10.11] Omega Engineering, *Triaxial Strain Gages 0/45°/90°*, 2008.

[10.12] Omega Engineering, *General Purpose Strain Gages for Static and Dynamic Applications*, 2008.

[10.13] S. Somkun, A. J. Moses, S. Zurek, and P. I. Anderson, "Development of an induction motor core model for measuring rotational magnetostriction under PWM magnetisation," *Przegląd Elektrotechniczny (Electrical Reviews)*, Vol. R. 85, pp. 103-107, 2009.

[10.14] Yokogawa Electric Corporation, *WT1600 Digital Power Meter: User's manual*, 2004.

[10.15] National Instruments, *DAQ PCI-6052E/6053E User Manual*, 1999.

[10.16] National Instruments, *NI USB-9237 User Guide and Specifications*, 2008.

[10.17] Agilent Technologies, *Agilent 34420A Nano Volt/Micro Ohm Meter: User's guide*, 2003.

[10.18] National Grid, *GB Transmission System Performance Report: 2008 - 2009*, 2009.

[10.19] COMSOL AB., *COMSOL Multiphysics 3.3: Structural mechanics module user's guide*, 2006.

Chapter 11

Measurements and Simulations of Localised Flux Densities and Deformation of the Induction Motor Model Core

This chapter presents measurement results of localised flux densities and deformation measured in the induction motor model core. Magnetostriction and specific power loss measured in the disc sample of the core material under magnetisation conditions present in the motor model core are provided, leading to an estimation of loss distribution in the stator core. Stator core deformation obtained from FEM described in **Chapter 10** is also shown.

11.1 Measurements of Components of Localised Flux Density in the Induction Motor Model Core

Results of localised flux density measurements in the induction motor model core under three-phase sinusoidal voltage excitation at the nominal phase voltage of 95 V ± 0.5 %, 50 Hz using the system described in **Section 10.1.7** are presented in this section. The uncertainties in localised flux density and deformation measurements are presented in **Section 10.1.9**.

The instantaneous back iron flux densities $b_A(t)$, $b_B(t)$ and $b_C(t)$ are shown in Fig. 11-1. The waveforms of radial tooth flux densities ($b_{r_{T0}}$ to $b_{r_{T9}}$), calculated from the voltage induced in the b coils of **T** group shown in Fig. 10-9, are compared in Fig. 11-

2. Components of flux density at the back of stator teeth, point **1** of **YA** group are electrically and physically identical to those at the back of the stator tooth **T5** as described in **Section 10.1.3**. Thus, the components of flux density at the stator tooth, tooth root and back of stator teeth along the radial distance of the stator tooth **T5** are displayed in Fig. 11-3.

Loci of flux densities in the radial-tangential coordinate at the tooth roots, back of stator teeth and back of stator slots are displayed in Figs. 11-4 to 11-6 respectively. The b vectors at ωt =0° are indicated by the red arrows and the RD are also shown in the figures. All loci rotate in the anticlockwise direction.

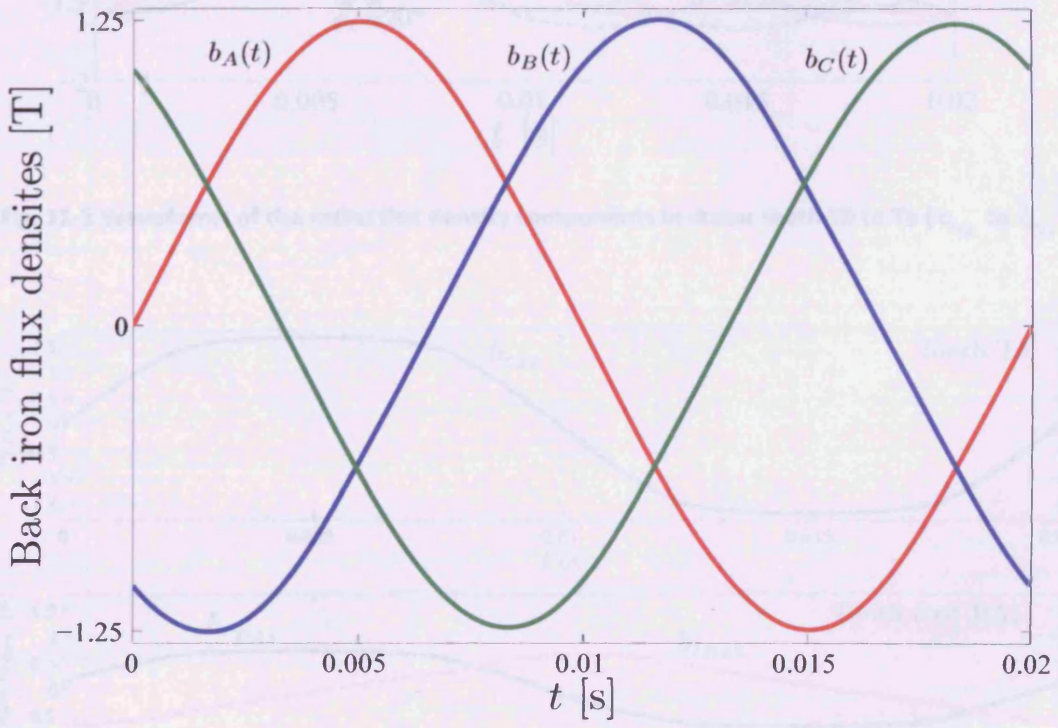

Fig. 11-1 Flux density waveforms $b_A(t)$, $b_B(t)$ and $b_C(t)$ at the back iron of the induction motor model core

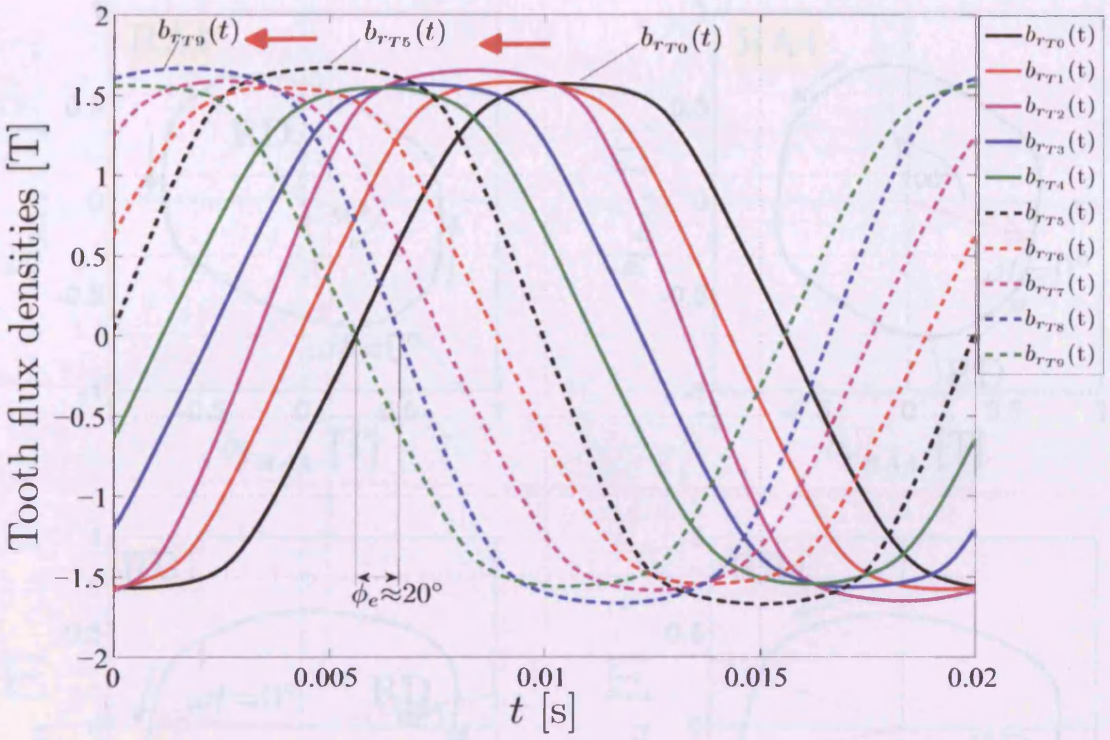

Fig. 11-2 Waveforms of the radial flux density components in stator teeth T0 to T9 ($b_{r_{T0}}$ to $b_{r_{T9}}$)

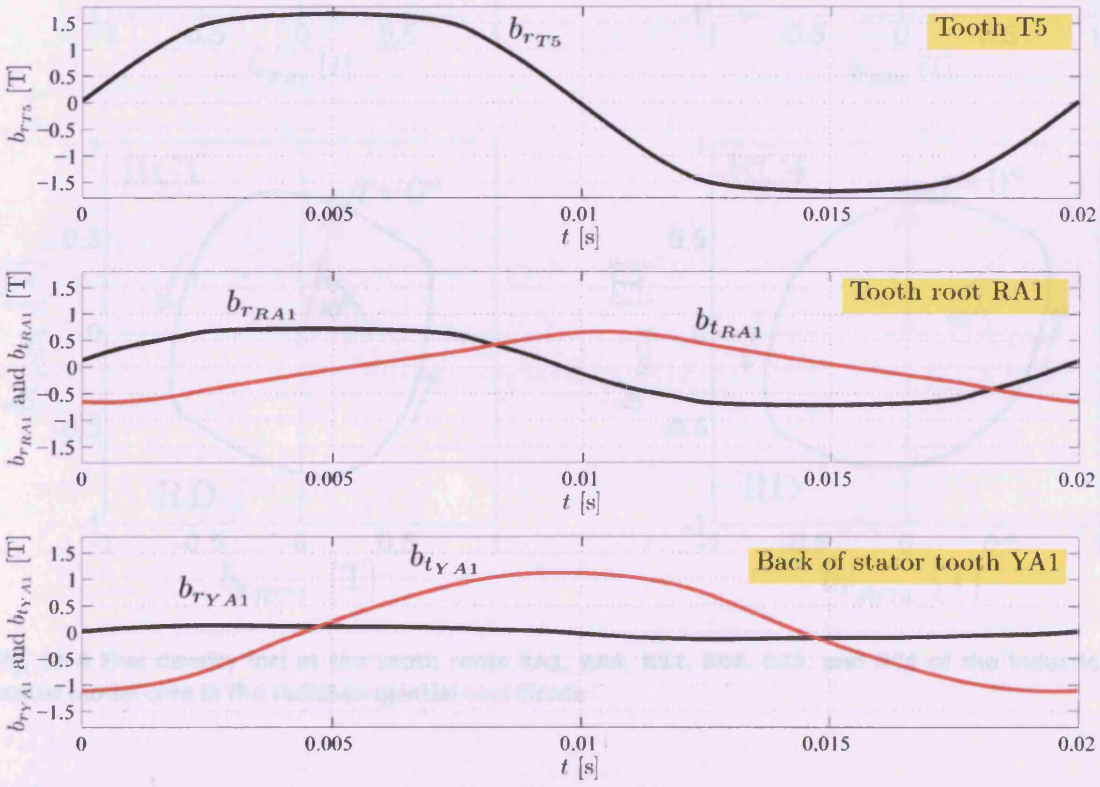

Fig. 11-3 Components of flux density at the stator tooth T5, tooth root RA1 and back of stator tooth YA1

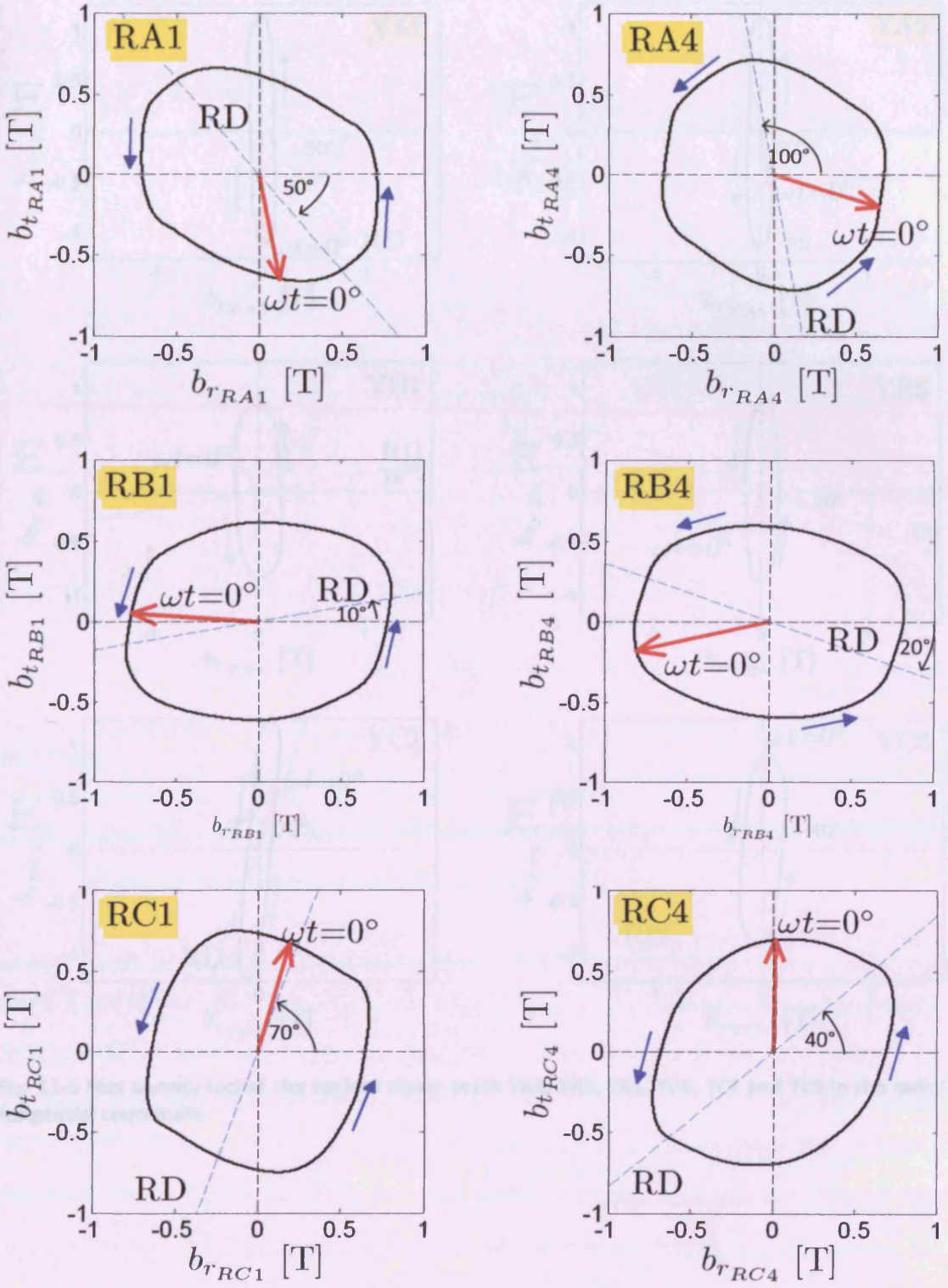

Fig. 11-4 Flux density loci at the tooth roots RA1, RA4, RB1, RB4, RC1, and RC4 of the induction motor model core in the radial-tangential coordinate

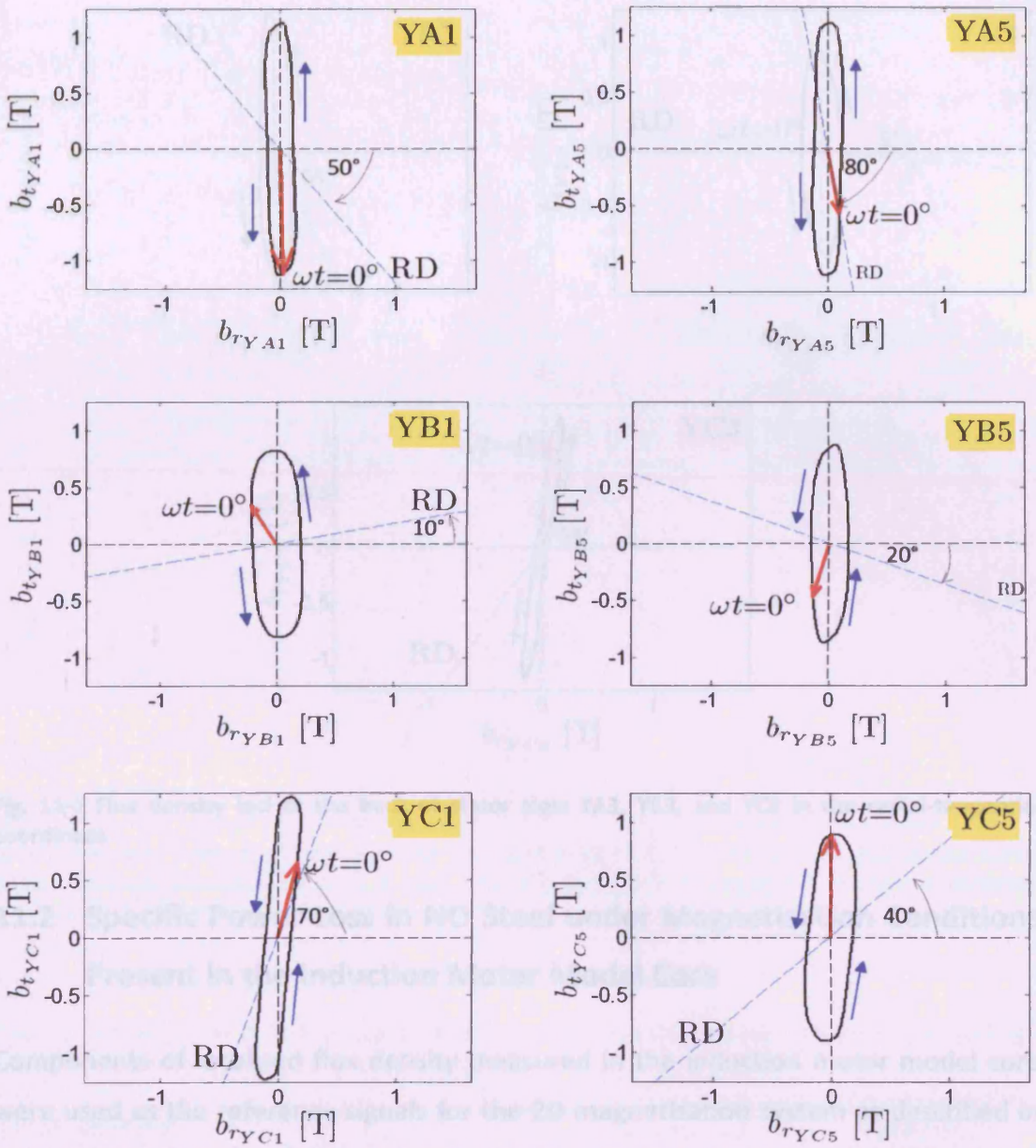

Fig. 11-5 Flux density loci at the back of stator teeth YA1, YA5, YB1, YB5, YC1 and YC5 in the radial-tangential coordinate

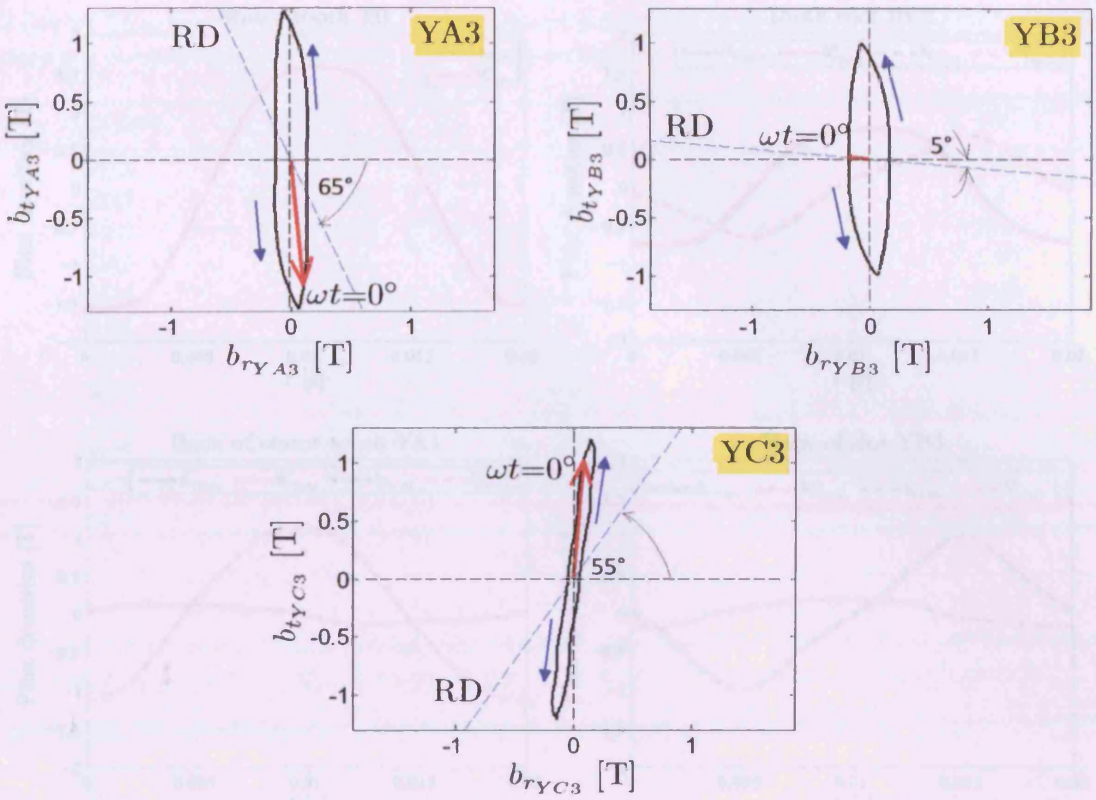

Fig. 11-6 Flux density loci at the back of stator slots YA3, YB3, and YC3 in the radial-tangential coordinate

11.2 Specific Power Loss in NO Steel under Magnetisation Conditions Present in the Induction Motor Model Core

Components of localised flux density measured in the induction motor model core were used as the reference signals for the 2D magnetisation system as described in **Section 10.2**. Radial and tangential flux density waveforms measured in stator tooth **T0**, tooth root **RC2**, back of the stator tooth **YA1**, and back of the stator slot **YB3** are compared with those controlled and measured in the 0.50 mm thick disc sample in Fig. 11-7. Tables 11-1 to 11-3 list the peak radial and tangential flux densities ($\hat{B}_r$ and $\hat{B}_t$) measured in the motor model core and the corresponding specific power loss measured in the disc sample. The angle between the RD to the radial direction is ϕ_m. The uncertainties in flux density, loss and magnetostriction measurements evaluated in **Section 6.5** also cover the measurements in this section. Loss distribution in a section of the core estimated from the loss measurements in the disc sample under localised magnetisation conditions in the core is shown in Fig. 11-8.

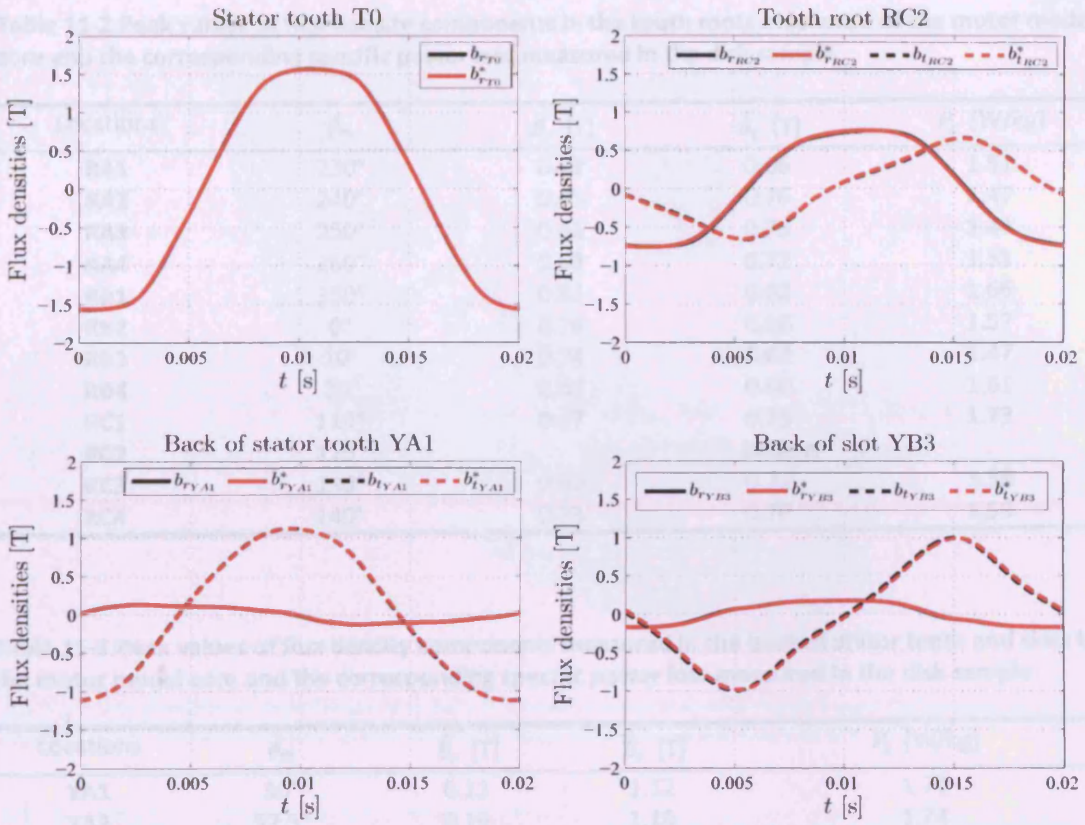

Fig. 11-7 Comparisons of the radial and tangential flux density components of the stator tooth T0, tooth root RC2, back of the stator tooth YA1, and back of the slot YB3, measured in the motor model core and simulated in the 0.50 mm thick disc sample (The symbol * denotes the simulated waveforms in the 2D magnetisation system)

Table 11-1 Peak values of tooth flux density measured in the motor model core and corresponding specific power loss measured in the disk sample

Locations	ϕ_m	$\hat{B}_r$ [T]	P_s [W/kg]
T0	0°	1.57	3.21
T1	10°	1.58	3.38
T2	20°	1.65	4.33
T3	30°	1.57	3.65
T4	40°	1.55	3.59
T5	50°	1.67	5.22
T6	60°	1.55	3.97
T7	70°	1.59	4.42
T8	80°	1.67	5.36
T9	90°	1.55	4.19

Table 11-2 Peak values of flux density components in the tooth roots measured of the motor model core and the corresponding specific power loss measured in the disk sample

Locations	ϕ_m	$\hat{B}_r$ [T]	$\hat{B}_t$ [T]	P_s [W/kg]
RA1	230°	0.72	0.66	1.51
RA2	240°	0.65	0.76	1.47
RA3	250°	0.65	0.75	1.44
RA4	260°	0.68	0.72	1.53
RB1	350°	0.81	0.62	1.66
RB2	0°	0.76	0.66	1.57
RB3	10°	0.74	0.63	1.47
RB4	20°	0.82	0.60	1.61
RC1	110°	0.67	0.75	1.73
RC2	120°		Broken	
RC3	130°	0.69	0.72	1.58
RC4	140°	0.73	0.70	1.59

Table 11-3 Peak values of flux density components measured in the back of stator teeth and slots in the motor model core and the corresponding specific power loss measured in the disk sample

Locations	ϕ_m	$\hat{B}_r$ [T]	$\hat{B}_t$ [T]	P_s [W/kg]
YA1	50°	0.13	1.12	1.70
YA2	57.5°	0.16	1.19	1.74
YA3	65°	0.14	1.28	1.84
YA4	72.5°	0.12	1.17	1.56
YA5	80°	0.13	1.11	1.51
YB1	170°	0.22	0.82	1.30
YB2	177.5°	0.22	0.90	1.40
YB3	185°	0.17	1.00	1.60
YB4	192.5°	0.15	0.94	1.44
YB5	200°	0.16	0.87	1.31
YC1	290°	0.19	1.22	1.87
YC2	297.5°	0.18	1.20	1.80
YC3	305°	0.18	1.20	1.78
YC4	312.5°	0.25	1.07	1.58
YC5	320°	0.21	0.89	1.34

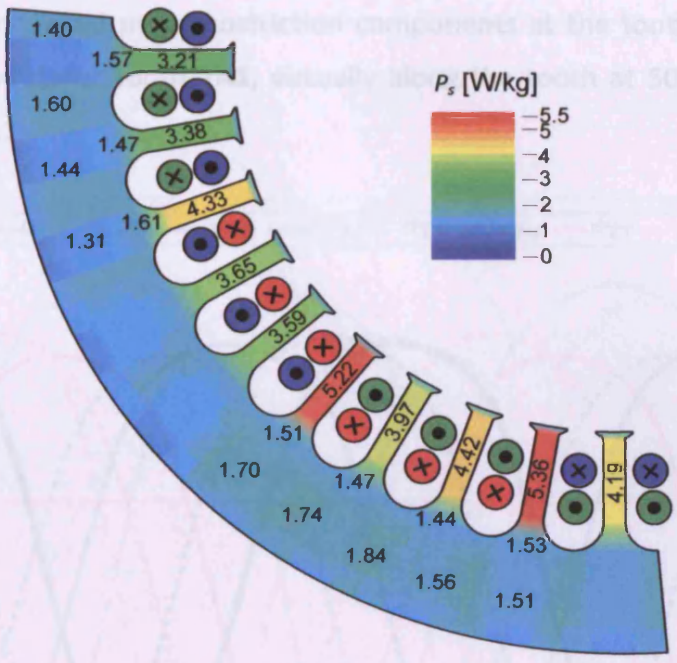

Fig. 11-8 Distribution of specific power loss in a section of the motor model core obtained from simulations in the disc sample under localised magnetisation conditions in the core

11.3 Measurements and Simulations of Localised Core Deformation and Magnetostriction

Waveforms of Maxwell stresses σ_{Tn} acting on stator teeth **T0** to **T9** calculated from (10.11) are displayed in Fig. 11-9. A strain due to the Maxwell force in each stator tooth ($\varepsilon^{M}_{r_{Tn}}$) was calculated from σ_{Tn} and the corresponding Young's modulus at angles to the RD (ϕ_m) as

$$\varepsilon^{M}_{r_{Tn}} = \frac{1}{E(\phi_m)} \cdot \sigma_{Tn} \,. \tag{11.1}$$

Tooth flux density waveforms were fed into the 2D magnetisation system and the corresponding magnetostriction $\lambda_{r_{Tn}}$ along the magnetisation direction in the 0.50 thick disc sample was measured. Peak to peak values of $\varepsilon_{r_{Tn}}$, $\varepsilon^{M}_{r_{Tn}}$ and $\lambda_{r_{Tn}}$ ($\varepsilon_{r_{T}PP}$, $\varepsilon^{M}_{r_{Tn}PP}$ and $\lambda_{r_{Tn}PP}$) of stator teeth **T0** to **T9** with respect to the RD are compared in Fig. 11-10. Table 11-4 provides the peak to peak values of components of localised deformation measured in the tooth root and back iron regions of the motor model core, and magnetostriction measured in the 0.50 mm thick disc sample under localised magnetisation conditions in the core. The waveforms of localised deformation, and

measured and modelled magnetostriction components at the tooth **T5**, tooth root **RA1**, and back of stator tooth **YA1**, virtually along the tooth at 50° to the RD, are given in Fig. 11-11.

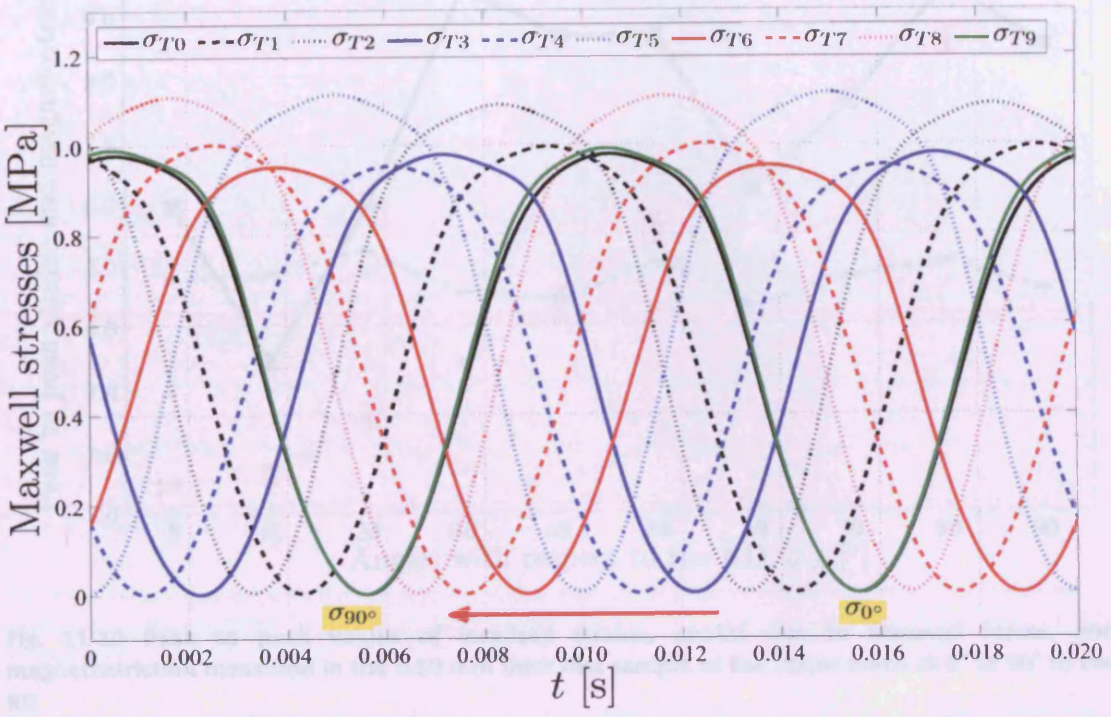

Fig. 11-9 Calculated Stresses due to the Maxwell forces acting on the tips of stator teeth T0 to T9

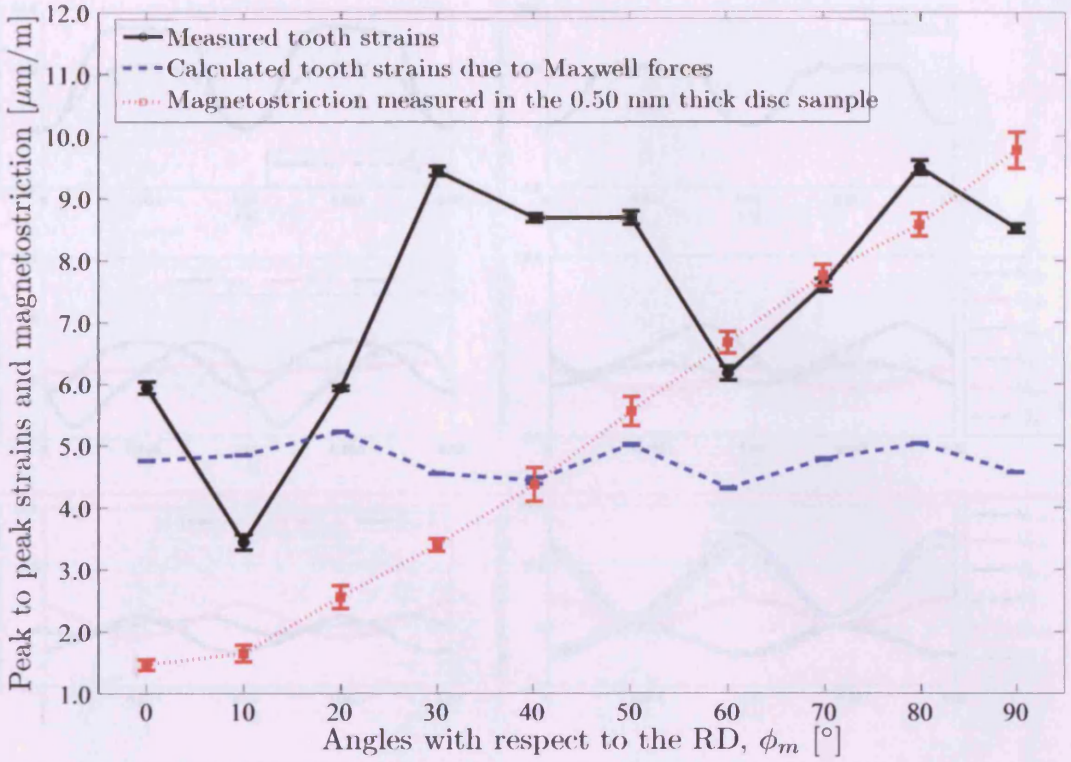

Fig. 11-10 Peak to peak values of localised strains, strains due to Maxwell forces, and magnetostriction measured in the 0.50 mm thick disc sample of the stator teeth at 0° to 90° to the RD

Table 11-4 Peak to peak values of components of localised deformation measured in the motor model core and magnetostriction measured in the 0.50 mm disc sample

Locations	Peak to peak localised deformation [μm/m]			Peak to peak magnetostriction [μm/m]		
	$\varepsilon_{r_{pp}}$	$\varepsilon_{t_{pp}}$	$\gamma_{rt_{pp}}$	$\lambda_{r_{pp}}$	$\lambda_{t_{pp}}$	$\gamma^{\lambda}_{rt_{pp}}$
YA1	3.1	2.9	1.6	3.0	2.6	7.4
YA2	2.8	3.9	1.7	1.8	1.3	5.1
YA3	2.8	2.8	0.7	1.6	1.2	4.8
YA4	2.5	2.7	1.1	1.2	1.1	2.9
YA5	1.9	3.3	1.2	1.1	1.0	2.1
YB1	5.5	3.7	2.0	3.4	3.1	4.9
YB2	4.2	2.5	1.9	4.3	4.0	4.2
YB3	4.2	3.1	1.2	5.5	4.9	3.8
RA1	4.4	1.2	7.1	2.3	2.0	4.4
RA4	2.8	0.9	6.9	2.8	2.3	4.2
RB2	2.7	1.4	4.5	2.2	2.8	4.2

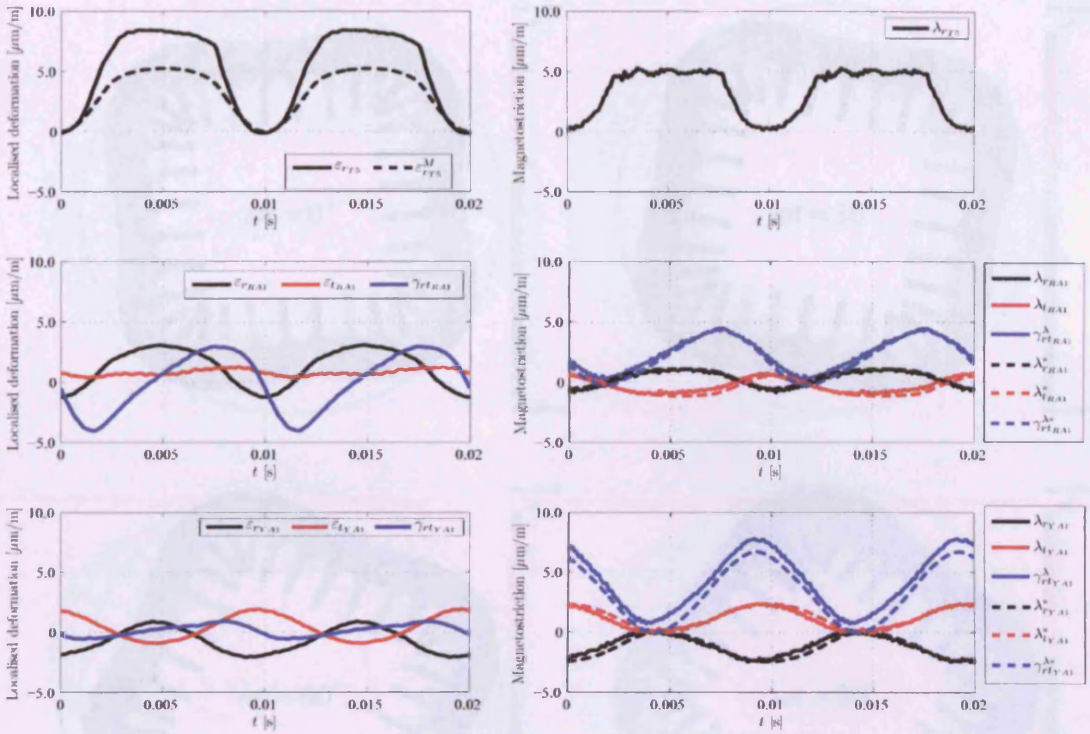

Fig. 11-11 Components of localised deformation, measured and modelled magnetostriction at the tooth T5, tooth root RA1, and back of stator tooth YA1 (virtually three points along the tooth at 50° to the RD)

Simulated core deformation at ωt = 0°, 30°, 60°, 90°, 120° and 150° using FEM with the Maxwell stresses σ_{Tn}, magnetostrictive-profiled stresses σ_{Tn}^{λ}, and the products of tooth strains and Young's modulus $\sigma_{Tn}^{\varepsilon}$ obtained from (10.11) to (10.13) applied to the stator teeth are shown in Figs. 11-12 to 11-14 respectively. Space harmonics of σ_{Tn} and $\sigma_{Tn}^{\varepsilon}$ under a pole at ωt = 0°, 30°, 60°, 90°, 120° and 150° are compared in Fig. 11-15.

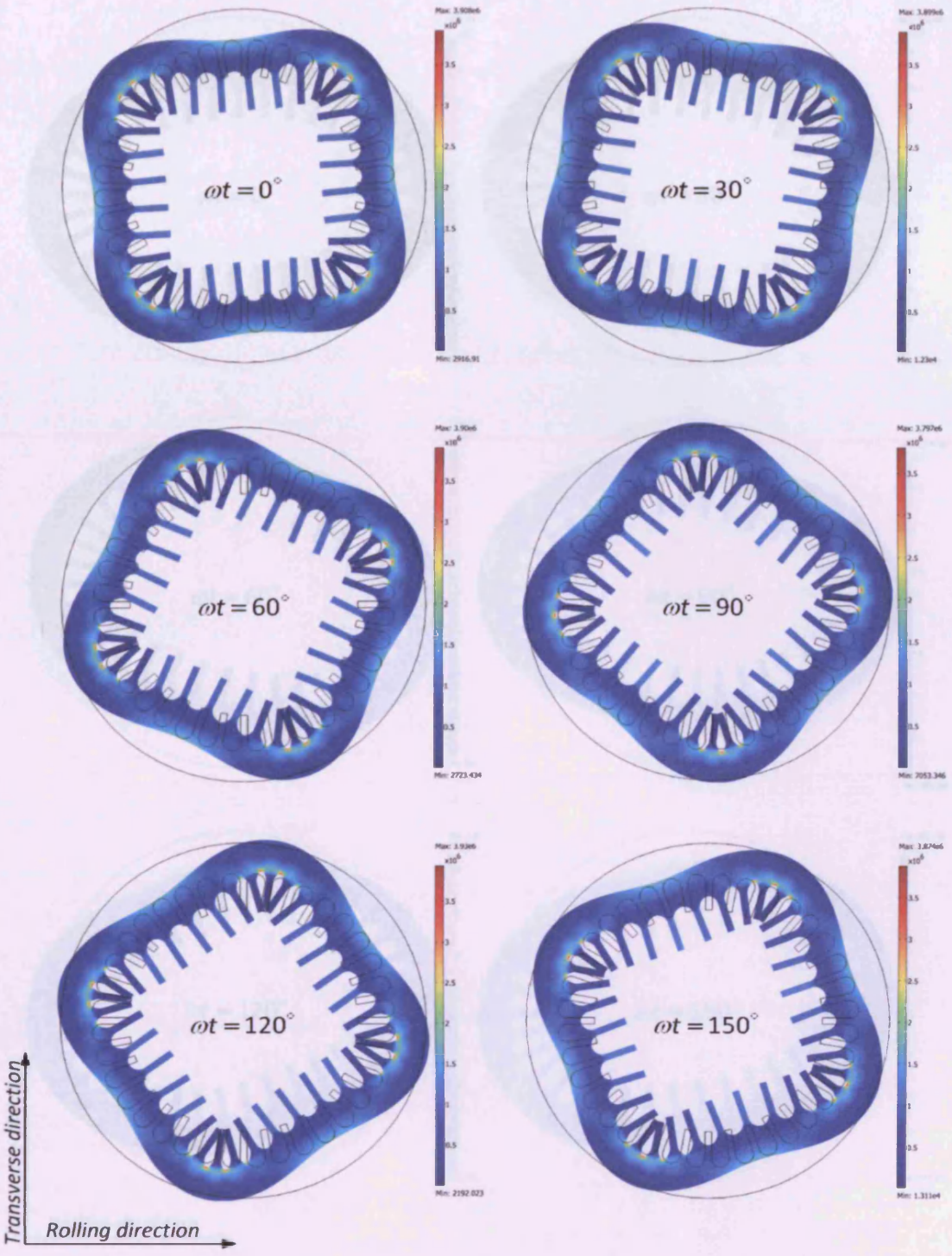

Fig. 11-12 Simulated core deformation due to the Maxwell stresses σ_{Tn} at the time instances ωt = 0°, 30°, 60°, 90°, 120° and 150°. The colour bars indicate the von Mises (scalar) stress.

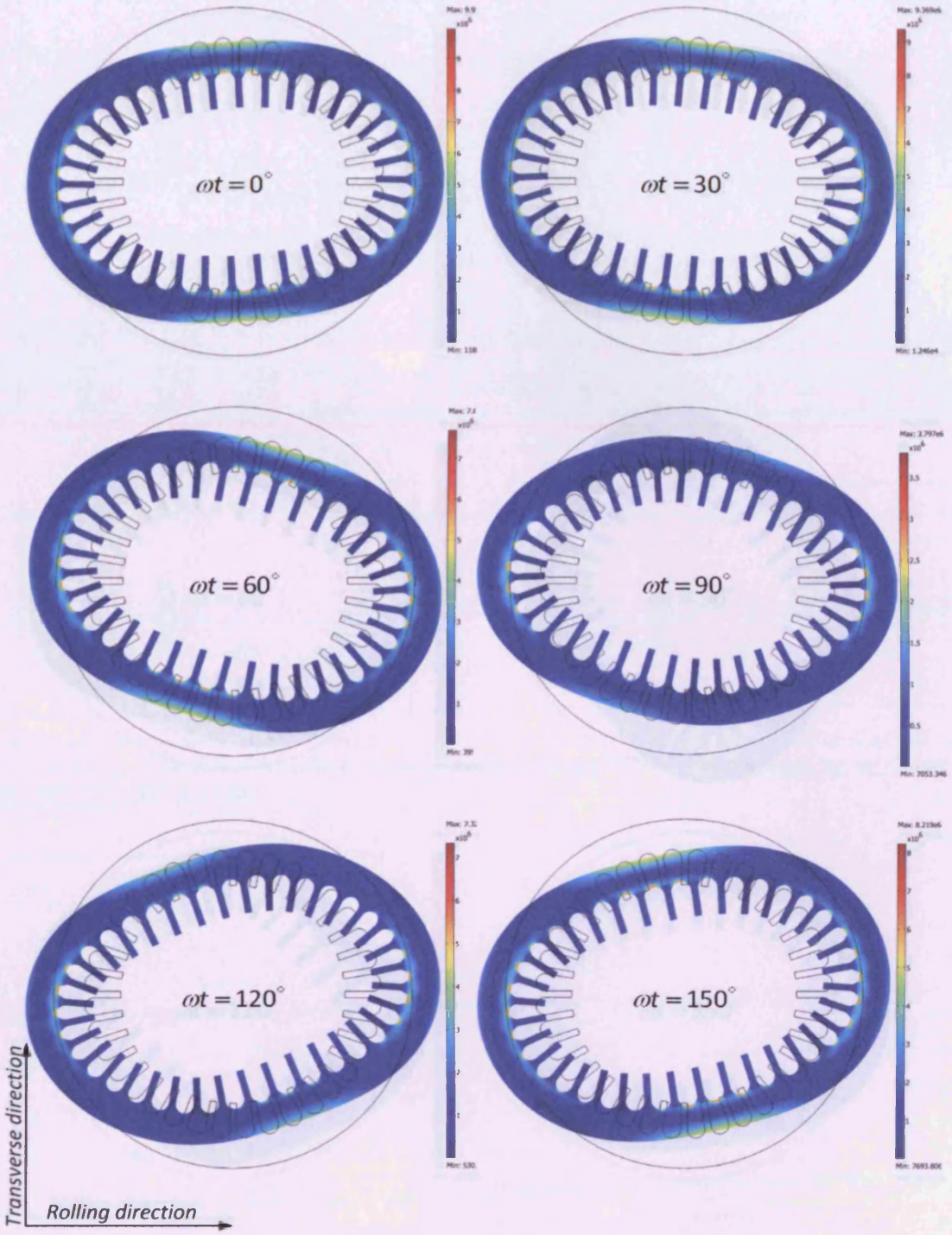

Fig. 11-13 Simulated core deformation due to the magnetostrictive-profiled stresses σ_{Tn}^{λ} at the time instances ωt = 0°, 30°, 60°, 90°, 120° and 150°. The colour bars indicate the von Mises (scalar) stress.

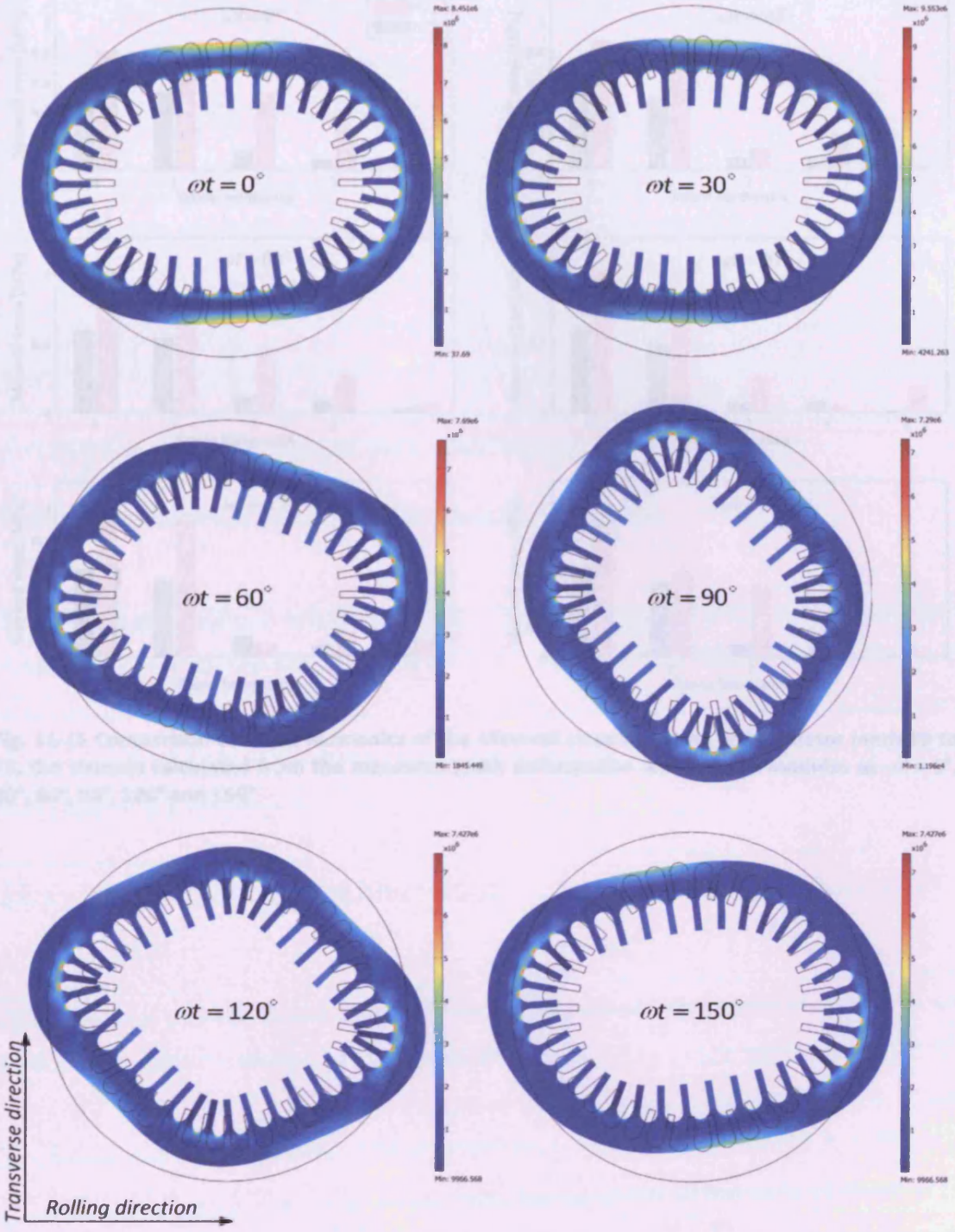

Fig. 11-14 Simulated core deformation due to the combination of Maxwell stresses and magnetostriction ($\sigma^{\varepsilon}_{T_n}$) at the time instances ωt = 0°, 30°, 60°, 90°, 120° and 150°. The colour bars indicate the von Mises (scalar) stress.

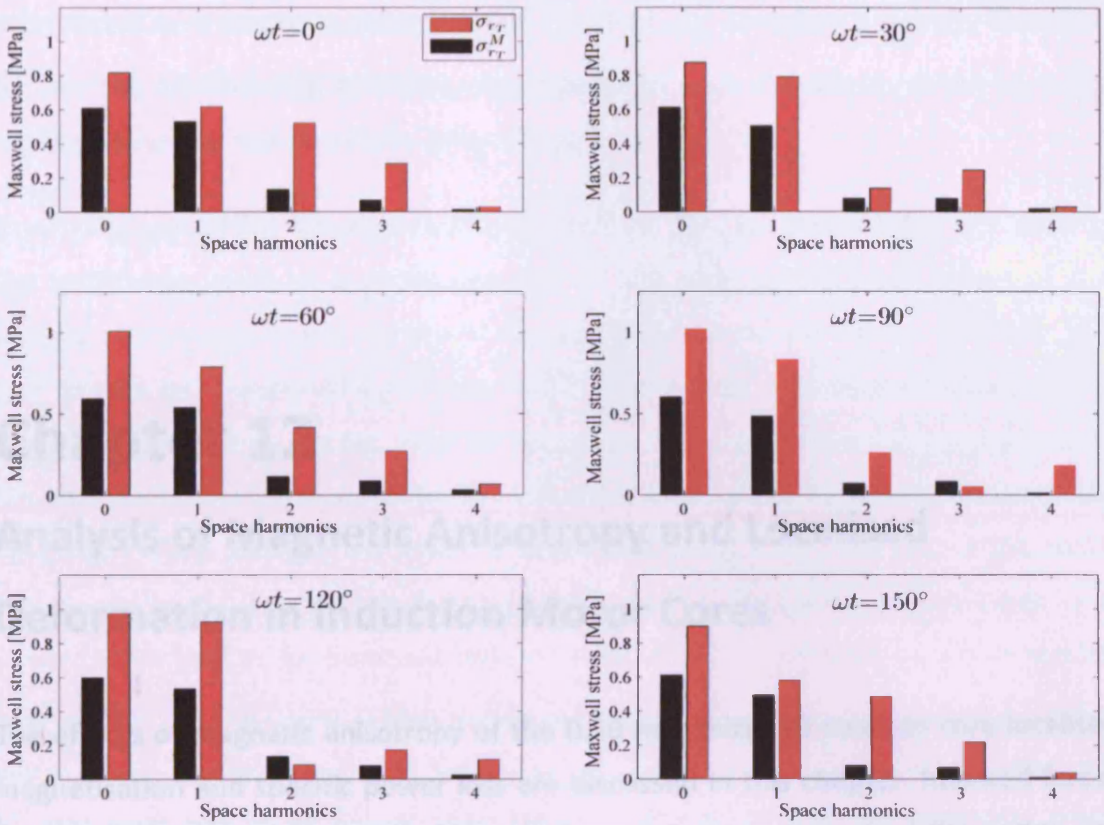

Fig. 11-15 Comparison of space harmonics of the Maxwell stresses acting on the stator teeth T0 to T9, the stresses calculated from the measured tooth deformation and Young's modulus at ωt = 0°, 30°, 60°, 90°, 120° and 150°

Chapter 12

Analysis of Magnetic Anisotropy and Localised Deformation in Induction Motor Cores

The effects of magnetic anisotropy of the 0.50 mm thick NO steel on core localised magnetisation and specific power loss are discussed in this chapter. Maxwell forces and the influence of magnetostrictive anisotropy on stator core deformation are described. Analytical calculations of localised deformation in the tooth root and back iron regions are presented.

12.1 Effects of Magnetic Anisotropy on Localised Flux Densities and Losses

At the back iron region, the shapes of flux density loci are angular dependent and their major axes lie along the tangential direction. The loci are slim and long if the tangential direction is close to the RD (**YA5** and **YC1** in Fig. 11.5, and **YA3** and **YC3** in Fig. 11-6), and become wider and shorter when rotating towards the TD (**YB1** and **YB5** in Fig. 11.5, and **YB3** in Fig. 11-6). Peak flux densities at the back of stator slots are always greater than those at the back of stator teeth due to flux concentration in smaller areas. The peak flux densities vary from 0.82 to 1.22 T at the back of stator teeth and 1.00 T to 1.28 T behind stator slots. This phenomenon can be explained by the anisotropy of AC relative permeability measured in Epstein strips of the core material shown in Fig. 8-3. At $\hat{B}$=1.00 T, $\mu_{r_{AC}}$ along the TD is about 32 % of that when magnetised along the RD because domain walls start to rotate at lower magnetisation when the magnetisation direction deviates from the RD as discussed

in **Section 9.1**. In addition, the anisotropy factor of $\mu_{r_{AC}}$ is high in the range from 0.90 to 1.10 T as shown in Fig. 9-5. Thus, the variation of peak flux density in the back iron regions should be higher than in other areas.

According to the FEM simulations displayed in Fig. 10-7 (a), circular flux loci occur in the tooth root areas at a radial distance of 132 mm, where peak values of flux density components in the radial and tangential directions are similar. However, the flux density loci measured by orthogonal *b* coils whose centres are located at the same radial distance (see Fig. 10-9 for locations of the *b* coils) exhibit a preference towards the RD as displayed in Fig. 11-4. Flux penetrates into the higher permeability direction before changing direction as illustrated in Fig. 12-1. The flux in the tooth cut along the TD (Fig. 12-1 (b)) rotates towards the RD quickly at the tooth root region, while that in the tooth cut along the RD (Fig. 12-1 (a)) tries to stay in the RD further into the back iron region before turning to the TD. The peak flux densities along the radial direction in the tooth roots and back iron of the teeth cut near the RD are expected to be higher than those of the teeth cut near the TD, which corresponds to the measurement results shown in Table 11-2 (between **RB2** and **RA4**) and Table 11-3 (between **YB1** and **YA5**).

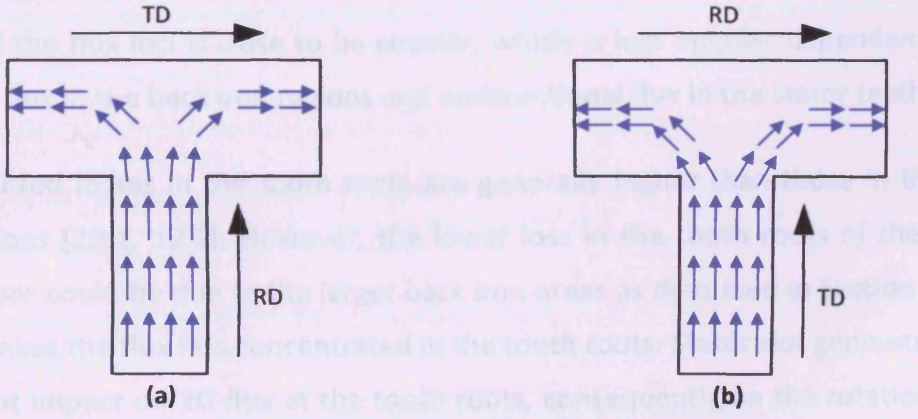

Fig. 12-1 Illustration of flux rotation towards the back iron of AC machine stator cores: (a) tooth cut along the RD, (b) along the TD

Peak flux densities in the stator teeth ($\hat{B}_{r_{T0}}$ to $\hat{B}_{r_{T9}}$) vary from 1.55 to 1.67 T as shown in Table 11-1. The highest tooth flux densities occurring in teeth **T2**, **T5** and **T8** are due to the flux concentration between coil groups of each phase of the stator windings as discussed in **Section 10.1.2**. Comparing peak flux densities among the teeth **T2**, **T5** and **T8**, and among the remaining teeth, the magnetic anisotropy has a

small impact. The first reason is $\mu_{r_{AC}}$ at 1.50 and 1.70 T as shown in Figs. 8-3 and 8-4 does not drop drastically when magnetised at angles to the RD compared with that at lower magnetisation, which is due to the dominance of domain wall rotation at high induction. The second reason is each stator tooth is subjected to a tension due to the Maxwell force in the air gap. The maximum stress is approximated as $\hat{B}_{r_m}^2/(2\mu_0)$, which ranges from 0.96 to 1.10 MPa. As discussed in Section 9.3, the magnetic properties along the tooth length could be improved by the tension due to the Maxwell force.

The corresponding localised specific power loss in the stator teeth simulated in the 2D magnetisation system shown in Fig. 11-8 has a similar trend as that measured in the Epstein strips under sinusoidal magnetisation 50 Hz displayed in Fig. 8-1. However, the tooth localised loss is greater than the loss in the Epstein strips due to the presence of harmonics in the tooth flux waveforms. Although the major axes of the flux loci of the back iron **YB** group are close to the TD, their resulting loss is less than **YA** and **YC** groups because of lower magnetisation levels as described earlier. The averaged localised losses in the teeth, tooth roots and back iron are 4.16, 1.56 and 1.58 W/kg and the loss variations in those regions are 52, 19, and 36 % respectively. The lowest loss variation in the tooth roots is due to the fact that the shape of the flux loci is close to be circular, which is less angular dependence than elliptical flux in the back iron regions and unidirectional flux in the stator teeth.

The localised losses in the tooth roots are generally higher than those in the back iron regions [*12.1, 12.2*]. However, the lower loss in the tooth roots of the motor model core could be due to the larger back iron areas as discussed in **Section 10.1.8**, which makes the flux less concentrated in the tooth roots. Stator slot geometry has a significant impact on 2D flux at the tooth roots, consequently on the rotational loss [*12.3*]. Shorter stator teeth imply higher rotational loss [*12.4*]. The circumferential variation of localised loss in the stator teeth is expected to cause errors in thermal rating calculation during the design stages. Temperature rise prediction of AC electrical machines relies on the accuracy of loss distribution, which is usually considered to be identical around the core circumference [*12.5, 12.6*].

12.2 Effect of Magnetostrictive Anisotropy on the Localised Deformation in the Stator Teeth

In this section, only the localised deformation, stresses due to Maxwell forces and magnetostrictive forces in the stator teeth are considered and the magnetostrictive forces in the tooth root and back iron regions are neglected. The localised deformation in the stator teeth has almost the same phase angle as their corresponding calculated Maxwell forces. For example, $\sigma_{r_{Ts}}$ in Fig. 11-9, and $\varepsilon_{r_{Ts}}$ and $\varepsilon^{M}_{r_{Ts}}$ in Fig. 11-11 reach minima at 0, 10 and 20 ms. The phase shift is not noticeable as the Maxwell stress is in the linear elastic range and the width of magnetostriction butterfly loops is also narrow (as observed from τ_m =0.17 ms in Table 8-3). The tooth deformation due to the Maxwell force $\varepsilon^{M}_{r_{Tn}PP}$ shown in Fig. 11-10 is isotropic. However, flux concentration in stator teeth **T2**, **T5** and **T8** makes their $\varepsilon^{M}_{r_{Tn}PP}$ greater than the others. In addition, $\varepsilon^{M}_{r_{Tn}PP}$ also slightly decreases with ϕ_m due to the increase in E as given in Fig. 8-12. It is observed that the magnetostrictive anisotropy contributing to the deformations in teeth **T0**, **T1** and **T2** are significantly lower than the others.

If the air gap is uniform, the stator winding is ideally sinusoidal distributed and there is only a radial component of flux density due to high permeability of the core material, the tooth flux density as a function of time and space is given by

$$b_{r_T}(t,\phi_m)=\hat{B}\sin(\omega t+p\phi_m)\,. \tag{12.1}$$

Using (10.11), the Maxwell stress is obtained from

$$\sigma_{r_T}(t,\phi_m)=\frac{\hat{B}^2}{4\mu_0}(1-\cos 2(\omega t+p\phi_m))\,. \tag{12.2}$$

It can be observed from (12.2) that there are two components of Maxwell force pulling the stator teeth towards the air gap: static and dynamic forces as demonstrated in Fig. 12-2 for the case of an ideal four-pole machine. The cycle number of the dynamic force wave equals the pole number of the stator winding and it travels around the stator teeth at twice the supply frequency.

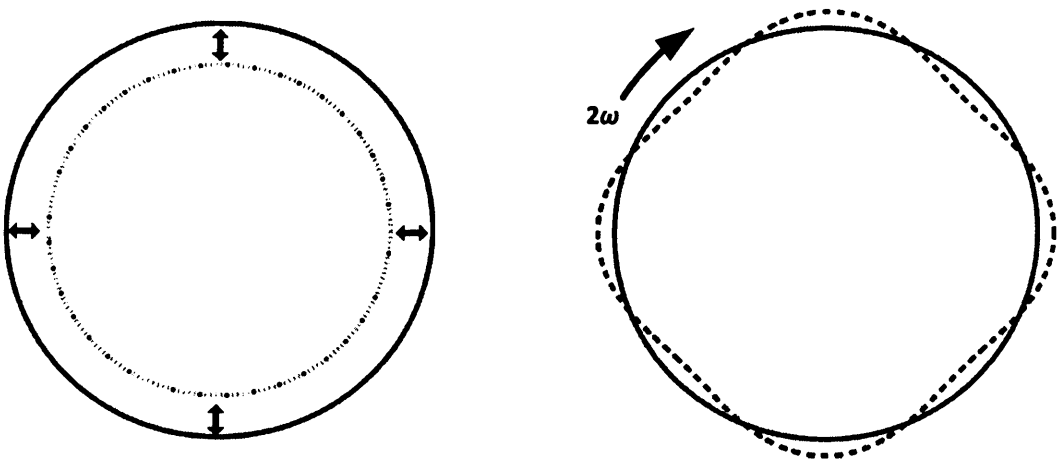

Fig. 12-2 Illustration of Maxwell force wave types in an ideal four-pole induction machine

If magnetostriction of the core material is zero or ideally isotropic, the couple between the Maxwell forces and magnetostriction will cause symmetrical deformation in the stator teeth with the dominant mode shape corresponding to the stator winding pole number as illustrated in Fig 11-12.

If the Maxwell forces were absence and only the magnetostrictive forces were considered, the stator core was able to deform only near the TD as shown in Fig. 11-13. This is mainly due to the magnetostrictive anisotropy. The presence of the anisotropy in magnetostriction can be still seen when coupled with the Maxwell forces as exhibited in Fig. 11-14. This causes the stator core to deform asymmetrically [*12.7*].

The fundamental component of the Maxwell stress in (12.2) is not considered as a source of acoustic noise because it is overshadowed by mechanical noise [*12.8*]. Magnetic sources of the acoustic noise radiated from an induction motor conventionally account for slot harmonics due to discontinuity of the air gap flux, stator and rotor winding space harmonics (high flux density at stator teeth **T2**, **T5**, **T8** etc.), rotor eccentricity, and saturation in flux density [*12.9*]. Considering the space harmonics of the calculated Maxwell stresses acting on the stator teeth **T0** to **T9** as shown in Fig. 11-15, the harmonic orders 2, 3, 4 etc., are found and they remain almost unchanged at difference time instances. These harmonics are due to the saturation of flux density in the stator teeth and flux concentration due to the stator winding. However, the measurements of the tooth deformations reveal that the magnetostriction of the core material increases magnitudes of space harmonics into

the radial stresses, especially those of higher harmonic orders. More importantly, the additional harmonics are time dependent because of the magnetostrictive anisotropy. It is expected that excess vibration and acoustic noise arise due to the magnetostriction, and the magnetostrictive anisotropy causes more complex shapes in the core vibration.

12.3 Localised Deformation in the Tooth Root and Back Iron Regions

The radial and tangential magnetostriction components measured in the disc sample under magnetisation conditions present in the back iron region provided in Table 11-4 correlate to those measured in the motor model core. However, the lower values of $\gamma_{rt_{pp}}$ compared to $\varepsilon_{r_{pp}}$ and $\varepsilon_{t_{pp}}$ indicate that the principal axes stay close to the radial and tangential axes, whereas the principal axes of magnetostriction try to stick to the TD due to the anisotropy as illustrated in Fig. 8-22. At the tooth root region where the flux loci are more circular, the core material mainly deforms along the radial direction, which can be observed from the lower values of $\varepsilon_{t_{pp}}$ at points **RA1**, **RA2**, and **RB2** in Table 11-4 and the waveforms shown in Fig. 11-11. Although the back iron and tooth root regions are not acted by the Maxwell forces directly, their resulting stress and strain from the stator teeth are still present. This makes the magnetostriction partially couple with the Maxwell forces.

The localised deformation ($\boldsymbol{\varepsilon}^*$) could be calculated analytically using

$$\boldsymbol{\varepsilon}^* = k_\lambda \boldsymbol{\lambda}^* + \boldsymbol{\varepsilon}^{M*} \tag{12.3}$$

where $\boldsymbol{\lambda}^*$ is the magnetostriction component obtained from the 2D magnetostriction model in (5.21), k_λ is the magnetostriction coupling constant, and $\boldsymbol{\varepsilon}^{M*}$ is the calculated components of strain due to the Maxwell forces. The back of stator slot **YB3**, back of stator tooth **YA1**, and tooth root **RA1** were selected and their $\boldsymbol{\varepsilon}^{M*}$ are determined from the schematic diagrams in Fig. 12-3. The Maxwell coupling constants k_M, k_{M1} and k_{M2} are introduced to adjust the intensity of the Maxwell stresses.

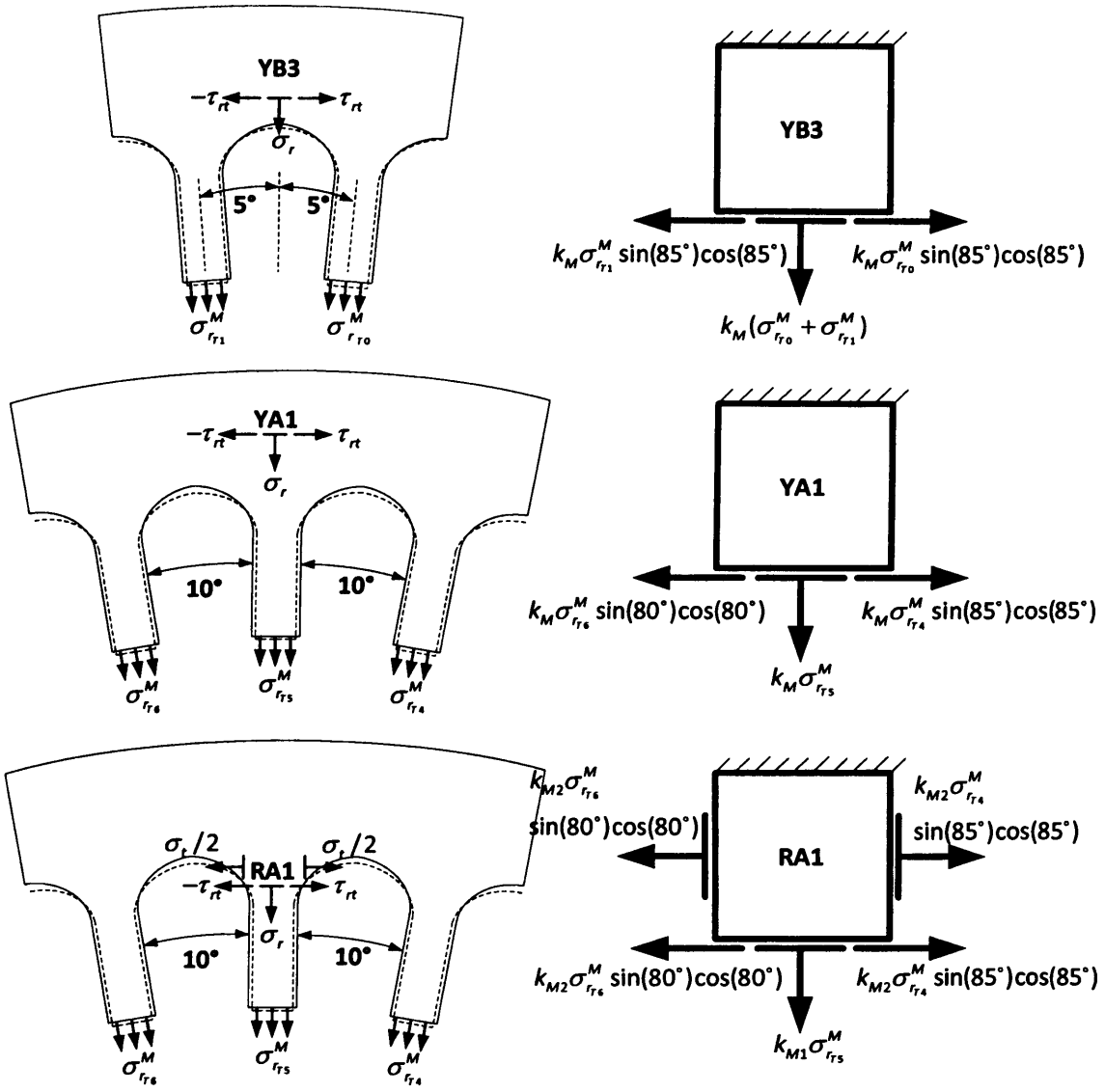

Fig. 12-3 Components of stress due to Maxwell forces at the back of slot YB3, back of stator tooth YA1 and tooth root RA1 for analytical determination of the corresponding strain components

At point **YB3**, the Maxwell stresses acting on teeth **T0** and **T1** ($\sigma_{r_{T0}}$ and $\sigma_{r_{T1}}$) are considered as the radial stress and their transformed tangential components are the shear components. The stator circumference is assumed to be fixed due to the clamping shown in Fig. 10-11. The averaged Young's modulus and Poisson's ratio taken from Fig. 8-12 (214 GPa and 0.30) were used and the resulting strains were obtained by (4.24). $\boldsymbol{\lambda}^*$ was simulated using the parameters listed in Table 8-3. Fig. 12-4 shows the calculated $\boldsymbol{\lambda}^*$, $\boldsymbol{\varepsilon}^{M*}$ and $\boldsymbol{\varepsilon}^*$ with k_λ=0.55 and k_M=0.15, compared with the measurements. The symbol * denotes the calculated waveforms.

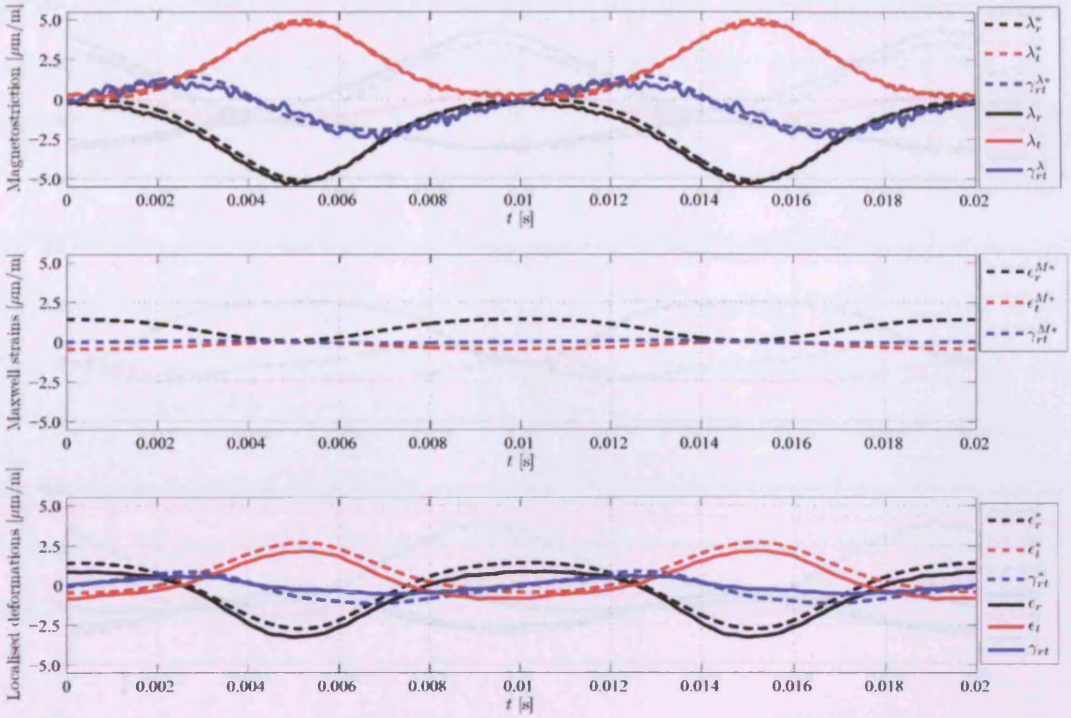

Fig. 12-4 Components of measured and calculated magnetostriction, strains due to Maxwell forces, and localised deformation at the back of stator slot YB3 with the coupling constants k_λ=0.55 and k_M=0.15

For **YA1**, $\sigma_{r_{T5}}$ is considered as the radial stress and the transformed tangential components of $\sigma_{r_{T4}}$ and $\sigma_{r_{T6}}$ of the adjacent teeth are the shear components. $\boldsymbol{\lambda}^*$, $\boldsymbol{\varepsilon}^{M*}$ and $\boldsymbol{\varepsilon}^*$ of **YA1** with k_λ=1.00 and k_M=0.20 are compared with the measurements in Fig. 12-5. ε_r^* and ε_t^* agree closely with the measured values, but γ_{rt}^* largely differs from the γ_{rt} because of the anisotropy. This large difference was not found in **YB3** because the major axis of its flux locus is already close to the TD. It was reported that a compressive stress applied to the RD of a GO steel decreased the anisotropy level [*12.10*]. Thus, the radial Maxwell stress and clamping stress could affect the domain structure of the material. In addition, the decrease of the magnetostrictive anisotropy may be due to the geometry-dependent magnetostriction as discussed in **Section 9.5**. Isotropic $\boldsymbol{\lambda}^*$ was simulated using the parameters shown in the Fig. 12-6. These parameters provided the same peak to peak values as the identified parameters in Table 8-3. It shows a better agreement between γ_{rt}^* and γ_{rt}, and the AC components of ε_r^* and ε_t^* remain close to the measured waveforms.

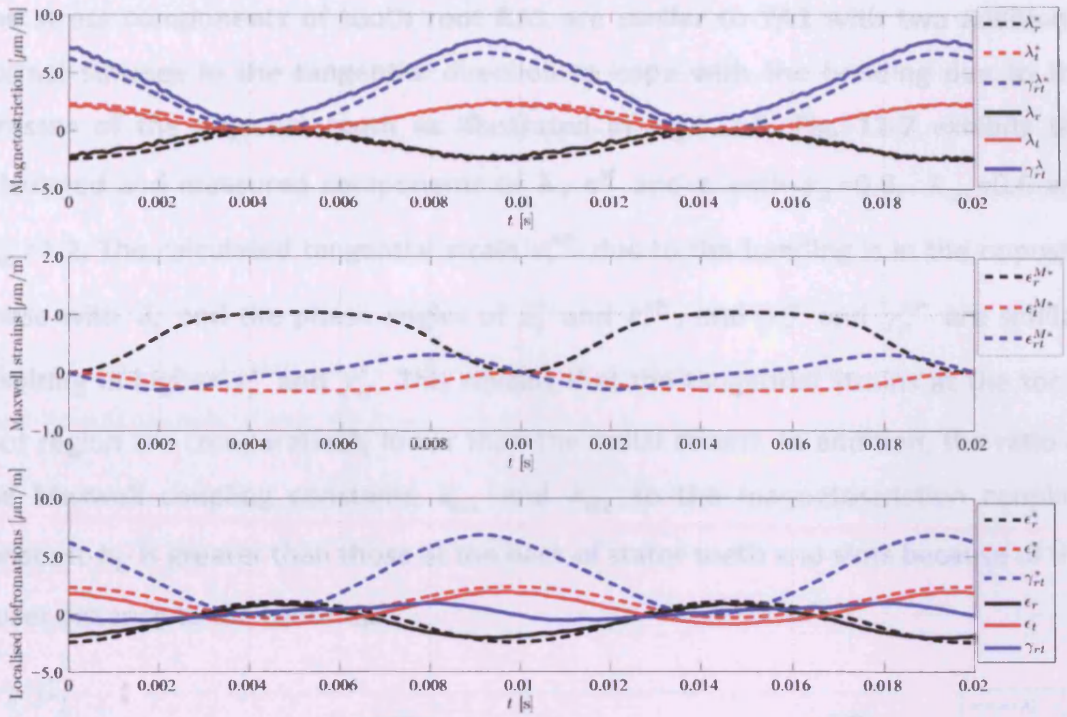

Fig. 12-5 Components of measured and calculated magnetostriction, strains due to Maxwell forces, and localised deformation at the back of stator tooth YA1 with the coupling constants k_λ =1.00 and k_M =0.20

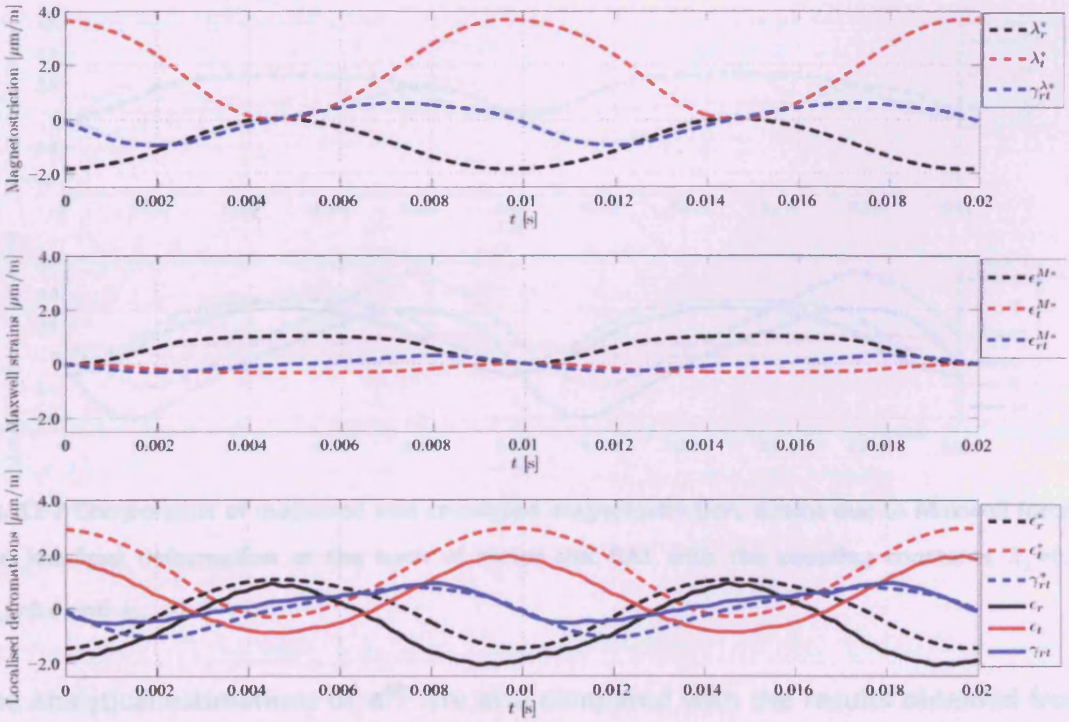

Fig. 12-6 Components of calculated magnetostriction ($P_x = P_y = P$ =136 GPa, $\xi_x = \xi_y = \xi$ =0.5, and $D = P/(2(1+\xi))$), strains due to Maxwell forces, and localised deformation at the back of stator tooth YA1 with the coupling constants k_λ =0.8 and k_M =0.2

The stress components of tooth root **RA1** are similar to **YA1** with two additional normal stresses in the tangential direction to cope with the bending due to the stresses of the adjacent teeth as illustrated in Fig. 12-3. Fig. 12-7 exhibits the calculated and measured components of $\boldsymbol{\lambda}$, $\boldsymbol{\varepsilon}^{M}$ and $\boldsymbol{\varepsilon}$ with k_{λ}=0.8, k_{M1}=0.6 and k_{M2}=1.2. The calculated tangential strain ε_t^{M*} due to the bending is in the opposite phase with λ_t and the phase angles of λ_r^* and ε_r^{M*}, and $\gamma_{rt}^{\lambda*}$ and γ_{rt}^{M*} are similar, resulting in higher ε_r^* and γ_{rt}^*. This reveals that the tangential strains at the tooth root region are comparatively lower than the radial strains. In addition, the ratio of the Maxwell coupling constants k_{M1} and k_{M2} to the magnetostriction coupling constant k_{λ} is greater than those at the back of stator teeth and slots because of the closer distance to the tooth tips.

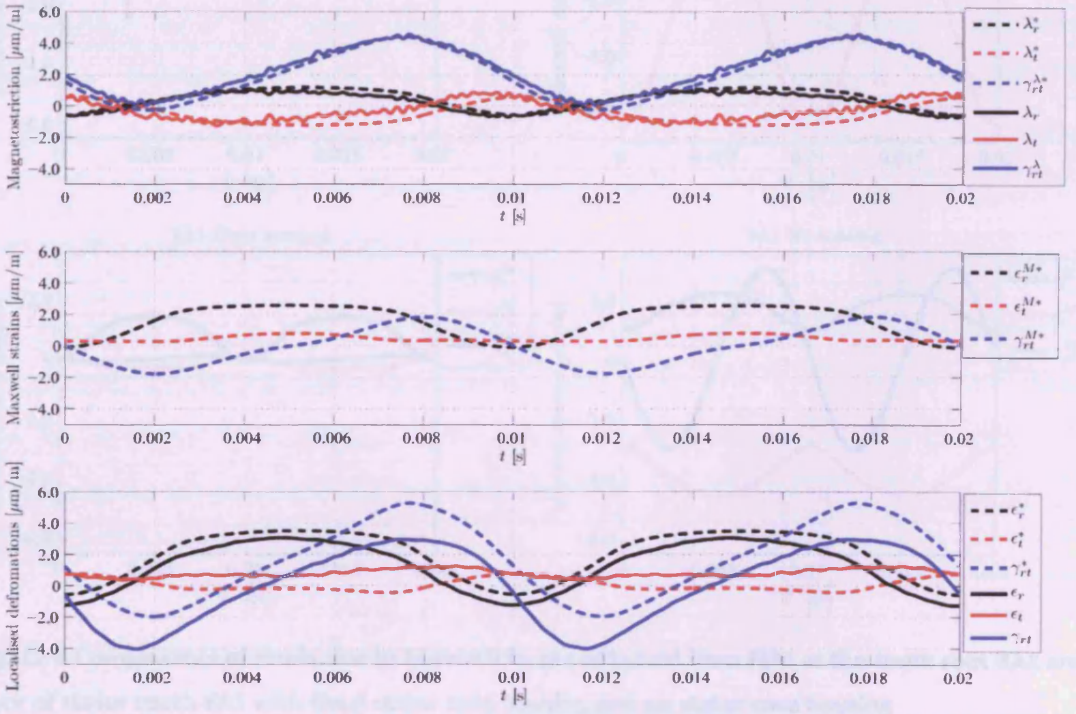

Fig. 12-7 Components of measured and calculated magnetostriction, strains due to Maxwell forces, and localised deformation at the back of stator slot RA1 with the coupling constants k_{λ}=0.8, k_{M1}=0.6 and k_{M2}=1.2

The analytical estimations of $\boldsymbol{\varepsilon}^{M*}$ are also compared with the results obtained from FEM. However, the results of $\boldsymbol{\varepsilon}^{M*}$ from FEM could not be used directly because the clamping on the stator yoke area is too complicated for a 2D problem. Despite this limitation another model was made with a fixed housing around the stator

circumference and the Maxwell stresses as the loads. At tooth root **RA1**, the model without housing as shown in Fig. 11-12 is closer to the analytical calculation since the phase angle of ε_t^M given in Fig. 12-8 is opposite to that of λ_t. However, the stator yoke of the model without housing is free to bend towards the rotor as seen from the large negative value of ε_t^M in Fig. 12-8. Thus, the stator yoke deformation of the fixed housing model should be closer to the conditions present in the motor model core as the waveforms of $\boldsymbol{\varepsilon}^M$ of this model at **YA1** are similar to the analytical calculations shown in Figs. 12-5 and 12-6.

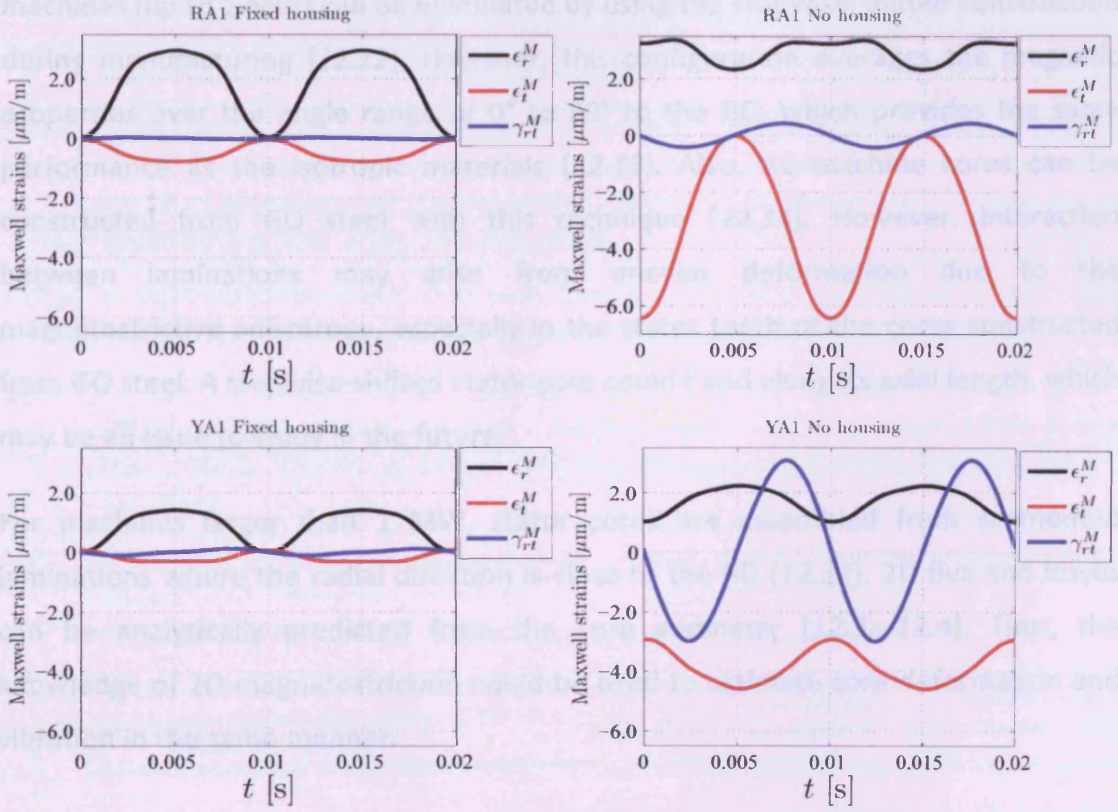

Fig. 12-8 Components of strain due to Maxwell forces obtained from FEM at the tooth root RA1 and back of stator tooth YA1 with fixed stator core housing and no stator core housing

12.4 Discussion

As discussed in **Section 3.4**, the radial component of the Maxwell forces is considered as the main source of core vibration and the stator core may be simplified to a ring shape as shown in Fig. 3-3. In this case, the estimated audible noise depends only on the radial stresses of the stator core acting on the inner surface of the housing [*12.11*]. However, the magnetostrictive forces in the back iron

and tooth root areas are expected to cause additional radial stresses. Based on the analytical estimation of the core localised deformation, the contribution of magnetostriction to the radial deformation can be calculated from $k_\lambda/(k_\lambda + k_M)$ for the back iron and $k_\lambda/(k_\lambda + k_{M1})$ for the tooth roots. It is found that the magnetostriction is responsible for about 80% and 55% of the radial deformation in the back iron and the tooth root regions respectively. Thus, magnetostriction should not be neglected for the analysis of core deformation, vibration and acoustic noise.

The effect of magnetic anisotropy on the performance of small to medium size AC machines (up to 1 MW) can be eliminated by using the stepwise-shifted construction during manufacturing [*12.12*]. However, this configuration averages the magnetic properties over the angle range of 0° to 90° to the RD, which provides the same performance as the isotropic materials [*12.13*]. Also, AC machine cores can be constructed from GO steel with this technique [*12.14*]. However, interaction between laminations may arise from uneven deformation due to the magnetostrictive anisotropy, especially in the stator teeth of the cores constructed from GO steel. A stepwise-shifted stator core could bend along its axial length, which may be an issue to study in the future.

For machines larger than 1 MW, stator cores are assembled from segmented laminations where the radial direction is close to the RD [*12.12*]. 2D flux and losses can be analytically predicted from the core geometry [*12.3, 12.4*]. Thus, the knowledge of 2D magnetostriction could be used to estimate core deformation and vibration in the same manner.

12.5 References for Chapter 12

[*12.1*] A. J. Moses and H. Rahmatizadeh, "Effects of stress on iron loss and flux distribution of an induction motor stator core," *IEEE Transactions on Magnetics*, Vol. 25, pp. 4003-4005, 1989.

[*12.2*] N. Tutkun, *Investigation of Power Loss under PWM Voltage Excitation in Wound Toroidal and Stator Cores*, PhD Thesis, Cardiff University, United Kingdom, 1998.

[*12.3*] G. Díaz, C. González-Morán, P. Arboleya, and J. Gómez-Aleixandre, "Analytical interpretation and quantification of rotational losses in stator cores of induction motors," *IEEE Transactions on Magnetics*, Vol. 43, pp. 3861-3867, 2007.

[*12.4*] M. Ranlof, A. Wolfbrandt, J. Lidenholm, and U. Lundin, "Core loss prediction in large hydropower generators: Influence of rotational fields," *IEEE Transactions on Magnetics*, Vol. 45, pp. 3200-3206, 2009.

[*12.5*] D. G. Dorrell, D. A. Staton, and M. I. McGilp, "Design of brushless permanent magnet motors - A combined electromagnetic and thermal approach to high performance specification," *Proceedings of the 32nd Annual Conference on IEEE Industrial Electronics (IECON)*, pp. 4853-4858, Paris, France, November 6-10, 2006.

[*12.6*] A. Bousbaine, "Thermal modelling of induction motors based on accurate loss density distribution," *Electric Machines and Power Systems*, Vol. 27, pp. 311-324, 1999.

[*12.7*] S. Somkun, A. J. Moses, and P. I. Anderson, "Effect of magnetostriction anisotropy in nonoriented electrical steels on deformation of induction motor stator cores," *IEEE Transactions on Magnetics*, Vol. 45, pp. 4744-4747, 2009.

[*12.8*] J. Le Besnerais, V. Lanfranchi, M. Hecquet, G. Friedrich, and P. Brochet, "Characterisation of radial vibration force and vibration behaviour of a pulse-width modulation-fed fractional-slot induction machine," *IET Electric Power Applications*, Vol. 3, pp. 197-208, 2009.

[*12.9*] P. Vijayraghavan and R. Krishnan, "Noise in electric machines: A review," *IEEE Transactions on Industry Applications*, Vol. 35, pp. 1007-1013, 1999.

[*12.10*] C. Krell, N. Baumgartinger, G. Krismanić, E. Leiss, and H. Pfützner, "Stress effects on the multidirectional magnetic behaviour of grain-oriented silicon iron sheets," *Journal of Magnetism and Magnetic Materials*, Vol. 215, pp. 63-65, 2000.

[*12.11*] C. Schlensok, D. van Riesen, M. van der Giet, and K. Hameyer, "Deformation analysis of induction machines by means of analytical and numerical methods," *IEEE Transactions on Magnetics*, Vol. 44, pp. 1498-1501, 2008.

[*12.12*] W. M. Arshad, T. Ryckebusch, F. Magnussen, H. Lendenmann, B. Eriksson, J. Soulard, and B. Malmros, "Incorporating lamination processing and component manufacturing in electrical machine design tools," *Proceedings of IEEE Industry Applications Society Annual Meeting (IAS2007)*, pp. 94-102, New Orleans, Louisiana, USA, 23-27 Sept. 2007, 2007.

[*12.13*] A. Daikoku, "Motor design technologies considering detailed magnetic properties in magnetic core," *Mitsubishi Electric ADVANCE*, pp. 5-7, 2006.

[*12.14*] S. Lopez, B. Cassoret, J. F. Brudny, L. Lefebvre, and J. N. Vincent, "Grain oriented steel assembly characterization for the development of high efficiency AC rotating electrical machines," *IEEE Transactions on Magnetics*, Vol. 45, pp. 4161-4164, 2009.

Chapter 13

Conclusion and Future Work

13.1 Conclusion

Magnetostrictive anisotropy in NO steels plays an important role in magnetostriction under 2D magnetisation. Peak to peak values of 2D magnetostriction are dependent on the flux density along the highly magnetostrictive direction in the sheet plane and the magnetic Poisson's ratios. The magnetic Poisson's ratios of NO steels were found to be nearly unity, higher than the theoretical value of 1/2. A 2D magnetostriction model was effective to represent magnetostriction of anisotropic NO steel under 2D magnetisation. 2D magnetostriction can be predicted from magnetostrictive anisotropy and vice versa.

AC magnetostriction measured in disc samples of NO steels was greater than that measured in Epstein strips due to sample shape and magnetic anisotropy in the material. Thus, magnetostriction characterised in narrow samples such as Epstein strip form should be used with caution for calculation of core deformation and vibration of large electrical machines.

Magnetic anisotropy of the 0.50 mm thick NO steel caused localised losses in stator core laminations to vary around the core circumference. High loss variation was found at the stator teeth and back iron. Loss variation also occurred at the tooth roots, where flux density loci are close to circular. This can lead to errors in temperature rise prediction of stator cores if the magnetic anisotropy is not taken into account.

Results showed that the magnetostrictive anisotropy in the 0.50 mm thick NO steel made the deformation non-uniform around the core circumference. The accuracy of deformation, vibration and acoustic noise prediction in induction motors could be improved if the magnetostrictive anisotropy is taken into account.

Results also inferred that the magnetostrictive anisotropy of NO steel may cause uneven deformation from lamination to lamination of small to medium size machine stator cores, where stepwise-shifted core configuration is used, which could be an issue to study in the future.

This research demonstrated that additional deformation due to magnetostriction in stator cores can be estimated analytically using the 2D magnetostriction model, which can be useful for predicting core deformation and vibration of large electrical machines, where segmented stator cores are used.

13.2 Future Work

This investigation has identified the need for further research in two areas: material characterisation and contributions of magnetostriction to core deformation and vibration.

Geometry-dependent magnetostriction should be investigated because the demagnetisation factor affects magnetostriction, which may cause high errors in calculation of deformation and vibration of large stator cores. Magnetostriction and magnetic properties under a dynamic stress should be studied as core materials are subjected to dynamic Maxwell stresses in AC machine cores. The uncertainties in loss and magnetostriction measurements of the 2D magnetisation system could be improved by using the measured surface magnetic field to compensate the air flux in the flux density measurement.

Magnetostrictive forces should be included in the calculations of stator core deformation and vibration using the 2D magnetostriction model. This can be done by analytical and numerical methods compared with experimental measurements. It is interesting to investigate deformation and vibration of stepwise-shifted stator cores

because the magnetostrictive anisotropy of NO steel could cause peculiar deformation along the axial length of the cores.

Appendix A

Calibration and Preliminary Test of Orthogonal *h* coils

A.1 Calibration of Orthogonal *h* coils

As discussed in **Section 6.3.4**, the orthogonal h coils were used to measure the tangential components of magnetic field on the surface of the samples in the 2D magnetisation system so that the specific power loss under 2D magnetisation can be calculated. To obtain accurate field measurement, the turn-area constants (K_{h_x} and K_{h_y}) of h_x and h_y coils were calibrated in a controlled magnetic field. Fig. A-1 displays a schematic diagram of the h coil calibration system which was used. A 1.15 m long cylindrical solenoid (internal diameter = 0.3 m) with a single layer 729 turns winding was used to provide an AC reference magnetic field (h_{ref}). The solenoid was connected to a power amplifier scaling up the sinusoidal voltage from the output of an NI PCI-6052E DAQ card [*A.1*] generated by a LabVIEW program. The voltage across the 0.1 Ω ± 1 % shunt resistor R_{sh} ($V_{i_{ref}}$) was read into the DAQ card to calculate the generating reference field current (i_{ref}) so that h_{ref} could be calculated from

$$h_{ref} = \frac{Ni_{ref}}{L_{sol}} = \frac{Nv_{i_{ref}}}{L_{sol}R_{sh}} \tag{A.1}$$

where N and L_{sol} are the winding turn number and length of the solenoid. The h_x and h_y coils were also connected with the analogue inputs of the DAQ card to obtain their induced voltage (e_{h_x} and e_{h_y}). All the lead wires were twisted to minimised voltages induced by stray fields. To obtain accurate values of K_{h_x} and K_{h_y}, each h coil has to be precisely aligned perpendicular to h_{ref}, where the maximum induced voltage occurs. Therefore, the h coils were placed on the high-ratio gearbox (1800:1) providing an angular resolution of 0.2° as shown in Fig. A-2 [*A.2*]. This gearbox was made from plastic components so it did not disturb the field.

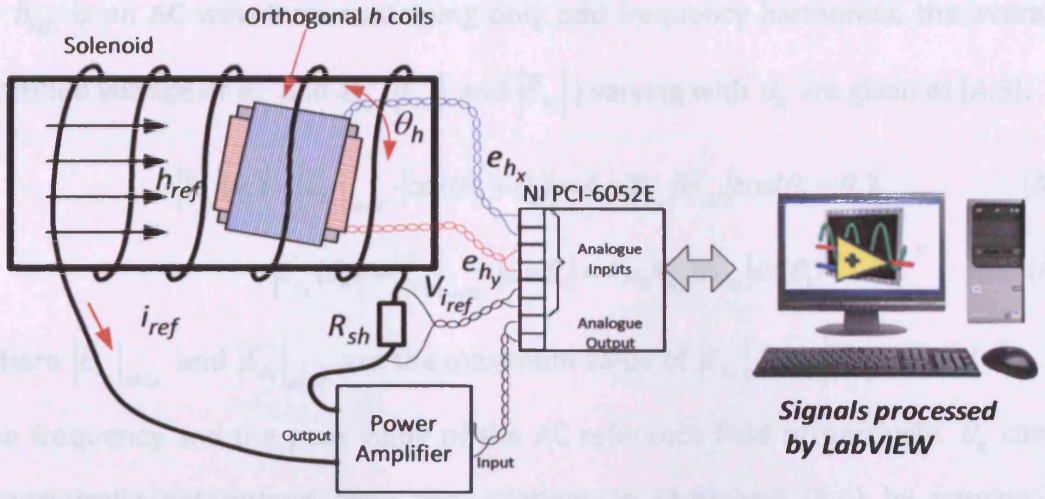

Fig. A-1 Schematic diagram of the *h* coil calibration system

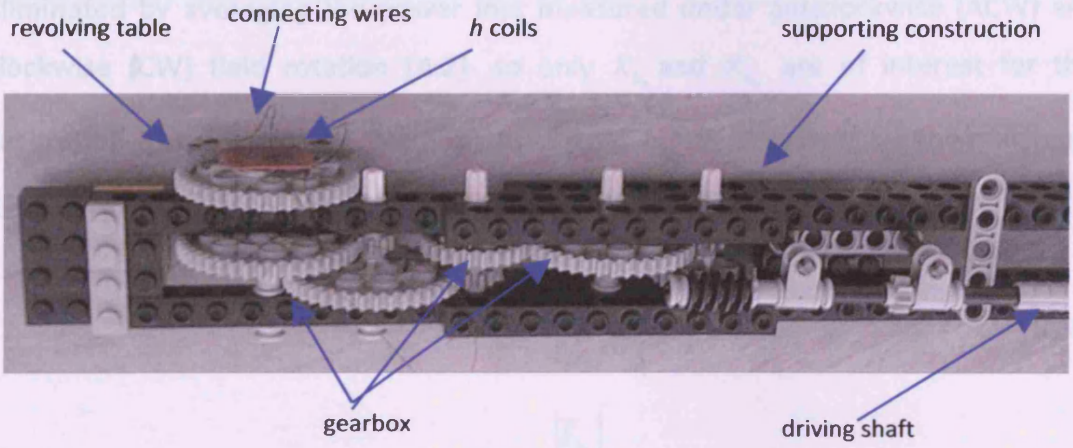

Fig. A-2 Photograph of the high-ratio gearbox used in the calibration of orthogonal *h* coils [*A.2*]

When one of h coil is exactly perpendicular to h_{ref}, its induced voltage is maximum and the voltage induced in the other coil should be zero if the two coils are orthogonal. In practice, the misalignment angle θ_e as show in Fig. A-3 causes non-zero voltage in one coil when the induced voltage in the other coil is at its maximum peak value. e_{h_x} and e_{h_y} can be written as functions of the angle θ_h as follows

$$e_{h_x}(\theta_h,t) = -\mu_0 K_{h_x} \frac{dh_{ref}}{dt} \cdot \cos(\theta_h + \theta_e) \qquad \text{(A.2)}$$

$$e_{h_y}(\theta_h,t) = -\mu_0 K_{h_y} \frac{dh_{ref}}{dt} \cdot \sin\theta_h \,. \qquad \text{(A.3)}$$

If h_{ref} is an AC waveform containing only odd frequency harmonics, the averaged rectified voltage of e_{h_x} and e_{h_y} ($|\bar{E}_{h_x}|$ and $|\bar{E}_{h_y}|$) varying with θ_h are given as [*A.3*].

$$|\bar{E}_{h_x}(\theta_h)| = |\bar{E}_{h_x}|_{MAX} \cdot |\cos(\theta_h + \theta_e)| = 4\mu_0 K_{h_x} f \hat{H}_{ref} |\cos(\theta_h + \theta_e)| \quad \text{(A.4)}$$

$$|\bar{E}_{h_y}(\theta_h)| = |\bar{E}_{h_y}|_{MAX} \cdot |\sin\theta_h| = 4\mu_0 K_{h_y} f \hat{H}_{ref} |\sin\theta_h| \quad \text{(A.5)}$$

where $|\bar{E}_{h_x}|_{MAX}$ and $|\bar{E}_{h_y}|_{MAX}$ are the maximum value of $|\bar{E}_{h_x}|$ and $|\bar{E}_{h_y}|$, f and $\hat{H}_{ref}$ are the frequency and the peak value of the AC reference field respectively. θ_e can be theoretically determined from the relations in (A.4) and (A.5) by varying θ_h. However, in the 2D magnetisation system described in **Chapter 6**, the effect of θ_e is eliminated by averaging the power loss measured under anticlockwise (ACW) and clockwise (CW) field rotation [*A.2*], so only K_{h_x} and K_{h_y} are of interest for this calibration. The value of $\hat{H}_{ref}$ was obtained from h_{ref} in (A.1) by using the maximum function in LabVIEW so that it was used to calculated K_{h_x} and K_{h_y} from

$$K_{h_x} = \frac{|\bar{E}_{h_x}|_{MAX}}{4\mu_0 f \hat{H}_{ref}} \quad \text{(A.6)}$$

$$K_{h_y} = \frac{|\bar{E}_{h_y}|_{MAX}}{4\mu_0 f \hat{H}_{ref}} \quad \text{(A.7)}$$

Three orthogonal h coils were calibrated. The h coils#1 and h coils#2 in Table A-1 were made and preliminarily calibrated in the Department of Electrical and Electronic Engineering, Okayama University, Japan but the calibration conditions were not recorded. h coils#3 in Table A-1 was wound on the same size former as the others in Cardiff. All h coils were then calibrated using the system in Fig. A-1. The calibration process was carried out in a sinusoidal reference field at $\hat{H}_{ref}$ =765 ± 10 A/m, 50 Hz, which corresponded to the maximum current available from the power amplifier. Fifty readings of each induced voltage were recorded and each reading was the averaged value of 100 cycles of the reference field waveform. The uncertainties of $\hat{H}_{ref}$, K_{h_x} and K_{h_y} were estimated from the expressions in (A.1), (A.6) and (A.7) in accordance with the procedure described in **Section 6.5**. It can be seen

in Table A-1 that the values of K_{h_x} and K_{h_y} agree closely with those calibrated at Okayama University.

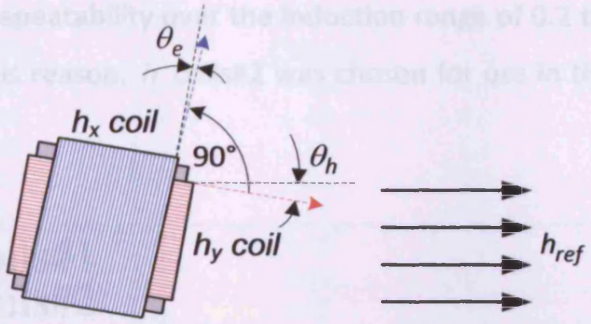

Fig. A-3 Schematic diagram of orthogonal h coils with misalignment angle θ_e in a reference magnetic field h_{ref}

Table A-1 Physical data and calibrated turn-area constants (K_{h_x} and K_{h_y}) of the h coils

	h coils#1		h coils#2		h coils#3	
	h_x coil	h_y coil	h_x coil	h_y coil	h_x coil	h_y coil
Former dimension	20 mm × 20 mm × 0.5 mm					
Wire diameter [mm]	0.05	0.05	0.05	0.05	0.1	0.1
Turn numbers	230	230	230	230	122	122
K_{h_x} and K_{h_y} [m^2] calibrated at Okayama University	0.0029124	0.0017843	0.0030484	0.0021576	-	-
K_{h_x} and K_{h_y} [m^2] Calibrated at Wolfson Centre for Magnetics	0.00290 ±0.00005	0.001857 ±0.000044	0.003119 ±0.000057	0.001989 ±0.000036	0.002151 ±0.000038	0.001733 ±0.000031

A.2 Preliminary Test of the Orthogonal *h* coils

The three orthogonal h coils were used to measure the tangential magnetic field components at the surface of a 0.50 mm thick NO electrical steel magnetised by the 2D magnetisation system described in **Section 6.3** under circular flux loci at the peak flux density from 0.2 T to 1.9 T, 50 Hz and the specific power loss P_s was calculated. The average values of P_s measured under ACW and CW field rotation were taken and repeated five times. Between measurements the h coils were removed and re-attached. As expected, the variation of the specific power loss is high at peak inductions greater than 1.60 T, where slight geometrical errors cause inaccuracy of field measurement as shown in Fig. A-4 [*A.4*]. Below 1.60 T, the difference in P_s

measured using different h coils was not noticeable. However, the repeatability of P_s calculated accordingly to (6.26) shows that h coils#2, having the highest constants, provided the best repeatability over the induction range of 0.2 to 1.8 T as compared in Table A-2. For this reason, h coils#2 was chosen for use in the 2D magnetisation system

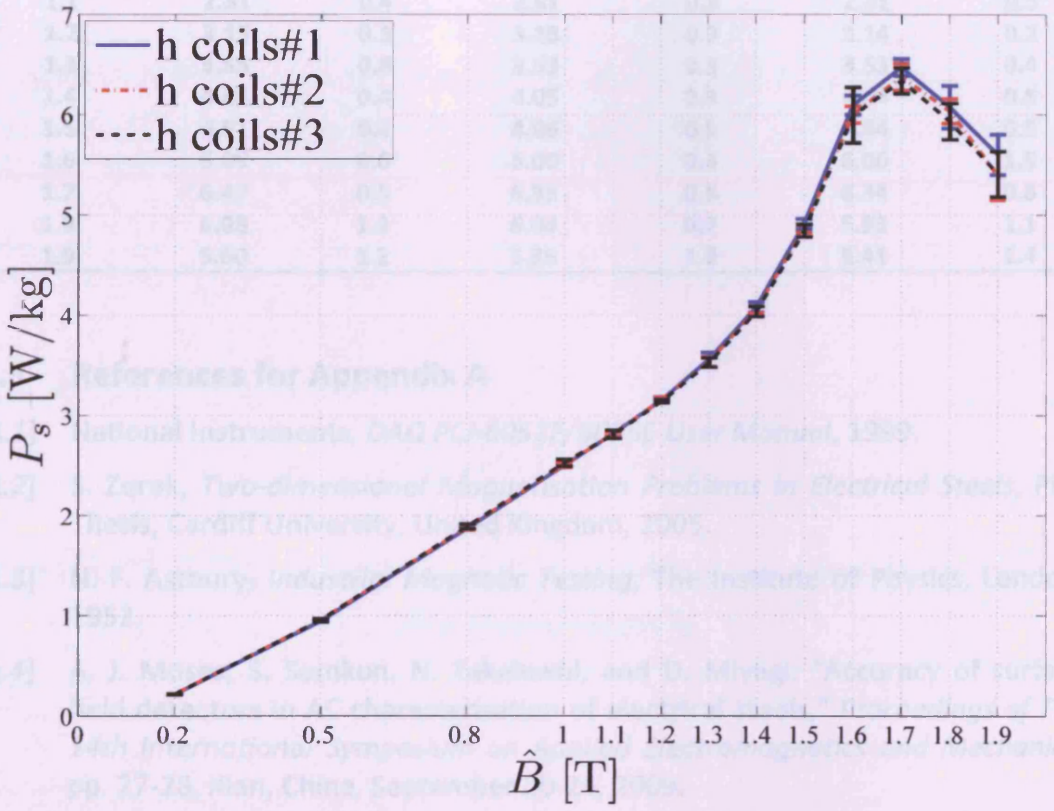

Fig. A-4 Comparison of specific power loss P_s of the 0.50 mm thick NO steel under circular flux density (50 Hz) using the three orthogonal h coils to detect surface field. Error bars show the spread of P_s measurements.

Table A-2 Comparison of repeatability of P_s ($u_A(P_s)$) of the 0.50 mm thick steel under circular flux density (50 Hz) using the three orthogonal h coils to detect surface field

Nominal $\hat{B}$ [T]	h coils#1		h coils#2		h coils#3	
	Average P_s [W/kg]	$u_A(P_s)$ ± %	Average P_s [W/kg]	$u_A(P_s)$ ± %	Average P_s [W/kg]	$u_A(P_s)$ ± %
0.2	0.21	0.7	0.22	0.5	0.21	0.8
0.5	0.94	0.4	0.95	0.5	0.95	0.5
0.8	1.87	0.3	1.88	0.5	1.89	0.4
1.0	2.50	0.2	2.50	0.3	2.52	0.4
1.1	2.81	0.4	2.81	0.3	2.81	0.5
1.2	3.15	0.3	3.15	0.3	3.14	0.2
1.3	3.55	0.8	3.53	0.5	3.53	0.4
1.4	4.08	0.4	4.05	0.3	4.04	0.5
1.5	4.91	0.4	4.86	0.3	4.84	0.5
1.6	6.09	0.6	6.00	0.4	6.00	1.5
1.7	6.47	0.5	6.38	0.8	6.34	0.8
1.8	6.08	1.3	6.04	0.7	5.93	1.1
1.9	5.60	1.2	5.39	1.8	5.41	1.4

A.3 References for Appendix A

[*A.1*] National Instruments, *DAQ PCI-6052E/6053E User Manual*, 1999.

[*A.2*] S. Zurek, *Two-dimensional Magnetisation Problems in Electrical Steels*, PhD Thesis, Cardiff University, United Kingdom, 2005.

[*A.3*] N. F. Astbury, *Industrial Magnetic Testing*, The Institute of Physics, London, 1952.

[*A.4*] A. J. Moses, S. Somkun, N. Takahashi, and D. Miyagi, "Accuracy of surface field detectors in AC characterisation of electrical steels," *Proceedings of The 14th International Symposium on Applied Electromagnetics and Mechanics*, pp. 27-28, Xian, China, September 20-24, 2009.

Appendix B

List of Type A Uncertainty of Measurements in NO Electrical Steels

Table B-1 Type A uncertainty of $\hat{B}$ measured in the SST of the 0.50 mm thick Epstein samples cut along the RD

Nominal	NO1-00A		NO1-00B		NO1-00C	
$\hat{B}$ [T]	Average $\hat{B}$ [T]	$u_A(\hat{B})$ [%]	Average $\hat{B}$ [T]	$u_A(\hat{B})$ [%]	Average $\hat{B}$ [T]	$u_A(\hat{B})$ [%]
0.10	0.1000	0.004	0.1000	0.000	0.1000	0.000
0.20	0.2000	0.000	0.2000	0.000	0.2000	0.000
0.30	0.3000	0.000	0.3000	0.000	0.3000	0.007
0.40	0.4000	0.009	0.4000	0.000	0.4000	0.005
0.50	0.5000	0.004	0.5000	0.005	0.5000	0.008
0.60	0.6000	0.006	0.6000	0.006	0.6000	0.008
0.70	0.7000	0.005	0.7000	0.006	0.7000	0.004
0.80	0.8000	0.005	0.8000	0.006	0.8000	0.007
0.90	0.8999	0.005	0.8999	0.003	0.9000	0.004
1.00	0.9999	0.004	1.0000	0.000	0.9999	0.004
1.10	1.1000	0.000	1.1000	0.000	1.1000	0.000
1.20	1.2000	0.000	1.2000	0.000	1.2000	0.000
1.30	1.3000	0.000	1.3000	0.000	1.3000	0.000
1.40	1.4000	0.000	1.4000	0.000	1.4000	0.000
1.50	1.5000	0.000	1.5000	0.000	1.5000	0.000
1.60	1.6000	0.000	1.6000	0.000	1.6000	0.000
1.70	1.7000	0.000	1.7000	0.000	1.7000	0.000

Table B-2 Type A uncertainty of P_s of the NO1-00 sample set measured in the SST

Nominal	NO1-00A		NO1-00B		NO1-00C	
$\hat{B}$ [T]	Average P_s [W/kg]	$u_A(P_s)$ [%]	Average P_s [W/kg]	$u_A(P_s)$ [%]	Average P_s [W/kg]	$u_A(P_s)$ [%]
0.10	0.016	0.98	0.016	0.27	0.017	1.98
0.20	0.07	0.85	0.067	0.12	0.071	0.26
0.30	0.151	0.53	0.146	0.26	0.156	0.32
0.40	0.253	0.48	0.246	0.12	0.263	0.30
0.50	0.373	0.39	0.366	0.99	0.39	0.25
0.60	0.509	0.31	0.499	0.57	0.533	0.27
0.70	0.662	0.50	0.649	0.37	0.694	0.26
0.80	0.837	0.32	0.816	0.26	0.875	0.27
0.90	1.028	0.30	1.009	0.14	1.073	0.19
1.00	1.242	0.29	1.223	0.17	1.295	0.19
1.10	1.488	0.35	1.463	0.13	1.547	0.11
1.20	1.757	0.31	1.742	0.11	1.833	0.18
1.30	2.092	0.21	2.070	0.15	2.176	0.18
1.40	2.488	0.21	2.463	0.13	2.603	0.13
1.50	2.962	0.15	2.927	0.13	3.093	0.13
1.60	3.421	0.15	3.382	0.12	3.537	0.11
1.70	3.784	0.15	3.752	0.12	3.878	0.11

Table B-3 Type A uncertainty of $\hat{H}$ of the NO1-00 sample set measured in the SST

Nominal	NO1-00A		NO1-00B		NO1-00C	
$\hat{B}$ [T]	Average $\hat{H}$ [A/m]	$u_A(\hat{H})$ [%]	Average $\hat{H}$ [A/m]	$u_A(\hat{H})$ [%]	Average $\hat{H}$ [A/m]	$u_A(\hat{H})$ [%]
0.10	24	1.4	23	1.1	25	1.4
0.20	33	1.4	32	1.4	34	1.1
0.30	38	0.7	37	2.1	40	0.8
0.40	42	0.6	41	2.0	44	0.5
0.50	45	0.6	45	1.5	48	0.5
0.60	49	0.8	49	1.4	51	0.4
0.70	52	0.8	52	1.2	55	0.4
0.80	56	0.7	57	0.9	59	0.5
0.90	62	0.8	64	0.8	65	0.5
1.00	71	1.0	74	0.7	76	0.6
1.10	88	1.0	93	0.4	95	0.5
1.20	119	0.7	127	0.3	129	0.3
1.30	181	0.5	193	0.3	202	0.3
1.40	333	0.4	351	0.2	398	0.2
1.50	831	0.1	837	0.3	1062	0.1
1.60	2205	0.1	2147	0.1	2732	0.1
1.70	4739	0.0	4587	0.0	5522	0.0

Table B-4 Type A uncertainty of $\mu_{r_{AC}}$ of the NO1-00 sample set measured in the SST

Nominal	NO1-00A		NO1-00B		NO1-00C	
$\hat{B}$ [T]	Average $\mu_{r_{AC}}$	$u_A(\mu_{r_{AC}})$ [%]	Average $\mu_{r_{AC}}$	$u_A(\mu_{r_{AC}})$ [%]	Average $\mu_{r_{AC}}$	$u_A(\mu_{r_{AC}})$ [%]
0.10	3310	1.32	3424	1.06	3159	1.38
0.20	4871	1.40	5032	1.37	4621	1.11
0.30	6334	0.71	6385	2.01	5967	0.79
0.40	7651	0.56	7718	1.88	7213	0.53
0.50	8821	0.56	8893	1.51	8326	0.52
0.60	9791	0.85	9849	1.40	9296	0.38
0.70	10638	0.73	10612	1.19	10140	0.50
0.80	11292	0.76	11118	0.87	10790	0.43
0.90	11592	0.80	11272	0.79	11022	0.53
1.00	11170	0.97	10720	0.68	10482	0.61
1.10	9915	0.89	9394	0.41	9212	0.57
1.20	8002	0.77	7502	0.30	7384	0.31
1.30	5722	0.49	5348	0.28	5132	0.25
1.40	3349	0.38	3176	0.22	2801	0.15
1.50	1436	0.09	1427	0.26	1123	0.05
1.60	577	0.06	593	0.05	466	0.05
1.70	285	0.04	295	0.04	245	0.03

Table B-5 Type A uncertainty of λ_{pp} of the NO1-00 sample set measured in the AC magnetostriction measurement system without stress applied

Nominal	NO1-00A		NO1-00B		NO1-00C	
$\hat{B}$ [T]	Average λ_{pp} [μm/m]	$u_A(\lambda_{pp})$ [%]	Average λ_{pp} [μm/m]	$u_A(\lambda_{pp})$ [%]	Average λ_{pp} [μm/m]	$u_A(\lambda_{pp})$ [%]
1.00	0.6	3.4	0.4	1.6	0.7	2.3
1.10	0.7	1.7	0.5	2.6	0.9	3.5
1.20	1.0	2.3	0.7	1.3	1.1	2.9
1.30	1.2	1.9	0.9	1.6	1.4	2.2
1.40	1.5	2.1	1.1	1.2	1.7	2.5
1.50	1.8	1.7	1.3	0.9	2.0	2.0
1.60	2.0	1.7	1.6	0.8	2.2	1.8
1.70	2.2	1.5	1.7	0.9	2.3	1.8

Table B-6 Type A uncertainty of λ_{pp} of the NO1-00 sample set measured in the AC magnetostriction measurement system with the applied stress of 10 MPa

Nominal	NO1-00A		NO1-00B		NO1-00C	
$\hat{B}$ [T]	Average λ_{pp} [μm/m]	$u_A(\lambda_{pp})$ [%]	Average λ_{pp} [μm/m]	$u_A(\lambda_{pp})$ [%]	Average λ_{pp} [μm/m]	$u_A(\lambda_{pp})$ [%]
1.00	-0.2	4.0	-0.2	2.9	-0.3	3.0
1.10	-0.3	3.8	-0.2	2.2	-0.3	2.4
1.20	-0.4	3.6	-0.3	2.3	-0.4	2.1
1.30	-0.5	2.9	-0.3	1.9	-0.5	2.0
1.40	-0.6	3.6	-0.4	1.6	-0.5	1.5
1.50	-0.7	3.3	-0.4	1.0	-0.6	1.3
1.60	-0.7	3.8	-0.5	1.2	-0.6	1.1

Table B-7 Type A uncertainty of λ_{pp} of the NO1-00 sample set measured in the AC magnetostriction measurement system with the applied stress of -5 MPa

Nominal	NO1-00A		NO1-00B		NO1-00C	
$\hat{B}$ [T]	Average λ_{pp} [μm/m]	$u_A(\lambda_{pp})$ [%]	Average λ_{pp} [μm/m]	$u_A(\lambda_{pp})$ [%]	Average λ_{pp} [μm/m]	$u_A(\lambda_{pp})$ [%]
1.00	2.1	2.0	1.6	1.6	2.3	1.5
1.10	2.6	1.7	2.0	2.2	2.9	2.1
1.20	3.2	1.7	2.6	1.6	3.5	2.1
1.30	3.9	1.3	3.2	1.4	4.1	2.0
1.40	4.5	1.6	3.8	1.3	4.7	1.4
1.50	5.1	1.2	4.4	1.0	5.3	1.1
1.60	5.5	1.1	4.8	1.0	5.8	1.0

Table B-8 Type A uncertainty of λ_{pp} of the NO1-00 sample set measured in the AC magnetostriction measurement system with the applied stress of -10 MPa

Nominal	NO1-00A		NO1-00B		NO1-00C	
$\hat{B}$ [T]	Average λ_{pp} [μm/m]	$u_A(\lambda_{pp})$ [%]	Average λ_{pp} [μm/m]	$u_A(\lambda_{pp})$ [%]	Average λ_{pp} [μm/m]	$u_A(\lambda_{pp})$ [%]
1.00	4.2	2.3	3.5	2.4	4.1	2.5
1.10	4.9	1.5	4.2	2.5	4.9	2.4
1.20	5.8	1.6	4.9	1.3	5.7	2.4
1.30	6.6	1.6	5.8	1.2	6.5	1.3
1.40	7.6	1.5	6.6	1.2	7.4	1.3
1.50	8.4	1.4	7.4	1.0	8.2	1.2
1.60	9.0	1.4	8.0	1.2	8.8	0.8

Table B-9 Type A uncertainty of Young's modulus of Epstein strips of the 0.50 mm thick NO steel cut at the angle of θ to the RD

Sample cut at θ	Young modulus, E [GPa]			Type A uncertainty, $u_A(E)$
[°]	Average	Maximum	Minimum	[%]
0	205	207	202	0.6
10	208	210	205	0.5
20	208	209	206	0.3
30	215	215	214	0.1
40	216	217	215	0.2
50	219	220	216	0.5
60	219	221	217	0.4
70	217	219	214	0.4
80	218	218	217	0.1
90	215	216	213	0.3

Table B-10 Type A uncertainty of Poisson's ratio of Epstein strips of the 0.50 mm thick NO steel cut at the angle of θ to the RD

Sample cut at θ	Poisson's ratio, ν			Type A uncertainty, $u_A(\nu)$
[°]	Average	Maximum	Minimum	[%]
0	0.28	0.29	0.28	0.4
10	0.28	0.28	0.28	0.0
20	0.30	0.30	0.30	0.3
30	0.28	0.28	0.27	0.2
40	0.34	0.35	0.34	0.1
50	0.29	0.29	0.29	0.2
60	0.32	0.32	0.31	0.5
70	0.27	0.27	0.27	0.3
80	0.30	0.30	0.30	0.1
90	0.30	0.30	0.30	0.1

Table B-11 Type A uncertainty of $\hat{B}_x$, $\hat{B}_y$ and P_s of the 0.50 mm thick NO steel under circular flux density 50 Hz

Nominal $\hat{B}$ [T]	Average $\hat{B}_x$ [T]	$u_A(\hat{B}_x)$ ± %	Average $\hat{B}_y$ [T]	$u_A(\hat{B}_y)$ ± %	Average P_s [W/kg]	$u_A(P_s)$ ± %
0.50	0.501	0.04	0.499	0.04	0.92	0.18
0.80	0.799	0.02	0.799	0.03	1.82	0.27
1.00	0.999	0.03	0.998	0.04	2.43	0.39
1.10	1.099	0.03	1.100	0.02	2.73	0.24
1.20	1.200	0.02	1.202	0.01	3.07	0.09
1.30	1.300	0.01	1.302	0.00	3.45	0.08
1.40	1.400	0.02	1.401	0.01	4.02	0.28
1.50	1.501	0.01	1.500	0.04	4.80	0.27
1.60	1.603	0.02	1.601	0.05	5.99	0.19
1.70	1.699	0.02	1.694	0.02	6.31	0.89
1.80	1.796	0.01	1.793	0.01	5.99	0.54
1.90	1.893	0.02	1.892	0.01	5.45	0.91

Table B-12 Type A uncertainty of $\hat{B}_x$, $\hat{B}_y$ and P_s of the 0.50 mm thick NO steel under elliptical flux density at α =0.25, θ =0°, 50 Hz

Nominal $\hat{B}$ [T]	Average $\hat{B}_x$ [T]	$u_A(\hat{B}_x)$ ± %	Average $\hat{B}_y$ [T]	$u_A(\hat{B}_y)$ ± %	Average P_s [W/kg]	$u_A(P_s)$ ± %
0.50	0.499	0.04	0.125	0.03	0.42	0.26
0.80	0.798	0.02	0.200	0.06	0.92	0.23
1.00	0.997	0.02	0.250	0.04	1.31	0.21
1.10	1.096	0.01	0.275	0.02	1.55	0.21
1.20	1.195	0.01	0.300	0.02	1.79	0.15
1.30	1.295	0.01	0.325	0.03	2.04	0.33
1.40	1.395	0.02	0.350	0.03	2.33	0.52
1.50	1.495	0.01	0.375	0.03	2.73	0.34
1.60	1.594	0.00	0.400	0.03	3.36	0.37
1.70	1.694	0.01	0.425	0.03	4.29	0.20
1.80	1.793	0.00	0.450	0.03	5.19	0.29
1.90	1.893	0.01	0.475	0.02	5.84	0.18

Table B-13 Type A uncertainty of $\hat{B}_x$, $\hat{B}_y$ and P_s of the 0.50 mm thick NO steel under elliptical flux density at α =0.25, θ =90°, 50 Hz

Nominal $\hat{B}$ [T]	Average $\hat{B}_x$ [T]	$u_A(\hat{B}_x)$ ± %	Average $\hat{B}_y$ [T]	$u_A(\hat{B}_y)$ ± %	Average P_s [W/kg]	$u_A(P_s)$ ± %
0.50	0.125	0.08	0.499	0.02	0.58	0.13
0.80	0.201	0.05	0.802	0.05	1.22	0.34
1.00	0.250	0.05	1.003	0.03	1.72	0.31
1.10	0.275	0.05	1.103	0.03	2.01	0.41
1.20	0.300	0.02	1.202	0.03	2.31	0.15
1.30	0.326	0.05	1.301	0.03	2.64	0.10
1.40	0.351	0.04	1.398	0.03	3.07	0.38
1.50	0.375	0.05	1.496	0.02	3.66	0.45
1.60	0.401	0.03	1.595	0.01	4.47	0.31
1.70	0.425	0.04	1.695	0.01	5.38	0.50
1.80	0.451	0.02	1.794	0.00	6.12	0.35

Table B-14 Type A uncertainty of $\hat{B}_x$, $\hat{B}_y$ and P_s of the 0.35 mm thick NO steel under circular flux density 50 Hz

Nominal $\hat{B}$ [T]	Average $\hat{B}_x$ [T]	$u_A(\hat{B}_x)$ ± %	Average $\hat{B}_y$ [T]	$u_A(\hat{B}_y)$ ± %	Average P_s [W/kg]	$u_A(P_s)$ ± %
0.50	0.501	0.06	0.499	0.06	0.60	0.16
0.80	0.801	0.03	0.798	0.03	1.18	0.16
1.00	1.003	0.02	0.997	0.02	1.57	0.12
1.10	1.103	0.03	1.099	0.03	1.75	0.18
1.20	1.203	0.02	1.202	0.03	1.96	0.22
1.30	1.303	0.04	1.302	0.03	2.22	0.29
1.40	1.403	0.04	1.401	0.02	2.66	0.24
1.50	1.502	0.02	1.499	0.02	2.95	0.52
1.60	1.601	0.05	1.605	0.05	2.93	0.24
1.70	1.698	0.04	1.693	0.03	2.58	1.05
1.80	1.794	0.03	1.793	0.01	2.18	2.42
1.90	1.892	0.01	1.892	0.01	1.73	2.53

Table B-15 Type A uncertainty of $\hat{B}_x$, $\hat{B}_y$ and P_s of the 0.35 mm thick NO steel under elliptical flux density at α =0.25, θ=0°, 50 Hz

Nominal $\hat{B}$ [T]	Average $\hat{B}_x$ [T]	$u_A(\hat{B}_x)$ ± %	Average $\hat{B}_y$ [T]	$u_A(\hat{B}_y)$ ± %	Average P_s [W/kg]	$u_A(P_s)$ ± %
0.50	0.499	0.10	0.125	0.08	0.33	0.40
0.80	0.801	0.08	0.200	0.04	0.70	0.43
1.00	1.002	0.08	0.250	0.08	0.99	0.42
1.10	1.101	0.10	0.274	0.04	1.15	0.42
1.20	1.200	0.13	0.300	0.09	1.32	0.24
1.30	1.301	0.11	0.325	0.04	1.52	0.49
1.40	1.400	0.12	0.350	0.05	1.78	0.32
1.50	1.499	0.10	0.376	0.06	2.13	0.59
1.60	1.596	0.06	0.400	0.04	2.41	0.39
1.70	1.694	0.04	0.425	0.06	2.60	0.31
1.80	1.794	0.02	0.451	0.05	2.70	0.74

Table B-16 Type A uncertainty of $\hat{B}_x$, $\hat{B}_y$ and P_s of the 0.35 mm thick NO steel under elliptical flux density at α =0.25, θ=90°, 50 Hz

Nominal $\hat{B}$ [T]	Average $\hat{B}_x$ [T]	$u_A(\hat{B}_x)$ ± %	Average $\hat{B}_y$ [T]	$u_A(\hat{B}_y)$ ± %	Average P_s [W/kg]	$u_A(P_s)$ ± %
0.50	0.125	0.10	0.499	0.05	0.35	0.60
0.80	0.200	0.07	0.798	0.03	0.74	0.45
1.00	0.250	0.06	0.997	0.04	1.06	0.45
1.10	0.275	0.06	1.099	0.02	1.24	0.56
1.20	0.300	0.06	1.202	0.03	1.44	0.40
1.30	0.325	0.07	1.302	0.03	1.66	0.40
1.40	0.350	0.04	1.401	0.04	1.94	0.47
1.50	0.375	0.04	1.499	0.02	2.32	0.18
1.60	0.400	0.04	1.605	0.02	2.59	0.33
1.70	0.425	0.03	1.693	0.03	2.77	0.72
1.80	0.450	0.03	1.793	0.04	2.94	0.40

Table B-17 Type A uncertainty of $\lambda_{x_{pp}}$, $\lambda_{y_{pp}}$, $\hat{\lambda}_1$ and $\hat{\lambda}_2$ of the 0.50 mm thick NO steel under circular flux density 50 Hz

Nominal $\hat{B}$ [T]	Average $\lambda_{x_{pp}}$ [μm/m]	$u_A(\lambda_{x_{pp}})$ ± %	Average $\lambda_{y_{pp}}$ [μm/m]	$u_A(\lambda_{y_{pp}})$ ± %	Average $\hat{\lambda}_1$ [μm/m]	$u_A(\hat{\lambda}_1)$ ± %	Average $\hat{\lambda}_2$ [μm/m]	$u_A(\hat{\lambda}_2)$ ± %
0.50	1.6	2.2	1.7	2.0	1.6	2.2	-1.7	1.9
0.80	3.1	2.2	3.4	2.2	3.2	2.2	-3.4	2.2
1.00	4.7	1.0	5.0	1.5	4.8	1.0	-5.0	1.6
1.10	5.8	0.8	6.1	1.0	5.8	0.8	-6.1	1.0
1.20	7.2	1.2	7.3	0.8	7.2	1.2	-7.3	0.8
1.30	8.8	0.9	8.4	0.7	8.9	1.0	-8.4	0.8
1.40	10.8	1.0	9.3	1.0	10.9	1.0	-9.4	1.0
1.50	12.6	1.1	9.9	1.2	12.7	1.1	-10.2	1.0
1.60	13.8	1.1	10.6	1.6	14.1	1.0	-11.1	1.3
1.70	14.3	1.9	10.8	1.5	14.7	1.7	-11.4	0.9
1.80	14.3	2.8	10.6	2.1	14.7	2.7	-11.4	1.5
1.90	14.1	3.9	10.0	3.0	14.6	3.9	-11.1	2.5

Table B-18 Type A uncertainty of $\lambda_{x_{pp}}$, $\lambda_{y_{pp}}$, $\hat{\lambda}_1$ and $\hat{\lambda}_2$ of the 0.50 mm thick NO steel under elliptical flux density at a =0.25, θ =0°, 50 Hz

Nominal $\hat{B}$ [T]	Average $\lambda_{x_{pp}}$ [μm/m]	$u_A(\lambda_{x_{pp}})$ ± %	Average $\lambda_{y_{pp}}$ [μm/m]	$u_A(\lambda_{y_{pp}})$ ± %	Average $\hat{\lambda}_1$ [μm/m]	$u_A(\hat{\lambda}_1)$ ± %	Average $\hat{\lambda}_2$ [μm/m]	$u_A(\hat{\lambda}_2)$ ± %
0.50	0.7	4.3	0.7	4.2	0.5	4.0	-0.6	1.9
0.80	0.8	3.8	0.8	4.2	0.7	3.9	-0.8	2.5
1.00	0.8	4.9	1.0	4.5	0.9	3.5	-0.9	3.7
1.10	0.9	4.6	1.1	3.3	1.0	3.0	-1.0	1.8
1.20	1.0	3.8	1.1	4.0	1.1	3.8	-1.1	1.8
1.30	1.1	4.7	1.2	3.2	1.3	2.4	-1.3	2.2
1.40	1.2	4.0	1.3	2.9	1.4	3.0	-1.5	1.9
1.50	1.7	4.5	1.4	3.4	1.8	1.8	-1.6	2.6
1.60	2.2	3.7	1.7	3.5	2.6	1.4	-1.6	1.3
1.70	2.3	4.5	1.8	3.7	3.1	1.4	-1.7	1.6
1.80	2.2	4.5	1.9	4.8	3.9	0.8	-1.3	1.7
1.90	2.1	4.4	1.9	4.9	5.1	0.7	-0.8	4.3

Table B-19 Type A uncertainty of $\lambda_{x_{pp}}$, $\lambda_{y_{pp}}$, $\hat{\lambda}_1$ and $\hat{\lambda}_2$ of the 0.50 mm thick NO steel under elliptical flux density at α =0.25, θ =90°, 50 Hz

Nominal $\hat{B}$ [T]	Average $\lambda_{x_{pp}}$ [μm/m]	$u_A(\lambda_{x_{pp}})$ ± %	Average $\lambda_{y_{pp}}$ [μm/m]	$u_A(\lambda_{y_{pp}})$ ± %	Average $\hat{\lambda}_1$ [μm/m]	$u_A(\hat{\lambda}_1)$ ± %	Average $\hat{\lambda}_2$ [μm/m]	$u_A(\hat{\lambda}_2)$ ± %
0.50	1.6	1.9	1.7	2.3	1.5	2.1	-1.5	1.1
0.80	3.4	1.0	3.5	1.7	3.2	1.8	-3.3	1.4
1.00	5.1	0.9	5.2	0.8	5.0	2.1	-5.2	1.6
1.10	6.1	0.9	6.1	0.6	6.1	2.3	-6.3	1.7
1.20	7.4	0.5	7.1	0.7	7.1	1.3	-7.6	1.4
1.30	8.8	0.4	7.9	0.4	8.1	1.2	-9.0	1.1
1.40	10.4	0.4	8.8	0.5	9.0	1.0	-10.6	0.8
1.50	11.7	0.3	9.4	0.3	9.4	0.7	-12.0	0.4
1.60	12.3	0.4	9.5	0.7	9.6	0.3	-12.8	0.3
1.70	12.5	0.3	9.4	0.5	9.4	0.4	-13.1	0.3
1.80	12.8	0.3	9.4	0.5	9.6	0.7	-13.1	0.3

Table B-20 Type A uncertainty of $\lambda_{x_{pp}}$, $\lambda_{y_{pp}}$, $\hat{\lambda}_1$ and $\hat{\lambda}_2$ of the 0.35 mm thick NO steel under circular flux density 50 Hz

Nominal $\hat{B}$ [T]	Average $\lambda_{x_{pp}}$ [μm/m]	$u_A(\lambda_{x_{pp}})$ ± %	Average $\lambda_{y_{pp}}$ [μm/m]	$u_A(\lambda_{y_{pp}})$ ± %	Average $\hat{\lambda}_1$ [μm/m]	$u_A(\hat{\lambda}_1)$ ± %	Average $\hat{\lambda}_2$ [μm/m]	$u_A(\hat{\lambda}_2)$ ± %
0.50	1.6	2.1	1.8	1.3	1.1	2.1	-1.0	2.2
0.80	3.4	0.9	3.9	1.5	2.6	1.0	-1.8	1.9
1.00	5.3	0.9	5.9	0.9	4.1	3.6	-2.8	0.7
1.10	6.7	0.9	7.0	0.6	5.1	1.7	-3.5	2.9
1.20	8.1	0.9	8.2	0.5	6.1	0.4	-4.4	0.5
1.30	9.7	0.6	9.5	0.5	6.6	1.2	-5.8	1.6
1.40	11.3	0.7	10.6	0.5	7.8	1.1	-7.0	1.2
1.50	12.8	0.4	11.7	0.4	8.6	2.1	-8.0	1.4
1.60	14.0	0.6	12.5	0.4	8.8	2.0	-9.0	1.1
1.70	14.7	0.6	13.1	0.5	9.1	2.2	-9.3	1.6
1.80	14.9	0.7	13.2	0.5	9.1	2.9	-9.4	1.4
1.90	14.8	1.1	12.7	1.1	8.9	1.2	-9.1	0.5

Table B-21 Type A uncertainty of $\lambda_{x_{pp}}$, $\lambda_{y_{pp}}$, $\hat{\lambda}_1$ and $\hat{\lambda}_2$ of the 0.35 mm thick NO steel under elliptical flux density at α =0.25, θ=0°, 50 Hz

Nominal $\hat{B}$ [T]	Average $\lambda_{x_{pp}}$ [μm/m]	$u_A(\lambda_{x_{pp}})$ ± %	Average $\lambda_{y_{pp}}$ [μm/m]	$u_A(\lambda_{y_{pp}})$ ± %	Average $\hat{\lambda}_1$ [μm/m]	$u_A(\hat{\lambda}_1)$ ± %	Average $\hat{\lambda}_2$ [μm/m]	$u_A(\hat{\lambda}_2)$ ± %
0.50	1.5	2.7	1.1	3.1	0.8	4.5	-1.3	2.4
0.80	2.7	1.2	1.9	1.3	1.6	4.6	-1.5	4.0
1.00	3.4	1.3	2.7	1.9	2.2	1.7	-2.4	3.1
1.10	3.7	0.6	3.2	1.2	2.3	4.7	-3.1	1.5
1.20	4.0	0.6	4.0	1.1	2.6	3.3	-3.8	0.7
1.30	4.2	0.7	4.8	1.1	2.7	3.4	-4.8	1.3
1.40	4.3	0.8	6.0	0.7	2.6	3.4	-6.1	0.9
1.50	4.3	0.7	7.3	0.8	2.5	6.2	-7.5	0.6
1.60	4.5	1.1	8.1	0.5	2.6	5.1	-8.5	0.5
1.70	4.8	0.9	8.6	0.5	2.9	6.2	-9.1	0.4
1.80	4.8	0.6	9.1	0.4	2.8	6.5	-9.7	0.4

Table B-22 Type A uncertainty of $\lambda_{x_{pp}}$, $\lambda_{y_{pp}}$, $\hat{\lambda}_1$ and $\hat{\lambda}_2$ of the 0.35 mm thick NO steel under elliptical flux density at α =0.25, θ=90°, 50 Hz

Nominal $\hat{B}$ [T]	Average $\lambda_{x_{pp}}$ [μm/m]	$u_A(\lambda_{x_{pp}})$ ± %	Average $\lambda_{y_{pp}}$ [μm/m]	$u_A(\lambda_{y_{pp}})$ ± %	Average $\hat{\lambda}_1$ [μm/m]	$u_A(\hat{\lambda}_1)$ ± %	Average $\hat{\lambda}_2$ [μm/m]	$u_A(\hat{\lambda}_2)$ ± %
0.50	1.1	3.3	1.6	1.6	1.4	2.7	-0.8	4.3
0.80	2.2	2.4	2.8	1.3	2.7	4.1	-1.9	3.9
1.00	3.4	1.1	3.8	1.1	3.4	4.0	-3.3	3.3
1.10	4.1	0.8	4.1	0.7	3.8	3.3	-4.0	4.4
1.20	5.0	0.8	4.5	0.6	4.0	2.5	-5.0	3.7
1.30	6.2	0.4	5.0	0.6	4.5	2.9	-6.2	2.2
1.40	7.5	0.6	5.3	0.6	4.6	2.0	-7.7	2.2
1.50	8.9	0.4	5.4	1.2	4.7	2.8	-9.1	1.5
1.60	9.8	0.4	5.5	0.8	4.8	4.2	-10.1	1.5
1.70	10.1	0.3	5.6	1.2	4.6	4.7	-10.7	1.8
1.80	10.4	0.5	5.7	0.8	4.5	4.6	-10.9	1.8

Appendix C

List of Publications

International Journals

1. **S. SOMKUN**, A. J. Moses, and P. I. Anderson, "Mechanical resonance in nonoriented electrical steels induced by magnetostriction under PWM voltage excitation," *IEEE Transaction on Magnetics*, vol. 44, pp. 4062-4065, Nov. 2008.
2. **S. SOMKUN**, A. J. Moses, S. Zurek, and P. I. Anderson, "Development of an induction motor core model for measuring rotational magnetostriction under PWM magnetisation," *Przegląd Elektrotechniczny (Electrical Reviews)*, vol. R. 85, pp. 103-107, 2009.
3. **S. SOMKUN**, A. J. Moses, and P. I. Anderson, "Effect of magnetostriction anisotropy in nonoriented electrical steels on deformation of induction motor stator cores," *IEEE Transaction on Magnetics*, vol. 45, pp. 4744-4747, Oct. 2009.
4. **S. SOMKUN**, A. J. Moses, P. I. Anderson and P. Klimczyk, "Magnetostriction anisotropy and rotational magnetostriction of a nonoriented electrical steel," *IEEE Transaction on Magnetics*, vol. 46, pp. 302-305, February 2010.
5. **S. SOMKUN**, P. Klimczyk, A. J. Moses and P. I. Anderson, "Comparisons of AC magnetostriction of non-oriented electrical steels measured in Epstein and disc samples," Accepted for publication in *Journal of Electrical Engineering.*
6. P. Klimczyk, **S. SOMKUN**, P. I. Anderson and A. J. Moses, "Comparison of uniaxial and rotational magnetostriction of non-oriented and grain-oriented electrical steel," Submitted to *Przegląd Elektrotechniczny (Electrical Reviews)* for consideration.

International Conferences

1. X. Yao, A. J. Moses, **S. SOMKUN**, F. Anayi, "Rotating flux and estimation rotational loss in the joints of a model three-phase three-limb transformer core under sinusoidal and PWM voltage excitation," in the abstract CD of *IEEE International Magnetics Conference (INTERMAG 2009)*, May 4-8, 2009, Sacramento, California, USA.
2. A. J. Moses, **S. SOMKUN**, N. Takahashi, and D. Miyagi, "Accuracy of surface field detectors in AC characterisation of electrical steels," in proceedings of *The 14th International Symposium on Applied Electromagnetics and Mechanics (ISEM)*, September 20-24, 2009, Xian, China, pp. 27-28.
3. **S. SOMKUN**, A. J. Moses, P. I. Anderson and P. Klimczyk, "Quantification of magnetostriction for analysis of vibration of electrical machine cores," in the proceeding CD of *The 45th International Universities' Power Engineering Conference (UPEC 2010)*, Cardiff, UK, August 31–September 3, 2010.
4. **S. SOMKUN**, A. J. Moses, and P. I. Anderson, "Measurement and modelling of 2D magnetostriction of non-oriented electrical steel," Submitted to *The 18th International Conference on the Computation of Electromagnetic Fields (COMPUMAG2011)*, Sydney, Australia, July 12-15, 2011, for consideration.